SISSA
Scuola
Internazionale
Superiore di
Studi Avanzati



International School for Advanced Studies

Physics Area — PhD course in
Theory and Numerical Simulation of Condensed Matter

PhD Thesis

Quantum information insights into strongly correlated electrons

Gabriele Bellomia

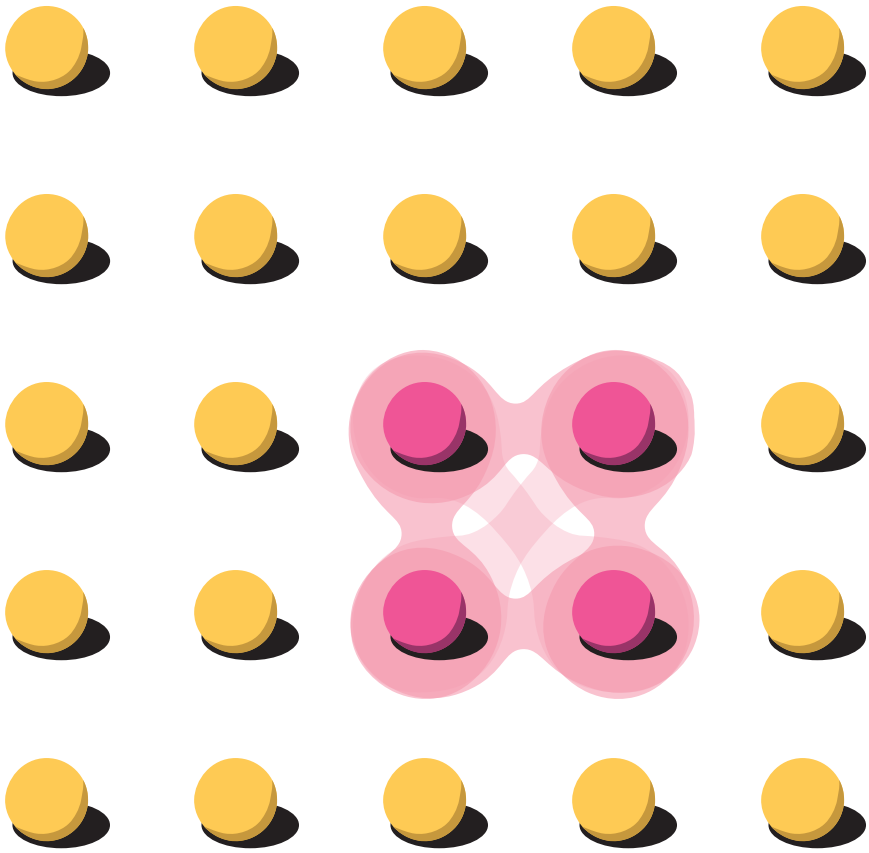
Supervisor: Massimo Capone
Condensed Matter Theory
International School for Advanced Studies

Co-supervisor: Adriano Amaricci
Officina dei Materiali
Consiglio Nazionale delle Ricerche

April 2024

Quantum information insights into strongly correlated electrons

Gabriele Bellomia



April 2024

Gabriele Bellomia

Quantum information insights into strongly correlated electrons

PhD Thesis, April 2024

Supervisors: Massimo Capone and Adriano Amaricci

International School for Advanced Studies

Condensed Matter Theory

Physics Area

via Bonomea, 265

34136 — Trieste

Abstract

Recent theoretical and experimental advances have opened new perspectives on the characterization of strongly correlated phases of matter, adding a new layer of understanding based on concepts and tools borrowed from quantum information theory. We join the effort by investigating, within dynamical mean-field theory and its cluster extension, the local and quasilocal (*i.e.* short-range) quantum information content of salient landmarks in the phase diagram of the two-dimensional Hubbard model, the cornerstone model for the description of the physics of cuprate materials, and of a closely related model for interacting topological states on the honeycomb lattice.

In the first part of the thesis, we focus on the dynamical mean-field theory solution of the Kane-Mele-Hubbard model, at zero temperature. In the thermodynamic limit we find evidence of an interaction-driven discontinuous quantum phase transition between the $\mathbb{Z}_2$ quantum spin-Hall insulator and anisotropic antiferromagnetic solutions, with an intermediate regime of coexistence of nontrivial topology and magnetic order.
A clear-cut interpretation of these results is given in terms of a rigorous quantification of quantum and classical correlations contained in a single local orbital (which we refer to as *intra-orbital* mutual information), providing a notion of "statistical distance" from the Hartree-Fock description of the system. The resulting analysis complements the established Green's function based understanding of the relationship between dynamical and static mean-field theories. In particular, we find the magnetic solutions of dynamical mean-field theory to asymptotically approach the corresponding uncorrelated Hartree-Fock states, in the strong coupling limit, in stark contrast with the paramagnetic Mott-Hubbard solution, which in turn reveals a maximally correlated local spin-orbital pair at large interaction strength. Furthermore, these findings cast some light on the relationship between Mott localization and the possible development of nonlocal entanglement.

In the second part of the thesis, we provide an alternative view of both the interaction-driven and density-driven paramagnetic Mott transitions in the two-dimensional Hubbard model, in terms of rigorous measures of entanglement and correlation between two spatially separated electronic orbitals, with no contribution from their environment. A space-resolved analysis of cluster dynamical mean-field theory results elucidates the prominent role of the *nearest-neighbor* entanglement in probing Mott localization: two traditional upper bounds and two recently introduced lower bounds for its magnitude sharply increase at the

metal-insulator transition, in contrast with the moderate variation found at all interaction strengths that are sufficiently far from the transition point. At half-filling, the two-site entanglement *beyond nearest neighbors* is shown to be quickly damped as the inter-site distance is increased within the cluster, suggesting that Mott-Hubbard insulators may follow an *area law*. However, the size of the simulated clusters does not allow a quantitative analysis of the decay, so that a precise classification of the spatial entanglement properties of the system is left for future study. In the presence of hole-doping, we show how the pseudogap metal separating the Mott-Hubbard insulator from the hole-dominated Fermi liquid features quasilocal entanglement properties that are strikingly similar to the localized Mott phase, while it is separated from the low-entangled Fermi liquid by a discontinuous jump in all the computed entanglement and correlation measures.

All the presented results ultimately resolve a conundrum of previous analyses based on the single-site von Neumann entropy, which has been found to monotonically decrease when the interaction is increased, defeating the purpose of capturing and understanding strong electronic correlations with the aid of quantum information concepts. Both the intra-orbital mutual information and the quasilocal two-site entanglement, on the other hand, recover instead the distinctive character of Mott insulators and pseudogap metals as strongly correlated many-body states, demonstrating its central role in future advancements in the field of quantum materials.

Publications

[1] G. Bellomia and R. Resta *Drude weight in systems with open boundary conditions*
↪ not covered in this thesis Phys. Rev. B **102**, 205123 (2020)

[2] G. Bellomia *et al. Mottness, magnetism and topology of interacting Dirac fermions: a dynamical mean-field theory study of intra-orbital correlations*
↪ covered in chapters 1, 2, 3, 4 in preparation

[3] G. Bellomia *et al. Quasilocal entanglement across the Mott-Hubbard transition*
↪ covered in chapters 6, 7, 8, 9 Phys. Rev. B **109**, 115104 (2024)

[4] G. Bellomia *et al. Quasilocal entanglement in the doped 2d Hubbard model*
↪ covered in chapters 6, 7, 8, 10 in preparation

Preface

The field of strongly correlated electrons has been among the most lively in condensed matter in the last few decades. A new era started with the discovery of high-temperature superconductivity in a family of doped copper oxides, with the realization that the vicinity of a Mott insulating state could be a central key to, at least partially, understand the pairing mechanism and ultimately engineer materials with higher, possibly room-temperature transition points. The two-dimensional Hubbard model, as a minimal description of the relevant physics in these systems, has then turned into one of the most studied model Hamiltonians, marking the history of many recent achievements in the field and leading to the development of new concepts and methods. Among the various milestones, a prominent spot is reserved to dynamical mean-field theory (DMFT) and its extensions, bringing the first coherent description of interaction-driven metal-insulator transitions, in a nonperturbative, field-theory based, treatment of the local dynamical correlations.

On the other hand, the recent explosion of interest in quantum information theory, mostly projected towards the development of robust quantum computing schemes, has sprout an abundance of new results in fundamental quantum mechanics, filling the gap between the highly complex developments in the last decades of quantum field theory and the minimal simplicity of the quantum systems that, so far, we are able to control. One of the greatest achievements of the quantum information community has surely been the development of a quantitative theory of entanglement detection, extended also to many-body systems. Therein, the concept of bipartite and multipartite entanglement has proven to be of stark relevance for the characterization of quantum phase transition, and the classification of exotic phases, especially in absence of a clearly defined order parameter.

This thesis has been carried out in the effort of building a solid bridge between the two disciplines (and hopefully the two communities), with the ultimate goal of reaching an enhanced understanding of the role of strong correlations, and possibly entanglement, in driving and/or probing the complex transformations that a many-electron system undergoes when the (static) mean-field description breaks apart. Field-theory methods have generally no direct access to many-body wavefunctions, making the connection to quantum information concepts particularly hard.

As virtually any PhD journey, these four years of work have been filled with discontinued paths, continuous excitement with new ideas and a fair deal of hopping between different projects. As a result, the two main pillars of this thesis are derived from research ideas in principle not straightforwardly related to each other. Nevertheless, for my personal taste and hopefully the reader delight, I decided to report them as a somewhat unitary story, bound together by the *fil rouge* of importing quantum information insights into the field of strongly correlated electrons. For this reason, an introductory chapter, perhaps longer than usual, has been added, obviously discussing the common concepts and tools, but also reporting some results that have been produced expressly for the thesis. It is called *ouverture* and, as the name suggests, it is intended to be read before starting with the main courses. The rest of the thesis is divided in two parts, made as independent as possible on each other, as all the needed shared foundation has been included in the ouverture.

The first part reports on our study of correlated topological phase transitions, in particular the transformation of a quantum spin-Hall insulator into an antiferromagnetic Mott insulator, on the minimal model Hamiltonian for interacting Dirac electrons. The single-site DMFT results are compared with a standard Hartree-Fock theory and a quantum information "distance" is defined to complement the traditional, Green's function based, understanding of the difference between the two descriptions.

The second part, in turn, extends the analysis to short-range nonlocal correlations, this time analyzed in the Hubbard model on the square lattice. The results are obtained within cluster dynamical mean-field theory (CDMFT), an extension of the single-site theory, able to include nonlocal effects within small clusters. A careful review of some entanglement measures for bipartite open quantum system is included, as we are interested in the evaluation of correlations and entanglement between two electronic orbitals residing on different lattice sites, without any contribution from the surrounding lattice. This fairly specific request comes from a lesson taught by some recent works, which have thoroughly analyzed the so-called local (single-site) von Neumann entropy. While this quantity can indeed mark all the features in the phase diagram, along the interaction, temperature and doping axes, its physical meaning has not been, in our opinion, fully identified (or communicated), leading to an apparently misleading depiction of the Mott-Hubbard transition. We show that two-site entanglement measures are indeed much more revealing of the strongly correlated character that is universally attributed to paramagnetic Mott insulators and pseudogap metals. In this light they represent "useful" entanglement measures to be used in more involved models describing competing phenomena. Finally, we amend the physical interpretation of the local entropy, connecting it with the notion of local *fluctuations* and demonstrate how the local *correlations* are much better captured by the *intra-orbital* mutual information, the same "distance" we have leveraged for the topological transitions, mentioned above.

Contents

Abstract v

Preface vii

O Ouverture: correlated insulators 1
- O.1 Failure of band theory . . . 1
- O.2 The Hubbard model for interacting electrons in localized orbitals . . . 3
- O.3 Dynamical mean-field theory and the Mott-Hubbard transition . . . 9
- O.4 Slater vs Mott insulators . . . 15
- O.5 Quantifying the *distance* from Slater states with quantum information theory 18
- O.6 Other correlated insulators: nontrivial electronic topology . . . 26
- O.7 There is much more to strong correlations . . . 30

I Local classical correlations in the honeycomb lattice 33

1 Introduction 35
- 1.1 Topological and magnetic phases of interacting Dirac fermions . . . 35
- 1.2 Outline of the following chapters . . . 37

2 The Kane-Mele-Hubbard model 39
- 2.1 Static mean-field theory . . . 42
- 2.2 Dynamical mean-field theory . . . 44
- 2.3 Intra-orbital correlations in presence of magnetic anisotropy . . . 47

3 Mott transitions in the Kane-Mele-Hubbard model 49
- 3.1 QSHI to $\mathrm{AFM}_{\parallel}$ transition . . . 49
- 3.2 QSHI to $\mathrm{AFM}_{\perp}$ transition . . . 54
- 3.3 QSHI to Mott-Hubbard transition . . . 57
- 3.4 Landscape of intra-orbital correlations . . . 60

4 Stability of the AFM phases 63
- 4.1 Computing the total energy in DMFT/ED . . . 63

4.2 Energy separation between the two competing AFM solutions 66
4.3 Switching ground state with an external field 69
4.4 Switching ground state at the nanoscale 71

5 Summary and outlook **79**

II Quasilocal quantum correlations in the square lattice **81**

6 Introduction **83**
6.1 Success and failure of the local entropy 83
6.2 Outline of the following chapters 86

7 Quantifying quasilocal entanglement **87**
7.1 Single- and two-site von Neumann entropy 88
7.2 Two-site mutual information 89
7.3 Lower bounds to the quasilocal entanglement from superselection rules . 91
7.3.1 Superselected single-site entanglement 92
7.3.2 Superselected two-site entanglement 93
7.3.3 Superselected two-site correlations 98
7.4 Distillable entanglement and the two-site logarithmic negativity 98
7.4.1 Superselected two-site negativity 100
7.5 Summary of nonlocal correlation measures 100

8 Cellular extension of dynamical mean-field theory (CDMFT) **103**
8.1 Tiling the lattice 104
8.2 Bath optimization to enforce the self-consistency 105
8.3 Reconstructing the momentum dependence 108
8.4 Short-range correlations and Mott physics 109
8.5 Implementation details 112
8.5.1 Calculation of reduced density matrices 114

9 Quasilocal entanglement of a Mott-Hubbard insulator **117**
9.1 Size scaling of the von Neumann entropy 118
9.2 Local fluctuations and correlations 125
9.3 Entanglement between nearest neighbors 128
9.4 Role of the SSR on computable quantities 130
9.5 Entanglement beyond nearest neighbors 134
9.6 Summary and outlook 137

10 Quasilocal entanglement of a pseudogap metal **141**

10.1 CDMFT modeling of the pseudogap metal . . . 142
10.2 Hole-doping phase diagram . . . 143
10.3 Single-site von Neumann entropy and local classical correlations . . . 144
10.4 Two-site entanglement and a hint on the quasilocal nature of the pseudogap 146
10.5 Final remarks . . . 148

Conclusion: future directions **151**

Appendix 155

A Geometrical approach to entanglement and correlations **157**
A.1 An information distance for quantum states . . . 157
A.2 Quantifying correlations . . . 159
A.3 Classifying correlations . . . 160
A.3.1 Separable states and entanglement . . . 161
A.3.2 Pseudo-classical states and quantum discord . . . 162
A.3.3 Classical correlations and correlation sum rule . . . 163
A.4 Effect of restrictions on local operations . . . 164

B Sum-rule for the two-site mutual information **165**

Bibliography **167**

Acronyms **196**

Acknowledgements **197**

Ouverture: correlated insulators



> *I first heard of it when Fowler was explaining it to one of Rutherford's closest collaborators, who said 'very interesting' in a tone which implied that he was not interested at all. Neither was I.*
>
> — **Nevill Francis Mott**
> about Bloch-Wilson's theory of insulators

O.1 Failure of band theory

The band theory of solids [5–9] is the cornerstone of our understanding of the electronic properties of crystalline materials. The main idea is that the properties of the electrons in a solid can be approximated as those of a gas of effective fermionic quasiparticles, which can tunnel between localized atomic orbitals for a relatively large lifetime (so that they constitute *coherent* charge carriers), leading to a description of the system in terms of delocalized single-particle states. For a given number N of electrons in the solid, N quasiparticles will populate these states according to the Fermi-Dirac thermal statistics wich, at zero temperature, results in a filling of the $N/2$ lowest-lying eigenstates, each with two quasiparticles of opposite spins.

The underlying assumption of band theory is that the electron-electron repulsion is sufficiently screened (hence weak) as to ensure a one-to-one correspondence of the effective fermions with the actual interacting electrons, so that the quasiparticle states (though not being eigenstates of the many-body Hamiltonian) can be defined and labeled by the same quantum numbers of the corresponding noninteracting reference state. Furthermore, their motion is simply characterized by a renormalization of their physical properties, such as the interaction-induced enhancement of the electronic effective mass. The phenomenological introduction of these concepts is due to Landau [10], and the later formalization in the framework of diagrammatic perturbation theory is known as *Fermi liquid theory* [11–14].

The simplest approximation of Fermi liquid theory amounts to model the screened electron-electron repulsion as an effective one-body potential, emerging from the interaction of a single electron with the *averaged* effect of the presence of all the others. This amounts to assume the lifetime of the quasiparticles as infinite and neglect all the dynamical effects of the electronic repulsion, hence defining what is called a *static mean-field* approximation of the many-body problem. The mean-field potential is added to the periodic potential

introduced by the underlying lattice of positive charged ions, resulting overall in a spectrum formed by continuous energy bands, possibly separated by gaps where no single-particle eigenstates are present. According to Bloch's theorem, each of these eigenstates can be written as a modulated plane wave [5]

$$\psi_{n\boldsymbol{k}}(\boldsymbol{r}) = u_{n\boldsymbol{k}}(\boldsymbol{r})\mathrm{e}^{i\boldsymbol{k}\cdot\boldsymbol{r}}, \tag{O.1}$$

where $\boldsymbol{k}$ is the so-called crystalline momentum and n is a quantum number labeling the modulating function $u_{n\boldsymbol{k}}$, that in turn has the same periodicity of the lattice. The energy eigenvalue $\varepsilon_{n\boldsymbol{k}}$ associated to the $\psi_{n\boldsymbol{k}}$ eigenstate defines the n-th band of the solid [7, 8]. The existence of these bands is the crucial element of the theory and has historically led to a great number of successful predictions, paving the road for the understanding of the physical properties of materials. Among these achievements, a fundamental role is assumed by a criterion introduced by Wilson [6] for the classification of the transport character of solids: solids where the number of electrons completely fills the highest occupied (valence) band, leaving the next (conduction) band empty, will be insulators; solids that feature a partially filled conduction band will be metals; semiconductors are simply insulators with a small gap, so that the conduction band can be populated by thermal excitations.

The band theory of solids has proven to be extremely successful in describing the qualitative features of many solids. In particular, the development of density functional theory[1], especially in the Kohn-Sham formulation [16], and the continuous improvement of the approximations for the exchange-correlation functional, has affirmed the possibility to compute band structures for real materials, in impressive agreement with experiments.

Yet, there are spectacular examples in which band theory completely fails to describe the properties of materials, even on a qualitative level. Among these, a central role is played by the so-called Mott insulators [17–20], materials that display all the phenomenology of insulators, despite the electron count would suggest a partially filled conduction band. This discovery dates back to 1939, in the early stages of band theory, when it was reported that transition-metal oxides displayed this behavior [21]. It became rapidly clear that electron-electron interactions, which are either neglected or treated at the Fermi liquid level in band theory calculations, were the most likely reason for its breakdown [17, 22].

However, the physical mechanism underlying the transformation of band metals into interaction-induced insulators, has been debated since the early days, with the opposition of two main ideas: one, proposed by Slater [22], identifies the transition mechanism in the nesting property of the Fermi surface (see section O.2 for a definition), that enables strong

[1] To be fair, density functional theory should not be regarded as any kind of mean-field approximation, but rather as a highly sophisticated many-body method [15]. Nevertheless, many features of the practical implementations are essentially akin to traditional band-theory and the two theories are in fact often referred to as synonyms in the community.

magnetic fluctuations ultimately leading to an instability towards Néel (antiferromagnetic, AFM) ordering. The other, introduced by Mott [17], predicts the formation of localized magnetic moments, of the Heisenberg type, at temperatures that are incompatible with long range ordering and thus leading to a paramagnetic insulating state. Upon decreasing the temperature, a paramagnetic Mott insulator would indeed order with a Néel transition that cannot be driven by nesting, as the Fermi surface is absent in the high-temperature Mott state. These observations can be considered as the beginning of the field of strongly correlated electrons.

A turning point in the field has been the discovery of high-temperature superconductivity, by doping a class of layered copper oxides (cuprates) [23] which, when not doped, are almost two-dimensional antiferromagnetic Mott insulators. After the original proposal by Anderson [24, 25], the idea that the understanding of high-temperature superconductivity boils down to unveiling the physics of doping a Mott insulator [26] has been the main guideline in the community.

In the following be briefly discuss the simplest model that accounts for this physics, the single-band Hubbard model [27–32], and we provide a concise description of some of its properties. The purpose of the section is by no means a complete review of an immense and diverse field, but simply to introduce some of the concepts that are essential to discuss the original research reported in this thesis. For a review of the properties of the model and the vast multitude of related computational methods we direct the reader to [33, 34]

O.2 The Hubbard model for interacting electrons in localized orbitals

A simple derivation of the band theory of solids can be obtained by assuming the so-called tight-binding approximation: recognizing that the electrons occupying the lower energy levels in each atom are tightly bound to its nucleus and significantly screen its positive charge, we can model the so-called "outer" electrons as occupying largely extended wavefunctions, that partially intersect with each other. The corresponding *overlap integral*, gives the probability amplitude for the tunneling between different atoms and is consequently called *hopping* amplitude t. We can then model a simple lattice of noninteracting electrons as a series of on-site energies (equal for all sites if the lattice is homogeneous) and a sum over all the possible hopping terms. In second quantization it reads

$$\mathbf{H}_0 = \sum_{i\sigma} \varepsilon_i n_{i\sigma} + \sum_{\langle ij \rangle} t_{ij} c^\dagger_{i\sigma} c_{j\sigma} \,, \tag{O.2}$$

where $c_{i\sigma}$ ($c^\dagger_{i\sigma}$) is the annihilation (creation) operator of an electron with spin σ at the site i of the lattice and $n_{i\sigma} = c^\dagger_{i\sigma} c_{i\sigma}$ is the corresponding number operator.

Formally, the hopping amplitudes t_{ij} can be obtained by computing explicit overlap integrals between the Wannier functions, defined as the lattice Fourier transform of the Bloch waves in Eq. O.1 [35]:

$$\phi_{n\boldsymbol{R}}(\boldsymbol{r}) \propto \sum_{\boldsymbol{k}} \mathrm{e}^{-i\boldsymbol{k}\cdot\boldsymbol{R}}\psi_{n\boldsymbol{k}}(\boldsymbol{r}), \tag{O.3}$$

where $\boldsymbol{R}$ stands for any lattice vector. If the Wannier functions are sufficiently localized, as it happens for the d and f orbitals in transition metals, the tight-binding approximation provides a fairly good description of the material's band structure, often even with the truncation of the hopping matrix at the nearest neighboring sites. In the Wannier basis, the band index directly translates to a localized orbital.

Once the hopping integrals have been obtained, to consider a strongly correlated material, *i.e.* a system in which the band theory of solids fails, a term accounting for the electron-electron interaction must be added. In principle, in considering the interaction between electrons sitting at different lattice sites one has to include every term of the Coulomb tensor, with elements

$$U_{ijkl} = \int \mathrm{d}\boldsymbol{r}_1 \mathrm{d}\boldsymbol{r}_2 \phi_i^*(\boldsymbol{r}_2)\phi_j^*(\boldsymbol{r}_1)V_{\mathrm{ee}}(\boldsymbol{r}_1-\boldsymbol{r}_2)\phi_k(\boldsymbol{r}_1)\phi_l(\boldsymbol{r}_2), \tag{O.4}$$

where i, j, k and l represent in principle indices for all the site-orbital pairs in the lattice. In the assumption of well-localized Wannier functions, and considering only one orbital per site (as we will always do in this thesis), the calculation can be greatly simplified into considering only the so-called Hubbard terms, measuring the Coulomb repulsion of electrons residing on the same lattice site [27–32]

$$U_i = \int \mathrm{d}\boldsymbol{r}_1 \mathrm{d}\boldsymbol{r}_2 |\phi_i(\boldsymbol{r}_1)|^2 V_{\mathrm{ee}}(\boldsymbol{r}_1-\boldsymbol{r}_2)|\phi_i(\boldsymbol{r}_2)|^2. \tag{O.5}$$

Considering a lattice of all-equivalent sites and truncating the hopping amplitudes to nearest neighbors we obtain the single-band Hubbard model:

$$\mathbf{H} = -t\sum_{\sigma}\sum_{\langle ij\rangle}\left(c_{i\sigma}^\dagger c_{j\sigma} + \mathrm{h.c.}\right) + U\sum_i n_{i\uparrow}n_{i\downarrow} - \mu\sum_{i\sigma} n_{i\sigma} \tag{O.6}$$

where t is the (uniform) nearest-neighbor hopping amplitude, μ is the chemical potential and U is the aforementioned (uniform) local electronic repulsion. After its introduction, the Hamiltonian in Eq. O.6 turned into a minimal but paradigmatic model to introduce the effects of electron-electron repulsion in the tight-binding description of solids.

Despite its deceiving formal simplicity, the Hubbard model still defies most of the attempts to solve it, except for the one-dimensional case, where the Bethe *Ansatz* [36] allows for an analytical solution, and the limit of infinite dimensions [37], where dynamical mean-field theory (DMFT) [38] leads to a numerically exact solution of the model at any temperature

and U/t ratio (see section O.3). In two and three dimensions, the model proves extremely hard to solve due the intrinsic competition between the kinetic and interaction terms. We can build an intuition around this point by examining two limiting cases, the noninteracting ($U = 0$) and the atomic ($t = 0$) limits, where a simple analytical solution can be obtained for any dimensionality.

For $U = 0$, the Hubbard model becomes a simple tight-binding Hamiltonian, which can always be diagonalized in momentum space (also for general hopping matrices, as in Eq. O.2). Thus we can Fourier transform it in the form

$$\mathbf{H}(\boldsymbol{k}) = \sum_{\boldsymbol{k}\sigma} \varepsilon_{\boldsymbol{k}} c^{\dagger}_{\boldsymbol{k}\sigma} c_{\boldsymbol{k}\sigma}, \tag{O.7}$$

where the dispersion $\varepsilon_{\boldsymbol{k}}$ for a d-dimensional hypercubic lattice with only nearest-neighbor hopping reads $\varepsilon_{\boldsymbol{k}} = -2t \sum_i \cos(k_i a)$, where $i = 1, \dots d$ runs over the spatial coordinates and a is the lattice spacing. Any eigenstate of the Hamiltonian is the direct product of delocalized states of momentum $\boldsymbol{k}$ and it describes a metal for any number of electrons except zero or those filling the whole band. In particular, the system is metallic also when the number of electrons equals the number of sites, corresponding to a half-filled band.

In the opposite limit, $t = 0$, the Hubbard model becomes a collection of disconnected atoms (hence the name of atomic limit) and the model is trivially diagonal in real space. Now every Fock state in the basis of the local occupations is an eigenstate and the ground states are all those states that minimize the number of *doublons*, *i.e.* doubly occupied sites hosting two electrons with opposite spins, as the creation of a doublon leads inevitably to an energy cost of U. At half-filling, this implies a vanishing population of doublons, as well as of empty sites (sometimes also called *holons*), so that all the configurations with one electron per site are degenerate ground states at zero energy, regardless of the arrangement of the electronic spins. This state is trivially localized in each atomic orbital and it can be considered as the extreme version of a Mott insulator.

The strikingly different behavior in the two extreme noninteracting and atomic limits provide us a first clue about the reason for the difficulties to solve exactly the Hubbard model. The two terms are both extremely simple, but they are diagonal respectively in momentum space and in real space, so that they describe naturally contrasting tendencies and it is hard to envisage a simple picture to describe the outcome of their competition. From a purely qualitative point of view, we can picture the evolution of the half-filled Hubbard model from the noninteracting limit by increasing the ratio U/t in terms of a progressive reduction of doubly occupied sites. As the interaction grows, their dynamical average will decrease from the noninteracting value, which at half-filling can be easily checked to be 1/4. During this process the electrons lose their mobility, as a consequence of the increasing energetic cost for exciting a doublon/holon pair. While for $U = 0$ all the

hopping processes respecting Pauli principle are allowed, as U grows the processes that create doubly occupied sites become less and less likely, so that at some *critical* value of U, for which the interaction is comparable with the kinetic energy of the electrons, the electronic motion will become so energetically unfavorable that the electrons will become fully localized, thus leading to an interaction-driven insulating state, whereas the electron count would lead to a metallic system, according to the band theory of solids. This process, that by no means requires the assumption of antiferromagnetic ordering, transforms a metal into a insulator by the pure action of the Hubbard repulsion U, and for that reason is traditionally called a *Mott-Hubbard* transition. Based on the very general arguments we discussed above, we can expect that the Mott-Hubbard transition takes place for a critical value of U proportional to the hopping amplitude t, or in other terms to the bare electronic kinetic energy. In this view, we cannot expect that perturbation theory starting from either of the two extreme limits is likely to describe this transition, as it takes place when the two energy scales of the model are comparable. As a matter of fact, only nonperturbative methods such as the dynamical mean-field theory [38] can access this kind of physics.

Once again, it is important to stress that the simple argument we discussed, as well as the more concrete theoretical description that we will present in the next section, are totally independent on the onset of long-range magnetic ordering. This is a very concrete point given that a magnetic state, often with alternate Néel ordering, is observed at low temperature in many Mott insulators, including the parent (undoped) compounds of high-temperature superconductors. The Mott-Hubbard insulator that we described is instead in principle free of any symmetry breaking and, in virtue of the local magnetic moments that characterize its electronic configuration, it is often simply called as paramagnetic Mott insulator. The study of the transition from a nonmagnetic metal to a paramagnetic Mott insulator has a fundamental value, as it provides a picture of the *intrinsic* effects of electron-electron interactions, beyond any symmetry breaking mechanism. In fact, this perspective has been widely assumed in the literature employing DMFT and related methods and it has provided a powerful paradigm for the understanding of strongly correlations, even beyond electronic systems [39–43]. Nevertheless, the study of the role of strong correlations in symmetry-broken, antiferromagnetic states can in principle aid to pinpoint the fundamental difference between the aforementioned mechanism proposed by Slater [22], defining what we will call Slater insulators and Slater metal-insulator transitions, and a mechanism based on the sole assumption of strong correlations that, as mentioned above, relies on the notion of localized magnetic moments that order by means of superexchange interactions of the Heisenberg type, so defining the concept of Mott-Heisenberg insulators.

In this thesis we will address both Mott-Hubbard and Mott-Heisenberg insulators for the Kane-Mele-Hubbard model, providing a minimal description of topological insulators on the honeycomb lattice, with a local electron repulsion modeled by the same on-site term of Eq. O.5. We will also consider the paramagnetic metal-insulator transition for

the two-dimensional Hubbard model (Eq. O.6, where the underlying lattice defining the summations is hypercubic with $d = 2$). Therein we will address local and quasilocal entanglement and correlation properties, at half-filling and in presence of hole-doping, completely discarding magnetic ordering.

Before delving into a brief introduction of DMFT and the way it captures the Mott-Hubbard transition, we spend some words to further examine the connection between Mottness and magnetism, elucidating some key aspects to distinguish Mott-Heisenberg insulators from their simpler Slater description. This important discussion will be reprised in sections O.4 and O.5, analyzing the concept of correlation-induced local magnetic moments under the lens of quantum information theory and building the foundation for a rigorous study of the role of local fluctuations and correlations in Mott physics.

Indeed, for a half-filled Hubbard model with only nearest-neighbour hoppings, on a hypercubic lattice, the ground state is always antiferromagnetic (AFM) for every nonzero value of U/t. We can spend a few lines to provide solid analytical arguments for this statement, in the two regimes of weak-coupling $U \ll t$ and strong coupling $U \gg t$.

In a weak-coupling regime, we can study the model using a mean-field Hartree-Fock approximation. In particular we can decouple the interaction term as

$$U \sum_i n_{i\uparrow} n_{i\downarrow} \simeq U \sum_i n_{i\uparrow} \langle n_{i\downarrow} \rangle + U \sum_i \langle n_{i\uparrow} \rangle n_{i\downarrow} - U \sum_i \langle n_{i\uparrow} \rangle \langle n_{i\downarrow} \rangle, \tag{O.8}$$

amounting to a variational search for the optimal Slater determinant description of the electronic ground state [9, 13, 14, 22]. If we define the AFM order parameter as

$$m = \sum_i (-1)^{\boldsymbol{R}_i} (n_{i\uparrow} - n_{i\downarrow}) \tag{O.9}$$

we find that a solution with $m \neq 0$ is found for every value of U and follows an exponential law of the form $m \propto \mathrm{e}^{-\alpha t/U}$. This state is insulating with a gap given by Um and it describes a system with a small magnetization that changes sign each time we move of one site along any direction. The same behavior is found in principle for any bipartite lattice, *i.e.* a lattice which can be partitioned in two sublattices A and B such that all the nearest-neighbor hopping amplitudes only connect sites of the A sublattice with those of sublattice B and viceversa. In fact, the onset of this magnetic state can be seen as an instability of the Fermi sea associated to the nesting of the Fermi surface at the reciprocal vector $\boldsymbol{Q} = (\pi, \pi, \dots)$. This leads to a doubling of the unit-cell, associated with the broken translational symmetry, and consequently leads to a folding of the single, metallic band into two bands defined in the so-called reduced Brillouin zone [7, 8], separated by the aforementioned gap. Hence, despite the origin of the magnetic ordering and the insulating behavior is the presence of the interaction, the system can be described in terms of an

effective band structure, where the gap is simply explained by the doubling of the unit-cell. In this sense, the Slater mechanism for the metal-insulator transition does not require a failure of band theory and arguably describes the state of the system only when the interaction is indeed much smaller than the hopping.

In the strong-coupling limit $U \gg t$, the starting point is the atomic limit where, as we mentioned above, we have a large manifold of degenerate ground states, all characterized by one electron localized on each lattice site. We notice immediately that the only active degree of freedom left is the spin on each site. In other words, our Hubbard model becomes a spin model as the charge is, of course, completely localized. If the presence of the hopping does not change this situation, the system remains insulating. Indeed, as long as $t \ll U$, there is no way to induce charge fluctuations, whose energy cost is larger than any possible kinetic gain. What a small t can induce is instead a lifting of the degeneracy: among the many degenerate ground states, only some will be favored by a finite hopping. A simple perturbative argument suggests that nearest-neighbor sites gain an energy $E' = -2t^2/U$ if they host electrons with opposite spin (with respect to electrons with the same spin). This leads to the prediction of an antiferromagnetic ground state for any bipartite lattice. Indeed, this result can be well formalized by deriving an effective strong coupling Hamiltonian [44], which reads

$$\mathbf{H} = J \sum_{\langle ij \rangle} \boldsymbol{S}_i \cdot \boldsymbol{S}_j, \tag{O.10}$$

where $J = 4t^2/U$ is an the antiferromagnetic superexchange coupling [45, 46], and $\boldsymbol{S}_i$ is the quantum mechanical spin vector for the i-th site. Eq. O.10 can be recognized as an Heisenberg model with positive coupling, obviously favoring opposite spin on neighbouring sites. The model hence describes an insulator with localized spins that tend to align in a AFM pattern (but do not order at high temperature). In this regime the insulating behavior descends directly from the presence of a large U, as a strong repulsion inherently entails the *formation* of local moments $\boldsymbol{S}_i$, and antiferromagnetism is expected only at low temperatures. Indeed the high temperature state described by Eq. O.10 describes an extreme Mott-Hubbard insulator, while the antiferromagnet at low temperature is our definition of an extreme Mott-Heisenberg insulator. So, in both the two extreme limits we find antiferromagnetism in the ground state, but with a radically different origin and arguably an underlying difference in the many-body quantum state. The two regimes are connected continuously, hence the ground state is always an insulating antiferromagnet for every nonzero U/t. The critical temperature vanishes in both directions when we approach the two limits, $U = 0$ and $t = 0$, and it reaches its maximum value in the intermediate coupling region.

The discussed phenomenology might appear in contrast with the existence of a true metal-insulator transition, as the metallic region expected at weak coupling is replaced by a Slater antiferromagnetic state. However, the two pictures are overall compatible and a complete phase diagram of the half-filled Hubbard model features both phenomena. Even if the ground state is always magnetic and insulating, the antiferromagnetic region is limited to low temperatures, in particular in realistic configurations where the lattice and/or the structure of the hopping amplitudes can *frustrate* the magnetic ordering [47–50]. On the other hand, the Mott-Hubbard transition can take place at higher temperatures, where magnetism is no longer present and the above-described mechanism leading to charge localization by formation of unordered magnetic moments can take place. Thus, the phase diagram of the half-filled Hubbard model in function of interaction U and temperature T is expected to host at least an antiferromagnetic phase (with an internal evolution from the Slater to the Mott-Heisenberg description as the interaction is increased) and a nonmagnetic metallic phase, which is realized for small U when the temperature exceeds an exponentially small critical temperature, eventually transformed in a paramagnetic insulator when the interaction reaches a critical value U_c and the metal is transformed by the Mott-Hubbard mechanism.

O.3 Dynamical mean-field theory and the Mott-Hubbard transition

The hunt for accurate solutions of the Hubbard model has been one of the main stories in condensed matter theory after the discovery of high-temperature superconductivity in doped layered Mott insulators. This search led to the development of new methods and the improvement of many other approaches, substantially enhancing our ability to study quantum many-body systems. Indeed, despite an exact solution of the Hubbard model in two dimensions could not be obtained, a great amount of information has been gathered in the effort. In this thesis we do not attempt to review this incredible effort and we limit ourselves to refer the interested reader to recent reviews [33, 34].

Our focus is on a significant success story, which is based on the development of dynamical mean-field theory (DMFT). The history and the origin of DMFT may appear very far from the two-dimensional Hubbard model as they are rooted in the study of the Hubbard model in the limit of infinite dimensions [37], where many aspects of the perturbation theory are simplified, yet the physical picture remains highly nontrivial.

As the name suggest, the simplest way to understand DMFT is to picture it as a dynamical (in the sense of quantum fluctuations) version of the standard mean-field theory, where the effect of the rest of the system on a single site is parameterized by a time-dependent effective field (see left and middle panel in Fig. O.1). The key point making the theory

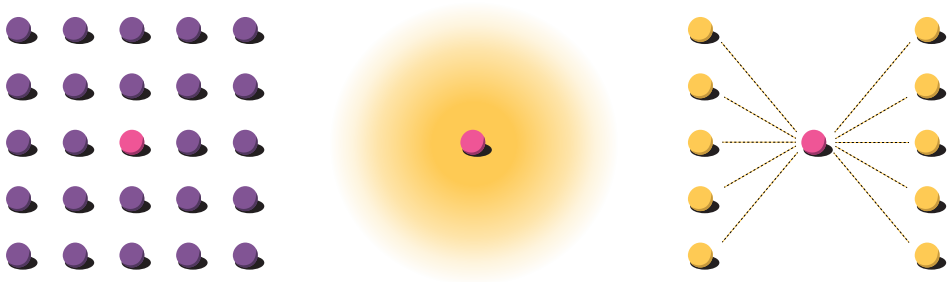


Fig. O.1.: Pictorial view of the DMFT approximation. Starting from a lattice model (left panel), DMFT builds an effective theory for a given site in which the effect of the rest of the lattice is described in terms of a self-consistently determined bath, which acts like a dynamical (frequency-dependent) field, as shown in the middle panel. The right panel shows a discretized parametrization of the bath, defining the impurity Hamiltonian solved in practical implementations based on exact diagonalization and similar methods. Dashed lines indicate hybridization amplitudes connecting the noninteracting bath levels to the correlated impurity (see Eq. O.15).

immensely more powerful than a static mean-field method is the dynamical nature of the effective field, which makes even the effective local theory a nontrivial many-body problem. The mean-field *Ansatz* and the equivalence with the lattice model are enforced by a self-consistency condition on the Green's function. More precisely, we build an effective local theory whose Green's function has to coincide with the local component of the lattice Green's function, with the assumption of a momentum independent self-energy.

We now briefly outline the relevant equations and ideas. As we mentioned above DMFT defines an effective local theory for an arbitrary site "$\circ$" of the original lattice associated with the effective action

$$S_{\text{eff}} = \int \mathrm{d}\tau \mathrm{d}\tau' c^{\dagger}_{\circ\sigma}(\tau) \mathcal{G}^{-1}_{\circ}(\tau - \tau') c_{\circ\sigma}(\tau') + U \int d\tau n_{\circ\uparrow}(\tau) n_{\circ\downarrow}(\tau), \tag{O.11}$$

where τ and τ' are imaginary time variables, $c^{\dagger}_{\circ\sigma}$ and $c_{\circ\sigma}$ are Grassman fields describing creation and annihilation of fermions with spin σ on site $\circ$, $n_{\circ\sigma} = c^{\dagger}_{\circ\sigma} c_{\circ\sigma}$. The effective action describes the (imaginary) time evolution of site $\circ$ in the presence of the local repulsion, which is controlled by the dynamical Weiss field $\mathcal{G}^{-1}_{\circ}(\tau - \tau')$, which contains the effect of the rest of the lattice on site $\circ$. Similarly to a mean-field theory for classical magnetic moments, the dynamical mean-field is determined by a self-consistency condition which requires that the Green's function of the effective theory

$$G_{\text{imp}}(\tau) = -\langle \mathrm{T} c_{\circ\sigma}(\tau) c^{\dagger}_{\circ\sigma}(0) \rangle_{S_{\text{eff}}} \tag{O.12}$$

coincides with the local component of the lattice Green's function.

Namely, in Matsubara frequencies[2]

$$G_{\mathrm{loc}}(i\omega_n) \stackrel{\mathrm{def}}{=} \frac{1}{N_{\boldsymbol{k}}} \sum_{\boldsymbol{k}} \frac{1}{i\omega_n + \mu - \varepsilon_{\boldsymbol{k}} - \Sigma(i\omega_n)} \equiv G_{\mathrm{imp}}(i\omega_n) \tag{O.13}$$

where $\Sigma(i\omega_n)$ is the *self-energy* of the effective theory, connected to the Weiss field and the Green's function by a Dyson equation

$$\Sigma(i\omega_n) = \mathcal{G}_{\circ}^{-1}(i\omega_n) - G_{\mathrm{loc}}^{-1}(i\omega_n). \tag{O.14}$$

The three conditions (Eqs. O.12, O.13 and O.14) are a closed set of equations that allow in principle to find a self-consistent set of $\Sigma(i\omega_n)$, $\mathcal{G}_{\circ}^{-1}(i\omega_n)$ and $G_{\mathrm{loc}}^{-1}(i\omega_n)$ satisfying them.

In practice, the implementation of DMFT amounts to a recursive solution of the effective theory (Eq. O.11). One first computes the impurity Green's function (Eq. O.12), starting from a (possibly educated) guess for the dynamical Weiss field $\mathcal{G}_{\circ}^{-1}(i\omega_n)$. Then one retrieves the impurity self-energy from the Dyson equation (Eq. O.14). Finally, the self-consistency condition (Eq. O.13) is used to compute a new $\mathcal{G}_{\circ}^{-1}(i\omega_n)$ and the procedure is iterated until convergence is achieved, *i.e.* when the three conditions are all satisfied to a given target precision. The solution of the effective theory usually exploits a mapping onto an impurity Hamiltonian which, for the single-band Hubbard model, amounts to an Anderson impurity model (AIM) [51]:

$$\mathbf{H}_{\mathrm{AIM}} = \sum_{\ell\sigma} \varepsilon_{\ell\sigma} b_{\ell\sigma}^{\dagger} b_{\ell\sigma} + \sum_{\sigma} \varepsilon_{\circ\sigma} c_{\circ\sigma}^{\dagger} c_{\circ\sigma} + U c_{\circ\uparrow}^{\dagger} c_{\circ\uparrow} c_{\circ\downarrow}^{\dagger} c_{\circ\downarrow} + \sum_{\ell\sigma} V_{\ell\sigma} (c_{\sigma}^{\dagger} b_{\ell\sigma} + b_{\ell\sigma}^{\dagger} c_{\sigma}), \tag{O.15}$$

where $b_{\ell\sigma}^{\dagger}$ and $c_{\circ\sigma}^{\dagger}$ are creation operators for electrons with spin σ, respectively in the ℓ-th bath level and in the impurity site $\circ$. With reference to the right panel in Fig. O.1, we observe that the $V_{\ell\sigma}$ amplitudes represent the *hybridization* between the impurity site and the noninteracting bath levels. We observe that, in the AIM, the single interacting site cannot spontaneously break the SU(2) spin symmetry, as phase transitions can only happen in the thermodynamic limit and surely not on a single site. Hence, the only way to allow the simulation to order in an antiferromagnetic state is to grant a spin-dependency to the bath parameters $\varepsilon_{\ell\sigma}$ and $V_{\ell\sigma}$, as indeed we have done in Eq. O.15, and to define two inequivalent impurity models, each addressing a different sublattice in the original bipartite crystal. The two inequivalent impurity Green's function will be then coupled at the self-consistency level, as the two resulting local Green's functions will be coupled by the presence of the full lattice dispersion in Eq. O.13. More details about the treatment of antiferromagnetic states in DMFT will be given in chapter 2, section 2.2.

[2] In principle, all DMFT equations must be satisfied in the whole complex frequency plane. Yet, the smooth properties of the imaginary axis make for the ideal subset of frequencies on which perform all operations, until convergence is achieved and the self-consistency condition holds also on the real axis.

If instead one imposes a *paramagnetic constraint*, in the form of $\varepsilon_{k\sigma} = \varepsilon_k$ and $V_{k\sigma} = V_k$, the system has no means of break the spin SU(2) symmetry and a Mott-Hubbard insulator can be stabilized, at large enough U/t ratio. In this case, the Mott transition of the original lattice can be fruitfully interpreted in terms of the Kondo physics of the auxiliary impurity model [52]. For a review of the intimate connection between the two phenomenologies, we suggest the reading of Ref. [53].

Despite being much simpler than the original Hubbard model, the auxiliary AIM is still a strongly correlated system and cannot generically be solved analytically. To actually obtain the impurity Green's function (Eq. O.12) different "impurity solvers" can be employed, each with specific advantages and disadvantages. Historically, the combined use of different solvers has led the DMFT community to a rich understanding of the Mott transition in the single-band Hubbard model and beyond [38]. In sections 2.2 and 8.5 we will give some details about the specific impurity solvers we leveraged for the research presented in the thesis, focusing on the main difficulties and/or the evaluation of nonstandard quantities.

Furthermore, we observe that within any Hamiltonian-based solver, the dynamical mean-field $\mathcal{G}_\circ(i\omega_n)$ has an explicit dependence on the bath parameters $\varepsilon_{k\sigma}$ and $V_{k\sigma}$ [54]

$$\mathcal{G}_\circ^{-1}(i\omega_n) = i\omega_n - \varepsilon_{\circ\sigma} - \mu - \sum_{k=1}^{N_{\text{bath}}} \frac{|V_{k\sigma}|^2}{i\omega_n - \varepsilon_{k\sigma}}, \tag{O.16}$$

so that we can recast its update, at each iteration of the DMFT cycle, as a multidimensional optimization problem, enticing the minimization of a distance between a. the continuous dynamical field that one obtains from the self-consistency relation (Eq. O.13) and b. the discretized expression in terms of the bath parameters (Eq. O.16). The usual choice for this distance is a, possibly weighted, *chi-squared* statistics [54], evaluated on the Matsubara frequencies (for its smooth properties). At zero temperature, the imaginary axis is discretized numerically, defining an artificial inverse temperature, that defines the frequency resolution of the calculation (the larger the β, the finer the frequency grid). The number of bath levels, on the other hand, controls the power and flexibility of the discretized Hamiltonian to *fit* the given Weiss field, so that a larger bath would in principle lead to better fits, and so to better numerical properties of the converged solution. However, the long-time experience in the community has repeatedly corroborated the notion that pretty small baths ($N_{\text{bath}} \simeq 10$) can give outstanding convergence properties and high quality in the output quantities. We give more details about the bath optimization for the cluster extension of the method in section 8.2, as the additional real-space structure of the dynamical Weiss field and the need to preserve the punctual symmetry of the (cluster-)impurity makes the choice of the both the bath parametrization and the weights for the *chi-squared* cost function much more critical.

In the following, we proceed to give a concise account of the DMFT description of the paramagnetic Mott-Hubbard transition, in very general terms. As mentioned above, DMFT is exact in the limit of infinite dimension (or coordination), but also, in finite dimensionality, in the opposite limits of $U = 0$ (noninteracting limit) and $t = 0$ (atomic limit). This makes the theory ideally suited to study the Mott-Hubbard transition, as it does not rely in the similarity to either of the two limiting regimes. We notice *en passant* that the same holds for other strongly correlated systems, as long as the interactions are local, so that their competition and interplay is captured by DMFT without assuming any hierarchy in the relevant energy scales of the model.

The scenario of the paramagnetic Mott transition for the half-filled Hubbard model within DMFT is highlighted in Fig. O.2, where we report a schematic sketch of the evolution of the local single-particle spectral function

$$A(\omega) = -\frac{1}{\pi}\mathrm{Im}G(\omega) \tag{O.17}$$

which, for many body systems, plays the same role as the density of states in noninteracting models. In particular $A(\omega)$ can be measured by photoemission spectroscopy [55].

When $U = 0$, DMFT recovers the exact noninteracting density of states of the problem, amounting to a metal with a half-filled band. Increasing the interaction U, some of the spectral weight moves towards higher energy as a result of the constraint to the electronic motion. When U becomes comparable with the bare bandwidth $2D$, the spectrum develops a characteristic nature with three different features: a quasiparticle peak around the Fermi level which becomes narrower and narrower as the interaction grows, and two "Hubbard bands" centered approximately around $\mu \pm U/2$ associated with empty and doubly occupied sites. While the central peak shrinks, these bands acquire more weight and move to higher energy. The width of the peak and its total weight are proportional to the quasiparticle weight Z [12], which for a $\boldsymbol{k}$-independent self-energy can be expressed as

$$Z = \left(1 - \frac{\partial \Sigma(\omega)}{\partial \omega}\bigg|_{\omega=0}\right)^{-1}. \tag{O.18}$$

At the critical interaction for the Mott-Hubbard transition Z indeed vanishes, signaling the disappearance of any low-energy metallic features: the system becomes an insulator with two incoherent spectral features separated by a preformed gap. The disappearance of the quasiparticle peak is indeed the hallmark of the Mott-Hubbard transition which, at zero temperature, is continuous as a function of U/t for the simple single-band Hubbard model. In chapter 8, section 8.4, we present the phase diagram of the Hubbard model in the U/T plane within DMFT and we will compare it with the counterpart obtained within cluster dynamical mean-field theory (CDMFT), an extension of DMFT that includes short-range correlations in a systematic way.

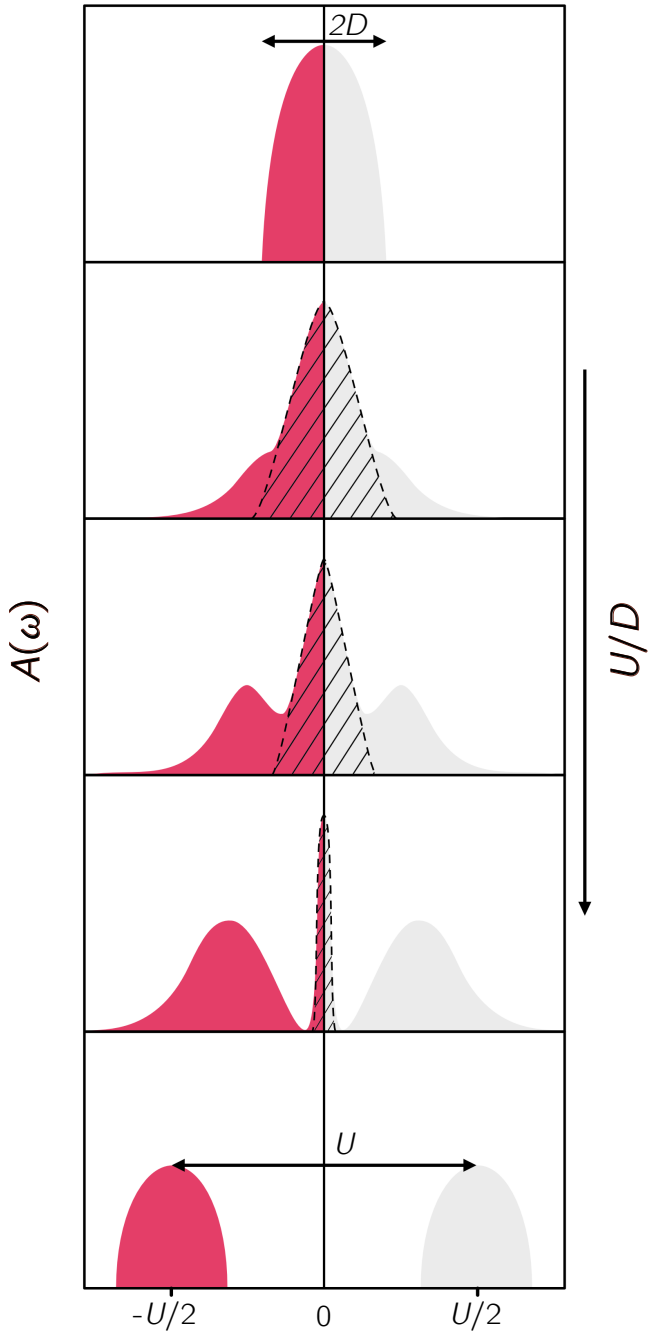


Fig. O.2.: Schematic representation of the evolution of the interacting density of states $A(\omega)$ (see Eq. O.17) with respect to an increasing interaction strength U, on a half-filled single band Hubbard model, solved within DMFT for the paramagnetic Mott-Hubbard transition. Assuming the Fermi level at zero energy, the red color indicates occupied single-particle states (in the sense of photoemission experiments) and the grey color identifies empty single-particle states, at zero temperature. The shaded region at low energy indicates the so-called quasiparticle peak, whose spectral weight is measured by Z (Eq. O.18). D is the half-bandwidth of the noninteracting density of states (top panel). Adapted from Ref. [56]

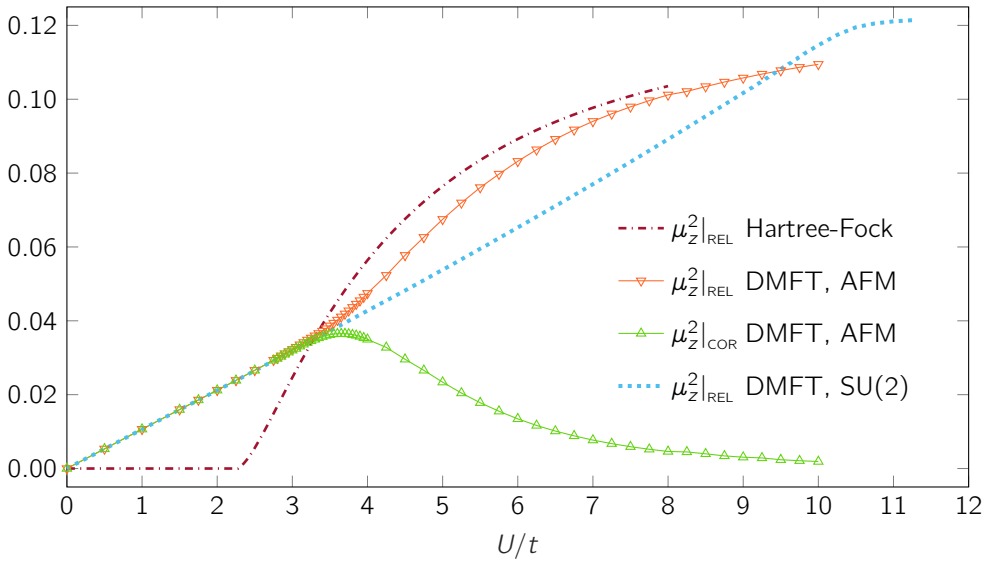


Fig. O.3.: Analysis of the local magnetic moments in the half-filled Hubbard model on the honeycomb lattice at zero temperature, as computed in DMFT and Hartree-Fock theory. The latter can capture only the AFM (Slater) phase at large U/t. The DMFT correlated part is reported as separate curve for the AFM (Mott-Heisenberg) solution, while it coincides with the relative mean square for the SU(2) symmetric solutions.

O.4 Slater vs Mott insulators

The ground state of the half-filled Hubbard model on the square lattice (and in bipartite lattices with a Fermi surface) is antiferromagnetic for every value of U/t. Yet, as introduced above, there is a clear distinction between a weak coupling Slater regime, in which the insulating state is a consequence of the doubling of the unit cell, leading to an effective single-particle band insulator, and a Mott-Heisenberg regime, in which the electrons are localized by the repulsion and magnetism arises from the ordering of their spins. The latter regime cannot be accessed by any single-particle description and it is inherently distinct from a band insulator, while the former can be described within the Hartree-Fock mean-field theory.

In the strong-coupling regime, one can consider an insulating solution without magnetic ordering. As we discussed above, we can label this solution as Mott-Hubbard insulator, to emphasize that the pure Mott phenomenon is sufficient to stabilize this state. However, despite the clear conceptual difference between a Slater insulator and a Mott-Heisenberg insulator, the two regimes share the same order parameter and it is not obvious how to distinguish them based on standard ground state estimators.

A possible quantity to track the evolution between the two regimes and to characterize the difference between them is the local magnetic moment [20], which is expected to grow from the small values typical of the Slater regime, where it starts as exponentially small, to large (saturated) values in the Mott-Heisenberg regime. Assuming full spin isotropy (as ensured by the SU(2) symmetry of the Hubbard interaction) we define the mean square of the local magnetic moment as [20]

$$\mu_z^2 = \frac{\left\langle (n_{i\uparrow} - n_{i\downarrow})^2 \right\rangle}{4}. \tag{O.19}$$

For a paramagnetic phase we expect that the other components μ_x^2 and μ_y^2 are equivalent, while we consider antiferromagnetic solution where the magnetization vector is parallel to the z axis. While not being directly measurable, the local magnetic moments can be analyzed within NMR experiments, which probe the low-frequency Fourier component of the time correlation function $\langle \mu_z(t)\mu_z(t_0)\rangle$ [7, 20].

The mean square moment defined by Eq. O.19 can be decomposed into three parts, amounting to (i) a Fermi gas contribution, ascribed to the Pauli exclusion, (ii) a term arising from the onset of long-range magnetic order and (iii) a *correlated part*, that cannot be captured by single-body methods, including static (Hartree-Fock) mean-field theory [20]

$$\mu_z^2 = \mu_z^2|_{\text{FG}} + \mu_z^2|_{\text{LRO}} + \mu_z^2|_{\text{COR}} \tag{O.20}$$

$$\text{(i)}\ \ \mu_z^2|_{\text{FG}} = \frac{\langle n_i \rangle \left(2 - \langle n_i \rangle\right)}{8} \tag{O.21}$$

$$\text{(ii)}\ \ \mu_z^2|_{\text{LRO}} = \frac{\left\langle (n_{i\uparrow} - n_{i\downarrow})^2 \right\rangle}{8} \tag{O.22}$$

$$\text{(iii)}\ \ \mu_z^2|_{\text{COR}} = \frac{\langle n_{i\uparrow} \rangle \langle n_{i\downarrow} \rangle - \langle n_{i\uparrow} n_{i\downarrow} \rangle}{2} \tag{O.23}$$

Given that $\mu_z^2|_{\text{FG}}$ is independent on the electron-electron interaction (as it reflects only the Fermi statistics) we can neglect it in the rest of the discussion. Hence we define the *relative* mean square magnetic moment as

$$\mu_z^2|_{\text{REL}} \stackrel{\text{def}}{=} \mu_z^2 - \mu_z^2|_{\text{FG}} \equiv \mu_z^2|_{\text{LRO}} + \mu_z^2|_{\text{COR}}. \tag{O.24}$$

In Fig. O.3 we report DMFT and Hartree-Fock relative mean square magnetic moments for the Hubbard model on the honeycomb lattice, at half-filling and zero temperature. We choose the half-filled honeycomb lattice in light of the vanishing density of states at the Fermi level, which impairs the perfect-nesting instability towards antiferromagnetic long range order and moves the critical interaction to a finite value, in contrast with other bipartite lattices [57, 58]. In this way we obtain a model that supports semimetal-insulator transitions (SMIT) to both a Mott-Heisenberg and a Mott-Hubbard phase. The former is

the ground state of the model at large U/t, while the latter can be stabilized, in DMFT only, by imposing a SU(2) constraint in the parametrization of the self-consistent bath, as discussed in section O.3.

Comparing the Hartree-Fock and DMFT estimates for $\mu_z^2|_{\text{REL}}$ in the AFM state, we readily notice how the former simulation does not generate any local magnetic moment beyond Fermi statistics, in the semimetal, according to the fact that $\langle n_{i\uparrow} n_{i\downarrow} \rangle = \langle n_{i\uparrow} \rangle \langle n_{i\downarrow} \rangle$, by construction of the static mean-field decoupling (compare Eqs. O.8 and O.23). The dynamical mean-field theory, on the other hand, grows a correlation-induced $\mu_z^2|_{\text{COR}}$ term as it renormalizes the double occupancy.

At the onset of antiferromagnetic order, both calculations acquire a $\mu_z^2|_{\text{LRO}}$ contribution (Eq. O.22) that quickly grows to dominate over the other terms. Remarkably, the DMFT correlated part starts to decrease at the critical interaction for the magnetic transition and asymptotically vanishes for large U/t, as a natural consequence of the freezing of the charge and spin freedom, as an electron is localized as soon as the system enters the antiferromagnetic phase and, in absence of long-range quantum correlations, its spin cannot flip in the limit of a perfectly saturated magnet. This leads to a coalescence of the static and dynamical mean-field predictions for the relative mean square moment at the strong coupling limit. We infer that the Hartree-Fock and DMFT ground states are well distinguished whenever the equal-position correlation function $g_{\uparrow\downarrow}(i,i) = \langle n_{i\uparrow} \rangle \langle n_{i\downarrow} \rangle - \langle n_{i\uparrow} n_{i\downarrow} \rangle$ has a large finite value, thus highlighting the strongly correlated nature of the Mott-Heisenberg insulator found within dynamical mean-field theory at intermediate interaction values, as opposed to the single-particle description in the Hartree-Fock theory, that defines the concept of a Slater insulator. On the other end, the SU(2)-constrained DMFT solution grows the relative mean square moment monotonically for all U/t ratios, saturating to $1/8$ at very large interaction. Given that at half-filling $\mu_z^2|_{\text{FG}} = 1/8$ (see Eq. O.21), we infer that at strong coupling the paramagnetic Mott-Hubbard insulator realizes a total mean square local moment of $1/4$, corresponding to maximal fluctuations of the local spin.

Overall, the reader would have noticed that the key ingredient to set apart Mott insulators from their simpler Slater description, lies in the equal-position correlation function, as a natural quantity to mark local moments beyond the Hartree-Fock mean-field *Ansatz*. In the next section we would like to make a step further and substitute this *ad hoc* quantifier with a general notion of *statistical "distance"* from the set of uncorrelated states, within the framework of quantum information theory. This would allow a deeper understanding of the nature of local correlations underpinning interaction-driven metal-insulator transitions. Further it entices a natural extension to the realm of nonlocal correlations, that will be explored in the second part of this thesis, chapters 7, 9 and 10. We inform the reader that a brief review of the quantum information geometrical concepts leveraged to define the statistical "distance" mentioned above is given in appendix A.

O.5 Quantifying the *distance* from Slater states with quantum information theory

Given the conservation of total charge and magnetization, assured by the symmetries of the Hubbard interaction [27–30] we can always write the density matrix of a single lattice site ρ_i as to conserve the *local* charge and magnetization. The global conservation is *inherited* by the subsystem in virtue of the additivity of charge and spin projections. Indeed, we can always write the total charge as $n = \langle n_1 \rangle + \langle n_2 \rangle + \dots$ and the total magnetization as $m = \langle \mu_1 \rangle + \langle \mu_2 \rangle + \dots$, where $\langle \mu_i \rangle = \langle n_{i\uparrow} - n_{i\downarrow} \rangle /2$, so that these global quantities are described by *local* operators, in the form[3]

$$\langle Q \rangle = \langle q_1 \otimes \mathbb{1}_2 \otimes \dots \rangle + \langle \mathbb{1}_1 \otimes q_2 \otimes \mathbb{1}_3 \otimes \dots \rangle + \dots \tag{O.25}$$

Whenever a global quantity can be expressed as in Eq. O.25, the generated unitary group $U_Q = \exp(i\alpha Q)$ is factorized on the local subspaces:

$$U_Q = U_{q_1} \otimes U_{q_2} \otimes \dots = \exp(i\alpha q_1) \otimes \exp(i\alpha q_2) \otimes \dots \tag{O.26}$$

Given that the conservation of the global expectation value $\langle Q \rangle$ is equivalent to constraining the global density matrix ρ to satisfy the relation $U_Q \rho U_Q^\dagger = \rho$, it directly follows that the local reduced density matrices ρ_i must satisfy $U_{q_i} \rho_i U_{q_i}^\dagger = \rho_i$ [59, 60].

For models in which a single site is populated by just one electronic orbital, this condition leads to a diagonal form of the local reduced density matrix [61–65]

$$\rho_i = \lambda_\bullet |\bullet\rangle\langle\bullet| + \lambda_\uparrow |\uparrow\rangle\langle\uparrow| + \lambda_\downarrow |\downarrow\rangle\langle\downarrow| + \lambda_{\uparrow\downarrow} |\uparrow\downarrow\rangle\langle\uparrow\downarrow| \tag{O.27}$$

where the $\lambda_\circ$ coefficients define a probability distribution for the four local states $|\bullet\rangle = |0\rangle \otimes |0\rangle$, $|\uparrow\rangle = |1\rangle \otimes |0\rangle$, $|\downarrow\rangle = |0\rangle \otimes |1\rangle$ and $|\uparrow\downarrow\rangle = |1\rangle \otimes |1\rangle$, expressed in the number occupation basis $|n_\uparrow\rangle \otimes |n_\downarrow\rangle$ of any arbitrary spin projection. For a Néel ordered phase, the density operator ρ_i will still be diagonal if written in the basis of the spin projection in which the order parameter is developed, so that Eq. O.27 is a general description of the local physics of paramagnetic Fermi liquids, Mott-Hubbard insulators and Mott-Heisenberg antiferromagnets, as modeled by the single-band Hubbard model. In chapter 2 we will discuss in detail how to treat magnetic anisotropy, as introduced by spin-orbit coupling in the Kane-Mele-Hubbard model.

Given that Eq. O.27 represents by definition a classical mixture of product states, hence a separable state with respect to the bipartition into the selected spin-projection orbitals, we

[3] Not all global quantities can be written in this form, of course. A notable counter-example is given by the total spin $\boldsymbol{S}^2$.

can readily infer that the two local spin orbitals are never entangled [66–71]. Furthermore, Eq. O.27 is manifestly diagonal in the two spin-projection sectors, hence satifying the form of a *pseudo-classical state* (Eq. A.14), so that all bipartite correlations between them are due to the probability distribution $\{\lambda_\circ\}$ and, as such, they should be considered classical [72, 73]. A discussion on the classification of correlations as classical, quantum and entanglement-induced is given in appendix A. We can furthermore quantify these classical correlations in the most general way by evaluating the *intra-orbital mutual information* between the selected local spin states. Indeed, given the density matrix of a generic bipartite quantum system ρ_{AB}, and ρ_{A} and ρ_{B} the reduced density matrices for the two subsystems, the mutual information between ρ_{A} and ρ_{B}, defined as $I(\mathrm{A}:\mathrm{B}) = s_{\mathrm{A}} + s_{\mathrm{B}} - s_{\mathrm{AB}}$, in terms of the von Neumann entropies $s_{\mathrm{A}} = -\operatorname{tr}\rho_{\mathrm{A}}\log(\rho_{\mathrm{A}})$, $s_{\mathrm{B}} = -\operatorname{tr}\rho_{\mathrm{B}}\log(\rho_{\mathrm{B}})$ and $s_{\mathrm{AB}} = -\operatorname{tr}\rho_{\mathrm{AB}}\log(\rho_{\mathrm{AB}})$, satisfies the inequality [74]

$$I(\mathrm{A}:\mathrm{B}) \geqslant \frac{\left(\langle \mathcal{O}_{\mathrm{A}} \otimes \mathcal{O}_{\mathrm{B}} \rangle_{\rho_{\mathrm{AB}}} - \langle \mathcal{O}_{\mathrm{A}} \rangle_{\rho_{\mathrm{A}}} \langle \mathcal{O}_{\mathrm{B}} \rangle_{\rho_{\mathrm{B}}}\right)^2}{2\|\mathcal{O}_{\mathrm{A}}\|^2 \|\mathcal{O}_{\mathrm{B}}\|^2} \tag{O.28}$$

for any pair $\mathcal{O}_{\mathrm{A}}$, $\mathcal{O}_{\mathrm{B}}$ of many-body operators acting on the Fock spaces of subsystems A and B, respectively, and with $\|\mathcal{O}_\circ\|$ denoting the Euclidean operator norm of $\mathcal{O}_\circ$ (its largest-modulus eigenvalue). A broader discussion on the role of the mutual information as a "distance" from the set of uncorrelated states, can be found, again, in appendix A.

Notating, for brevity, a generic spin-orbital basis as $|n_{i\uparrow}\rangle \otimes |n_{i\downarrow}\rangle$, we can explicitly write the local density matrix as [61–65]

$$\begin{aligned}
\rho_i &= \begin{pmatrix}
\langle (1-n_{i\uparrow})(1-n_{i\downarrow})\rangle & 0 & 0 & 0 \\
0 & \langle n_{i\uparrow}(1-n_{i\downarrow})\rangle & 0 & 0 \\
0 & 0 & \langle (1-n_{i\uparrow})n_{i\downarrow}\rangle & 0 \\
0 & 0 & 0 & \langle n_{i\uparrow}n_{i\downarrow}\rangle
\end{pmatrix} \\
&= \begin{pmatrix}
\delta_i + \mathcal{D}_i & 0 & 0 & 0 \\
0 & \langle n_{i\uparrow}\rangle - \mathcal{D}_i & 0 & 0 \\
0 & 0 & \langle n_{i\downarrow}\rangle - \mathcal{D}_i & 0 \\
0 & 0 & 0 & \mathcal{D}_i
\end{pmatrix}
\end{aligned} \tag{O.29}$$

where $\delta_i = 1 - \langle n_i \rangle$ and $\mathcal{D}_i = \langle n_{i\uparrow} n_{i\downarrow} \rangle$ are the local doping fraction and double occupancy.

At half filling $\langle n_{i\uparrow}\rangle + \langle n_{i\downarrow}\rangle = 1$, so that we can write the von Neumann entropy of ρ_i (*i.e.* the Shannon entropy of $\{\lambda_\circ\}$) in terms of only the magnetization $m_i = |\langle n_{i\uparrow}\rangle - \langle n_{i\downarrow}\rangle|$ and the double occupancy $\mathcal{D}_i$:

$$\begin{aligned} s_i &= -\operatorname{tr}\rho_i \log\rho_i = \sum_\circ \lambda_\circ \log\lambda_\circ \\ &= -\left(\frac{1-m_i}{2} - \mathcal{D}_i\right)\log\left(\frac{1-m_i}{2} - \mathcal{D}_i\right) \\ &\quad -\left(\frac{1+m_i}{2} - \mathcal{D}_i\right)\log\left(\frac{1+m_i}{2} - \mathcal{D}_i\right) \\ &\quad - 2\,\mathcal{D}_i \log\mathcal{D}_i . \end{aligned} \tag{O.30}$$

To access the intra-orbital mutual information we then partition the local orbital into its two spin-projection states and compute the respective partial traces

$$\rho_{i\uparrow} = \operatorname{tr}_\downarrow \rho_i = \begin{pmatrix} \langle n_{i\uparrow}\rangle & 0 \\ 0 & 1-\langle n_{i\uparrow}\rangle \end{pmatrix}, \tag{O.31}$$

$$\rho_{i\downarrow} = \operatorname{tr}_\uparrow \rho_i = \begin{pmatrix} \langle n_{i\downarrow}\rangle & 0 \\ 0 & 1-\langle n_{i\downarrow}\rangle \end{pmatrix}, \tag{O.32}$$

and the sum of the respective von Neumann entropies

$$\begin{aligned} s_{i\uparrow} + s_{i\downarrow} &= -\operatorname{tr}\left(\rho_{i\uparrow}\log\rho_{i\uparrow} + \rho_{i\downarrow}\log\rho_{i\downarrow}\right) \\ &= -\left(1-m_i\right)\log\left(\frac{1-m_i}{2}\right) \\ &\quad -\left(1+m_i\right)\log\left(\frac{1+m_i}{2}\right). \end{aligned} \tag{O.33}$$

Finally the intra-orbital mutual information between the two spin orbitals in the chosen basis is given, in terms of Eqs. O.30 and O.33 as

$$I(\uparrow\!:\!\downarrow) \;=\; s_{i\uparrow} + \; s_{i\downarrow} - \; s_i\,, \tag{O.34}$$

So far, we have established that two local spin orbitals are never entangled for a spin-conserving model with local Hubbard interactions and we have provided a general recipe to quantify the classical correlations, in terms of their von Neumann mutual information.

We deepen the significance of our analysis by showing that, within a local Hartree-Fock mean-field theory of the Hubbard model, also the classical correlations vanish, for any paramagnetic or antiferromagnetic state. By construction of the mean-field *Ansatz* (Eq. O.8), the double occupancy is expressed as the product of single-particle expectation values, in the appropriate spin-orbital basis:

$$\begin{aligned} \mathcal{D}_i^{\mathrm{HF}} &= \frac{\left\langle \delta \mathbf{H}^{\mathrm{HF}} \right\rangle_{\rho_i}}{U} = \langle n_{i\uparrow} \rangle \langle n_{i\downarrow} \rangle \\ &= \left(\frac{1-m_i}{2} \right) \left(\frac{1+m_i}{2} \right) \end{aligned} \tag{O.35}$$

Inserting this expression in Eq. O.30 we obtain

$$\begin{aligned} s_i^{\mathrm{HF}} &= -\frac{(1-m_i)^2}{2} \log\left(\frac{1-m_i}{2} \right) - \frac{(1+m_i)^2}{2} \log\left(\frac{1+m_i}{2} \right) \\ &\quad - \frac{(1-m_i)(1+m_i)}{2} \left[\log\left(\frac{(1-m_i)}{2} \right) + \log\left(\frac{(1+m_i)}{2} \right) \right] \\ &= -\frac{(1-m_i)^2 + (1-m_i)(1+m_i)}{2} \log\left(\frac{1-m_i}{2} \right) \\ &\quad - \frac{(1+m_i)^2 + (1-m_i)(1+m_i)}{2} \log\left(\frac{1+m_i}{2} \right) \\ &= -(1-m_i) \log\left(\frac{1-m_i}{2} \right) - (1+m_i) \log\left(\frac{1+m_i}{2} \right) \end{aligned} \tag{O.36}$$

which exactly matches Eq. O.33, proving that at the Hartree-Fock level the intra-orbital correlation (Eq. O.34) vanishes, regardless of the value of m_i, both in the antiferromagnetic and paramagnetic states. This confirms the expectation that the Hartree-Fock approximation neglects any kind of dynamical, *local* correlation. As we will discuss in chapters 7, 9 and 10 nonlocal correlations can indeed exist in quadratic models, and we can observe a finite nonlocal mutual information even for noninteracting systems.

We end this section by a direct inspection of the intra-orbital mutual information in the model calculations introduced in the previous section O.4, *i.e.* for both the Mott-Heisenberg and the Mott-Hubbard semimetal-insulator transitions (SMIT) of the Hubbard model on the honeycomb lattice.

In the left panel of Fig. O.4 we report the evolution of the single-orbital von Neumann entropy s_i, the single-spin von Neumann entropy $s_{i\sigma}$ and the intra-orbital mutual information $I(\uparrow:\downarrow)$, as a function of the local Hubbard interaction U/t, for a DMFT calculation that is allowed to develop an antiferromagnetic order parameter. In the noninteracting limit the single-orbital entropy s_i assumes its maximal value $\log(4)$, corresponding to

an equal distribution of single-orbital Fock states in the local reduced density matrix: $\lambda_\bullet = \lambda_\uparrow = \lambda_\downarrow = \lambda_{\uparrow\downarrow} = 1/4$. As the interaction is increased, the energy cost of having doubly occupied states (and consequently empty states, at half-filling) grows larger and larger, reducing the value of s_i. At the Mott-Heisenberg transition a finite magnetic order parameter m_i is developed, so that s_i starts to decrease significantly faster (see Eq. O.30). Eventually, for a fully saturated antiferromagnetic state, s_i vanishes, as all the freedom on the single-orbital configuration is removed.

On the other hand, the two single-spin entropies can be shown to always coincide $s_{i\uparrow} = s_{i\downarrow}$, since the density of each spin species is fixed by the half-filling condition. They are moreover fixed at their maximal value log(2) as long as no AFM order parameter is developed. We can understand this by realizing that the von Neumann entropy of a single spin can be reduced only by an imbalance of of $\langle n_\uparrow \rangle = 1 - \langle n_\downarrow \rangle$ and $\langle n_\downarrow \rangle = 1 - \langle n_\uparrow \rangle$, as evident from a comparison of Eqs. O.31, O.32 and O.33. At the Mott-Heisenberg transition, both the spin-entropies start to rapidly decrease, as the spin population imbalance is directly introduced by the magnetization $m_i = |\langle n_\uparrow \rangle - \langle n_\downarrow \rangle|$.

The combined behavior of s_i and $s_{i\uparrow}$ leads to an interesting evolution of the intra-orbital mutual information $I(\uparrow:\downarrow) = s_{i\uparrow} + s_{i\downarrow} - s_i$, that vanishes at $U = 0$, as $s_i = \log(4) = s_{i\uparrow} + s_{i\downarrow}$, gradually increases in the interacting semimetal until it reaches a maximum at the Mott-Heisenberg transition point. After the transition, the onset of a finite magnetization slowly depletes it, as the system is completely frozen and no information content can be extracted from neither the single orbital or one of the two spin orbitals and without information, correlation cannot exist! [75, 76]

On the right panel of Fig. O.4 we report the same quantities, but this time for the paramagnetic simulation, *i.e.* a calculation that does not allow the development of a finite order parameter. In view of the preceding discussion, we can surely expect the static and dynamical mean-field solutions to progressively depart away from each other, as the interaction is increased, and reach a maximal "distance" when the latter realizes the paramagnetic Mott insulating state. Indeed the absence of spion symmetry breaking leads to a monotonically increasing intra-orbital mutual information that approaches log(2) in the limit of strong coupling $U \gg t$. The growth is very fast before the Mott transition, which happens when $I(\uparrow:\downarrow)$ is already very close to the asymptotic value, at $U/t \approx 10.75$. We can locate the transition point by inspecting (see Fig. O.5) the behavior of the quasiparticle weight Z (Eq. O.18), which must vanish for a Mott state, as a witness of the death of quasiparticles and consequently of a valid description in terms of single-body entities.

We finally observe that the asymptotic value of log(2) for the intra-orbital mutual information does directly descend from the strong coupling limit of the single-orbital entropy s_i, as the single-spin entropy is fixed to log(2) at all interaction values. Indeed, the former quantity has been intensely studied across paramagnetic MITs, both in the limit of infinite

dimensions [61] and for the square lattice in two dimensions [3, 62], displaying essentially the same behavior discussed above. Yet, it does not capture the signature of Mott insulators as strongly correlated electronic systems, as it always decreases, monotonically with the growth of the interaction.

As we will thoroughly discuss in chapters 7 and 9, it instead bounds from above all the local *fluctuations* in the many-body state. Intuitively, one can consider Eq. O.28 and take A=B, leading to a "diagonal" mutual information $I(\mathrm{A}:\mathrm{A}) = s_{\mathrm{A}}$ (it is often referred to as *self-information*, in this context) that bounds from above all the fluctuation functions $\langle \mathcal{O}_{\mathrm{A}}^2 \rangle - \langle \mathcal{O}_{\mathrm{A}} \rangle^2$. The argument can be made rigorous, see Ref. [75]. Indeed, an inspection of two prominent fluctuation functions, *i.e.* the charge and spin local fluctuations, as reported in Fig. O.6, demonstrates (i) a monotonic reduction of the charge fluctuations, for both the Hubbard-Heisenberg and the Mott-Hubbard transitions, as indeed expected for a transition to an insulating state, and (ii) a monotonic increase of the spin fluctuations in the semimetal phase, that continues up to saturation for the paramagnetic calculation but, on the contrary, is interrupted by the onset of antiferromagnetism at the Mott-Heisenberg transition, where instead it starts to decrease and eventually vanish in the strong coupling limit.

In light of the above discussion, we can suggest (of course not prove, since an upper bound is not obliged to follow the behavior of one specific quantity that it bounds), that the global reduction of the single-orbital von Neumann entropy across both the Mott-Heisenberg and the Mott-Hubbard transitions is dominated by the progressive reduction of the charge fluctuations, in the semimetal, while the different behavior in the two Mott insulators, can indeed be explained by the opposite fate of the spin fluctuations: on one hand, for the Mott-Heisenberg transition we have a system where the two physically significant fluctuation functions vanish in the strong coupling limit, and s_i indeed appears to approach the same limit, while on the other hand, the Mott-Hubbard insulator displays strong (in fact, maximal) spin fluctuations, giving a clear-cut explanation of the log(2) value of the single-orbital entropy.

Whereas we have shown that the single-orbital behavior correctly accounts for the local fluctuation properties of the system, we can indeed argue that the correct measure of local *correlation* is given by the intra-orbital mutual information. A direct comparison of Figs. O.3 and O.4 clearly demonstrates that $I(\uparrow:\downarrow)$ perfectly accounts for the observed behavior of the correlated part of the local moment $\mu_z^2|_{\mathrm{cor}}$, which undoubtedly represent a key property to witness the genuine Mott character of a (semi)metal-insulator transition. We will report the same quantities and briefly recall the same arguments in chapter 9, section 9.2, to confirm that the Hubbard model on the square lattice, at least for the paramagnetic Mott transition, displays the same phenomenology, which then is not to be considered as a specific feature of the honeycomb lattice.

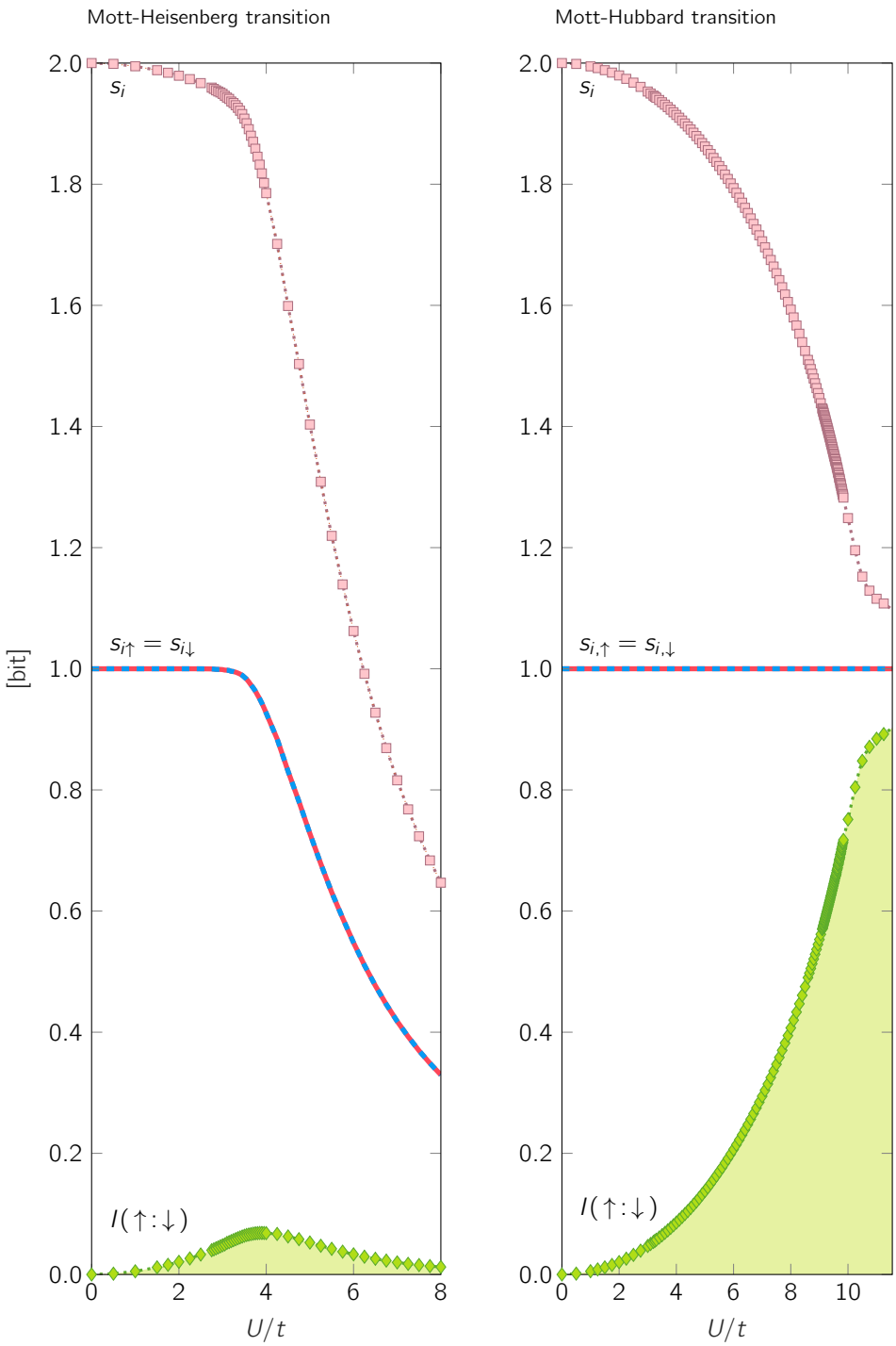


Fig. O.4.: Single-orbital entropy, single-spin entropy and intra-orbital mutual information for the Mott-Heisenberg (left) and the Mott-Hubbard (right) semimetal-insulator transitions found in the DMFT solutions for the Hubbard model on the honeycomb lattice. All values are reported in bits (units of log(2)).

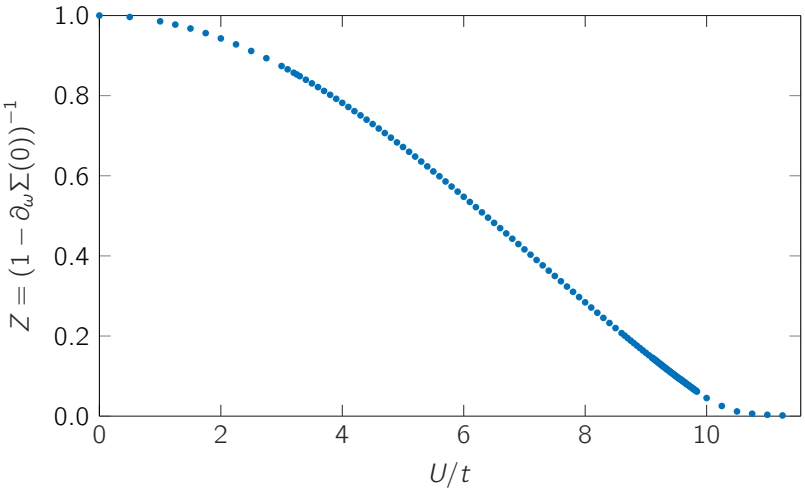


Fig. O.5.: Evolution of the quasiparticle weight Z as a function of the Hubbard interaction strength U/t, for the paramagnetic Mott transition found in the Hubbard model on the honeycomb lattice. The vanishing of Z signals the death of Fermi liquid theory and hence the transition to a strongly-correlated insulating state.

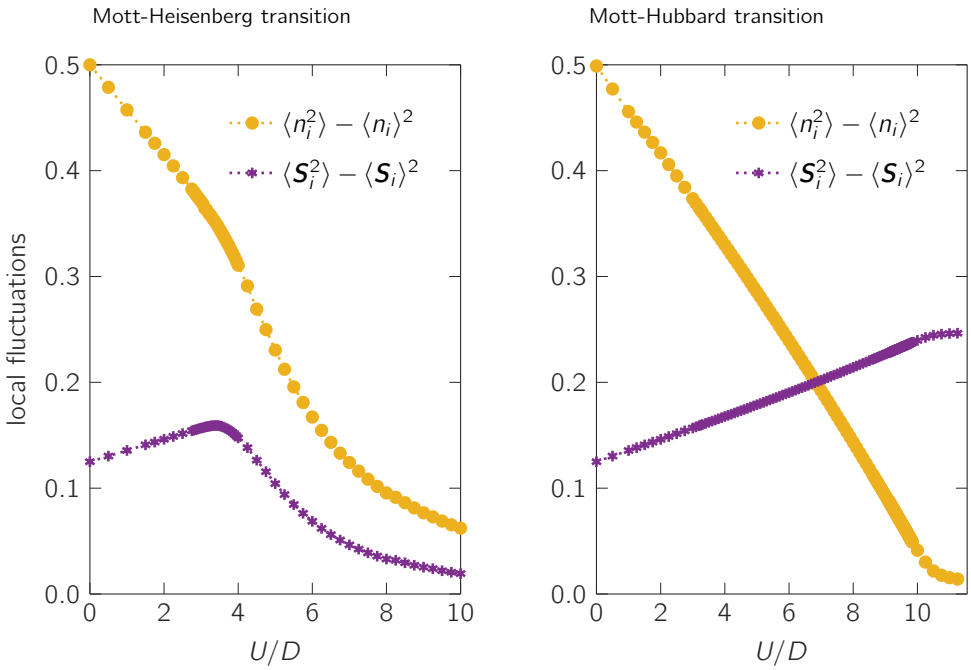


Fig. O.6.: Local charge and spin fluctuation for the Mott-Heisenberg (left) and the Mott-Hubbard (right) semimetal-insulator transitions found in the DMFT solutions for the Hubbard model on the honeycomb lattice.

O.6 Other correlated insulators: nontrivial electronic topology

The existence of interaction-induced metal-insulator transitions (MIT) and semimetal-insulator transitions (SMIT), that we have concisely described in the previous sections, underlines the possibility of phase transitions that are not associated to the traditional paradigm of spontaneous symmetry breaking, the incredibly influential masterpiece of statistical physics introduced by Ginzburg and Landau in 1950 [77]. Or, at least, an order parameter for the paramagnetic Mott-Hubbard transition as not yet been found and its definition constitutes an outstanding open problem in condensed matter physics, despite some early attempts, relevant only for the critical endpoint at high-temperature [78].

Yet, the experimental discovery of topological insulators, happened almost two decades ago [79, 80], has attracted a fast growing attention to a whole other class of phase transitions that cannot be associated to any kind of local order parameter. We will not delve, here, into the description of this vast and complex field. However we will give a brief review of some selected concepts that will be useful for the description of our results on the Kane-Mele-Hubbard model, in the second part of the thesis (chapters 1, 2, 3, 4, 5). For reviews of this evolving field, we suggest Refs. [81–83].

The very first theoretical model for a topological insulator dates back to the '80s [84], hypothesizing a possible effect in graphene many years before the first synthesis of the material (which, however, has a too small spin-orbit coupling to actually host the predicted properties). In this way Haldane devised the model that now is named after himself, giving a minimal description of what now is usually called a *Chern insulator*. The main, spectacular property of a Chern insulator is that it sustains a quantum Hall effect, without the need of an external magnetic field. The resulting edge currents, in a bounded sample, can be proven to be dissipation-less, as no back-scattering is allowed for electrons residing in the relevant quantum states of the material. In the top-left panel of Fig. O.7 we show a schematic illustration of this situation, together with, on the right, the corresponding properties of the band structure. It features an energy gap, for the Bloch states in the bulk of the material, and a single edge state, crossing the gap, that is associated to the dissipation-less currents described above. As we anticipated there is no local order parameter for the transition between a metal, or another kind of insulator, and this electronic phase and the theoretical tool to uniquely characterize it is the so-called Chern number. The Chern number is what we call a *topological invariant*, namely an integer that is associated with highly nonlocal features of the energy bands and their correspondent eigenstates.[4] Most remarkably, the Chern number is exactly proportional to the quantum Hall current in the

[4] This is crucial: the energies alone do not determine the Chern number!

edge states, in terms of fundamental constants. For this reason, a zero Chern number identifies a *trivial*, *i.e.* nontopological state, while any nonzero value for the Chern number identifies an equivalence class of states with the same topology. The sign of the Chern number determines the *chirality* of the edge currents, such that opposite Chern numbers with the same magnitude correspond to distinct topological families. It has been shown that many kind of perturbations are not able to easily change the Chern number, hence the topological properties of a system. On the other hand, when a transition occurs it is always associated with the closure of the energy gap (breaking the adiabatic connection with the original system) and/or with the presence of dramatic effects, like extreme disorder or strong electronic correlations, invalidating the whole band theory picture that underlies the elementary description of these states. There are many other aspects associated with the concept and the realization of a Chern insulator, but here we do not enter in further details.

Another family of topological insulators is given by the so-called quantum spin-Hall insulators (QSHI), depicted in the lower panels of Fig. O.7. These states can be generally decomposed into the superposition of two "copies" of a Chern insulator, where one copy describes the properties of one spin family (*e.g.* the electrons in a $|\uparrow\rangle$ spin state) and the other describes the remnant electrons (the ones in a $|\downarrow\rangle$ state). In fact, the very first model for a QSHI has been developed by Kane and Mele [85, 86], assembling together two copies of the aforementioned Haldane model [83]. Crucially, the two copies of the Chern state are characterized by opposite Chern numbers, so that the total charge current at the edge of the system vanishes (as the Chern numbers are additive, for independent bands, or spin bands). However, the two spin bands are effectively in a Chern state, hence there would be counter-propagating currents, with opposite spin character, defining the so-called *helical spin currents*, that do not transport charge but indeed transport spin. These currents are less robust against perturbations than the corresponding charge currents in Chern insulators. In particular they are protected by time-reversal symmetry [86], meaning that any process that can flip a spin does indeed cause back-scattering, dissipating the edge currents. Yet, quantum spin-Hall insulators have been successfully realized in experiments [79], effectively driving the growth of the whole field and attracting intense research in both the theoretical and applied domains. Given that the total Chern number of a QSHI vanishes, the topology of the system must be characterized by a different integer. It has been show that this integer indeed exists and can assume just two values (even or odd) [86]. For this reason it is universally referred to as the $\mathbb{Z}_2$ topological invariant. Under rather general conditions, the $\mathbb{Z}_2$ invariant can be computed directly from the two individual Chern numbers associated to the opposite spin polarizations, as $\mathbb{Z}_2 = (\mathbb{C}_\uparrow - \mathbb{C}_\downarrow)/2$. Whenever the spin projection is conserved, the two individual Chern numbers are well defined and one can directly compute either of them, as $\mathbb{Z}_2 \equiv \mathbb{C}_\uparrow \equiv \mathbb{C}_\downarrow$. In this case the $\mathbb{Z}_2$ invariant is also called *spin-Chern* number.

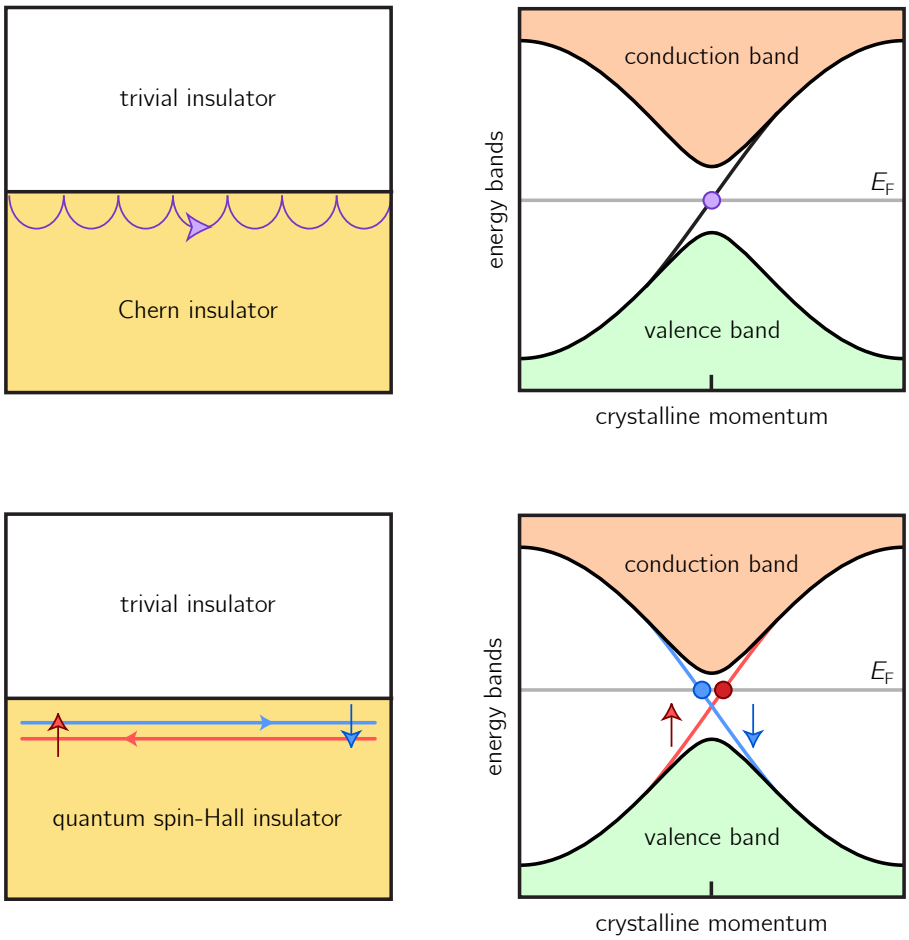


Fig. O.7.: Schematic representations of a Chern insulator (top) and of a quantum spin-Hall insulator (bottom). On the left an illustration of the typical interface between the topological insulator and a trivial insulator (*e.g.* the vacuum). On the right the corresponding features in the band structure of the material, for bounded crystallites, solved in open boundary conditions. The Chern insulator presents a single edge-state that lies within the band gap. If the Fermi level E_F crosses this state the interface with the vacuum (or with a trivial insulator) sustains a dissipationless current. The quantum spin-Hall insulator, on the other hand, features two distinct edge states, with an opposite, well-defined spin character. The corresponding edge states are counter-propagating, resulting in zero charge current, but a finite spin current, that is protected by time-reversal symmetry (*i.e.* spin-flip processes can indeed dissipate its flow). Adapted from Hasan and Kane [81].

Returning to our main motivation, namely the analysis of correlated insulating states of matter, we point out that notwithstanding the possibility of defining and realizing topological insulating systems that are well described within a single-particle picture, the study of the effect of electron-electron interactions and in particular of strong correlation effects on these states has been very fruitful, revealing a multitude of interesting research directions. We leave a full coverage of the progress made in the last two decades to Refs. [87, 88] and focus on two main points, relevant for our discussion of the phase diagram of the Kane-Mele-Hubbard (KMH) model, which is nothing but the inclusion of the local Hubbard repulsion (Eq. O.5) into the minimal model for QSHI states proposed by Kane and Mele [85, 86].

- Topological insulators are quite robust against the electronic repulsion, yet they can undergo interaction-induced phase transitions to topologically trivial band insulators. In this case the interaction renormalizes the relevant physical parameters in the Hamiltonian and makes the system cross its topological phase boundary. Despite the apparent simplicity, many interesting effect can be associated with this class of phenomena, as the conversion of a continuous topological transition, *i.e.* the standard picture in noninteracting and Hartree-Fock band theories, to a discontinuous transition that does not close the gap nor it is associated with any spontaneous symmetry breaking [89–93].

- Topological insulators can be completely transformed in strongly correlated many-body states, such as Mott-Heisenberg and Mott-Hubbard insulators. In this case it is not easy to determine if the nontrivial topology survives or it is removed by the Mott transition. The onset of magnetism should in principle significantly "endanger" the existence of a QSHI state, as it breaks the protecting time-reversal symmetry. Yet, many observations and theoretical predictions have been made for weakly magnetized topological insulators, or strongly magnetized systems that are transformed from quantum spin-Hall insulators to Chern insulators, by the onset of antiferromagnetism. In both cases the the resulting phase is usually referred to as antiferromagnetic topological insulator (AFMTI) [94, 95]. In chapter 3 we discuss our prediction for a weakly magnetized AFMTI state, found in the Kane-Mele-Hubbard model, in the proximity of a discontinuous Mott-Heisenberg transition at intermediate interaction strength. On the other hand, a Mott-Hubbard transition makes for an even more difficult determination of the topological character of the resulting many-body state, generating heated debates in the community [96–98]. Of particular interest in this context is the concept of *topological Mott insulator* [47], recently brought to renovated attention as evidence of nontrivial topology has been reported for the Mott-Hubbard phase in the Kane-Mele-Hubbard model [99], as well as in closely related systems [100].

We end this section by noting that, as isolated as the attempt to develop of a Ginzburg-Landau theory [78], there have been recent proposals for classifying the Mott-Hubbard transition as inherently topological, with an invariant related to generalizations of the Luttinger theorem [101, 102]. A remarkable connection can be made with the concept of Luttinger surface and hence to the possible extension of Fermi liquid theory to the spin degrees of freedom of a Mott-Hubbard insulator [103]. This in turn suggests a renovated interest in the historically influential proposal to describe the parent compound of cuprate superconductors as a resonating valence bond insulator [24, 25] or, more in general, as a quantum spin liquid [48]. This, once again, suggests a deep connection between the physics of Mott-Hubbard localization and the development of large nonlocal entanglement. While we are not able, within DMFT or its cluster extension, to model the long-range properties of quantum spin liquids, we make a small step towards the answer to these significant questions with a study of the quasilocal, *i.e.* extremely short-range, entanglement between electronic orbitals residing at different lattice sites, as thoroughly discussed in the second part of the thesis, chapters 6, 7, 8, 9, 10.

O.7 There is much more to strong correlations

In the beginning of the chapter, we have briefly mentioned that the parent compound of cuprate superconductors is always a Mott-Heisenberg insulator, and that the general understanding of high-temperature superconductivity in these materials is believed to be intimately connected to the physics of doping a Mott insulator [24–26].

A deeper exploration of the topic, immediately reveals that the doping phase diagram of these materials is extremely rich and that superconductivity and Mott-Heisenberg antiferromagnetic ordering are just a tiny piece of the puzzle. In Fig. O.8 we report a qualitative representation of the cuprate phase diagram, highlighting with a vertical line the parent (undoped) compound.

In the vicinity of half-filling, a large antiferromagnetic region dominates the low temperature landscape. But once we inject enough holes (or electrons, even if the electron doping is much less favorable in practice, due to the asymmetry of the antiferromagnetic dome) the system is transformed in either a superconductor (at low enough temperature) or a so-called *pseudogap* metal. The experimental features of the latter phase have long puzzled the community [55, 104], eventually enforcing the idea that a complete theoretical understanding of the underlying strongly correlated physics is probably needed, as a partial key to unlock the understanding and hence the engineering of superconducting states with high(er) critical temperature. In this thesis we will contribute to essentially a single aspect of this puzzle, focusing on the evaluation of the intra-orbital mutual information, defined above in section O.5, and the short-range two-site entanglement, which together will provide a hint for an intimate connection between the quasilocal physics of pseudogap

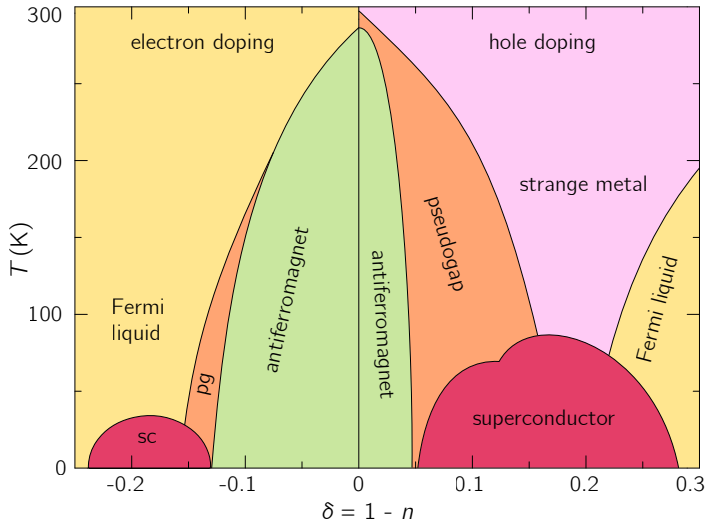


Fig. O.8.: Schematic phase diagram of a cuprate high-temperature superconductor. The parent (undoped) compound is an antiferromagnetic Mott-Heisenberg insulator, at sufficiently low temperatures. Upon doping exotic, strongly correlated phases can arise, including unconventional superconductivity.

metals and the properties of a Mott-Hubbard insulator. The discussion of these results is included in chapter 10, while a brief outlook on the what can be done to extend the analysis to the notable long-distance properties of the Fermi surface will be given in the conclusion of the thesis.

Returning to the phase diagram in Fig. O.8, we observe that, only on the hole-doped side, another exotic metallic phase can be stabilized, at high temperature and/ore large doping fraction. This *strange* metal violates the Ohm law, with a linear temperature dependence of the resistivity and of the Hall coefficient [26, 105]. While significant progress has been made on more complicated models, featuring random interactions at all distances in a disordered medium, with notable connections with the physics of black-holes [106, 107], recent evidence suggests that the strange metal phase of cuprates can be, at least partially, captured by the doped single-band Hubbard model [108].

Overall, the tight competition between different energy scales makes for beautifully rich phase diagrams in all strongly correlates systems, ranging from alternative platforms for unconventional superconductivity [109–118], to multiferroic perovskites [119–121], twisted bilayers [122–124], SU(N) systems in cold-atom simulators [125–127], and even catalytic molecular complexes, relevant to biology [128, 129]. In turn, the understanding and the classification of the emerging complexity can be often fruitfully exploited for controlling new phenomena and engineering novel devices, spanning the different pillars of materials science, soft matter and quantum technologies.

Part I

Local classical correlations in the honeycomb lattice

Introduction

1

> *Hexagons are the bestagons.*
> *The rest just can't compete with the best.*
>
> — **CGP Grey**
> referring (also) to graphene

1.1 Topological and magnetic phases of interacting Dirac fermions

The study of interaction effects on Dirac fermions has an intense, if relatively recent, history in the field of strongly correlated materials, dating back to the first explorations on graphene, where theoretical efforts [57] have anticipated the experimental discovery [58]. The birth of topological insulators [80–83], on the other hand, has brought renovated attention on the role of the intrinsic spin-orbit coupling, whose central role was earlier emphasized, in the absence of interactions, by Haldane [84] and Kane and Mele [85, 86].

The so-called Kane-Mele-Hubbard (KMH) Hamiltonian [87, 88] promised to become a paradigm for the interplay between topology and spin-orbit coupling with electron correlations. The search for a solution of this model has been boosted by the quick realization that, at half-filling where it describes interacting quantum spin-Hall insulators (QSHI), it is not affected by a sign-problem in projective quantum Monte Carlo schemes [87, 88]. The consequent fervent activity has spanned the entirety of the last decade, involving a multitude of analytical and numerical techniques in the field of strongly correlated electrons [130–148].

So far, to the best of our knowledge, most research has focused mainly on the identification and characterization of the ground state properties of the model. On the other hand, the magnetic anisotropy introduced by the topological spin-orbit coupling suggests that it is important to characterize the different antiferromagnetic phases, and the mechanisms behind their stability, beyond the plain determination of the energetically favoured solutions at zero temperature. This can lead to opportunities to favour one or another phase, or to switch from one to the other by playing with geometry and/or introducing perturbations to the model.

For this reason, in this chapter we use dynamical mean-field theory (DMFT, see section O.3) to address the comparison and competition of solutions with different symmetries:

paramagnetic, in-plane and out-of-plane antiferromagnetic. We further compare the DMFT results to the Hartree-Fock (HF) static mean-field theory, in order to address the role of dynamical correlations in the stabilization of these solutions. Moreover, we support a conventional analysis of their properties with concepts from quantum information theory: a rigorous quantification of quantum and classical correlations between electrons populating the same local orbital, which we label as intra-orbital correlations, will allow a clear-cut assessment of the "distance" between the DMFT and HF solutions, complementing earlier studies on interaction-driven antiferromagnets [149, 150].

The peculiar effects of the intrinsic spin-orbit coupling are shown to lead to significantly strong local correlations in weakly-magnetized states, in contrast with the pure Hubbard model on the honeycomb lattice. Furthermore, these states are proven to preserve the nontrivial topology of the parent QSHI state, hinting at a possible antiferromagnetic topological insulating (AFMTI) [94, 95] phase in the model. Similar findings have been reported for the Bernevig-Hughes-Zhang-Kanamori model [151–154], describing interacting quantum spin-Hall insulating phases on the square lattice [87–89, 91].

Finally, the comparison with the symmetry unbroken solution establishes the fate of intra-orbital correlations in the strong-coupling limit of the model, for both the semimetallic noninteracting reference, at vanishing spin-orbit coupling, and the topological QSHI state. The resulting local reduced density matrix is shown to host maximal classical correlations, reflecting our recently proposed connection between genuine Mott localization without symmetry breaking and the development of short-range nonlocal entanglement [3], that will be discussed in detail in the second part of the thesis, chapters 6, 7, 8, 9 and 10.

We conclude the chapter with an outlook on future research opportunities, including the extension of the analysis to nonlocal physics, as to enable direct access to quantum and classical nonlocal correlations and the investigation of the role of Green's function zeros [96–98], recently proposed to describe topological Mott insulating phases [47] on the Kane-Mele-Hubbard Hamiltonian and closely related models [99, 100].

1.2 Outline of the following chapters

The following chapters are organized as follows:

- In chapter 2 we define the Hamiltonian, discuss its main features and give an overview of the existing literature. We proceed, in sections 2.1 and 2.2 to detail our static and dynamical mean-field calculations, underlining the different assumptions to get in-plane magnetized, out-of-plane magnetized and paramagnetic solutions. Finally, in section 2.3 we prove the absence of intra-orbital entanglement and define a rigorous measure of classical intra-orbital correlations, within the quantum information framework introduced in section O.5.
- In chapter 3 we present numerical results for the two anisotropic antiferromagnetic transitions (sections 3.1, 3.2) and compare the intra-orbital correlations to those of the paramagnetic Mott insulator (sections 3.3) and 3.4). Thus we outline an educated guess about the short-range nonlocal entanglement of Mott-Hubbard insulators, leaving a full exploration to chapter 9, in the second part of the thesis.
- In chapter 4 we provide further computational details, analyzing the energetic competition between the two anisotropic antiferromagnetic solutions, across the parameter space of the model. A discussion on possible, experimentally feasible strategies for stabilizing the unfavorable out-of-plane Néel state is included.
- Finally in chapter 5 we draw our conclusions and outline future research directions, concerning several aspect of the present discussion.

The Kane-Mele-Hubbard model

2

We consider the *minimal* Hamiltonian for noninteracting topological Dirac fermions on the honeycomb lattice, due to Kane and Mele [85, 86]

$$\mathbf{H}_{\mathrm{KM}} = t \sum_{\langle ij \rangle} c_i^\dagger c_j + i\lambda_{\mathrm{so}} \sum_{\langle\langle ij \rangle\rangle} c_i^\dagger (\boldsymbol{\nu}_{ij} \cdot \boldsymbol{\sigma}) c_j \,, \tag{2.1}$$

where $c_i = (c_{i\uparrow},\, c_{i\downarrow})$, $\langle ij \rangle$ and $\langle\langle ij \rangle\rangle$ indicate sums respectively over the nearest and next-nearest neighbors on the honeycomb lattice,

$$\boldsymbol{\nu}_{ij} = \frac{\boldsymbol{d}_{ik} \times \boldsymbol{d}_{kj}}{|\boldsymbol{d}_{ik} \times \boldsymbol{d}_{kj}|}, \quad \boldsymbol{\sigma} = (\sigma_x, \sigma_y, \sigma_z),$$

with $\boldsymbol{d}_{ik}$ and $\boldsymbol{d}_{kj}$ vectors connecting the i-th and j-th nearest neighbors sites in the lattice through the intermediate k-th site, and σ_x, σ_y and σ_z are the Pauli matrices associated to the spin degrees of freedom.

We define our model as minimal because, with respect to the original references [85, 86] here we neglect the staggered sublattice potential

$$\mathbf{H}_\nu = \lambda_\nu \sum_i \varepsilon_i c_i^\dagger c_i, \quad \varepsilon_i = \begin{cases} +1 & i \in \{\text{Sublattice A}\} \\ -1 & i \in \{\text{Sublattice B}\} \end{cases}$$

and the Rashba term

$$\mathbf{H}_{\mathrm{R}} = \frac{i\lambda_{\mathrm{R}}}{2} \sum_{\langle ij \rangle} c_i^\dagger \frac{(\boldsymbol{\sigma} \times \boldsymbol{d}_{ij})_z}{|\boldsymbol{d}_{ij}|} c_j$$

which are meant to model a possible ionic nature of the bond and the presence of a growth substrate, respectively. These two terms compete with the the λ_{so} spin-orbit coupling, closing the topological gap respectively for $\lambda_\nu \geqslant 3\sqrt{3}\lambda_{\mathrm{so}}$ and $\lambda_{\mathrm{R}} \geqslant 2\sqrt{3}\lambda_{\mathrm{so}}$ [86]. In their absence, Eq. 2.1 describes free-standing graphene for $\lambda_{\mathrm{so}} = 0$ and a model quantum spin-Hall insulator (QSHI) otherwise.

The noninteracting model in Eq. 2.1 can be solved exactly in reciprocal space, as

$$\mathbf{H}_{\mathrm{KM}} = \sum_{\boldsymbol{k}} \Psi_{\boldsymbol{k}}^\dagger \mathbf{H}(\boldsymbol{k}) \Psi_{\boldsymbol{k}}$$

$$\Psi_{\boldsymbol{k}} = (c_{\boldsymbol{k}\mathrm{A}\uparrow},\, c_{\boldsymbol{k}\mathrm{B}\uparrow},\, c_{\boldsymbol{k}\mathrm{A}\downarrow},\, c_{\boldsymbol{k}\mathrm{B}\downarrow})$$

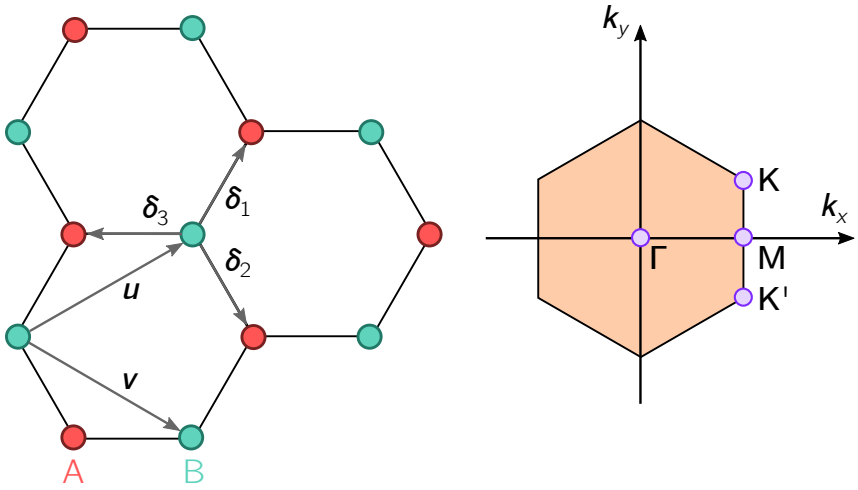


Fig. 2.1.: On the left a fragment of the honeycomb lattice, with the two sublattices marked in different colors. The arrows represent the two lattice basis vectors, $\boldsymbol{u}$ and $\boldsymbol{v}$, and the inter-sublattice nearest-neighbor displacements $\boldsymbol{\delta}_i$. On the right the hexagonal first Brillouin zone, whose extreme points are grouped into two inequivalent classes $\mathbf{K}$ and $\mathbf{K}'$, hosting the Dirac fermions at the Fermi level, for the half-filled semimetal.

with

$$\begin{aligned}
\mathbf{H}(\boldsymbol{k}) &= x_{\boldsymbol{k}}\Gamma_{01} + y_{\boldsymbol{k}}\Gamma_{02} + \delta_{\boldsymbol{k}}\Gamma_{33} \\
&= \begin{pmatrix} \delta_{\boldsymbol{k}}(\boldsymbol{k}) & x_{\boldsymbol{k}} - iy_{\boldsymbol{k}} & 0 & 0 \\ x_{\boldsymbol{k}} + iy_{\boldsymbol{k}} & -\delta_{\boldsymbol{k}}(\boldsymbol{k}) & 0 & 0 \\ 0 & 0 & -\delta_{\boldsymbol{k}}(\boldsymbol{k}) & x_{\boldsymbol{k}} - iy_{\boldsymbol{k}} \\ 0 & 0 & x_{\boldsymbol{k}} + iy_{\boldsymbol{k}} & \delta_{\boldsymbol{k}}(\boldsymbol{k}) \end{pmatrix} \\
&= \begin{pmatrix} \mathbf{H}_{\uparrow}(\boldsymbol{k}) & \mathbf{0}_{2\times 2} \\ \mathbf{0}_{2\times 2} & \mathbf{H}_{\downarrow}(\boldsymbol{k}) \end{pmatrix}, \qquad (2.2) \\
x_{\boldsymbol{k}} &= t\big[\cos(\boldsymbol{k}\cdot\boldsymbol{u}) + \cos(\boldsymbol{k}\cdot\boldsymbol{v}) + 1\big], \\
y_{\boldsymbol{k}} &= t\big[\sin(\boldsymbol{k}\cdot\boldsymbol{u}) + \sin(\boldsymbol{k}\cdot\boldsymbol{v})\big], \\
\delta_{\boldsymbol{k}} &= 2\lambda_{\mathrm{so}}\big[\sin(\boldsymbol{k}\cdot\boldsymbol{u}) - \sin(\boldsymbol{k}\cdot\boldsymbol{v}) - \sin(\boldsymbol{k}\cdot\boldsymbol{u} - \boldsymbol{k}\cdot\boldsymbol{v})\big],
\end{aligned}$$

where $\boldsymbol{u} = (3/2, \sqrt{3}/2)$, and $\boldsymbol{v} = (3/2, -\sqrt{3}/2)$ are suitable basis vectors for the honeycomb lattice (see the left panel in Fig. 2.1). The spinorial 4×4 matrices $\Gamma_{ij} = \sigma_i \otimes \tau_j$, are defined in terms of σ_i and τ_j Pauli matrices, respectively referred to spin and sublattice degrees of freedom, with the convention that σ_0 and τ_0 are 2×2 identity matrices.

The eigenvalues of $\mathbf{H}(\boldsymbol{k})$ are

$$E^{\pm}(\boldsymbol{k}) = \pm\sqrt{|x_{\boldsymbol{k}} + iy_{\boldsymbol{k}}|^2 + |\delta_{\boldsymbol{k}}|^2} \tag{2.3}$$

so that the two bands are gapped for any finite spin-orbit coupling λ_{so}. Otherwise they realize a semimetal with Dirac cones at $\mathbf{K} = \left(\frac{2\pi}{3}, \frac{2\pi}{3\sqrt{3}}\right)$ and $\mathbf{K}' = \left(\frac{2\pi}{3}, -\frac{2\pi}{3\sqrt{3}}\right)$. The minimal gap in the Brillouin zone (see the right panel in Fig. 2.1) is located at the Dirac points $\mathbf{K}$ and $\mathbf{K}'$ for $\lambda_{\text{so}} < 3\sqrt{3}t \simeq 0.2t$, with magnitude $\Delta_0 = 6\sqrt{3}\lambda_{\text{so}}$ [85], otherwise a smaller gap $\Delta_0 = 2t$ opens at $\mathbf{M} = \left(\frac{2\pi}{3}, 0\right)$ [130].

The spin block-diagonal form of Eq. 2.2 reveals the correspondence between Chern and quantum spin-Hall insulators: the Kane-Mele model can be seen as a superposition of two spinless Haldane Hamiltonians [84], with opposite next-nearest neighbor phases $\phi_{\uparrow} = \pi/2$ and $\phi_{\downarrow} = -\pi/2$ [81–83]. By virtue of the spin factorization of the Kane-Mele eigenvectors, the $\mathbb{Z}_2$ invariant can be computed, in principle, as the Chern number of an individual spin polarization $\mathbb{Z}_2 = (\mathbb{C}_{\uparrow} - \mathbb{C}_{\downarrow})/2 = \mathbb{C}_{\uparrow} = \mathbb{C}_{\downarrow}$, but, as we will discuss in detail, the emergence of in-plane magnetic ordering, in the presence of electron-electron interactions, spoils the conservation of the out-of-plane spin component and requires a general treatment. Throughout this work we compute the $\mathbb{Z}_2$ topological invariant of suitable effective quadratic models for the interacting system, from the evolution of Wannier charge centers [155], as implemented in the `Z2Pack` software [156].

To investigate the effects of electron-electron repulsion on the Kane-Mele model we include a local interaction in the Hubbard form (see Eq. O.5), leading to the Kane-Mele-Hubbard (KMH) Hamiltonian [87, 88]

$$\mathbf{H}_{\text{KMH}} = \mathbf{H}_{\text{KM}} + U\sum_i \left[\left(n_{i\uparrow} - \frac{1}{2}\right)\left(n_{i\downarrow} - \frac{1}{2}\right)\right], \tag{2.4}$$

where $n_{i\sigma} = c^{\dagger}_{i\sigma}c_{i\sigma}$ is the local spin-density operator. The interaction is written in an explicitly particle-hole symmetric form so that the model is half-filled for zero chemical potential (for this reason we omit the chemical potential term altogether).

The ground state of Eq. 2.4 has been extensively studied within a multitude of analytical [130–135] and numerical [136–142] approaches, including dynamical mean-field theory and its cluster extensions [139, 143–148], generating a rich debate around several open questions: from claims of a spin-liquid phase at low spin-orbit coupling [131, 136, 137, 146] and later disproving evidence [138, 139], to contrasting assessments of the nature of the magnetic transitions [130–132, 134] and the possible role of magnetic excitons and their condensation [133].

Nevertheless, the essential features of the ground state phase diagram can be now considered as established [88] and they have been confirmed to survive the introduction

of the full long-range Coulomb repulsion [157]. For $\lambda_{so} = 0$ the model describes a Dirac semimetal, up to relatively high repulsion, and magnetizes to an isotropic Néel state above above a critical U/t ratio.[1] With a finite spin-orbit coupling $\lambda_{so} \neq 0$, the quantum spin Hall state results increasingly stable against magnetic ordering, due to its symmetry protected nontrivial topology. Furthermore, the long range ordering eventually stabilized at large U/t, is characterized by a lowered easy-plane symmetry, due to the inherent coupling of spin and lattice degrees of freedom [134].

The interest in paramagnetic insulating solutions for large interaction $U \gg t$ has been revived by the recent reconsideration of possible topological Mott insulating states [47] in strongly interacting topological insulators [100], including analytical investigations on the Kane-Mele-Hubbard Hamiltonian [99]. Our quantum information analysis of local solutions within dynamical mean-field theory thus complements recent advances in the field, with a rigorous quantification of quantum and classical intra-orbital correlations, not only for the ground state, but at different levels of symmetry breaking, including the possibly topological paramagnetic Mott insulator.

2.1 Static mean-field theory

In this section we discuss the Hartree-Fock static mean-field theory for the half-filled KMH model. We will consider antiferromagnetic solutions with magnetization along the z (out-of-plane) axis or in the x-y (lattice) plane. Within Hartree-Fock theory, we decouple the quartic term in Eq. 2.4 into all the Wick contractions that we assume to have nonvanishing expectation values in the target state. If we consider solutions with an out-of-plane magnetization we can write the decoupling as

$$\begin{aligned}\delta \mathbf{H}_{\perp}^{\mathrm{HF}} \propto \big(& n_{\mathrm{A}\uparrow} \langle n_{\mathrm{A}\downarrow} \rangle + n_{\mathrm{A}\downarrow} \langle n_{\mathrm{A}\uparrow} \rangle - \langle n_{\mathrm{A}\uparrow} \rangle \langle n_{\mathrm{A}\downarrow} \rangle \\ & + n_{\mathrm{B}\uparrow} \langle n_{\mathrm{B}\downarrow} \rangle + n_{\mathrm{B}\downarrow} \langle n_{\mathrm{B}\uparrow} \rangle - \langle n_{\mathrm{B}\uparrow} \rangle \langle n_{\mathrm{B}\downarrow} \rangle \big)\end{aligned} \tag{2.5}$$

from which we can define the following order parameters within the bipartite unit-cell

$$\begin{aligned}\mathcal{F}_z &= \langle n_{\mathrm{A}\uparrow} \rangle + \langle n_{\mathrm{B}\uparrow} \rangle - \langle n_{\mathrm{A}\downarrow} \rangle - \langle n_{\mathrm{B}\downarrow} \rangle = \left\langle \Psi_{\boldsymbol{k}}^{\dagger} \Gamma_{30} \Psi_{\boldsymbol{k}} \right\rangle , \\ \mathcal{A}_z &= \langle n_{\mathrm{A}\uparrow} \rangle - \langle n_{\mathrm{B}\uparrow} \rangle - \langle n_{\mathrm{A}\downarrow} \rangle + \langle n_{\mathrm{B}\downarrow} \rangle = \left\langle \Psi_{\boldsymbol{k}}^{\dagger} \Gamma_{33} \Psi_{\boldsymbol{k}} \right\rangle , \\ \mathcal{P}_z &= \langle n_{\mathrm{A}\uparrow} \rangle - \langle n_{\mathrm{B}\uparrow} \rangle + \langle n_{\mathrm{A}\downarrow} \rangle - \langle n_{\mathrm{B}\downarrow} \rangle = \left\langle \Psi_{\boldsymbol{k}}^{\dagger} \Gamma_{03} \Psi_{\boldsymbol{k}} \right\rangle , \\ \mathcal{N}_z &= \langle n_{\mathrm{A}\uparrow} \rangle + \langle n_{\mathrm{B}\uparrow} \rangle + \langle n_{\mathrm{A}\downarrow} \rangle + \langle n_{\mathrm{B}\downarrow} \rangle = \left\langle \Psi_{\boldsymbol{k}}^{\dagger} \Gamma_{00} \Psi_{\boldsymbol{k}} \right\rangle ,\end{aligned}$$

[1] In contrast with the square lattice [158, 159] and with the expectations for a generic bipartite lattice, in which at half-filling the ground state is antiferromagnetic for any non-zero interaction, the honeycomb lattice generally displays a finite critical strength for antiferromagnetic ordering. This property descends from the peculiar properties of Dirac cones: the vanishing density of states at the Fermi level renders ineffective the logarithmic instability, even in the presence of perfect nesting [57, 58].

where the Γ_{ij} matrices and the spinorial basis $\Psi_{\boldsymbol{k}}$ are the same as in Eq. 2.2. $\mathcal{P}_z \neq 0$ describes a staggered charge-density wave, surely not expected to be realized in a half-filled repulsive model, while particle-hole symmetry fixes the total charge parameter $\mathcal{n}_z = 2$ at half-filling. We are thus left with a variational optimization over $\mathcal{F}_z$ and $\mathcal{A}_z$, which correspond to ferromagnetic and antiferromagnetic ordering, respectively.

Given that the λ_{so} spin-orbit coupling in Eq. 2.1 lowers the spin rotation symmetry from the full SU(2) of the standard Hubbard model, to a residual U(1) rotation around the out-of-plane axis [134], the z-axis magnetic ordering is no longer equivalent to the in-plane one. Hence we have to define a different mean-field decoupling, involving contractions of the spin-flip operators $u_i = c^\dagger_{i\uparrow} c_{i\downarrow}$ and $d_i = c^\dagger_{i\downarrow} c_{i\uparrow}$, as

$$\begin{aligned}\delta\mathbf{H}^{\mathrm{HF}}_{\parallel} \propto \big(& u_{\mathrm{A}} \langle d_{\mathrm{A}} \rangle + d_{\mathrm{A}} \langle u_{\mathrm{A}} \rangle - \langle u_{\mathrm{A}} \rangle \langle d_{\mathrm{A}} \rangle \\ & + u_{\mathrm{B}} \langle d_{\mathrm{B}} \rangle + d_{\mathrm{B}} \langle u_{\mathrm{B}} \rangle - \langle u_{\mathrm{B}} \rangle \langle d_{\mathrm{B}} \rangle \big).\end{aligned} \tag{2.6}$$

The corresponding unit-cell order parameters are

$$\begin{aligned}\mathcal{F}_x &= \langle u_{\mathrm{A}} \rangle + \langle u_{\mathrm{B}} \rangle + \langle d_{\mathrm{A}} \rangle + \langle d_{\mathrm{B}} \rangle = \left\langle \Psi^\dagger_{\boldsymbol{k}} \Gamma_{10} \Psi_{\boldsymbol{k}} \right\rangle, \\ \mathcal{F}_y &= i \langle u_{\mathrm{A}} \rangle + i \langle u_{\mathrm{B}} \rangle - i \langle d_{\mathrm{A}} \rangle - i \langle d_{\mathrm{B}} \rangle = - \left\langle \Psi^\dagger_{\boldsymbol{k}} \Gamma_{20} \Psi_{\boldsymbol{k}} \right\rangle, \\ \mathcal{A}_x &= \langle u_{\mathrm{A}} \rangle - \langle u_{\mathrm{B}} \rangle + \langle d_{\mathrm{A}} \rangle - \langle d_{\mathrm{B}} \rangle = \left\langle \Psi^\dagger_{\boldsymbol{k}} \Gamma_{13} \Psi_{\boldsymbol{k}} \right\rangle, \\ \mathcal{A}_y &= i \langle u_{\mathrm{A}} \rangle - i \langle u_{\mathrm{B}} \rangle - i \langle d_{\mathrm{A}} \rangle + i \langle d_{\mathrm{B}} \rangle = - \left\langle \Psi^\dagger_{\boldsymbol{k}} \Gamma_{23} \Psi_{\boldsymbol{k}} \right\rangle,\end{aligned}$$

so that $(\mathcal{F}_x, \mathcal{F}_y)$ and $(\mathcal{A}_x, \mathcal{A}_y)$ would describe respectively ferromagnetic and antiferromagnetic order in the plane. Unless we introduce terms breaking the symmetry within the plane, we can safely restrict to the x components.

In chapter 4 we will consider the competition between the two antiferromagnetic solutions, *i.e.* finite $\mathcal{A}_z$ or $\mathcal{A}_x$, in order to address the role of the spin-orbit coupling in their energetic balance. Owing to the variational principle, we can establish the relative stability of the two solutions by comparing their energies at zero temperature and we can gain further insight by comparing the evolution of relevant physical quantities.

Finally, we point out that the $\mathbb{Z}_2$ invariant can be evaluated with the same procedure adopted for the noninteracting Hamiltonian, given that the Hartree-Fock corrections are quadratic by construction, leading to an effective quadratic Hamiltonian with optimal parameters determined according to the variational principle.

2.2 Dynamical mean-field theory

As briefly introduced in section O.3, dynamical mean-field theory (DMFT) provides a nonperturbative approach to strongly correlated electrons, based on a self-consistent mapping between the original interacting lattice model and a quantum impurity embedded in a noninteracting bath (see section O.3). While the standard formulation of DMFT assumes the equivalence of all the sites of the lattice, hence one single quantum impurity model to be solved self-consistently, the method can be naturally extended to account for inequivalent sites, defining one impurity model and one self-energy for each of them.

The central quantity is the single-particle interacting Green's function matrix in the subspace spanned by the inequivalent impurities, which is imposed to match the projection of the lattice Green's function matrix onto the local subspace of the model, with the assumption of a site-diagonal self-energy matrix[2]

$$\mathbf{G}_{\text{loc}}(z) \overset{\text{def}}{=} \frac{1}{N_{\boldsymbol{k}}} \sum_{\boldsymbol{k}} \mathbf{G}(\boldsymbol{k}, z) = \frac{1}{N_{\boldsymbol{k}}} \sum_{\boldsymbol{k}} \big(z - \mathbf{H}(\boldsymbol{k}) - \boldsymbol{\Sigma}_{\text{imp}}(z)\big)^{-1} \equiv \mathbf{G}_{\text{imp}}(z) \tag{2.7}$$

where z is a generic complex frequency, $\mathbf{H}(\boldsymbol{k})$ is the noninteracting Hamiltonian of the full lattice, $\mathbf{G}_{\text{imp}}$ and $\boldsymbol{\Sigma}_{\text{imp}}$ are the Green's function and self-energy matrices describing the quantum impurities. Despite being originally formulated in the limit of infinite dimensions [37, 38], dynamical mean-field theory has proven successful for the realistic modeling of materials [160], with a growing literature in the field of strongly correlated topological systems in two and three dimensions [89, 91, 92, 100, 152, 161–164].

For the Kane-Mele-Hubbard model, Eqs. 2.2 and 2.4, we need to consider two inequivalent impurity models, accounting for the A and B sublattices that define the honeycomb structure (see Fig. 2.1). Hence, the self-energy matrix in Eq. 2.7 is characterized, by construction, by a block-diagonal structure in sublattice space. Given our interest for the in-plane magnetic solutions, we cannot assume a spin factorization in the S_z basis, as customarily leveraged in most implementations of the method. In particular, we adopt a Lanczos/Arnoldi exact diagonalization (ED) solver [54, 165], built upon a generalization of the `EDIpack` software [166], to allow a full spin dependency of the impurity self-energy. To alleviate the inherent computational effort of a spinful ED calculation, we leverage the antiferromagnetic symmetry of the target solutions, to solve only one of the two sublattices. For the out-of-plane calculation ($\text{AFM}_\perp$) we impose the standard Néel symmetry as $\Sigma^{\text{A}}_{\uparrow\uparrow} = \Sigma^{\text{B}}_{\downarrow\downarrow}$, $\Sigma^{\text{A}}_{\downarrow\downarrow} = \Sigma^{\text{B}}_{\uparrow\uparrow}$, and $\Sigma^{\text{A}}_{\uparrow\downarrow} = \Sigma^{\text{A}}_{\downarrow\uparrow} = \Sigma^{\text{B}}_{\uparrow\downarrow} = \Sigma^{\text{B}}_{\downarrow\uparrow} = 0$. For the easy-plane computation ($\text{AFM}_\parallel$) we impose the same conditions on the S_x projection, which rotated back to the computational S_z basis become $\Sigma^{\text{A}}_{\uparrow\uparrow} = \Sigma^{\text{B}}_{\uparrow\uparrow}$, $\Sigma^{\text{A}}_{\downarrow\downarrow} = \Sigma^{\text{B}}_{\downarrow\downarrow}$, $\Sigma^{\text{A}}_{\uparrow\downarrow} = -\Sigma^{\text{B}}_{\downarrow\uparrow}$,

[2] Notice that, while the self-energy and the impurity Green's functions are diagonal in the site index, the lattice Green's function is not, due to the nonlocal part of the noninteracting Hamiltonian.

$\Sigma^{A}_{\downarrow\uparrow} = -\Sigma^{B}_{\uparrow\downarrow}$. We stress that both set of conditions represent a lower symmetry with respect to the paramagnetic state that is found at low U/t ratio, so that the computation can safely impose either of them in the whole phase diagram, with no loss of generality.

The DMFT/ED homologue of the Hartree-Fock decoupling *Ansatz*, is the parametrization of the noninteracting bath, as it encodes the allowed properties of the resulting self-energy through the self-consistency condition defined by Eq. 2.7. Similarly to our Hartree-Fock treatment, we explore the competition between $\mathrm{AFM}_{\perp}$ and $\mathrm{AFM}_{\parallel}$ solutions, by defining two alternative *reduced* parametrizations [167]

$$\mathbf{H}^{\mathrm{bath}}_{\perp} = \sum_{i=1}^{N_b} (\varepsilon_i \sigma_0 + m_i \sigma_z), \tag{2.8}$$

$$\mathbf{H}^{\mathrm{bath}}_{\parallel} = \sum_{i=1}^{N_b} (\varepsilon_i \sigma_0 + m_i \sigma_x), \tag{2.9}$$

where σ_z and σ_x are Pauli matrices and σ_0 is the 2×2 identity in spin space. The $\mathrm{AFM}_{\perp}$ bath can be easily shown to match the traditional parametrization in terms of spin-dependent energy levels (see Eq. O.15), while the $\mathrm{AFM}_{\parallel}$ case exploits the reduced representation of Eq. 2.9 to elegantly encode the in-plane magnetic ordering. In the practical implementation, to ease the search for each of the two solutions, we provide nonzero initial guesses for the m_i bath parameters, imposing a small ($< 0.1t$) positive "kick" on the impurity model representing the A sublattice and an opposite term on the other one.[3] The self-consistent iteration would either kill or enhance these initial guesses, determining the phase diagram of the model, within the given DMFT *Ansatz*. To access the Mott-Hubbard state, with no symmetry breaking, we define a third parametrization in which the bath does not depend on the spin degrees of freedom, obtaining a bath Hamiltonian that is fully equivalent to the original Anderson impurity model [51]

$$\mathbf{H}^{\mathrm{bath}}_{\mathrm{para}} = \sum_{i=1}^{N_b} \varepsilon_i \sigma_0 \,. \tag{2.10}$$

In all cases the N_b bath sites have been connected to the interacting impurity with spin-independent real hybridization amplitudes V_i, initialized to a common value but free to evolve independently for each bath site. All the data presented in this part of the thesis have been obtained for $N_b = 6$. Explicit bath-size scaling, up to $N_b = 9$ has been performed on selected data points at fixed spin-orbit coupling $\lambda_{so} = 0.3t$, ensuring excellent convergence of all the significant features.

[3] We underline that this does not imply the presence of a magnetic field, which would be applied on the impurity sites, but it is simply a tool to initialize the iterative procedure.

Given a self-consistent solution of Eq. 2.7, local physical observables can be computed in principle from the resulting local Green's function matrix, which coincides by construction to the impurity propagator. Hence, within our DMFT/ED implementation, we can directly evaluate local observables from the Lanczos impurity solver, with great benefit in computational cost and accuracy. In particular we compute single-particle and two-particle occupations directly as $\langle n_{i\sigma} \rangle$ and $\langle n_{i\uparrow} n_{i\downarrow} \rangle$, where i is the label of the impurity site in the two inequivalent auxiliary models and the spin basis can be rotated as needed. From these expectation values the antiferromagnetic order parameter and the single-orbital and single-spin reduced density matrices (see section 2.3) are directly accessible, with the same definitions employed in Hartree-Fock theory. The impurity Green's function matrices are in turn evaluated in their continued-fraction representation, by a Lanczos tridiagonalization. From them, we can easily evaluate spectral properties, as *e.g.* the single-particle gap, which can be defined as the real-frequency distance between the two peaks in $\mathrm{Re}[G_{ii}(\omega)]$ that are closer to the Fermi level.[4]

Quantities involving nonlocal Green's function can sometimes require more costly procedures, as the $\boldsymbol{k}$-space integration and possible additional frequency convolutions can introduce numerical instability and/or unfavorable performance.

For this reason, instead of the general formulation of the interacting $\mathbb{Z}_2$ invariant, based on the lattice Green's function $\mathbf{G}(\boldsymbol{k}, z)$ [168–170], we exploit a simplified formulation based on an auxiliary quadratic model, allowing for a calculation as cheap as for a noninteracting Hamiltonian or within the Hartree-Fock approximation: the so called *topological Hamiltonian* [171, 172]

$$\mathbf{H}^{\mathrm{topo}}(\boldsymbol{k}) = \mathbf{H}(\boldsymbol{k}) + \boldsymbol{\Sigma}(\boldsymbol{k}, 0) = -\mathbf{G}^{-1}(\boldsymbol{k}, 0) \tag{2.11}$$

has been proven to give the same topological invariant as the full interacting model described by $\mathbf{G}(\boldsymbol{k}, z)$, provided that an adiabatic connection to the noninteracting propagator $\mathbf{G}_0(\boldsymbol{k}, z)$ is assured. Within dynamical mean-field theory the recipe is further simplified by the locality of the self-energy matrix, so that we compute the $\mathbb{Z}_2$ invariant from the Wannier charge center evolution of the simple $\mathbf{H}(\boldsymbol{k}) + \boldsymbol{\Sigma}(0)$ renormalized Hamiltonian.

Another nonlocal observable of interest for the analysis of the competition between the two anisotropic AFM orderings, is the kinetic energy $K = \langle \mathbf{H}(\boldsymbol{k}) \mathbf{G}(\boldsymbol{k}, z) \rangle$. A careful discussion about its evaluation within dynamical mean-field theory is given in chapter 4.

[4] Due to Kramers-Kronig relations, such peaks are directly related to the edges of the spectral function $A_i(\omega) = -\mathrm{Im}[G_{ii}](\omega)/\pi$.

2.3 Intra-orbital correlations in presence of magnetic anisotropy

In this section we briefly discuss how to generalize the measure of intra-orbital correlations, introduced in the introductory section O.5, to the case of magnetically anisotropic systems. In this way, we complement the description based on more conventional observables with a quantity which unveils the quantum information content of the analyzed solutions and gives important hints on the possible presence of nonlocal entanglement in the system [173].

We recall that for single-band models that conserve the total charge and magnetization, the single-site density matrix can be written in diagonal form, as [61–65] (see section O.5)

$$\rho_i = \lambda_1 |\bullet\rangle\langle\bullet| + \lambda_2 |\nearrow\rangle\langle\nearrow| + \lambda_3 |\swarrow\rangle\langle\swarrow| + \lambda_4 |\nearrow\swarrow\rangle\langle\nearrow\swarrow|, \qquad (2.12)$$

$$\text{with} \sum_i \lambda_i = 1, \quad \forall i : 0 \leqslant \lambda_i \leqslant 1.$$

where $|\nearrow\rangle$ and $|\swarrow\rangle$ indicate spin-orbitals associated to an arbitrary choice of the spin component, and the black dot stands for an empty lattice site. The form of Eq. 2.12 satisfies the condition for a classically correlated state,[5] thus implying that the two local spin states experience only correlations that should be regarded as classical. Furthermore, we remind that the intra-orbital correlation, defined as in Eq. O.34, does always vanish for a Hartree-Fock calculation, as proven in section O.5.

Even if the Kane-Mele spin-orbit coupling lowers the spin symmetry from the full SU(2) to the $U(1)|_\perp$ rotation around the out-of-plane axis [134], we can still work in the basis of the $S_\perp$ projection, as it is an eigenvector of the residual spin symmetry, or, alternatively, we can fix an arbitrary $S_\parallel$ direction in the plane. For a Néel ordered phase, the choice is obligated, as the spontaneous symmetry breaking associated with the onset of antiferromagnetism completely removes all freedom in the direction of spin quantization. In this respect, anisotropic magnetic phases are not fundamentally different from the usual scenario.

Hence, for the Kane-Mele-Hubbard model we will consider an intra-orbital mutual information in the form of Eq. O.34, which we can write for a the in-plane and out-of plane spin components respectively as $I(\rightarrow:\leftarrow) = s_{i\rightarrow} + s_{i\leftarrow} - s_i$ and $I(\uparrow:\downarrow) = s_{i\uparrow} + s_{i\downarrow} - s_i$, where in the expressions of s_i (Eq. O.30) and $s_{i\sigma}$ (Eq. O.33) we must insert the in-plane $m_{i\parallel}$ and out-of-plane $m_{i\perp}$ order parameters, respectively.

[5] For an in-depth analysis of the nature of classical and quantum correlations see Eq. A.14 and the associated discussion in appendix A.

3 Mott transitions in the Kane-Mele-Hubbard model

In this chapter we present our numerical results for the Kane-Mele-Hubbard model (Eq. 2.4), at zero temperature, within both Hartree-Fock and dynamical mean-field theory.

3.1 QSHI to AFM$_{\parallel}$ transition

We start by inspecting and comparing the Hartree-Fock and DMFT solutions in the case of a calculation that is able to develop in-plane antiferromagnetism (see sections 2.1 and 2.2, for details on the relevant parametrizations). At large U/t the AFM$_{\parallel}$-parametrized calculations are expected to develop a finite order parameter and to be more stable than the corresponding AFM$_{\perp}$ state, as long as an arbitrarily small spin-orbit coupling λ_{so}/t is included in the Hamiltonian [87, 88, 130, 141]. Hence we prospect these calculations to find the ground state of the model throughout the whole parameter space. The stability of the in-plane solution is indeed confirmed for every value of U/t and λ_{so}/t, by explicit calculation of the energies within both HF and DMFT. In chapter 4 we present more details about these energy calculations, including a discussion of possible strategies to stabilize the out-of-plane solution, in the context of cold-atom experiments and/or solid-state nanostructures.

In the two panels of Fig. 3.1 we report Hartree-Fock and DMFT results, for respectively the staggered magnetization $m_{\parallel}$ and the single-particle gap Δ, as a function of U/t and fixed $\lambda_{so} = 0.3t$, both superimposed on a background associated with the value of the $\mathbb{Z}_2$ invariant. The Hartree-Fock solution develops a finite magnetization, in a continuous way, for $U \gtrsim 3.3t$, preserving the nontrivial topology of the QSHI state up to $U \simeq 3.5t$, where the staggered magnetization reaches $m_{\parallel} \lesssim 0.25$. The single-particle gap remains instead fixed at its noninteracting value determined by λ_{so}, $\Delta_0 = 2t$, at all interaction strengths before the transition, due to the inability of the Hartree-Fock correction $\delta\mathbf{H}_{\parallel}^{\mathrm{HF}}$ to capture anything but constant energy shifts, when no order parameter is developed.

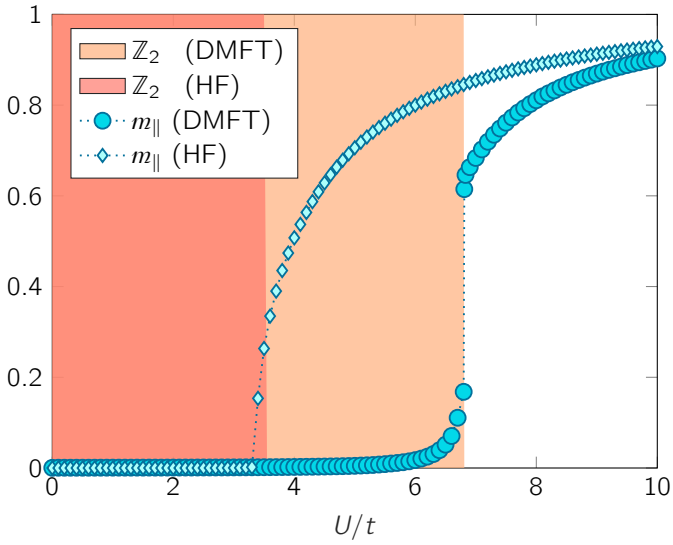
After the transition Δ increases linearly, approaching, for large U/t, the standard magnetic gap $\Delta_m = Um_{\parallel}$ found for spin-orbit-free models, at the Hartree-Fock level [148, 149]. The fact that at intermediate U/t, right after the transition, $\Delta < \Delta_0 + \Delta_m$ suggests a competition between the renormalization of the topological gap Δ_0, opened by λ_{so} in the noninteracting model, and the progressive opening of the magnetic gap.

The dynamical mean-field theory, on the other hand, show a discontinuous transition at much stronger interaction $U \simeq 6.8t$, matching exactly the death of the $\mathbb{Z}_2$ topological invariant. Yet, a finite order parameter $m_{\parallel} \lesssim 0.17$ is found for a significant range of interaction values, approximately $U \gtrsim 5t$, before the first-order jump. As a matter of fact the jump is not associated with the development of AFM ordering, bur rather with the change in the $\mathbb{Z}_2$ topological invariant.

The resulting coexistence of nontrivial topology and magnetic order has been checked to be robust against variation of the spin-orbit coupling and all the relevant computational parameters: number of bath sites in the auxiliary impurity model, tolerance of the minimization procedure in the update of the bath parameters across the DMFT iterations, frequency resolution on the imaginary axis for the computation of the Green's function matrices. The evolution with the spin-orbit coupling can be summarized in a phase diagram that we report in Fig. 3.2, confirming the existence of a magnetized topological ground state at least in the $0.0\bar{3}t \leqslant \lambda_{so} \leqslant 0.6t$ range. Smaller finite values of the spin-orbit coupling have not been addressed in our calculations. For $\lambda_{so} = 0$ we recover the well-known transition between a Dirac semimetal and an isotropic Néel state [57, 138, 139, 144, 145, 147, 148], that, to some extent, we have discussed in the introductory sections O.4 and O.5.

We remark that even if the coexistence between nontrivial topology and a weak antiferromagnetic magnetization has never been reported, to the best of our knowledge, for the Kane-Mele-Hubbard model, similar predictions of an *antiferromagnetic topological insulating* (AFMTI) [94, 95] phase have appeared for the closely related Bernevig-Hughes-Zhang-Kanamori model, within dynamical mean-field theory [151, 152], variational cluster approximation (VCA) [153] and the density matrix renormalization group (DMRG) [154].

Having established the behavior of the magnetic order parameter and the topological invariant, we turn back to Fig. 3.1 to observe that the single-particle gap in the DMFT calculation is strongly reduced by increasing the interaction, for U smaller than the critical value for magnetic ordering, in striking contrast with Hartree-Fock theory. After the transition Δ grows resembling a $Um_{\parallel}$ behavior, but shifted to a significantly smaller value with respect to the static mean-field. This effect is inherently dynamical and can be attributed to the large width of the Hubbard bands, describing the incoherent excitations at high energies in the single-particle spectral function, as discussed in depth in Ref. [149]. We point out that, while in DMFT the gap can be evaluated only from the spectral function, as described in section 2.2, in Hartree-Fock we can directly access the mean-field bands. Leveraging this, we have cross-checked our algorithm to extract the gap on the Hartree-Fock Green's function, computed by assuming a self-energy constant in frequency, and given by $Um_{\parallel}$. We find excellent agreement with the gap computed from the mean-field bands, hence validating the method for the, otherwise inaccessible, DMFT gap.



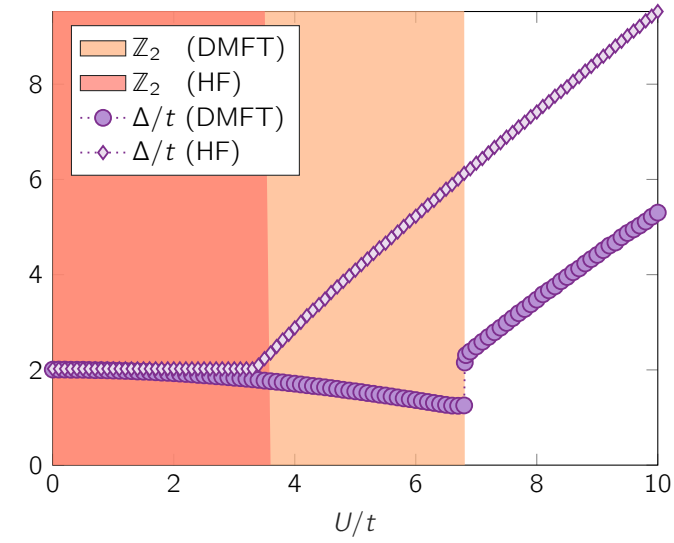


Fig. 3.1.: Transition between the quantum spin-Hall and the *easy-plane* antiferromagnetic insulators at $\lambda_{so} = 0.3t$. The colored regions represent an odd $\mathbb{Z}_2$ invariant for the Hartree-Fock and dynamical mean-field theory calculations. The white region is nontrivial in both calculations. $m_{\parallel}$ is the staggered magnetization. Δ/t is the single-particle gap, as computed from the diagonal components of the Green's function (section 2.2).

The comparison between HF and DMFT highlights some important differences between the two solutions, despite they both describe the same phase and a ground state with the same symmetry. To further analyze this difference we leverage on the measurements of classical correlations that we defined in section 2.3. In Fig. 3.3 we show the single-orbital and single-spin von Neumann entropies (Eqs. 7.2 and O.33, together with the intra-orbital mutual information (Eq. O.34). The latter bounds from above all local correlation functions, according to Eq. (O.28). Recalling that the intra-orbital mutual information exactly vanishes for any Hartree-Fock calculation, as proven by Eq. O.36, we propose it as a rigorous quantifier for the "distance" between static and dynamical mean-field predictions for the local structure of the ground state. At the noninteracting limit $U/t = 0$, we naturally have vanishing intra-orbital correlations, as the single-orbital entropy assumes its maximal value $s_i = \log(4)$, corresponding to equal occupation probabilities $p_\bullet = p_\uparrow = p_\downarrow = p_{\uparrow\downarrow} = 1/4$, while the single-spin entropies are fixed at $\log(2)$ by the absence of a finite magnetization. Switching on the interaction and progressively increasing the U/t ratio, s_i decreases monotonically, following the reduction of the double occupancy $\mathcal{D}_i$. This in turn leads to a finite and monotonically increasing intra-orbital mutual information, up to the first-order transition at $U \simeq 6.8t$. Therein, the jump in the order parameter results in a sudden reduction of both single-orbital and single-spin von Neumann entropies. After the transition, the single-spin entropy quickly decays as a consequence of the increasing magnetization, while the reduction of s_i, which in principle is ascribed to both $\mathcal{D}_i$ and m_i, is progressively dominated by the latter. In fact, in the AFM phase the double occupancy gradually approaches zero, as the local magnetic moments align towards a fully ordered Néel state. At infinite interaction $U \gg t$, we have a saturated magnetization $m_i = 1$ and vanishing double occupancy $\mathcal{D}_i = 0$, leading to $s_i = s_{i,\rightarrow} = s_{i,\leftarrow} = 0$, as there is no statistical uncertainty on the electronic configuration of the local orbital. The behavior of single-orbital and single-spin von Neumann entropies for $U \gtrsim 6.8t$ stops the growth of intra-orbital correlations, abruptly quenching them by more than a half at the discontinuous topological transition and progressively approaching zero as the antiferromagnetic order parameter is saturated. Overall, we can then affirm that the local ground states of the static and dynamical mean-field theory calculations coincide at the noninteracting and strong coupling limits, while their distance reaches a maximum just before the first-order transition from the weakly magnetized topological state to the trivial antiferromagnet. The change in the $\mathbb{Z}_2$ invariant abruptly reduces the intra-orbital correlations, while the progressive development of a small finite magnetic order parameter in the topological phase has a little effect on their growth, remarking the strongly correlated character of the topological antiferromagnetic solution found within DMFT, as opposed to the coexistence found for $3.3 \lesssim U/t \lesssim 3.6$ at the Hartree-Fock level.

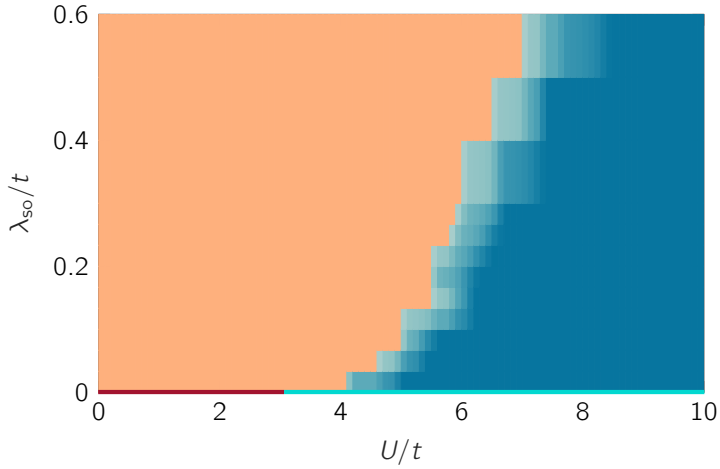


Fig. 3.2.: Phase diagram of the Kane-Mele-Hubbard model as predicted by DMFT. The orange region represents an odd $\mathbb{Z}_2$ invariant, the blue region a finite $\mathrm{AFM}_{\parallel}$ order parameter. The shaded region at intermediate interaction U, depicts the coexistence of topological and magnetic ordering. At $\lambda_{so} = 0$ there is an isotropic semimetal to AFM transition, characterized by trivial topology at all interaction values (solid lines).

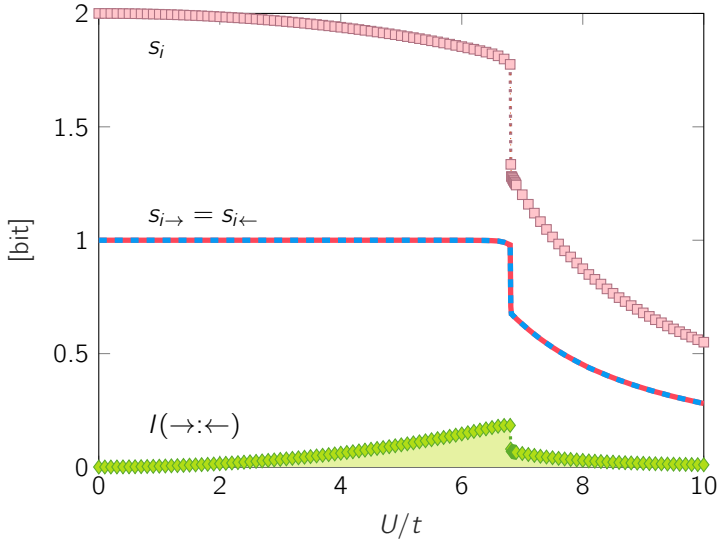


Fig. 3.3.: Single-orbital von Neumann entropy s_i, single-spin von Neumann entropies $s_{i\rightarrow}$ and $s_{i\leftarrow}$ and intra-orbital mutual information $I(\rightarrow{:}\leftarrow) = s_{i\rightarrow} + s_{i\leftarrow} - s_i$, across the QSHI to $\mathrm{AFM}_{\parallel}$ transition, at $\lambda_{so} = 0.3t$. The shaded area represents all possible local correlation functions. All quantities are expressed in units of $\log(2) = 1$ bit.

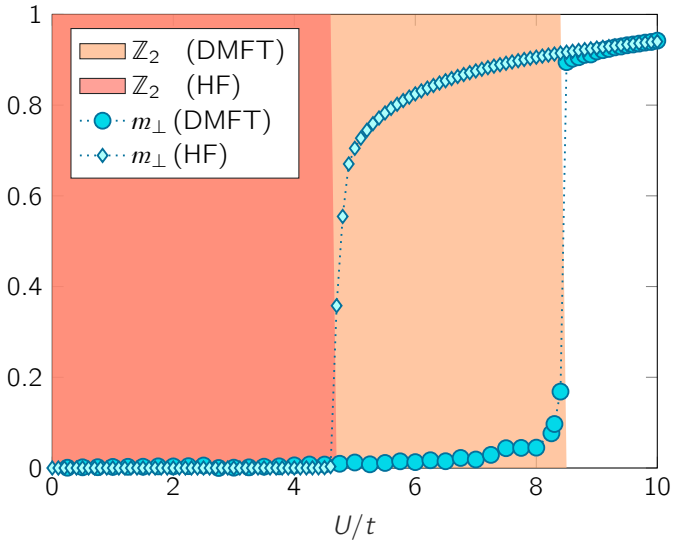
3.2 QSHI to AFM$_\perp$ transition

In this section we draw our attention to the out-of-plane Néel ordered state, which has generally higher energy with respect to the in-plane counterpart (as discussed in detail in chapter 4). Yet, solutions of this kind exist for sufficiently large U/t, using both the static and dynamical mean-field theory. The behavior of the Hartree-Fock magnetization and single-particle gap, at $\lambda_{so} = 0.3t$ (Fig. 3.4), reveals a transition at $U \simeq 4.6t$, which appears to be continuous, even if quite abrupt with respect to the in-plane case (Fig. 3.1).

The quick reduction of Δ after the transition reflects a fundamental change in the mean-field bands, caused by the sudden presence of a large order parameter. We report that this effect is even more pronounced for $\lambda_{so} < 3\sqrt{3}t$, featuring a shift of the minimal gap from the Dirac points **K**, **K′** to the **M** symmetry point (see Fig. 2.1), as the magnetic order parameter is developed. Hence, with respect to the easy-plane case, the competition between the progressive reduction of the topological gap introduced by λ_{so} and the opening of a magnetic gap $\Delta_m = Um_\perp$ is clearly dominated by the former effect, leading to a sharp minimum at $U \simeq 4.9t$.

On the other hand, the DMFT solution displays a first-order transition, reasonably similar to the one observed in the AFM$_\parallel$ calculation. We point out, though, that the discontinuous jump, placed at a significantly higher critical interaction $U \simeq 8.4t$, brings the magnetization at the very large value of $m_\perp \simeq 0.89$, quickly coalescing with the Hartree-Fock prediction at stronger interactions. This convergence towards an essentially mean-field picture, immediately after the transition, is clearly captured also by the intra-orbital mutual information (Fig. 3.5), which drops almost to zero right after the discontinuous topological transition.

Similarly to the AFM$_\parallel$ ground state, we remark that the AFM$_\perp$ dynamical mean-field theory calculation finds a coexistence between nontrivial topology and weak (out-of-plane) antiferromagnetic ordering at intermediate interaction values $6.5 \lesssim U/t \lesssim 8.4$, corresponding to a regime of strong intra-orbital correlations. This is not the case for the Hartree-Fock calculation, as the magnetization vanishes up to the antiferromagnetic transition. Therein the increase of the magnetization is so fast as to change the $\mathbb{Z}_2$ invariant within less than $\delta U = 0.1t$.



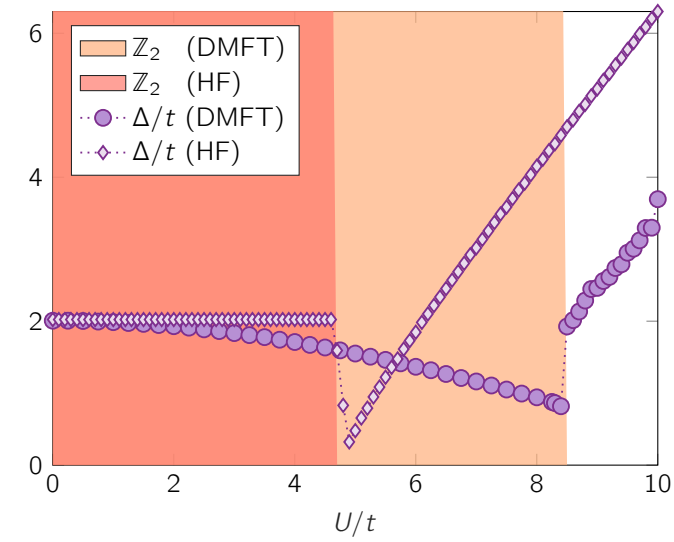


Fig. 3.4.: Transition between the quantum spin-Hall and the *out-of-plane* antiferromagnetic insulators at $\lambda_{so} = 0.3t$. The colored regions represent an odd $\mathbb{Z}_2$ invariant for the Hartree-Fock and DMFT calculations. The white region is nontrivial in both calculations. $m_\perp$ is the staggered magnetization. Δ/t is the single-particle gap, as computed from the diagonal components of the Green's function matrix (see section 2.2).

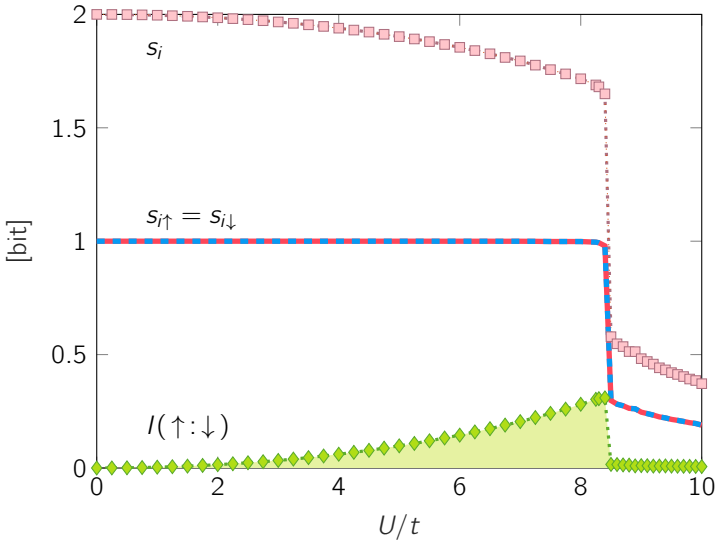


Fig. 3.5.: Single-orbital von Neumann entropy s_i, single-spin von Neumann entropies $s_{i\uparrow}$ and $s_{i\downarrow}$ and intra-orbital mutual information $I(\uparrow:\downarrow) = s_{i\uparrow} + s_{i\downarrow} - s_i$, across the QSHI to AFM$_\perp$ transition, at $\lambda_{so} = 0.3t$. The shaded area represents all possible local correlation functions. All quantities are expressed in units of $\log(2) = 1$ bit.

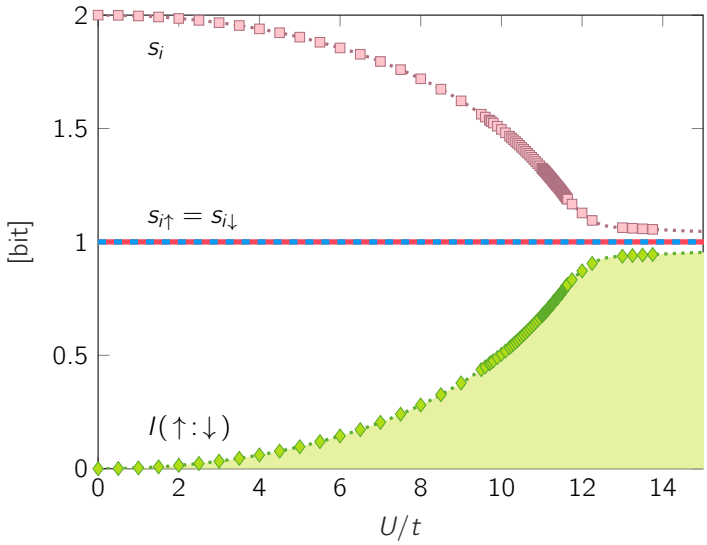


Fig. 3.6.: Single-orbital von Neumann entropy s_i, single-spin von Neumann entropies $s_{i,\uparrow}$ and $s_{i\downarrow}$ and intra-orbital mutual information $I(\uparrow:\downarrow) = s_{i\uparrow} + s_{i\downarrow} - s_i$, across the unbroken Mott transition, at $\lambda_{so} = 0.3t$. The shaded area represents all possible local correlation functions. All quantities are expressed in units of $\log(2) = 1$ bit.

3.3 QSHI to Mott-Hubbard transition

A careful comparison between Fig. 3.3 and Fig. 3.5 reveals how the largest value of the $I(\uparrow\!:\!\downarrow)$ intra-orbital mutual information, reached just before the sudden drop at the $\mathrm{AFM}_\perp$ topological transition, is naturally higher than the corresponding maximum of $I(\rightarrow\!:\!\leftarrow)$ found in the $\mathrm{AFM}_\parallel$ calculation, essentially because of the significantly stronger critical interaction: as long as the magnetization is weak, the nontrivial topology of the state survives, preserving the interaction-driven, monotonic growth of intra-orbital correlations. The onset of the large-magnetization trivial phase leads to a more or less rapid decrease of correlations. This phenomenon is not unexpected, as the broken-symmetry solution are usually assumed to be less correlated.

This observation finally brings us to ponder how strong we can let the intra-orbital correlations to grow, if we constrain the system in a symmetry-unbroken state. In search for an answer, we consider the transition between the interacting quantum spin-Hall insulator, which is notoriously adiabatic connected to the noninteracting limit of the model, to the Mott-Hubbard insulator, which must eventually be stabilized, at large enough interaction strength. As there is no symmetry breaking, the transition mechanism must inevitably amount to strong correlation effects, so that we cannot capture it in any way with Hartree-Fock theory. Hence we present only DMFT data, again for fixed $\lambda_{\mathrm{so}} = 0.3t$.

Recalling the introductory discussion in section O.5, we can surely expect the static and dynamical mean-field solutions to progressively depart away from each other, as the interaction is increased, and reach a maximal "distance" when the latter realizes the paramagnetic Mott insulating state.

In fact, as shown in Fig. 3.6, solving the DMFT equations within the paramagnetic *Ansatz* (Eq. 2.10), leads to a monotonically increasing intra-orbital mutual information, that approaches $\log(2)$ in the limit of large repulsion. The growth is very fast before the Mott transition, which happens when $I(\uparrow\!:\!\downarrow)$ is already very close to its asymptotic value. The residual slow growth is due to the long tail of finite double occupancy, that is never zero except for an extreme atomic insulator.

On the other hand, the single-spin von Neumann entropy remain fixed at $1\,\mathrm{bit} = \log(2)$, since there is no finite magnetization and the density of each spin species is fixed to 0.5, at half-filling. Hence, the monotonic growth of the mutual information directly descends from the behavior of the single-orbital von Neumann entropy. This latter quantity has been intensely studied across paramagnetic metal-insulator transitions, in the limit of infinite dimensions [61] and in the two-dimensional Hubbard model on the square lattice [3, 61–63]. Our results for the KMH model have indeed a very similar qualitative behavior as a function of U, across the QSHI to Mott-Hubbard transition, at all spin-orbit coupling values. In particular we recover also the semimetal-insulator transition transition

at $\lambda_{so} = 0$, that we have discussed in the introductory section O.5. The coalescence of the von Neumann entropy of the two spin subsystem with that of the whole local system (the spinful single-orbital) reveals the typical situation of a maximally correlated pair, wherein all the information stored in the composed system can be fully extracted by either of the two sub-parts [75, 76].

In contrast with a conventional Mott metal-insulator transition, in the present case the system is gapped also in the noninteracting limit. The noninteracting gap is associated with the topological nature of the system, and is renormalized (decreased) by the growing interaction. On the contrary, the Mott insulator displays a gap that stems directly from the local repulsion. We can thus pinpoint our Mott transition monitoring the behaviour of the single-particle gap, whose evolution at $\lambda_{so} = 0.3t$ is reported in Fig. 3.7. In section 2.2 we give a brief description of how we evaluate this quantity, directly from the impurity Green's function matrix, that at self-consistency satisfies Eq. 2.7 and provides direct information on the spectral properties of the lattice.

As witnessed by the single-particle gap, the Mott transition takes place at $U \simeq 12.5t$, where we clearly observe a sudden jump from the almost vanishing renormalized topological gap to the large Mott gap, which is already open as soon as we enter in the Mott state, as it happens also for the pure Hubbard model [38, 174–176]. Before the transition, the monotonic decrease of Δ can be shown to be proportional to the *quasiparticle weight* $Z = 1/(1 - \partial_\omega \Sigma_{i\sigma}(0^+))$, as computed for any sublattice i and spin state σ, outlining the dynamical nature of its renormalization. In very general terms Z, which ranges from 1 in a noninteracting system to 0 in a Mott state, renormalizes the single-particle dispersion, resulting in a shrinking of the gap.

After the Mott critical point, the spectral gap is determined by the position and width of the incoherent Hubbard bands, as there is no quasiparticle description for the purely many-body, interaction-driven, insulating state. We remark that within our resolution on the real frequency axis ($\delta\omega = 0.001t$), that directly descends from the numerical discretization of the imaginary axis, at zero temperature, the single-particle gap never closes as its minimum value is $\Delta_{\text{min}} \simeq 0.03t$, corresponding to an almost vanishing quasiparticle weight $Z \simeq 0.005$ at $U/t = 12.25$ and $Z \simeq 0.000008$ at $U/t = 13$, clearly placing the Mott transition in between.

Finally, turning to the characterization of the topological character of the phases, the $\mathbb{Z}_2$ invariant remains odd for every interaction value preceding the Mott transition, according to the topological Hamiltonian (Eq. 2.11). On the other hand, the latter quantity cannot be used in the Mott insulating state, where we cannot assume an adiabatic connection with the noninteracting model. This would apply for any phase transition, but in this specific case it is made particularly clear by the divergence of the self-energy at the Fermi level.

In fact, a recent work by N. Wagner *et al.* [99] has proposed the paramagnetic Mott insulating phase of the Kane-Mele-Hubbard model, as a realization of the topological Mott insulator conjectured in Ref. [47]. Similar claims have appeared for the Bernevig-Hughes-Zhang-Kanamori model and the interacting SSH chain [100]. In this chapter we do not delve into this new, exciting open question, as the single-site DMFT approximation (Eq. 2.7) assumes a $\boldsymbol{k}$-independent self-energy matrix and thus gives no access to the dispersion of the Green's function zeros, which is being discussed as the central ingredient to detect this kind of strongly correlated topological states [96–98].

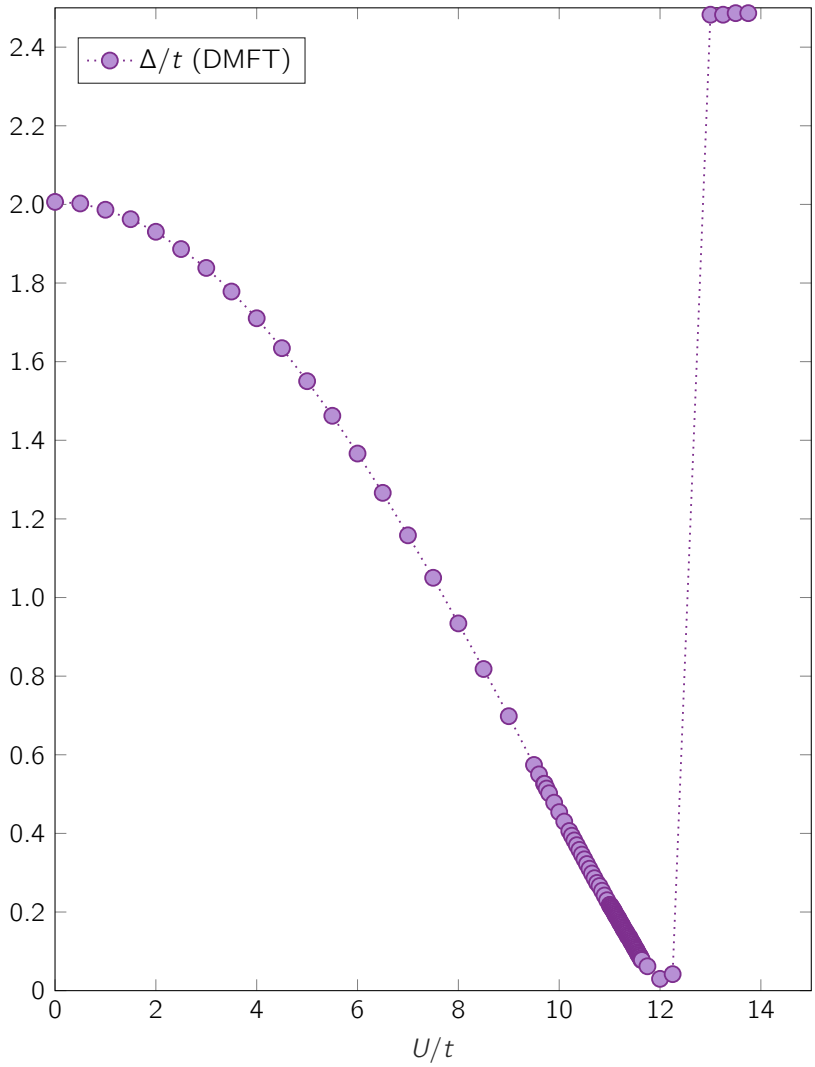


Fig. 3.7.: Transition between the quantum spin-Hall and the paramagnetic Mott insulators at $\lambda_{so} = 0.3t$, as witnessed by the evolution of the single-particle gap Δ/t, computed from the diagonal components of the Green's function matrix. (see section 2.2)

3.4 Landscape of intra-orbital correlations

We summarize our results and conclude our analysis by comparing and contrasting the intra-orbital mutual information across the whole parameter space of the model, for the three DMFT *Ansätze*, as defined by Eqs. 2.8, 2.9 and 2.10. The three correlation maps are reported in panels (a), (b) and (c) of Fig. 3.8.

The $\mathrm{AFM}_{\parallel}$ and $\mathrm{AFM}_{\perp}$ calculations coincide at vanishing spin-orbit coupling where the system has SU(2) spin-rotation symmetry [87, 88]. Therefore we have $I(\rightarrow:\leftarrow) \equiv I(\uparrow:\downarrow)$ at all interaction values, describing a gradual growth of local correlations in the Dirac semimetal and a progressive damping in the isotropic antiferromagnet. As already discussed in the introductory section O.5, the maximum mutual information value is attained at the critical point for the symmetry breaking (compare with Fig. O.4).

At any finite λ_{so}, the weakly interacting system becomes a quantum spin-Hall insulator and the quantum critical points for the first-order topological transition to the strongly polarized easy-plane and out-of-plane antiferromagnets detach from one another. In particular we have $U_{\perp}^{c} > U_{\parallel}^{c}$, at all values of the spin-orbit coupling. The resulting strong correlation ridges, culminating at the transition line, are characterized by significantly different "heights", with the $\mathrm{AFM}_{\perp}$ solution reaching up to $I(\uparrow:\downarrow) \simeq 0.3\,\mathrm{bit}$ and the $\mathrm{AFM}_{\parallel}$ ground state $I(\rightarrow:\leftarrow) \simeq 0.2\,\mathrm{bit}$. Hence, already a small intrinsic spin-orbit coupling allows the engineering of strongly correlated, weakly magnetized, topological states, especially when the order parameter is developed on the out-of-plane axis. In the next chapter 4 we discuss two possible strategies to stabilize the $\mathrm{AFM}_{\perp}$ solution, within cold-atom simulators or solid-state systems at the nanoscale. The latter recipe is especially effective at interaction strengths that are relevant for realizing the $\mathrm{AFM}_{\perp}$ weakly-magnetized topological solution.

Both the strongly magnetized antiferromagnets are characterized by vanishing intra-orbital correlations in the $U \gg t$ limit. Remarkably, at high spin-orbit values the $\mathrm{AFM}_{\perp}$ solution is characterized by an almost saturated Néel order immediately after the transition, directly connected with a vanishing intra-orbital correlation at any $U > U_{\perp}^{c}$.

Finally, following the behavior of the intra-orbital mutual information across the paramagnetic Mott transition (Fig. 3.8c) we clearly see that the paramagnetic Mott insulator is always characterized by *maximally correlated local spin-orbital pairs*, regardless of the nature of the weak-coupling phase that turns insulating by increasing U, which can either be the Dirac semimetal ($\lambda_{\mathrm{so}} = 0$) or the quantum spin-Hall insulator ($\lambda_{\mathrm{so}} \neq 0$). In these Mott states, the on-site spin states share almost 1 bit of information, at all interaction values beyond the Mott critical point.

We remind that in sections O.5 and 2.3 we have discussed, in very general terms, the local correlations on a single site must be considered classical in single-band models that

conserve charge and spin, as the corresponding single-orbital reduced density matrix is described by a so-called pseudo-classical expression.

However, at zero temperature the only two sources of classical correlations in a given open quantum subsystem, are I. the possible quantum degeneration of the global closed system (here the entire Kane-Mele-Hubbard lattice) and/or II. the presence of *nonlocal* entanglement beyond the boundary of the selected subsystem [173]. Indeed the latter possibility has been recently explored for the Mott-Hubbard phase found in the square lattice within a cluster extension of dynamical mean-field theory [3], paving the road for future investigation on the relationship between Mottness and nonlocal quantum correlations. We will discuss in great detail this intriguing observation in the second part of the thesis, chapters 6, 7, 8, 9 and 10.

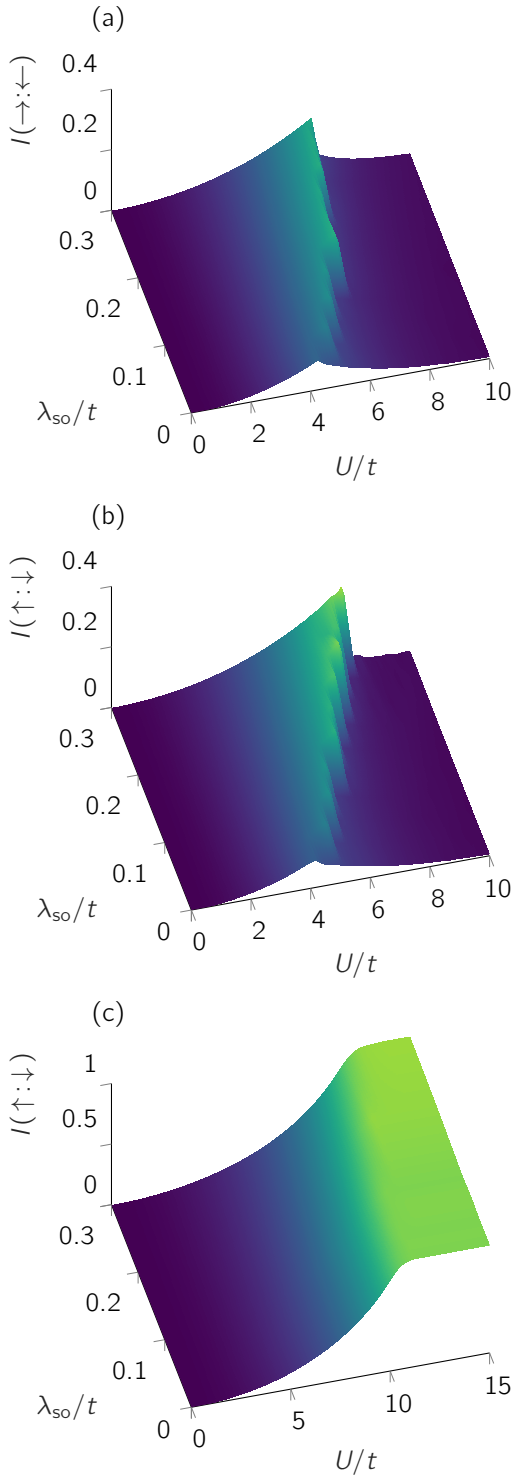


Fig. 3.8.: Intra-orbital correlations at different interactions U and spin-orbit couplings λ_{so} for (a) the $AFM_{\parallel}$-parametrized solution, (b) the $AFM_{\perp}$-parametrized solution and (c) the paramagnetic solution, within dynamical mean-field theory. Units of $\log(2) = 1$ bit.

Stability of the AFM phases

4

In this chapter we will analyze the competition between the in-plane and out-of-plane magnetic orderings in the KMH model, in terms of their total energies, at zero temperature. The subject has been extensively explored in the literature, with a multitude of techniques [87, 88, 130–135, 137, 140–142, 146]. In this work we focus on quantifying the energy difference between the two competing states, in view of the design of experimental strategies to control the magnetic and electronic properties of systems based on the honeycomb lattice.

After a brief introduction to the theoretical formulas we use to compute total energies within dynamical mean-field theory, and a benchmark against existing literature in the well-studied limit of vanishing spin-orbit coupling, we focus again on the way in which DMFT sets apart from standard mean-field theory, especially in the region where the latter predicts the most energy difference between the $\mathrm{AFM}_{\parallel}$ and $\mathrm{AFM}_{\perp}$ solutions.

We further provide evidence for an easy switch of the favored ordering, by either introducing a staggered external field, a situation which is hard to realize in a solid-state framework and it can be obtained only in cold-atom experiments, or by leveraging boundary effects in solid-state realizations of the model, at the nanoscale.

4.1 Computing the total energy in DMFT/ED

Within the Hubbard approximation for the electron repulsion, the total energy of an interacting electron lattice can be expressed as the sum of a local potential energy and the kinetic term, which is manifestly nonlocal

$$E = \sum_i U_i + K \tag{4.1}$$

The potential term on every site is given by the expectation value of the Hubbard interaction in the Hamiltonian Eq. 2.4

$$U_i = \left\langle U \left(n_{i\uparrow} - \frac{1}{2} \right) \left(n_{i\downarrow} - \frac{1}{2} \right) \right\rangle = U \left\langle n_{i\uparrow} n_{i\downarrow} \right\rangle - \frac{U}{2} \left\langle n_{i\uparrow} + n_{i\downarrow} \right\rangle + \frac{U}{4} , \tag{4.2}$$

Given the locality of all terms, this expectation value can be directly evaluated on the impurity site of the auxiliary model (it is equal in the two sublattices for all the nonmagnetic and antiferromagnetic solutions).

The kinetic energy can be computed in terms of a general interacting Green's function matrix, as

$$K = \frac{1}{\beta}\sum_{\boldsymbol{k},n} \mathrm{tr}\,\mathbf{H}(\boldsymbol{k})\mathbf{G}(\boldsymbol{k}, i\omega_n), \tag{4.3}$$

where $\mathbf{H}(\boldsymbol{k})$ indicates the noninteracting Hamiltonian matrix and $i\omega_n$ are fermionic Matsubara frequencies at the given inverse temperature β.The customary strategy to evaluate Eq. 4.3 within dynamical mean-field theory amounts to recast it in terms of the *local* ($\boldsymbol{k}$-summed) Green's function matrices, as

$$\begin{aligned}
K &= \mathrm{tr}\,\frac{1}{\beta}\sum_{\boldsymbol{k},n} \left(\mathbf{H}(\boldsymbol{k})\mathbf{G}(\boldsymbol{k}, i\omega_n) + \mathbf{G}(\boldsymbol{k}, i\omega_n)^{-1}\mathbf{G}(\boldsymbol{k}, i\omega_n) - \mathbf{G}^0(\boldsymbol{k}, i\omega_n)^{-1}\mathbf{G}^0(\boldsymbol{k}, i\omega_n)\right) \\
&= \mathrm{tr}\,\frac{1}{\beta}\sum_{\boldsymbol{k},n} (\mathbf{H}(\boldsymbol{k})\mathbf{G}(\boldsymbol{k}, i\omega_n) + (i\omega_n - \mathbf{H}(\boldsymbol{k}) - \mathbf{\Sigma}(\boldsymbol{k}, i\omega_n))\mathbf{G}(\boldsymbol{k}, i\omega_n) - (i\omega_n - \mathbf{H}(\boldsymbol{k}))\mathbf{G}_0(\boldsymbol{k}, i\omega_n)) \\
&= \mathrm{tr}\,\frac{1}{\beta}\sum_{\boldsymbol{k},n} \left(i\omega_n \left(\mathbf{G}(\boldsymbol{k}, i\omega_n) - \mathbf{G}^0(\boldsymbol{k}, i\omega_n)\right) - \mathbf{\Sigma}(\boldsymbol{k}, i\omega_n)\mathbf{G}(\boldsymbol{k}, i\omega_n) + \mathbf{H}(\boldsymbol{k})\mathbf{G}^0(\boldsymbol{k}, i\omega_n)\right) \\
&= \mathrm{tr}\,\frac{1}{\beta}\sum_{n} \left(i\omega_n \left(\mathbf{G}_{\mathrm{loc}}(i\omega_n) - \mathbf{G}^0_{\mathrm{loc}}(i\omega_n)\right) - \mathbf{\Sigma}_{\mathrm{imp}}(i\omega_n)\mathbf{G}_{\mathrm{loc}}(i\omega_n)\right) + \int_{-\infty}^{+\infty} \frac{\varepsilon\,\rho_0(\varepsilon)}{\exp[\beta(\varepsilon-\mu)]+1}\mathrm{d}\varepsilon
\end{aligned} \tag{4.4}$$

where we have used the lattice-model Dyson equation to evaluate $\mathbf{G}(\boldsymbol{k}, i\omega_n)^{-1}$ and $\mathbf{G}^0(\boldsymbol{k}, i\omega_n)^{-1}$ and the DMFT approximation of the self-energy $\mathbf{\Sigma}(\boldsymbol{k}, i\omega_n) \simeq \mathbf{\Sigma}_{\mathrm{imp}}(i\omega_n)$ [38]. The only term depending explicitly on $\mathbf{H}(\boldsymbol{k})$ can be trivially expressed in terms of the noninteracting density of states $\rho_0(\varepsilon)$. We observe nevertheless that the remaining imaginary frequency summations are affected by slow-decaying tails, due to the $i\omega_n$ prefactor in the first term of the last row in Eq. 4.4. The numerical evaluation of the kinetic energy could then be affected by the inevitable finite cutoff on the imaginary axis. An analytic tail correction can be implemented by defining an asymptotic model for the full interacting Green's function matrix, as [177, 178]

$$\mathbf{T}(\boldsymbol{k}, i\omega_n) = \frac{1}{i\omega_n} + \frac{\mathbf{H}(\boldsymbol{k}) + \mathbf{\Sigma}_{\mathrm{imp}}(\infty)}{(i\omega_n)^2} + \mathcal{O}\left(\frac{1}{(i\omega)^3}\right),$$

where the expansion coefficients can be derived by inspecting the high-frequency behavior of the impurity self-energy [179–182].

We can thus recast Eq. 4.3 as [183]

$$\begin{aligned}
K &= \mathrm{tr}\,\frac{1}{\beta}\sum_{\boldsymbol{k},n} \mathbf{H}(\boldsymbol{k})\left(\mathbf{G}(\boldsymbol{k}, i\omega_n) - \mathbf{T}(\boldsymbol{k}, i\omega_n) + \mathbf{T}(\boldsymbol{k}, i\omega_n)\right) \\
&= \mathrm{tr}\,\frac{1}{\beta}\sum_{\boldsymbol{k},n} \mathbf{H}(\boldsymbol{k})\left[\mathbf{G}(\boldsymbol{k}, i\omega_n) - \frac{1}{i\omega_n} - \frac{\mathbf{H}(\boldsymbol{k}) + \mathbf{\Sigma}^{\mathrm{imp}}(\infty)}{(i\omega_n)^2}\right] \\
&\qquad + \mathrm{tr}\sum_{\boldsymbol{k}}\left[\frac{\mathbf{H}(\boldsymbol{k})}{2} - \frac{\mathbf{H}(\boldsymbol{k})(\mathbf{H}(\boldsymbol{k}) + \mathbf{\Sigma}^{\mathrm{imp}}(\infty))}{4T}\right]
\end{aligned} \tag{4.5}$$

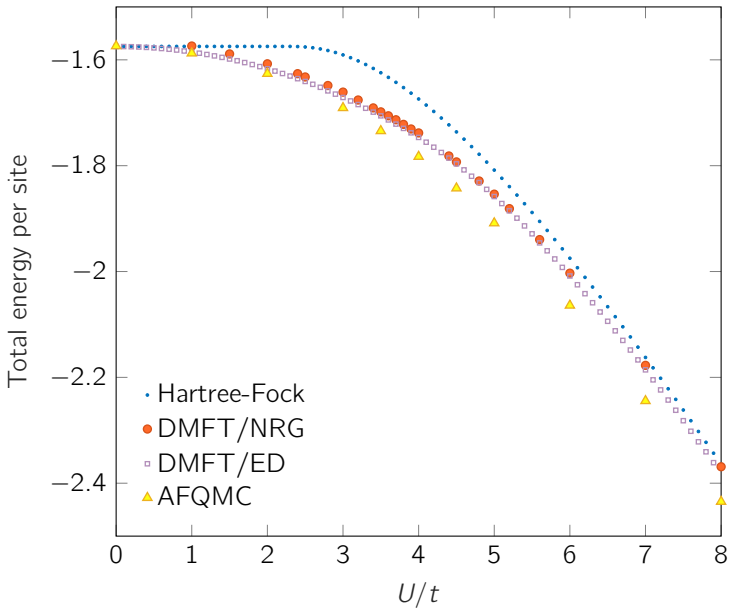


Fig. 4.1.: Total energy of the Hubbard model on the honeycomb lattice, corresponding to a Kane–Mele–Hubbard model with no spin-orbit coupling. The DMFT/NRG and AFQMC data are taken from Ref. [148]. The Hartree-Fock and DMFT/ED data have been generated for this benchmark.

where the last term is obtained from the exact Matsubara sums $1/\beta \sum_n (i\omega_n)^{-1} = 1/2$ and $1/\beta \sum_n (i\omega_n)^{-2} = \beta/4$.

To asses the accuracy and effectiveness of our estimate for the lattice total energy, we compare in Fig. 4.1 our data, for $\lambda_{so} = 0$, with the results published in Ref. [148] for the Hubbard model on the honeycomb lattice. Despite gradually approaching the Hartree-Fock prediction at the strong coupling limit, in full agreement with the quantum-information analysis reported in the main text, the DMFT/ED energy is found much closer to the auxiliary-field quantum Monte Carlo (AFQMC) values around the magnetic transition. It is worth noticing that the DMFT/NRG [184] calculations of Ref. [148] are essentially indistinguishable from our data throughout the whole phase diagram, signaling that our estimate is not significantly affected by the finite-bath limitations inherent to the ED solver [38, 165, 166]. Overall, we conclude that our DMFT/ED calculations provide reliable total energies (at least in the strongly correlated regime around the magnetic transitions) both in the sense that they correctly reproduce the available DMFT results, using a very different solver, and in the fact that they are comparable with state-of-the-art AFQMC calculations. This benchmark leads us to assume that our calculations can correctly represent the competition between the $\mathrm{AFM}_\perp$ and $\mathrm{AFM}_\parallel$ orderings and accurately reproduce the energy gap separating the two solutions.

4.2 Energy separation between the two competing AFM solutions

Having established the properties of the total lattice energy within dynamical mean-field theory in the $\lambda_{so} = 0$ limit, we compare the $AFM_{\parallel}$ to $AFM_{\perp}$ energy gap, between the DMFT/ED and the Hartree-Fock calculations, across the whole phase diagram of the model. As depicted in Fig. 4.2 both static and dynamical mean-field theories predict the $AFM_{\parallel}$ solution to be favored whenever the spin symmetry of the model is spontaneously broken and a finite order parameter is stabilized in the calculation. If both order parameters vanish the two solutions coincide and the energy gap obviously vanishes. Additionally, for small enough λ_{so} we recover the full SU(2) spin-rotation symmetry, so that the ordered phases are numerically indistinguishable.

In Fig. 4.3 we show both total energies at $\lambda_{so} = 0.3t$, where the separation between the two magnetic states is maximal. Both static and dynamical mean-field theories predict a very small gap, with respect to the overall energy scales. Additionally, the Hartree-Fock treatment significantly overemphasizes the stability of the $AFM_{\parallel}$ state, in a multifaceted fashion:

1. As it can be checked by inspecting also Fig. 4.2, the gap values are bigger per se, by almost a factor of two at its maximum magnitude.
2. While both calculations find the maximum energy difference at the critical interaction for the $AFM_{\perp}$ transition, the different nature of this quantum critical point in the two theories greatly affects the behavior after the transition: the Hartree-Fock energies smoothly decrease with the increasing order parameter while the DMFT/ED transition is abrupt and almost closes the gap right away.
3. Whereas the remnant gap in DMFT/ED rapidly closes with U, within the static mean-field it does so only asymptotically, very slowly.

Overall, the standard Hartree-Fock mean-field theory overestimates the extension, in parameter space, of the region where the in-plane magnetized phase is clearly stable as well as the size of the energy difference between the two magnetic solution.

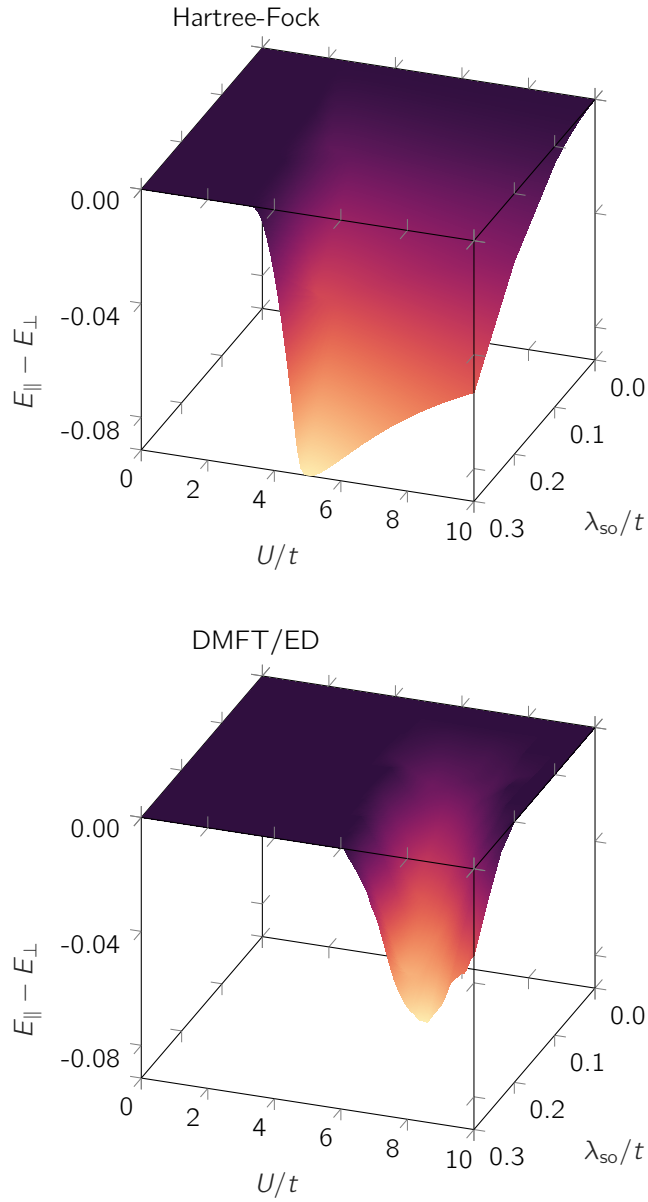


Fig. 4.2.: Total energy difference (per site) between the $\mathrm{AFM}_{\parallel}$ and the $\mathrm{AFM}_{\perp}$ solutions. Hartree-Fock on the left and dynamical mean-field theory on the right. Both calculations find the in-plane magnetization to be favored in a large portion of the phase diagram. Note that the $\lambda_{so} \to 0$ limit is characterized by a vanishing gap at all interaction values, according to the asymptotic restoring of the full SU(2) spin symmetry. The remaining region at weak coupling is paramagnetic and the two solutions are inherently indistinguishable. To aid the graphical rendering, the DMFT/ED data have been slightly smoothed in this figure.

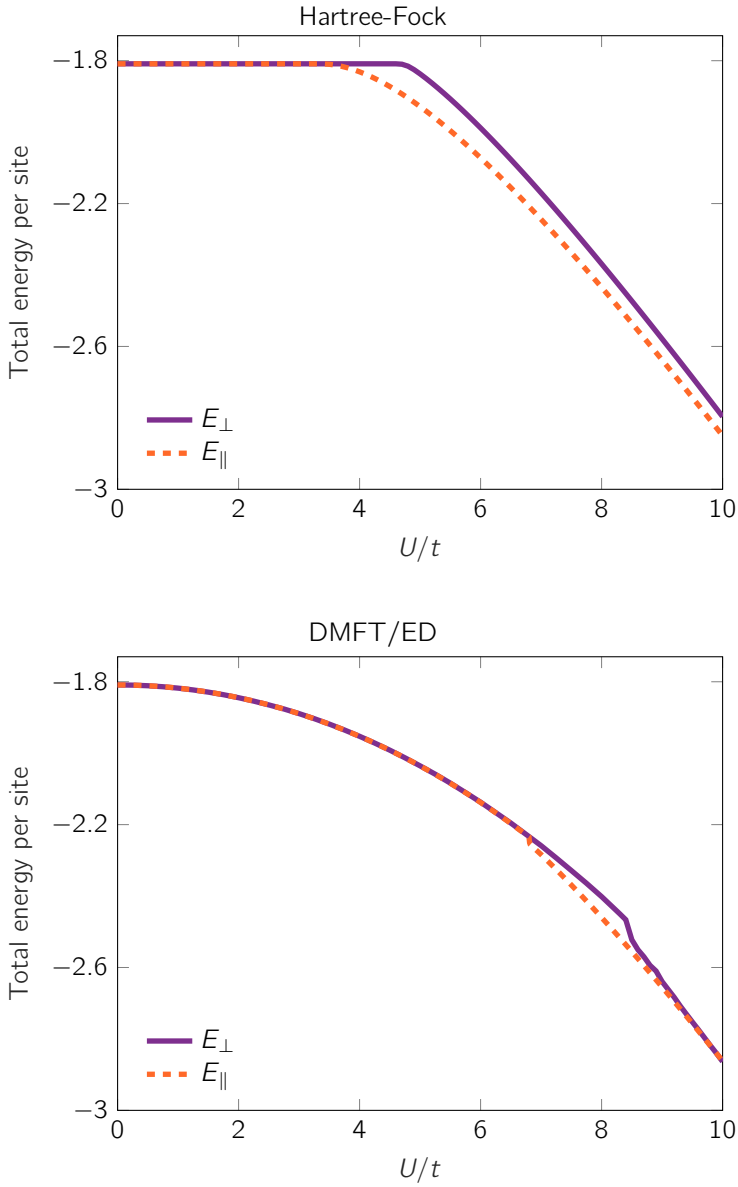


Fig. 4.3.: Total energies of the $\mathrm{AFM}_\perp$ and $\mathrm{AFM}_\parallel$ solutions at $\lambda_{so} = 0.3t$. Hartree-Fock on the left and dynamical mean-field theory on the right. The overall energy scales are very similar, with the DMFT solution slightly more stable. The gap between the two magnetic states is very different though: the Hartree-Fock solution overestimates the stability of the in-plane magnetization.

4.3 Switching ground state with an external field

The fact that, in the strongly-correlated intermediate regime, the two magnetic solutions of the KMH model are in fact very close in energy brings up a natural question: can we invert the energy difference of such states and make the $\mathrm{AFM}_{\perp}$ ordering favored?

A straightforward route to achieve this *magnetic gap inversion* is clearly to add a perturbation which favours explicitly the z-axis magnetization, in the form of a staggered external field along the z direction. Given the insulating character of the system and that we are interested in a regime of relatively high interaction values we model the staggered magnetic field as a Zeeman term in the Hamiltonian:

$$\mathbf{H}'_{\mathrm{KMH}} = \mathbf{H}_{\mathrm{KMH}} - h_{\perp}\sigma_z \otimes \tau_z \tag{4.6}$$

where σ_z and τ_z are Pauli matrices referred respectively to the spin and sublattice degrees of freedom, in the $\psi = (|A\uparrow\rangle, |B\uparrow\rangle, |A\downarrow\rangle, |B\downarrow\rangle)$ single-particle basis.

In Fig. 4.4 we show our Hartree-Fock and DMFT/ED data for $\lambda_{\mathrm{so}} = 0.3t$ and respectively $U = 5t$ and $U = 8t$, so to probe the robustness of the $\mathrm{AFM}_{\parallel}$ ground state very close to the estimated bottom of its stability valley (compare to Fig. 4.2).

The behavior of the total lattice energies is significantly different within the two methods, once again remarking the contrasting nature of the respective quantum many-body states. Both simulations find a critical field strength for which the energy difference is inverted and the $\mathrm{AFM}_{\perp}$ stabilized.

It is worth noticing that the estimated critical fields are smaller than the given spin-orbit coupling, which besides being the smallest bare energy scale in the unperturbed Hamiltonian, is the only term responsible for the magnetic anisotropy in the Kane-Mele-Hubbard model.

We report that for $\lambda_{\mathrm{so}} = 0.1t$ the critical field is even an order of magnitude under the spin-orbit coupling, which naturally follows from the fact that for smaller λ_{so} the energy gain itself is significantly reduced.

Overall, we argue that such small values for the critical staggered field suggest a realistic possibility of switching ground state in cold atom simulators, opening an interesting avenue for future research. We further acknowledge that a similar analysis has been considered in Ref. [135], where instead a *uniform* Zeeman field is considered, leading to the analytical prediction of a canted magnetic ground state.

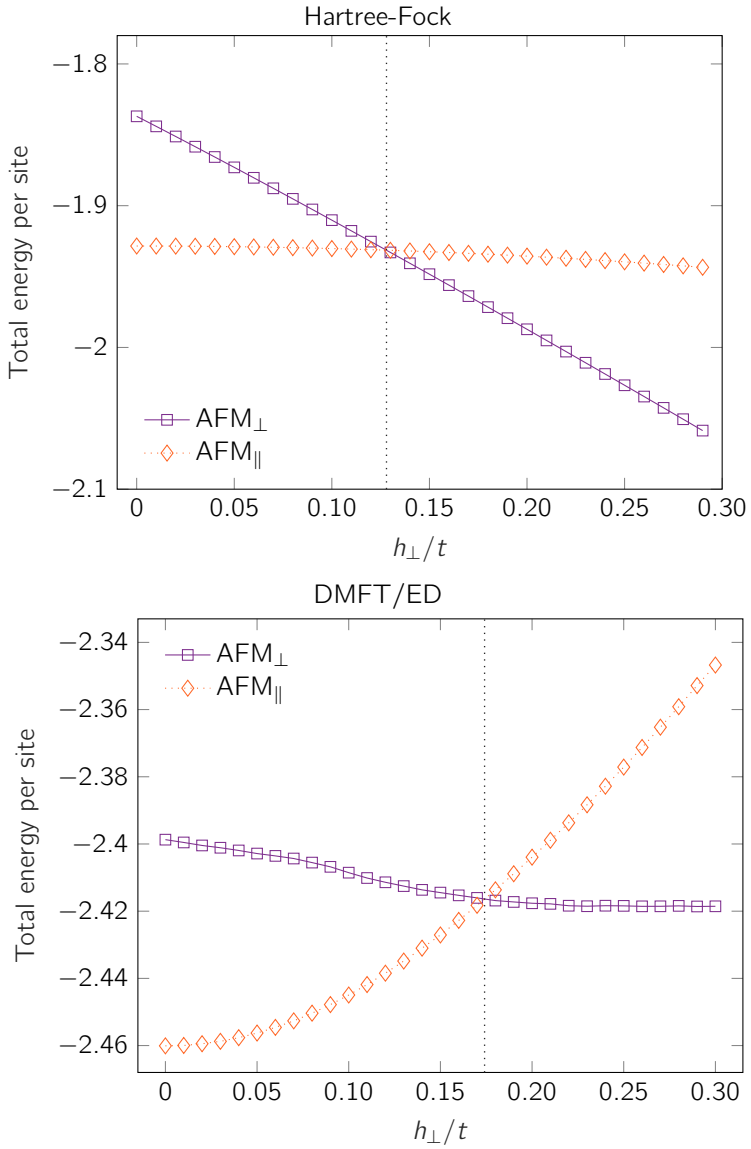


Fig. 4.4.: Variation of the total energy with an out-of-plane, staggered external field. Hartree-Fock data for $U = 5t$ on the left and dynamical mean-field theory data for $U = 8t$ on the right. The spin-orbit coupling is $\lambda_{so} = 0.3t$ for both calculations. The dotted vertical line marks respectively the $h_\perp \simeq 0.128t$ and $h_\perp \simeq 0.174t$ critical fields for the inversion of the magnetic gap.

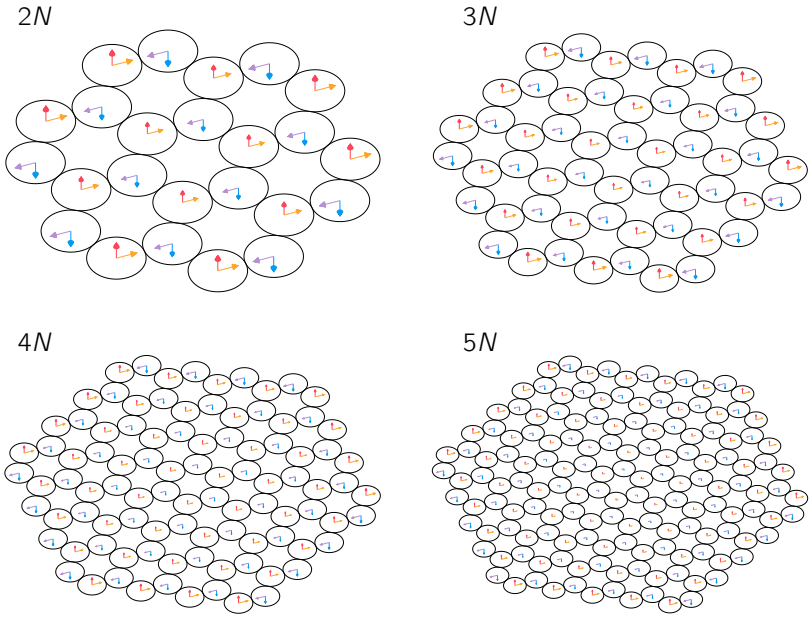


Fig. 4.5.: Schematic illustration of the $2N$, $3N$, $4N$ and $5N$ KMH nanoflakes. The arrows illustrate the two possible antiferromagnetic orderings, underlining that in the general case the local magnetization would not be uniform in the nanoflake.

4.4 Switching ground state at the nanoscale

Finally, we investigate a different route to introduce novel magnetic properties in a Kane-Mele-Hubbard system, by addressing the properties of the model on small-size *nanoflakes* that preserve the full point-symmetry of the lattice. Such systems have been extensively studied for the case of vanishing spin-orbit coupling [185, 186], within single-site inhomogeneous dynamical mean-field theory (RDMFT)[1] [38, 160], revealing the onset of magnetic order at any finite interaction U. Extended discussions around the accuracy of RDMFT for inhomogeneous systems and its relevance for modeling realistic solid-state materials can be found in [160, 187, 188]. Attention has also been given to correlated topological phases on the square lattice [152, 161], establishing a clear route to investigate the interplay between complex single-particle Hamiltonians and the local Hubbard interaction, whenever cluster theories [189] are out of reach.

[1] As we mentioned already in section 2.2, one can always treat an arbitrary number of auxiliary impurity models, to enlarge the unit-cell of the system. If one further transforms the noninteracting Hamiltonian from a $\boldsymbol{k}$-space function, obtained in periodic boundary conditions, to a $\boldsymbol{r}$-space function in open boundary conditions, single-site DMFT is readily extended to treat inhomogenous systems, with a computational complexity the scales almost as the number N of inequivalent sites (leading to solve N impurity models). The exceeding time is spent in evaluating the $N \times N$ lattice Green's function matrix, and enforcing the self-consistency Eq. 2.7, that couples the different impurity sites at this level. The method is often called also *nano*DMFT or *real-space* DMFT (RDMFT).

Following the notation of previous works [185, 190], we address $2N$, $3N$, $4N$ and $5N$ flakes, where $(r+1)N = 24, 54, 96, 150$ indicates the total number of sites in terms of the number of edge sites N, and the number of unit-cell translations r connecting the center and the edge of the flake. The structure of the nanoflakes can be inspected in Fig. 4.5. The corresponding noninteracting Hamiltonians $\mathbf{H}(i,j)$, $i,j = 1,\dots,(r+1)N$ have been generated leveraging the `HoneyTools` software [191]. No punctual symmetry has been enforced in the iterative solution of the DMFT equations, amounting to a self-consistent coupling of $(r+1)N$ impurity models. A real-space analysis of the $\mathbb{Z}_2$ invariant has been performed on the resulting topological Hamiltonians[2] $\mathbf{H}^{\text{topo}}(i,j) = \mathbf{H}(i,j) + \mathbf{\Sigma}(i,j,\omega=0)$, leveraging the recently introduced *generalized local spin-Chern marker* [192], as implemented in the `StraWBerryPy` software [193].

In Fig. 4.6 are reported the total, kinetic and potential energy differences of all flakes, for increasing repulsion values and fixed $\lambda_{\text{so}} = 0.3t$. The $\text{AFM}_\perp$ solution is significantly favored at intermediate U/t, in stark contrast with the energy landscape at the thermodynamic limit (Fig. 4.2). This energy gap between the two antiferromagnetic solutions keeps increasing with the electronic repulsion, until a size-dependent critical value, after which it is quickly reduced and eventually inverted at strong coupling. An inspection of the left panel of Fig. 4.7, reporting the interaction dependence of the $m_{i,\parallel}$ and $m_{i,\perp}$ order parameters, reveals that the maximum of the total energy difference roughly corresponds to a sudden increase of the easy-plane local magnetization $m_{i,\parallel}$. In particular, it is exactly located at its discontinuous jump for the $2N$ flake, and around the concavity inversion for the larger ones. The presence of a discontinuous transition on the smallest flake, with a critical interaction that is significantly smaller than its thermodynamic limit counterpart (see Fig. 3.1), can be attributed to the obviously strong boundary effects: the edge sites amount to half of the system and their lower coordination favors the electronic repulsion over the kinetic energy. Indeed they feature a larger magnitude of the order parameter at any interaction value. We argue that the critical interaction for the first-order transition is the same for edge and bulk sites because the magnetization of the former acts as a trigger for the latter. Larger flakes feature a smooth transition and a bulk-edge separation that grows significantly with the system size, suggesting a highly nontrivial finite-size scaling, as expected for nanoscale systems, which are inherently far from their thermodynamic limit. An important consequence of the strong finite size effects is the absence of a topological transition, as the local marker for the $\mathbb{Z}_2$ invariant [192] is odd for all the $\text{AFM}_\parallel$ and $\text{AFM}_\perp$ calculations, even when the magnetization is almost saturated ($2N$ and $3N$ flakes, in Fig. 4.7). In this sense, we can affirm that, at the nanoscale, the out-of-plane antiferromagnetic topological insulating phase is not only stabilized for a wide range of interaction strengths, but also enhanced in its observable properties, as the coexistence of topological and magnetic order is extended to large values of the staggered magnetization.

[2] We substitute the $\boldsymbol{k}$-dependence in Eq. 2.11, with a real-space dependence on the sites i and j.

A direct analysis of the site resolved intra-orbital correlation is reported in the right panel of Fig. 4.7, revealing an edge-bulk separation of the $I(\rightarrow{:}\leftarrow)$ mutual information that increases with the electronic repulsion up to a critical value that matches the location of the maximum in the total energy difference. At larger U/t, *i.e.* whenever the order parameter becomes *large enough*, the edge sites become suddenly less correlated than the bulk, and all intra-orbital correlations monotonically decrease towards zero at the strong coupling limit. As for the infinite lattice, we observe that the $\mathrm{AFM}_{\perp}$ solution reaches significantly larger intra-orbital correlations, as the critical interaction for the large magnetization is shifted at higher repulsion strengths. Overall, the out-of-plane magnetization seems favored whenever the edge correlation dominates, whereas at U/t beyond the maximum of $I(\rightarrow{:}\leftarrow)$, we have an $\mathrm{AFM}_{\parallel}$ solution that barely distinguishes between edge and bulk sites in the intra-orbital mutual information and, consequently, quickly approaches the energetic gain that characterizes the full phase-diagram in the thermodynamic limit. The boundary origin of the ground state inversion in the nanoflakes can be confirmed by a closer inspection at the energetic balance of the system. As reported in Fig. 4.6, bot the kinetic and potential energy differences between the easy-plane and out-of-plane magnetized states are nonmonotonic and strongly influenced by size. The kinetic energy favors the $\mathrm{AFM}_{\parallel}$ solution, as expected from the presence of a finite spin-orbit coupling in the noninteracting Hamiltonian. The potential energy favors instead the $\mathrm{AFM}_{\perp}$ solution, and given the lowered coordination at the boundary, wins the competition, as long as the actual edge correlation is stronger than the bulk correlation, in both solutions.

In Figs. 4.8 and 4.9 we provide fixed U/t real-space snapshots of the $\mathrm{AFM}_{\perp}$ and $\mathrm{AFM}_{\parallel}$ solutions. The magnetization is depicted with out-of-plane and in-plane arrows while the spin mutual information is proportional to the area of the drawn circles. Indeed we can appreciate how the weak repulsion snapshots depict very similar states for the $\mathrm{AFM}_{\perp}$ and $\mathrm{AFM}_{\parallel}$ calculations, both characterized by a small order parameter and strong, edge-dominated, intra-orbital correlations. At large U/t, however, we confirm an out-of-plane state that is essentially more correlated and (slightly) more magnetized but qualitatively unchanged, while the $\mathrm{AFM}_{\parallel}$ solution reveals an almost saturated easy-plane order and a (slightly) bulk-dominated mutual information profile.

Finally, we point out that the inhomogeneous dynamical mean-field theory has also been successfully applied to simulate harmonic trapping in cold atom experiments [194–196], in particular for graphene [190], where it provides a natural recipe to stabilize *artificial* flakes with the full rotational symmetry of the honeycomb lattice, as the ones addressed in this appendix. Furthermore, the harmonic confinement has been shown to greatly enhance the magnetic ordering, by enforcing a radially inhomogeneous filling of the orbitals. Extending our study of local correlations to this enriched setup would surely be of great interest.

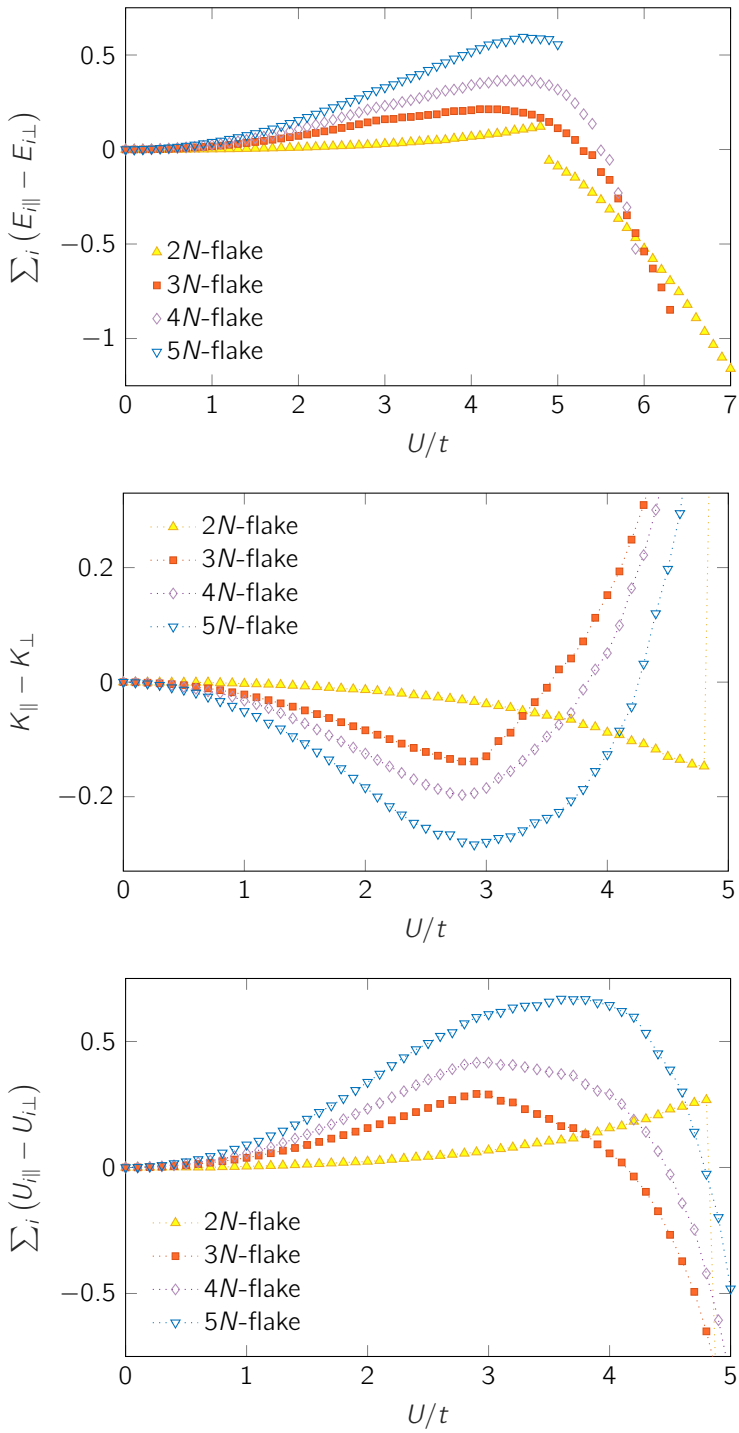


Fig. 4.6.: Difference of total, kinetic and potential energy for nanoflakes of $N_{\text{tot}} = (r+1)N$ sites, with N the number of sites at the edge and r the number of unit-cells to transverse radially to reach the edge from the central hexagon (see Fig. 4.5).

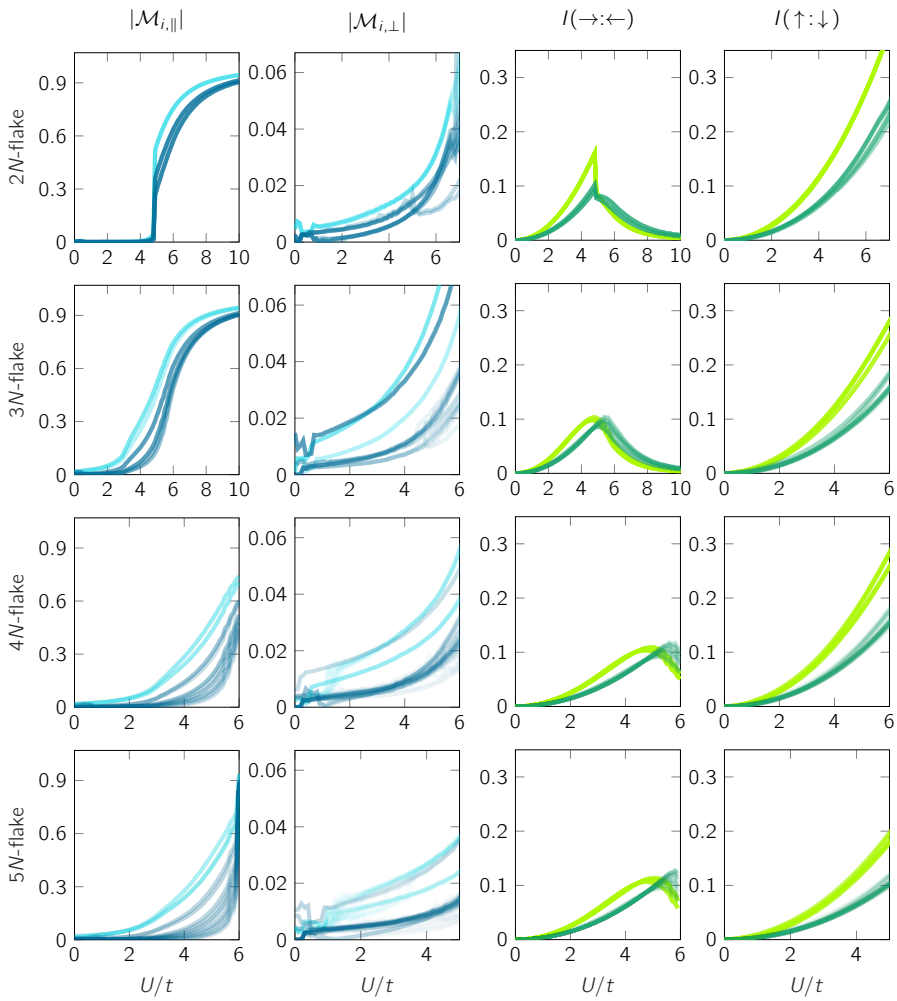


Fig. 4.7.: Site-resolved staggered magnetization (left) and intra-orbital correlation (right), for increasing values of the Hubbard interaction, at a fixed spin-orbit coupling $\lambda_{so} = 0.3t$. The light curves correspond to the orbitals at the edge of the flake, the dark ones to the bulk. Remarkably, the magnetization of the $2N$ flake features the least significant edge-bulk separation. The $2N$ in-plane magnetization, displays also a discontinuous jump, much similar to the observed phenomenology in the bulk. The magnetization of the larger flakes appear to slowly evolve towards the thermodynamic limit. This nontrivial and to large extent surprising finite-size scaling suggests a prominent role of the flake boundary in determining the magnetic properties of the system, as we are certainly very far from the large-size limit. We further highlight that the order parameter is finite for arbitrarily small U/t values, in all calculations, in sharp contrast with the infinite lattice solutions. This is a well-known property of honeycomb nanoflakes, as previously demonstrated in spin-orbit-free graphene [185, 190]. Regarding the intra-orbital correlations, the $\text{AFM}_{\parallel}$ solution is clearly more correlated at the boundary for small values of the interaction and the mutual information gap monotonically increases with U as long as the average magnetization does not saturate. In fact, a large magnetization quickly inverts the edge-bulk separation and gradually kills all correlations approaching the strong coupling limit. On the contrary, the $\text{AFM}_{\perp}$ solution does not reach a highly ordered state within the explored range of interaction values, thus allowing stronger intra-orbital correlations in both the edge and the bulk of the system.

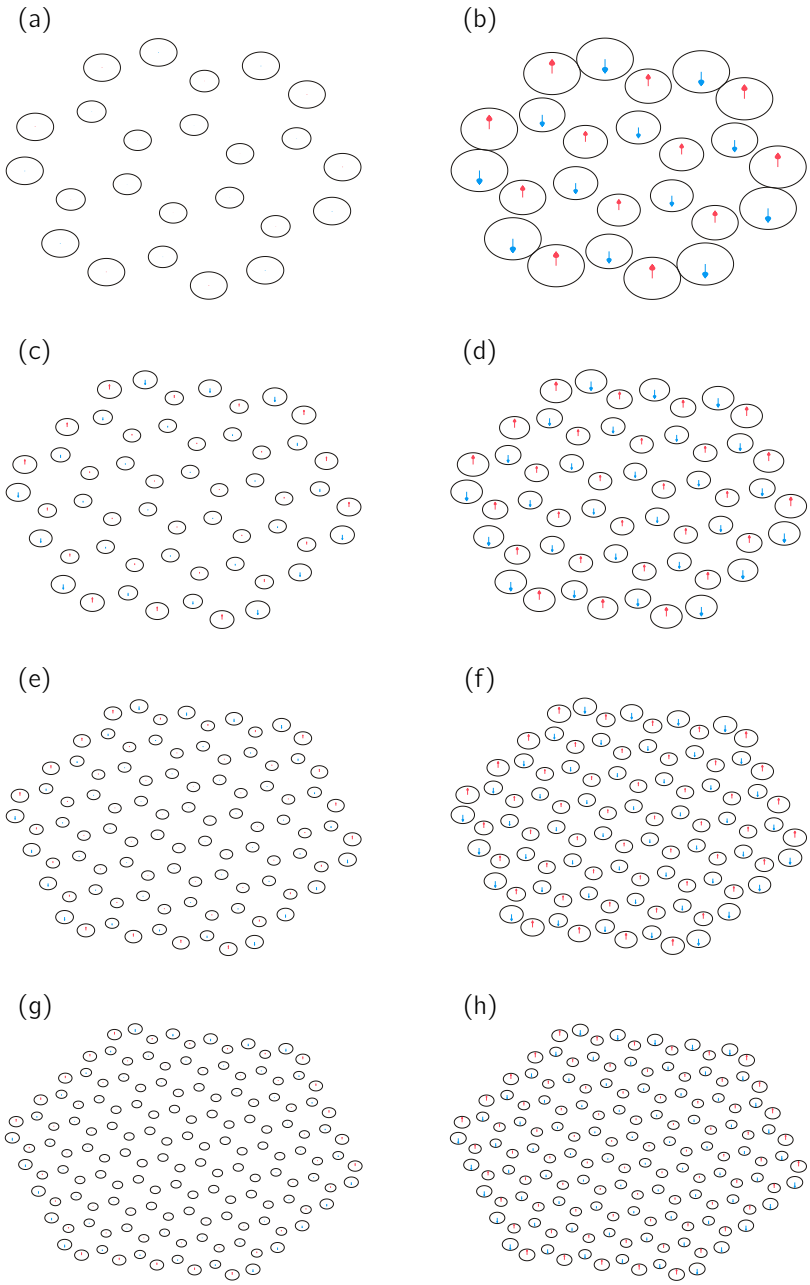


Fig. 4.8.: Magnetic order parameter and intra-orbital correlation in the $2N$ (a,b), $3N$ (c,d), $4N$ (e,f) and $5N$ (g,h) nanoflakes. The length of the arrows measures the $\mathrm{AFM}_{\perp}$ order parameter. The area of the circles measures the intra-orbital correlation $I(\uparrow{:}\downarrow)$. Data for $\lambda_{so} = 0.3t$ (a,b,c,d,e,f,g,h) and $U = 4.5t$ (a,c,e,g), $U = 5t$ (h), $U = 6t$ (b,d,f).

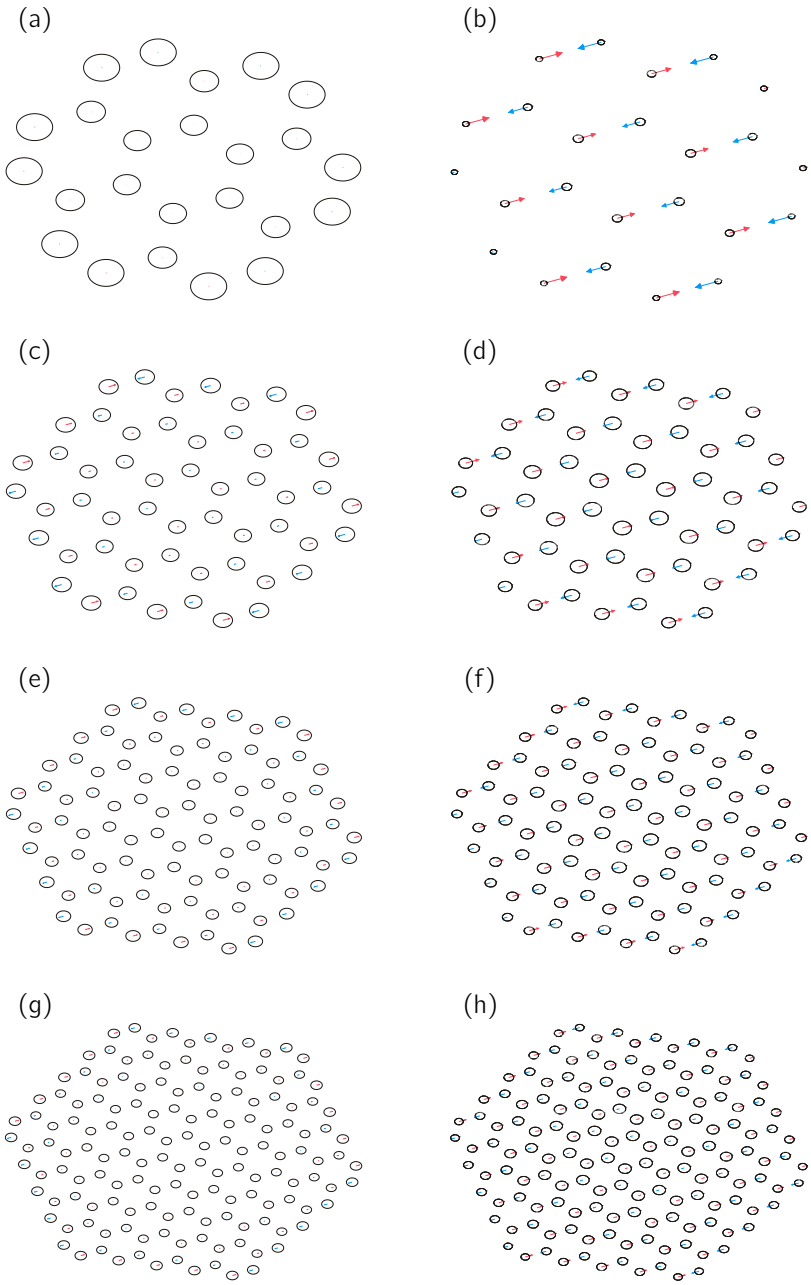


Fig. 4.9.: Magnetic order parameter and intra-orbital correlation in the $2N$ (a,b), $3N$ (c,d), $4N$ (e,f) and $5N$ (g,h) nanoflakes. The length of the arrows measures the $\mathrm{AFM}_{\parallel}$ order parameter. The area of the circles measures the intra-orbital correlation $I(\rightarrow:\leftarrow)$. Data for $\lambda_{so} = 0.3t$ (a,b,c,d,e,f,g,h) and $U = 4.5t$ (a,c,e,g), $U = 5.9t$ (h), $U = 6t$ (b,d,f).

Summary and outlook

5

In this chapter we have presented a thorough comparison of static and dynamical mean-field theory calculations for the Kane-Mele-Hubbard model, describing topological Dirac fermions in presence of a local electron repulsion [87, 88].

We have compared anisotropic antiferromagnetic solutions finding, in agreement with previous literature, that the phase with in-plane magnetization is always energetically favoured with respect to the out-of-plane state. Our results identify, however, some features of the Mott-Heisenberg transition that, to the best of our knowledge, have not been explored so far, namely the existence of a weakly-magnetized topological state, at intermediate interactions, and a subsequent discontinuous topological transition to an almost saturated Néel state.

We remark that our dynamical mean-field theory is solved, by construction, at the thermodynamic limit, whereas the multitude of sign-free quantum Monte Carlo simulations appeared throughout the years are all affected by finite-size effects [87, 88, 137], which require finite-size scaling to assess the thermodynamic limit. While in principle well under control due to the lack of sign problem, this extrapolation has led to some uncertainty and, consequently to a remarkable controversy regarding the existence of a spin-liquid phase in the phase diagram for small and vanishing values of the intrinsic spin-orbit coupling [136–139]. On the other hand, reports of an AFMTI phase similar to the one we observe, have appeared for the closely related Bernevig-Hughes-Zhang-Kanamori model, within DMFT, VCA and DMRG calculations [151–154].

We observe that the promotion of continuous topological transitions, found in the absence of interactions and/or at the Hartree-Fock level, to genuine first-order transitions with discontinuous jumps in all observables has been attributed to the inclusion of strong *local* electronic correlations beyond static mean-field theory [90–92, 162].Our analysis, based on the intra-orbital mutual information, directly measures correlations contained in a local orbital and quantifies the distance from a Hartree-Fock state, hence providing a foundation to this statement under the lens of quantum information theory.

Furthermore, we characterize the competing out-of-plane antiferromagnetic states, as well as forcefully paramagnetic solutions at very large repulsion, eventually fading into a Mott-Hubbard insulator. The comparison of the three different kind of interaction-driven insulating states depicts a colorful landscape for the intra-orbital correlation, suggesting interesting opportunities for the design of correlation-enhanced exotic topological states.

In particular the realization of a strongly-correlated antiferromagnetic topological insulator seems very promising, on both the easy-plane and out-of-plane axes. We prospect viable experimental realization in cold-atom simulators or solid-state nanostructures.

Finally, the Mott state without magnetic ordering, recently proposed to be possibly topological [47, 99, 100], has been shown to host a maximally correlated local state, shading light on a likely relationship between genuine, symmetry-unbroken, Mottness and the development of large nonlocal entanglement. We discuss a path to the direct analysis of short-range quantum and classical correlations between spatially separated electronic orbitals in the second part of the thesis, with an application to the Mott-Hubbard state found on the square lattice in chapter 9.

Part II

Quasilocal quantum correlations in the square lattice

Introduction

6

6.1 Success and failure of the local entropy

The Hubbard model is a cornerstone of condensed matter physics, which has been introduced as the minimal description of materials with strongly correlated electrons. The two-dimensional version of the model on a square lattice acquired an even more central role as the central building block to understand high-temperature superconductivity in copper oxides. Besides the various landmarks of the rich cuprate phase diagram, like *d*-wave superconductivity, antiferromagnetism and charge ordering/stripes, the most fundamental phenomenon described by the Hubbard model is perhaps the paramagnetic metal-insulator transition (MIT) happening at half-filling which, at least within cluster extensions of DMFT is directly linked to the pseudogap phase that is stabilized by underdoping the resulting Mott-Hubbard insulator. The Mott transition is indeed a much more general phenomenon, observed in a variety of strongly correlated oxides.

Both the Mott insulating state and the pseudogap arguably represent striking signatures of strong electronic correlations [17–19, 26, 55, 104, 197]; the pseudogap region has been growingly associated with the onset of large short-range spin correlations [198–200] and nonlocal entanglement which is also expected in the paramagnetic Mott insulator [24, 25, 48, 103, 201, 202].

On the other hand, the flourishing of quantum information theory has greatly emphasized the possibility to *quantify* the entanglement of quantum many-body systems and to use it to improve our understanding of quantum phase transitions [203–206], topological order [207–209], chemical bonding [73, 210, 211] and the development of highly efficient numerical methods [212–214]. Yet, the extension and adoption of quantum information concepts into the realm of fermionic models for strongly correlated matter presents significant theoretical subtleties [215–220], and it faces the severe practical limitations of wavefunction-based methods, either due to the infamous *sign problem* in quantum Monte Carlo (QMC) schemes [221–223] or high dimensionality in tensor networks [224–227].

In the last few years we have witnessed some pioneering efforts to introduce a systematic analysis of entanglement properties into traditionally successful descriptions of Mott-Hubbard physics, based on nonperturbative diagrammatic schemes. A seminal study within single-site DMFT (see section O.3) attempted to probe the development of entanglement across the interaction-driven Mott transition [61] through the *single-site* von Neumann

entropy. Indeed, the spatially local nature of the dynamical self-energy captured in this framework makes it natural to address on-site markers, in contrast with traditional analyses in terms of the entanglement *area law* [70, 71, 228].

A similar approach has been more recently pursued [62–64] within cluster dynamical mean-field theory (CDMFT) which improves on DMFT including effects of short-range spatial correlations within finite clusters [189, 229–232]. Yet, these studies have been also limited to single-site entropic measures despite the release of the single-site DMFT approximation. The limitation to local markers, in Refs. [62–64] is driven partly by sampling accessibility in the finite-temperature QMC solver for the auxiliary cluster problem (see chapter 8), as well as by their direct experimental access in cold-atom experiments [233].

Remarkably, the single-site von Neumann entropy has been shown to be sensitive to all the quantitative landmarks of the phase diagram at half-filling [62], as well as in presence of hole doping [63] and *d*-wave superconductivity [64].

Yet, the evolution as a function of the interaction strength for the half-filled transition does not seem to convey the expected physical picture for a correlation-driven Mott localization: in fact, despite being clearly influenced by the Mott transition, this quantity decreases from the metallic to the insulating phase [61, 62]. This seems in sharp conflict with the widespread notion, supported also by physical intuition, that nearly localized ("weak") Mott insulators are underpinned by the development of large entanglement among electronic orbitals at different sites [48].

We can understand this shortcoming of the local von Neumann entropy in describing the entanglement of the Mott insulator by noting that, regardless of the approximation, this quantity inevitably follows the behavior of the local double occupancy in the single-band Hubbard model (see Eq. 7.2). The double occupancy, in turn, naturally decreases across the Mott transition as a consequence of the freezing of charge fluctuations [61], thus leading to the decreasing of the local von Neumann entropy. We will discuss in depth this aspect in section 9.2.

At a more fundamental level, we notice that the local von Neumann entropy, as a measure of the entanglement between a single-site and the rest of the system, includes in a single quantity bipartite and multipartite correlations from all spatial ranges in the lattice, and therefore it does not necessarily capture the behavior of any such specific term [70]. Interestingly, recent extensions of the analysis to multi-site *collision* (2-Rényi) entropies [234, 235] share the same unsatisfactory qualitative picture of the MIT of the local von Neumann entropy, suggesting that some care should be taken in defining proper measures of nonlocal entanglement that capture the nature of the Mott insulating state and its difference with the metallic phase.

In this thesis, as reported in Ref. [3] we overcome these limitations by considering, within CDMFT, *quasilocal* measures of bipartite entanglement, namely the mode entanglement between two lattice sites at various distances ranging from nearest-neighbors to more distant pairs within the embedded interacting cluster. In this way we identify the key role of the nearest-neighbor contributions with respect to longer-distant counterparts.

To faithfully characterize the two-site fermionic entanglement we resort to quantum relative entropies (see appendix A) and the logarithmic negativity (see section 7.4), both of which provide measures of correlation and entanglement that are suited to be used for generic open quantum systems (as pairs of atomic orbitals embedded in a larger environment inherently are).

In particular we complement the upper bounds provided by the von Neumann mutual information and the logarithmic negativity with some new lower bounds, recently obtained by Ding *et al.* [219, 220] by imposing particle and charge *superselection rules* (SSR) [73, 211, 215–218, 236–242], with a strong operational relevance for prospected implementations of quantum information processing and computation tasks in condensed matter systems.

We compute all these quantities within zero-temperature CDMFT, leveraging a combination of numerically exact methods: a Lanczos/Arnoldi exact diagonalization scheme [54, 165, 166], which is limited to clusters of at most four sites, and a recently introduced configuration-interaction solver [243, 244], which gives access to the larger clusters required to assess the entanglement beyond next-nearest neighbors. In order to identify the fundamental information related to the Mott-Hubbard transition we consider paramagnetic solutions in which magnetic ordering is inhibited at zero temperature, thus ensuring a clean analysis of the quantum phase transition, free of any thermal effect.

Our analysis of the quasilocal two-site entanglement allows to obtain a terse physical picture of quantum and classical correlations across both the interaction-driven and density-driven Mott transition in the $2d$ Hubbard model, as well as a distinctive characterization of the metallic and insulating phases, under the lens of quantum information theory.

In particular, we show that the nearest-neighbor entanglement captures the physics of the model throughout the whole phase diagram at zero temperature providing a picture consistent with expectations and physical intuition. The two-site entanglement beyond nearest neighbors is shown to quickly decay with the lattice distance, at half-filling, as expected for low energy many-body states [74, 245, 246]. Overall, the quasilocal entanglement of the Mott insulator is larger with respect to the Fermi liquid state and it is found particularly stable with respect to variations in the interaction and of the chemical potential, as long as the insulating state is preserved. Moreover, when the chemical potential reaches the critical value to overcome the incompressibility of Mott gap, the system enters in a pseudogap metallic phase and the nearest-neighbor entanglement starts to decrease monotonically, as a function of the doping. Eventually, a first order

transition separates the pseudogap state from the weakly entangled hole-dominated Fermi liquid regime. The discontinuous jump in the nearest-neighbor entanglement across the doping-driven transition between the two metals, resembles the interaction-driven MIT observed at half-filling, highlighting the intimate connection between the Mott-Hubbard insulator and the pseudogap metal.

These results depict the Mott and pseudogap phases in the CDMFT solution of the $2d$ Hubbard model as intimate relatives, featuring large short-range entanglement, with respect to the weakly-correlated Fermi liquid phase found at weak repulsion and high hole concentration. Our short-range entanglement thus overcomes the limitations of previous analyses based on single-site (and multi-site) entanglement entropies, and provides an information which agrees with the widespread expectations for the strongly correlated phases [24, 25, 48, 103, 201, 202]. This success makes this quantity a serious candidate to properly measure the relative degree of entanglement of different systems even when we have no clear a priori expectations.

6.2 Outline of the following chapters

The following chapters 7, 8, 9, 10 are organized as follows.

- In chapter 7 we introduce the adopted measures of quasilocal correlation and entanglement. We further discuss the role of parity and charge SSR in the construction of lower bounds to the relative entropy of entanglement, as well as their relevance for a faithful operational definition of entanglement as a resource for quantum technologies.
- In chapter 8 we briefly review the cluster dynamical mean-field theory solution of the $2d$ Hubbard model, with particular focus on the adopted solvers and the strategy we devise for the evaluation of single- and two-site reduced density matrices, as the main ingredients to compute the measured of quasilocal entanglement.
- In chapter 9 we present and discuss our results for the interaction-driven MIT at half-filling, highlighting the strong physical interpretation of the two-site entanglement, as opposed to the von Neumann entropy.
- In chapter 10 we extend our analysis to the hole-doped model, shading some light on the physics of the pseudogap metal and its connection to the Mott-Hubbard insulator, in terms of the nearest-neighbor and next-nearest-neighbor entanglement.

7 Quantifying quasilocal entanglement

The quantification of entanglement between the constituents of a quantum system represents one of the greatest pursuits of quantum information theory. In the last few decades, a solid understanding has been established for bipartite pure states, where von Neumann entropies provide a rigorous and accessible measure of entanglement, thus assuming a leading role [69, 247, 248]. Many-body systems can be analyzed in this framework as long as one is interested to bipartitions involving at least one macroscopic subsystem, at zero temperature and in absence of ground state degeneracy [70, 71, 203, 204, 207, 224, 249, 250]. To characterize the spatial structure of entanglement at the microscopic level, instead, one has to resort to nontrivial generalizations, as the concept of *multipartite* entanglement measures [201, 241, 251–256] or bipartite measures well-suited for mixed states, as microscopic parties embedded in an environment must be described as open quantum systems [73, 219, 220, 257–269]. In this chapter we will adopt the latter approach, focusing on the entanglement between pairs of lattice sites., as we will show, in chapters 9 and 10, that this quantity is particularly sensitive to the onset of the Mott-Hubbard insulating state and the correlated pseudogap metal.

The key quantity for our analysis will be the quantum relative entropy (QRE) [270], a geometrical quantity akin to a pseudo-distance in the space of quantum states that is able to quantify and classify inter-orbital correlations, including quantum entanglement, in an elegant unified framework. We provide a brief summary of key results connecting the QRE with the notion of classical and quantum correlations in appendix A. In order to measure properly the entanglement within a pair of lattice sites, the QRE should be minimized with respect to the convex set of two-site separable states [270]. The resulting minimal "distance" between the given state and its closest separable relative is traditionally referred to as the relative entropy of entanglement (REE), and it quantifies in a rigorous way the bipartite entanglement between the two sites. It can be proven that the REE respects all the desired properties of a well-posed entanglement measure [247, 248], for the most generic mixed quantum states. In the following we will refer to this quantity simply as the two-site entanglement E_{ij} and recall explicitly the notion of REE only when strictly necessary to avoid confusion.

Provided that no simple parametrization for the set of two-site separable states is currently available [271], a closed expression for E_{ij} remains elusive [272] while a direct numerical

minimization has been proven to be a NP-complete problem [273]. Yet, lower bounds can be constructed by enforcing superselection rules (SSR) associated with conserved quantities [219, 220], as detailed in section 7.3. The importance of such restrictions to the set of *accessible* quantum states goes well beyond the need of an approximation for the unrestricted REE. In fact, the very definition of entanglement as a resource of the quantum world, crucially verges on the (im)possibility of preparing and manipulating some states by using only local operations and classical communication (LOCC). If there is a restriction on the allowed local operators (either fundamental or technological), no correlation associated to those physical observables would be detected, so the state would appear as effectively uncorrelated. Classical communication allows the extension of this concept to the set of separable (disentangled) states.[1] Hence, while in principle there might be more classical or quantum correlation in a given state, the enforcing of a carefully chosen superselection rule allows to estimate the operationally accessible portion of those correlations, at least within tradition quantum information protocols [274].

The relationship between the REE and other measures of entanglement, *e.g.* entanglement of formation, entanglement of distillation, entanglement cost, etc. are extensively discussed in Refs. [247, 248, 257, 259, 262, 263, 270, 275]. In particular, the notion of distillable entanglement can be formalized in the so-called positive partial transpose (PPT) criterion [67–69], allowing the definition of an upper bound for the two-site entanglement of distillation E_{ij}^{D}, not directly related to the geometrical notion of relative entropy of entanglement. This is possible thanks to the block-diagonal structure of the two-site reduced density matrix, in single-band models, as we dill discuss in detail in section 7.4.

In the following we describe the evaluation of all these entanglement and correlation measures, in terms of the ground state reduced density matrices for single- and two-orbital subsystems, as computed or measured within any theoretical or experimental method. The discussion about all the computational details that are specific to our numerical approach is deferred to chapter 8.

7.1 Single- and two-site von Neumann entropy

Let us consider the ground state density matrix ρ_{gs} for a model defined on a lattice $\mathcal{L}$. The reduced density matrix (RDM) for a subsystem A of the lattice $\mathcal{L}$ is defined as the trace over all the degrees of its complementary subsystem $\mathcal{L} \setminus \mathrm{A}$:

$$\rho_{\mathrm{A}} = \mathrm{tr}_{\bar{\mathrm{A}}} \left(\rho_{\mathrm{gs}} \right), \quad \bar{\mathrm{A}} = \mathcal{L} \setminus \mathrm{A}. \tag{7.1}$$

[1] A well-rounded discussion of these statements is given at the end of appendix A, after introducing the relevant geometrical concepts, *i.e.* a formal definition of the sets of uncorrelated and separable states.

Taking a single site i as the A subsystem, the von Neumann entropy of ρ_i is usually called *local entanglement entropy* [61–64, 70]

$$s_i = -\operatorname{tr}(\rho_i \log \rho_i). \tag{7.2}$$

For models in which a single site hosts only one orbital, the local entanglement entropy coincides with the single-orbital entropy defined in Eq. O.30, for the half-filled case. In the presence of doping, we would have a dependency also on the filling fraction δ_i, as evident from the application of Eq. 7.2 to the single-orbital expression of ρ_i, given in Eq. O.29.

If ρ_{gs} describes a pure state,[2] then s_i gives a well-defined measure of the bipartite entanglement between the single site and the surrounding lattice [70]. However, we stress that, being one of the entangled parties a macroscopic subsystem, this quantity includes quantum correlations for all the spatial ranges encoded in the model. In this sense, we believe that the name "local entanglement entropy" can be misleading, and we will limit its usage, in favor of single-site or single-orbital von Neumann entropy. Nevertheless, we note that s_i provides an upper bound to all local quantum and classical fluctuations, as we will demonstrate in the next section 7.2.

In a similar way, we can define a two-site von Neumann entropy from the RDM ρ_{ij} of two arbitrary sites, not necessarily neighbors or connected by any term in the Hamiltonian:

$$s_{ij} = -\operatorname{tr}(\rho_{ij} \log \rho_{ij}). \tag{7.3}$$

We indicate the particular case of nearest neighbors with the dedicated symbol $s_{\langle ij \rangle}$.
The two-site entanglement entropy s_{ij} shares most properties with s_i, being it a measure of the entanglement between a pair of sites and their environment, and –again– an upper bound to quantum and classical fluctuations in the two-site subsystem (see Sec. 7.2). However, differently from ρ_i (see Eq. O.29), the two-site RDM is not represented by a diagonal matrix even for Hubbard-like models with local interactions, so we cannot rule out *a priori* the presence of entanglement between its sub-parts. We will return to the matrix structure of ρ_{ij} later, to discuss the evaluation of *lower* bounds to the entanglement between site i and site j, with no reference to their environment.

7.2 Two-site mutual information

Given the entanglement entropies s_i and s_{ij}, respectively of a single- and a two-site subsystem, we can write the mutual information between the two sites as [70, 270]

$$I_{ij} = s_i + s_j - s_{ij}\,, \tag{7.4}$$

[2] *i.e.* if there is no ground state degeneracy, as single ground states can be proven to be extreme points of the set of all states [224] and extreme points are always pure (see appendix A)

reserving the symbol $I_{\langle ij\rangle}$ for the case of nearest neighbors. The mutual information I_{ij} gives a measure of all quantum and classical correlations between sites i and j. To elucidate this, let us rewrite explicitly the inequality in Eq. O.28, for the two-site bipartition

$$I_{ij} \geqslant \frac{\left(\langle \mathcal{O}_i \otimes \mathcal{O}_j \rangle_{\rho_{ij}} - \langle \mathcal{O}_i \rangle_{\rho_i} \langle \mathcal{O}_j \rangle_{\rho_j}\right)^2}{2\|\mathcal{O}_i\|^2 \|\mathcal{O}_j\|^2} \tag{7.5}$$

where $\mathcal{O}_i$ and $\mathcal{O}_j$ are generic operators acting on the Hilbert spaces of site i and site j, respectively, and $\|\square\|$ is the Euclidean operator norm. In virtue of Eq. 7.5, I_{ij} provides an explicit upper bound to all two-site correlation functions, hence quantifying the maximum correlation between site i and site j.

In appendix A we review an elegant geometrical rationale for this property, showcasing the derivation of two inequalities that relate the mutual information with suitable measures of classical and quantum correlation. In the two site setting they read as $I_{ij} \geqslant Q_{ij} \geqslant E_{ij}$ (Eq. A.17) and $I_{ij} \geqslant Q_{ij} + C_{ij}$ (Eq. A.21), where Q_{ij} is a measure of all quantum correlations (also those beyond entanglement) and C_{ij} is the corresponding measure of classical correlations. We observe that for pure composite systems (*e.g.* a pair of *isolated* sites at zero temperature and in absence of degeneracy), all correlations are fully determined by the REE ($Q_{ij} \equiv E_{ij}$). This is evident if we consider that a pure two-site state must have vanishing two-site von Neumann entropy ($s_{ij} = 0$), so we have that the two-site mutual information $I_{ij} = s_i + s_j$ gives a measure of the entanglement between the two sites $s_i = s_j$. If instead $s_{ij} \neq 0$, as it is generally the case in a condensed matter system, then ρ_{ij} describes a statistical mixture of pure quantum states and I_{ij} includes also the classical correlations arising from the correspondent probability distribution.

Another remarkable property of the two-site mutual information lies in the ability of detecting *area laws* [71, 228, 276–278] by means of a rigorous relationship with the decay rate of two-point correlations, as proposed by Wolf *et al.* [74] and recently confirmed in cold-atom experiments by Tajik *et al.* [245].

Finally, we point out that the *"diagonal"* mutual information I_{ii} (usually called *self-information*) coincides with the single-site entropy s_i (see Eq. 7.5 or Ref. [75] for a rigorous derivation). Consequently s_i bounds from above all the local fluctuations $\langle \mathcal{O}_i^2 \rangle_{\rho_i} - \langle \mathcal{O}_i \rangle_{\rho_i}^2$ encoded in ρ_i. More in general, the von Neumann entropy of a subsystem A always provides an upper bound for the quantum and classical fluctuations encoded in the corresponding state ρ_{A}, by virtue of Eq. O.28.

7.3 Lower bounds to the quasilocal entanglement from superselection rules

Since a closed mathematical expression for the two-site entanglement E_{ij}, as measured by the REE, is inaccessible and numerical minimization of the quantum relative entropy lies in the NP-complete class [273], we aim at characterizing E_{ij} by means of upper and lower bounds. As for the two-site entanglement entropy and mutual information, we will notate the special case of nearest neighbors with the symbol $E_{\langle ij \rangle}$.

As discussed above, the two-site mutual information I_{ij} clearly provides a rigorous and easy to compute upper bound to the two-site entanglement $E_{ij} \leqslant I_{ij}$. On the other hand, obtaining lower bounds to the entanglement of open systems, constitutes a nontrivial problem in quantum information theory [247]. Recently significant progress has been obtained by imposing the conservation of local quantities (either charge or parity) on all the physical density matrices of the entire open system and all the operators acting on the local Hilbert spaces of its subsystems [219, 269]. This restriction can be formulated in terms of suitable superselection rule (SSR), namely, generalizations of conventional selection rules that constrain the coherent superposition of states pertaining to different eigenvalues of selected local operators [279]. The relevance of local SSR in the definition of operationally accessible entanglement [215–218, 220, 236–242] has been recently challenged by new arguments in quantum thermodynamics [274], showcasing the consumption of SSR-forbidden entanglement in thermodynamic processes otherwise impossible for separable states. Here we do not contribute to this exciting scientific debate and just note that, notwithstanding their possible physical or operation interpretation, it can been shown that the parity superselection rule (P-SSR) and the charge superselection rule (N-SSR) allow for the definition of rigorous lower bounds to the two-site REE [219], in the form:

$$E_{ij}^{\text{N-SSR}} \leqslant E_{ij}^{\text{P-SSR}} \leqslant E_{ij} \, . \tag{7.6}$$

Before detailing their analytical expressions, in terms of the two-site reduced density matrix, we observe that the P-SSR and N-SSR can also be applied to the single-site entanglement E_i (measured exactly by the single-site von Neumann entropy s_i, in the absence of superselection rules) and the two-site mutual information I_{ij}, providing lower bounds to quantum and total correlations in the respective bipartitions [280]

$$E_i^{\text{N-SSR}} \leqslant E_i^{\text{P-SSR}} \leqslant E_i \equiv s_i \tag{7.7}$$

$$I_{ij}^{\text{N-SSR}} \leqslant I_{ij}^{\text{P-SSR}} \leqslant I_{ij} \tag{7.8}$$

In the following we report the explicit expressions for all these *superselected* measures of correlation and entanglement. In doing so, we will also comment on the matrix structure of the single-orbital and two-orbital density matrices, which has a crucial role in the construction of the two-site SSR formulas.

7.3.1 Superselected single-site entanglement

As already discussed in section O.5, the spin SU(2) and charge U(1) symmetries of the Hubbard model impose that the single site reduced density matrix ρ_i is diagonal in the Fock basis $|\bullet\rangle$, $|\uparrow\rangle$, $|\downarrow\rangle$, $|\uparrow\downarrow\rangle$, where the black dot represents an empty site:

$$\rho_i = \begin{pmatrix} \lambda_1 & 0 & 0 & 0 \\ 0 & \lambda_2 & 0 & 0 \\ 0 & 0 & \lambda_3 & 0 \\ 0 & 0 & 0 & \lambda_4 \end{pmatrix},$$

with $\lambda_1 = \langle (1-n_{i\uparrow})(1-n_{i\downarrow})\rangle$, $\lambda_2 = \langle n_{i\uparrow}(1-n_{i\downarrow})\rangle$, $\lambda_3 = \langle (1-n_{i\uparrow})n_{i\downarrow}\rangle$, $\lambda_4 = \langle n_{i\uparrow}n_{i\downarrow}\rangle$.

At zero temperature, in absence of degeneracies, the ground state of the full lattice is *pure* and can be written as the Schmidt decomposition

$$\begin{aligned} |\Psi_{\text{gs}}\rangle = \; & \sqrt{\lambda_1}\,|\bullet\rangle \;\otimes\; |N, M\rangle \;+ \\ & \sqrt{\lambda_2}\,|\uparrow\rangle \;\otimes\; |N-1, M-1/2\rangle \;+ \\ & \sqrt{\lambda_3}\,|\downarrow\rangle \;\otimes\; |N-1, M+1/2\rangle \;+ \\ & \sqrt{\lambda_4}\,|\uparrow\downarrow\rangle \otimes\; |N-2, M\rangle\,, \end{aligned}$$

where $|N, M\rangle$ represent a Fock state of N electrons and M magnetization, for the rest of lattice sites $j \neq i$. It is exactly the existence of a Schmidt decomposition that ensures that the entanglement between the single site i and the rest of the lattice $\{j \neq i\}$, which hereafter we will refer to as single-site entanglement E_i, is just given by the von Neumann entropy of ρ_i, namely

$$E_i \equiv s_i = -\operatorname{tr}(\rho_i \log \rho_i) = -\sum_n \lambda_n \log \lambda_n.$$

However, as soon as we consider a local superselection rule, namely a restriction on the allowed physical operators such that all of them must commute with a given local quantity $\mathcal{Q}_i$, the ground state Ψ_{gs} must be projected into the subspaces associated to the eigenvalues q_i of $\mathcal{Q}_i$, defining the *superselected* density matrix [73, 275, 280]

$$\rho_{\text{gs}}^{\mathcal{Q}\text{-SSR}} = \sum_{q_i} \mathcal{P}_{q_i}\, |\Psi_{\text{gs}}\rangle\langle\Psi_{\text{gs}}|\, \mathcal{P}_{q_i}.$$

In general, the sum defining $\rho_{\rm gs}^{\mathfrak{Q}\text{-SSR}}$ results in a mixed state, so that all its von Neumann reduced entropies (including the single-site one) are not legitimate measures of entanglement:

$$E_i^{\mathfrak{Q}\text{-SSR}} \neq -\operatorname{tr}(\rho_i^{\mathfrak{Q}\text{-SSR}} \log \rho_i^{\mathfrak{Q}\text{-SSR}}).$$

The single-site entanglement in a lattice that is globally in a mixed state can instead be measured by the REE and closed expression have been derived for the cases of $\mathfrak{Q}_i = N_i$ and $\mathfrak{Q}_i = P_i$ (where N_i is local electron number and P_i its parity) [280]:

$$E_i^{\text{N-SSR}} = (\lambda_2 + \lambda_3)\log(\lambda_2 + \lambda_3) - \lambda_2 \log \lambda_2 - \lambda_3 \log \lambda_3, \tag{7.9}$$

$$\begin{aligned} E_i^{\text{P-SSR}} = {} & (\lambda_1 + \lambda_4)\log(\lambda_1 + \lambda_4) + (\lambda_2 + \lambda_3)\log(\lambda_2 + \lambda_3) \\ & - \lambda_1 \log \lambda_1 - \lambda_2 \log \lambda_2 - \lambda_3 \log \lambda_3 - \lambda_4 \log \lambda_4. \end{aligned} \tag{7.10}$$

Remarkably, the λ_n entering the two expressions are the elements of the single-site local density matrix, as they are, since ρ_i is already diagonal on the N_i and P_i sectors. The full derivation of Eqs. 7.9 and 7.10 can be found in Ref. [280].

7.3.2 Superselected two-site entanglement

In this section we report some closed formulas for the two-site (two-orbital) relative entropy of entanglement under charge superselection rule and parity superselection rule, as originally derived by Ding *et al.* [219]. Given the complexity of a minimization over the set of separable states, which is equivalent to the formidable *separability problem* [271–273], these expressions hold only under the assumption of some key properties of the two-site state ρ_{ij}. Nevertheless, we can connect all these requirements to global symmetries of condensed matter systems, typically realized in low-energy states. Furthermore, all the requirements can be directly checked by inspecting selected matrix elements of ρ_{ij}, as we will point out through the text. The reader interested in the original derivations and a general discussion on the relevance of these superselected measures of the entanglement accessible in realistic quantum information processing on condensed matter systems, is strongly encouraged to approach references [219, 220].

Let us start by noting that, in analogy to Eq. 7.3.1, we can write the SSR-filtered reduced density matrix as

$$\rho_{ij}^{\mathfrak{Q}\text{-SSR}} = \sum_{q_i, q_j} \mathcal{P}_{q_i} \otimes \mathcal{P}_{q_j}\ \rho_{ij}\ \mathcal{P}_{q_i} \otimes \mathcal{P}_{q_j}\,, \tag{7.11}$$

where $\mathcal{P}_{q_i}$ and $\mathcal{P}_{q_j}$ are projectors on the single-site subspaces associated to the eigenvalues of the quantity $\mathfrak{Q}_i$. The action of Eq. 7.11 in our conventional basis for the two-site Fock space (Table 7.1) is illustrated in Fig. 7.1, for the cases of $\mathfrak{Q}_i = N_i$ and $\mathfrak{Q}_i = P_i$.

n	$\vert\Psi_n^{\uparrow}\rangle \otimes \vert\Psi_n^{\downarrow}\rangle$	n	$\vert\Psi_n^{\uparrow}\rangle \otimes \vert\Psi_n^{\downarrow}\rangle$	n	$\vert\Psi_n^{\uparrow}\rangle \otimes \vert\Psi_n^{\downarrow}\rangle$	n	$\vert\Psi_n^{\uparrow}\rangle \otimes \vert\Psi_n^{\downarrow}\rangle$
1	$\vert\bullet\,\bullet\rangle \otimes \vert\bullet\,\bullet\rangle$	5	$\vert\bullet\,\bullet\rangle \otimes \vert\downarrow\,\bullet\rangle$	9	$\vert\bullet\,\bullet\rangle \otimes \vert\bullet\,\downarrow\rangle$	13	$\vert\bullet\,\bullet\rangle \otimes \vert\downarrow\,\downarrow\rangle$
2	$\vert\uparrow\,\bullet\rangle \otimes \vert\bullet\,\bullet\rangle$	6	$\vert\uparrow\,\bullet\rangle \otimes \vert\downarrow\,\bullet\rangle$	10	$\vert\uparrow\,\bullet\rangle \otimes \vert\bullet\,\downarrow\rangle$	14	$\vert\uparrow\,\bullet\rangle \otimes \vert\downarrow\,\downarrow\rangle$
3	$\vert\bullet\,\uparrow\rangle \otimes \vert\bullet\,\bullet\rangle$	7	$\vert\bullet\,\uparrow\rangle \otimes \vert\downarrow\,\bullet\rangle$	11	$\vert\bullet\,\uparrow\rangle \otimes \vert\bullet\,\downarrow\rangle$	15	$\vert\bullet\,\uparrow\rangle \otimes \vert\downarrow\,\downarrow\rangle$
4	$\vert\uparrow\,\uparrow\rangle \otimes \vert\bullet\,\bullet\rangle$	8	$\vert\uparrow\,\uparrow\rangle \otimes \vert\downarrow\,\bullet\rangle$	12	$\vert\uparrow\,\uparrow\rangle \otimes \vert\bullet\,\downarrow\rangle$	16	$\vert\uparrow\,\uparrow\rangle \otimes \vert\downarrow\,\downarrow\rangle$

Tab. 7.1.: Basis for the two-site Fock space $\mathbb{F}_{ij}$. The indices n of the quantum states $|\Psi_n\rangle = |\Psi_n^{\uparrow}\rangle \otimes |\Psi_n^{\downarrow}\rangle$ define our conventional labeling for the matrix elements λ_{nm} of the reduced density matrix for the two-site subsystem. Black dots ($\bullet$) represent empty lattice sites.

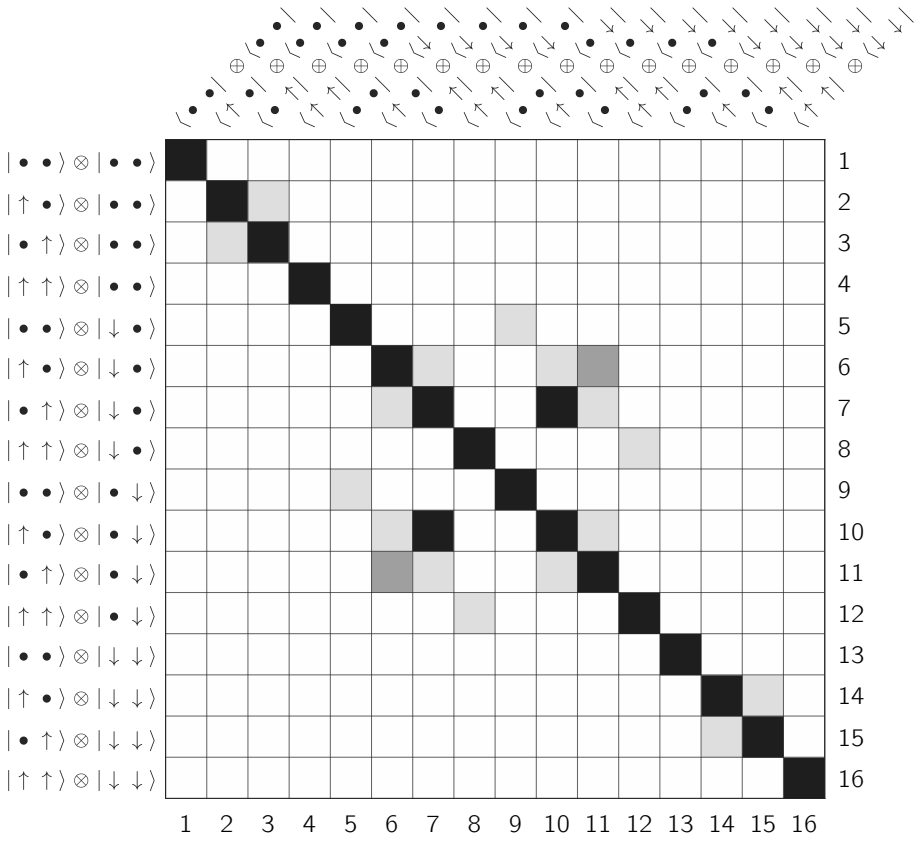


Fig. 7.1.: Representation of the two-site reduced density matrix ρ_{ij}, in the $|\Psi_n^{\uparrow}\rangle \otimes |\Psi_n^{\downarrow}\rangle$ basis. Most entries vanish (white) due to the spin and charge symmetries of the Hubbard model [281]. Superselecting for the local electron parity (P-SSR) sets all light-shaded entries to zero, while the charge superselection rule (N-SSR) removes the remaining local density fluctuations (dark-shaded entries). Black elements are always preserved.

Given that both $\rho_{ij}^{\text{N-SSR}}$ and $\rho_{ij}^{\text{P-SSR}}$ are block-diagonal (with respect to the bipartition of interest into sites i and j) we can apply the famous positive partial transpose (PPT) criterion to characterize the set of two-site separable states. In its orginal formulation, due to Peres and the Horodecki [67, 68], the PPT criterion gives a necessary condition for separability in systems of two *distinguishable* parts. The condition is sufficient only for Hilbert spaces of dimension $d(\text{AB}) = d(\text{A}) \times d(\text{B}) \leqslant 2 \times 3$. At first sight, the two-orbital[3] system described by ρ_{ij} appears to satisfy the dimensional condition, with $d_{ij} = 2 \times 2$. However, the indistinguishability of Fermions forces us to consider the bipartition into single-particle states (orbitals), hence adopting the formalism of second quantization, with an enlargement of the dimension of the states from the two-orbital Hilbert space, to the two-orbital Fock space, with dimension $d_{\text{Fock}} = 4 \times 4$. Here the block-diagonal structure of the ρ_{ij} and its superselected relatives comes to help, as we can effectively formulate the PPT criterion on each block, and get a necessary and sufficient condition for the separability of the whole ρ_{ij}.

We can write the most general ρ_{ij}, as

$$\rho_{ij} = \sum_{\Psi_n^i} \sum_{\Psi_m^i} \sum_{\Psi_n^j} \sum_{\Psi_m^j} \left\langle \Psi_n^i \Psi_n^j \middle| \rho_{ij} \middle| \Psi_m^i \Psi_m^j \right\rangle \left| \Psi_n^i \middle\rangle\middle\langle \Psi_m^i \right| \otimes \left| \Psi_n^j \middle\rangle\middle\langle \Psi_m^j \right| , \tag{7.12}$$

where Ψ_n^i and Ψ_m^j represent, respectively the n-th state of site i and the m-th state of site j. All these states live in the Fock space spanned by $\{ |\bullet\rangle, |\uparrow\rangle, |\downarrow\rangle, |\uparrow\downarrow\rangle \}$, but we can restrict Eq. 7.12 to any one of the sectors identified by the two-site particle number and the two-site magnetization. The *partial transpose* of ρ_{ij}, with respect to site j is given as

$$\begin{aligned} \rho_{ij}^{\mathsf{T}_j} &= \sum_{\Psi_n^i} \sum_{\Psi_m^i} \sum_{\Psi_n^j} \sum_{\Psi_m^j} \left\langle \Psi_n^i \Psi_n^j \middle| \rho_{ij} \middle| \Psi_m^i \Psi_m^j \right\rangle \left| \Psi_n^i \middle\rangle\middle\langle \Psi_m^i \right| \otimes \left(\left| \Psi_n^j \middle\rangle\middle\langle \Psi_m^j \right| \right)^{\mathsf{T}} \\ &= \sum_{\Psi_n^i} \sum_{\Psi_m^i} \sum_{\Psi_n^j} \sum_{\Psi_m^j} \left\langle \Psi_n^i \Psi_{\color{magenta}m}^j \middle| \rho_{ij} \middle| \Psi_m^i \Psi_{\color{magenta}n}^j \right\rangle \left| \Psi_n^i \middle\rangle\middle\langle \Psi_m^i \right| \otimes \left| \Psi_n^j \middle\rangle\middle\langle \Psi_m^j \right| , \end{aligned} \tag{7.13}$$

where we have used color to highlight the action of the transposition on the j-subspace. The PPT criterion then ensures that the state ρ_{ij} is separable with respect to the i/j bipartition if and only if $\rho_{ij}^{\mathsf{T}_j}$ has no negative eigenvalues. We observe that the operation in Eq. 7.13 is symmetric, with respect to the separability criterion, as $\rho_{ij}^{\mathsf{T}_j} = [\rho_{ij}^{\mathsf{T}_i}]^{\mathsf{T}}$ and the full transposition preserves the spectrum.

Let us now consider the N-SSR or P-SSR constrained two-site reduced density matrices. The effect of the two superselection rule is to suppress all matrix elements that do not preserve the single-site electron number and its parity. Hence, the only elements that are not invariant under the partial transposition of Eq. 7.13, are those connecting the states in $\{ |\Psi_7\rangle, |\Psi_{10}\rangle \}$ and $\{ |\Psi_6\rangle, |\Psi_{11}\rangle \}$ (see Table 7.1). This implies that the only subspaces in

[3] recall that we are considering systems with one orbital per site

which all the superselected two-site entanglement is developed, are those containing those states, namely $\mathbb{S} = \text{Span}\{\,|\Psi_4\rangle,\ |\Psi_7\rangle,\ |\Psi_{10}\rangle,\ |\Psi_{13}\rangle\,\}$ and $\mathbb{S}' = \text{Span}\{\,|\Psi_1\rangle,\ |\Psi_6\rangle,\ |\Psi_{11}\rangle,\ |\Psi_{16}\rangle\,\}$, corresponding respectively to the conditions $(P_i, P_i) = (\text{even}, \text{even})$, enforced by the P-SSR, and $(N_i, N_j) = (1, 1)$, which is enforced by both P-SSR and N-SSR.

Here we introduce the stronger restriction on the symmetry of ρ_{ij}, that finally leads to a viable minimization of the quantum relative entropy (QRE) defining the measure of entanglement. We assume the two sites i and j to be symmetric in the ρ_{ij} state. In particular, for the subspaces of interest, we have: $\langle\Psi_7|\rho_{ij}|\Psi_7\rangle = \langle\Psi_{10}|\rho_{ij}|\Psi_{10}\rangle$ and $\langle\Psi_6|\rho_{ij}|\Psi_6\rangle = \langle\Psi_{11}|\rho_{ij}|\Psi_{11}\rangle$. Unfortunately this rules out *a priori* the usage of the resulting closed formulas for any state that breaks translational symmetry, as in presence of disorder, antiferromagnetic order or charge density waves.[4]

At this point, we can define the following *probabilities*:

$$
\begin{aligned}
&\lambda_1 = \langle\Psi_1|\rho_{ij}|\Psi_1\rangle\,,\\
&\lambda_4 = \langle\Psi_4|\rho_{ij}|\Psi_4\rangle\,,\\
&\begin{pmatrix}\lambda_6 & 0\\ 0 & \lambda_{11}\end{pmatrix} = R^\dagger \begin{pmatrix}\langle\Psi_6|\rho_{ij}|\Psi_6\rangle & \langle\Psi_6|\rho_{ij}|\Psi_{11}\rangle\\ \langle\Psi_{11}|\rho_{ij}|\Psi_6\rangle & \langle\Psi_{11}|\rho_{ij}|\Psi_{11}\rangle\end{pmatrix} R,\\
&\begin{pmatrix}\lambda_7 & 0\\ 0 & \lambda_{10}\end{pmatrix} = R^\dagger \begin{pmatrix}\langle\Psi_7|\rho_{ij}|\Psi_7\rangle & \langle\Psi_7|\rho_{ij}|\Psi_{10}\rangle\\ \langle\Psi_{10}|\rho_{ij}|\Psi_7\rangle & \langle\Psi_{10}|\rho_{ij}|\Psi_{10}\rangle\end{pmatrix} R,\\
&\lambda_{13} = \langle\Psi_{13}|\rho_{ij}|\Psi_{13}\rangle\,,\\
&\lambda_{16} = \langle\Psi_{13}|\rho_{ij}|\Psi_{16}\rangle\,,\\
&\text{with}\ \ R = \begin{pmatrix}1 & -1\\ 1 & +1\end{pmatrix} \times \frac{1}{\sqrt{2}}.
\end{aligned}
$$

To build the N-SSR and P-SSR constrained measures of entanglement we further define the following auxiliary quantities:

$$
\begin{aligned}
\mu_7 = \frac{b_1 + c_1 + \sqrt{d_1}}{4(a_1 - \nu_{10})},\ \mu_{10} = \frac{b_1 - c_1 - \sqrt{d_1}}{4(a_1 - \nu_7)},\ \mu_6 = \frac{b_2 + c_2 + \sqrt{d_2}}{4(a_2 - \nu_{11})},\ \mu_{11} = \frac{b_2 - c_2 - \sqrt{d_2}}{4(a_2 - \nu_6)},\\
\mu_4 = \lambda_4 + \frac{\nu_7 + \nu_{10} - \mu_7 - \mu_{10}}{2},\quad \mu_{13} = \lambda_{13} + \frac{\nu_7 + \nu_{10} - \mu_7 - \mu_{10}}{2},\\
\mu_1 = \lambda_1 + \frac{\nu_6 + \nu_{11} - \mu_6 - \mu_{11}}{2},\quad \mu_{16} = \lambda_{16} + \frac{\nu_6 + \nu_{11} - \mu_6 - \mu_{11}}{2},
\end{aligned}
$$

[4] Further, any extension to multi-orbital systems has to be constructed with great care, ensuring to never mix orbitals with different character.

where we have

$$\nu_7 = \max(\lambda_7, \lambda_{10}), \quad \nu_{10} = \min(\lambda_7, \lambda_{10}),$$
$$\nu_6 = \max(\lambda_6, \lambda_{11}), \quad \nu_{11} = \min(\lambda_6, \lambda_{11}),$$
$$a_1 = \nu_7 + \nu_{10} + \lambda_4 + \lambda_{13}, \quad b_1 = a_1^2 - (\lambda_4 - \lambda_{13})^2, \quad c_1 = (\nu_7 - \nu_{10})a_1,$$
$$a_2 = \lambda_1 + \nu_6 + \nu_{11} + \lambda_{16}, \quad b_2 = a_2^2 - (\lambda_1 - \lambda_{16})^2, \quad c_2 = (\nu_6 - \nu_{11})a_2,$$
$$d_1 = (\lambda_4 + \lambda_{13})^2(\nu_7 - \nu_{10})^2 + 8\lambda_4\lambda_{13}(2\lambda_4\lambda_{13} + (\lambda_4 + \lambda_{13})(\nu_7 - \nu_{10}) + 2\nu_7\nu_{10}),$$
$$d_2 = (\lambda_1 + \lambda_{16})^2(\nu_6 - \nu_{11})^2 + 8\lambda_1\lambda_{16}(2\lambda_1\lambda_{16} + (\lambda_1 + \lambda_{16})(\nu_6 - \nu_{11}) + 2\nu_6\nu_{11}).$$

Finally the charge superselection rule (N-SSR) and parity superselection rule (P-SSR) entanglement measures are given as classical[5] relative entropies [219]:

$$E_{ij}^{\text{N-SSR}} = \sum_{n\in\mathbb{S}} \lambda_n \log \frac{\lambda_n}{\mu_n}, \quad E_{ij}^{\text{P-SSR}} = E_{ij}^{\text{N-SSR}} + \sum_{n\in\mathbb{S}'} \lambda_n \log \frac{\lambda_n}{\mu_n} \tag{7.14}$$

If we finally impose $\lambda_1 = \lambda_{16}$ which follows from particle-hole symmetry and $\lambda_4 = \lambda_{13}$ which is instead the condition for a singlet ground state, we obtain a valuable simplification of the two expressions in Eq. 7.14:

$$E_{ij}^{\text{N-SSR}} = \left[r \log\left(\frac{2r}{r+t}\right) + t \log\left(\frac{2t}{r+t}\right)\right], \tag{7.15}$$

$$E_{ij}^{\text{P-SSR}} = E_{ij}^{\text{N-SSR}} + \left[s \log\left(\frac{2s}{s+\tau}\right) + \tau \log\left(\frac{2\tau}{s+\tau}\right)\right], \tag{7.16}$$

where r, t, s, τ are defined as

$$t = \nu_7, \quad r = \nu_{10} + \lambda_4 + \lambda_{13}, \quad \tau = \nu_6, \quad s = \nu_{11} + \lambda_1 + \lambda_{16}.$$

We note that Eqs. 7.14, 7.15 and 7.16 require a check against the Peres-Horodecki separability criterion in the $\mathbb{S}$ and $\mathbb{S}'$ subspaces: applying them to PPT-separable states may result in a false finite value for $E_{ij}^{\text{N-SSR}}$ or $E_{ij}^{\text{P-SSR}}$. Finally, we highlight that Eqs. 7.15 and 7.16 differ for a term depending on τ and s alone, and so involve only diagonal occupations of pairs of *doublon* and *holon* states. Since both of them are gradually suppressed across the Mott-Hubbard transition (in order to have a half-filled insulator the number of doublons and holons has to coincide and eventually vanish, deep in the Mott state), one would expect the two superselected measures of two-site entanglement to be asymptotically indistinguishable in a Mott insulator. We anticipate here that this result is indeed found in our calculations [3] and that the related discussion is reported in chapter 9.

[5] The assumption of equivalent orbitals ensures that ρ_{ij} and its closest separable state are diagonal on the same basis, so that $\{\mu_i\}$ defines the spectrum of such state, on the subspaces that were not separable already. Elsewhere $\mu_i \equiv \lambda_i$, giving no contribution to the relative entropy.

7.3.3 Superselected two-site correlations

In this section we describe the application of the charge and parity superselection rule to filter the total (quantum and classical) correlations. This would allow us to analyze the effect of the restrictions on a quantity that we can easily compute in the absence of the SSR. Let us consider again a two-site subsystem, described by the ρ_{ij} reduced density matrix. As discussed at length in section 7.3.2, the spin SU(2) and charge U(1) symmetries of the Hubbard model disallow all fluctuations in the two-site charge and magnetization in ρ_{ij}, leading to the form illustrated in Fig. 7.1 [65, 281]. If we consider a bipartition of ρ_{ij} into single sites, the enforcement of the charge superselection rule (N-SSR) amounts to forbidding all changes in the single-site charge, while the parity superselection rule (P-SSR) allows only the charge fluctuations that preserve the parity of the local particle number N_i. Local spin-flips survive both superselection rules, as they commute with N_i [280].

Once either the charge or the parity SSR filtering is applied on ρ_{ij}, the superselected measures of the total correlation (see appendix A for a discussion of the term) between the two sites is just given by the two-site mutual information between, evaluated on the filtered ρ_{ij}. To be more explicit, if we write the von Neumann entropy of a generic density matrix ρ with the functional notation $s\{\rho\}$, we have

$$I_{ij}^{\text{N-SSR}} = s\Big\{\rho_i\Big\} + s\Big\{\rho_j\Big\} - s\Big\{\rho_{ij}^{\text{N-SSR}}\Big\}, \tag{7.17}$$

$$I_{ij}^{\text{P-SSR}} = s\Big\{\rho_i\Big\} + s\Big\{\rho_j\Big\} - s\Big\{\rho_{ij}^{\text{P-SSR}}\Big\}. \tag{7.18}$$

We stress that the single-site RDM, as computed from ρ_{ij} via the usual partial trace, are insensitive to the N-SSR and P-SSR filtering, once again because they are diagonal on the charge sectors. For this reason they are not superscripted in Eqs. 7.17 and 7.18.

7.4 Distillable entanglement and the two-site logarithmic negativity

In section 7.3.2 we have discussed how the positive partial transpose (PPT) separability criterion, which is in principle only a necessary condition for two-orbital fermionic systems, becomes also sufficient in virtue of the SU(2) and U(1) symmetries of the single-band Hubbard model, as can be seen by decomposing the two-site reduced density matrix in charge and magnetization sectors. In these conditions, one can obtain a relatively good measure of entanglement by a simple and direct quantification of how much the given state ρ_{ij} violates the PPT criterion.

In practice one can sum the negative eigenvalues of the partial transpose $\rho_{ij}^{\mathsf{T}_j}$ and already obtain a fair measure of entanglement, that does not increase under LOCC [282]. If one further defines the *logarithmic* negativity as [247, 283]

$$\mathcal{n}_{ij} = \log\left(1 + \sum_k \left|\lambda_k^{\mathsf{T}}\right| - \lambda_k^{\mathsf{T}}\right), \tag{7.19}$$

where λ_k^{T} are the eigenvalues of $\rho_{ij}^{\mathsf{T}_j}$, one obtains a rigorous upper bound to the distillable entanglement E_{ij}^{D}, namely, if one express Eq. 7.19 in bits (units of log(2)), it is always larger or equal to the portion of pure Bell pairs (singlet states) that can be extracted from n copies of the given (two-site, in our case) state. Unfortunately, $\mathcal{n}_{ij}$, that hereafter we will call simply as two-site negativity, is a strict upper bound to the purification ratio, in the sense that it does not recover the correct value for pure states (which instead is given by the von Neumann entropy of ρ_{ij}, or any other measure that coalesces to the von Neumann entropy in the limit of zero classical correlations).

Observing that the distillable entanglement is always lower or equal than the relative entropy of entanglement (REE) $E_{ij}^{\mathsf{D}} \leqslant E_{ij}^{\mathsf{REE}}$ [247, 248, 270], we cannot leverage the two-site negativity as a rigorous upper bound to the two-site entanglement, at least in the geometrical framework provided by the quantum relative entropy (for us $E_{ij}^{\mathsf{REE}} \equiv E_{ij}$). Nevertheless, it can be surely compared with our upper and lower bounds for the REE, providing additional validation and insight into our results for the two-site entanglement in the two-dimensional Hubbard model.

Before ending the section, we observe that even if the case of our interest (entanglement between two-sites in a single-band Hubbard model) escapes the failure of the PPT criterion, the possibility of a vanishing negativity for a separable state is very relevant for great multitude of open quantum systems. In that case, it has been shown that the negativity is still an upper bound to the distillable entanglement and it is this quantity that vanish for a certain classes of states. The amount of entanglement that cannot be purified, yet is present in the given (mixed)[6] quantum state, is often called *bound* entanglement [284]. For some fermionic systems, bound entanglement is typically present, invalidating the use of the logarithmic negativity as tool for the study of quantum criticality or topological order. This is the case *e.g.* of the failure of the PPT to detect the edge Majorana states in the Kitaev chain [264]. Some proposals to substitute the partial transpose with different transformations that do not preserve the spectrum of the state have been proposed in recent years [264–267], with a great degree of success. Nevertheless, bound entanglement cannot exist in density matrices with dimension $d < 6$, as proven by the necessary version of the PPT criterion [68], so we will not explore further the matter, given our interest in subspaces of dimension $d_{\mathsf{sub}} \leqslant 4$, as can be checked by inspecting Fig. 7.1.

[6] The PPT criterion does not ever fail for pure states

7.4.1 Superselected two-site negativity

In complete analogy to the case of total correlations (see section 7.3.3), we can define SSR-restricted two-site negativities, by applying its definition (Eq. 7.19), to the SSR-filtered RDM, as given in Eq. 7.11 and illustrated in Fig. 7.1. In practice, one first filters ρ_{ij}, according to the selected superselection rule, then rotates the Fock basis as to allow an easy implementation of the partial transpose. Finally one diagonalizes the resulting matrix and feeds the spectrum to Eq. 7.19. This approach can be fruitfully related to the concept of symmetry-resolved negativity [267, 285–289] and, within our program, will be used to further explore the role of the superselection rules in modifying the structure and correlation properties of the two-site reduced density matrix. In section 9.4 we will see how the resulting discussion indeed shades some significant light on the degree of influence we can attribute to the superselection rules in defining the observed entanglement features of the Mott-Hubbard transition.

7.5 Summary of nonlocal correlation measures

For ease of reference, here we provide a concise summary of all the correlation and entanglement markers we analyzed throughout this chapter spelling out their definition, the information they measure and their role to bound other markers from above or below. We remind that all these results assume zero temperature.

Marker		What it measures	What it bounds
Single-site entanglement entropy (7.2)	s_i	Entanglement between a single site i and the rest of the lattice, for pure ground states	All fluctuations on the site i [from above]
Single-site entanglement under charge SSR (7.9)	$E_i^{\text{N-SSR}}$	Accessible entanglement between a single site i and the rest of the lattice, within operations that conserve the local charge N_i	Entanglement between a single site i and the rest of the lattice, for all ground states [from below]
Single-site entanglement under parity SSR (7.10)	$E_i^{\text{P-SSR}}$	Accessible entanglement between a single site i and the rest of the lattice, within operations that conserve the parity of the local electron number N_i	Entanglement between a single site i and the rest of the lattice, for all ground states [from below]

Marker		What it measures	What it bounds
Two-site entanglement entropy (7.3)	s_{ij}	Entanglement between the two sites (i,j) and the rest of the lattice, for pure ground states	All fluctuations on the two sites (i,j) [from above]
Two-site mutual information (7.4)	I_{ij}	Total correlation between the two sites i and j	The entanglement between i and j, as well as any two-site correlator [from above]
Two-site mutual information under charge SSR (7.17)	$I_{ij}^{\text{N-SSR}}$	Accessible correlation between the two sites i and j, within operations that conserve the local charge N_i	The two-site mutual information I_{ij} [from below]
Two-site mutual information under parity SSR (7.18)	$I_{ij}^{\text{P-SSR}}$	Accessible correlation between the two sites i and j, within operations that conserve the parity of the local electron number N_i	The two-site mutual information I_{ij} [from below]
Two-site entanglement under charge SSR (7.15)	$E_{ij}^{\text{N-SSR}}$	Accessible entanglement between i and j, within operations that conserve the local charge N_i	The entanglement between i and j. [from below]
Two-site entanglement under parity SSR (7.16)	$E_{ij}^{\text{P-SSR}}$	Accessible entanglement between i and j, within operations that conserve the parity of the local electron number N_i	The entanglement between i and j. [from below]
Two-site logarithmic negativity (7.19)	n_{ij}	—	The distillable entanglement between i and j. [from above]

8 Cellular extension of dynamical mean-field theory (CDMFT)

A variety of complementary and competing approaches have been devised to extend the dynamical mean-field theory in order to include nonlocal correlations of different kind. A well-defined class of methods are *cluster* extensions of DMFT, where the role of the impurity site is taken by a finite cluster. Hence short-range correlations within the cluster are treated in their full dynamical nature [189, 229–232, 290].

Other approaches aim to include dynamical correlations without the limitations of a cluster. Among them we can mention *fluctuating field* methods [291–293] and *diagrammatic* expansions around DMFT [293–295], such as *GW*+DMFT [296], dual particles [297, 298], the dynamical vertex approximation (DΓA) [299], the triply irreducible local expansion (TRILEX) [300, 301] and its dual extension [302, 303], and the single-boson exchange approximation [304]. In principle, these techniques take into account the nonlocal correlations at all spatial ranges.

Obviously a complementary information to dynamical mean-field theory (DMFT) can be achieved with methods that provide a numerical solution of the models on finite systems, ranging from quantum Monte Carlo (QMC) schemes and tensor network extensions of the density matrix renormalization group (DMRG), whose combination has proven extremely fruitful for the investigation of complex long-range ordered phases [305–307]. For the strongly correlated paramagnetic regime at intermediate coupling, however, and despite considerable progress in recent years, there is still no complete picture of the nonlocal physics of even single-orbital models with local interaction.

In this chapter we will focus an a well-known and successful cluster extension of the dynamical mean-field theory, traditionally referred to as *cellular* DMFT (or just cluster dynamical mean-field theory, CDMFT), which has proven to provide a reliable account of the interaction-driven and density-driven Mott transitions in low-dimensional systems [145, 146, 167, 198, 229–232, 290, 308, 309]. First, we introduce the essential concepts, with a focus on the main differences and on the complications introduced with respect to single-site DMFT. Then we briefly review the role of cluster dynamical mean-field theory in enriching the description of the Mott-Hubbard transition, in the square lattice. Finally we delve into some implementation details of our calculations, including the evaluation of the single-site and two-site reduced density matrices that constitute a novel feature and the key ingredient for our analysis of the quasilocal entanglement in Mott insulators and pseudogap metals, as described in chapters 9 and 10.

8.1 Tiling the lattice

The auxiliary model that defines the cluster dynamical mean-field theory approximation features a cluster of N_{imp} impurity sites, arranged in a geometry compatible with the tiling of the original lattice. The hopping structure and interaction inside these cluster-impurities is described by the lattice Hamiltonian, restricted to the cluster sites. For the single-orbital Hubbard model we then have (see Eq. O.6):

$$\mathbf{H}_{\text{imp}} = -t \sum_{\sigma} \sum_{\langle ij \rangle = 1}^{N_{\text{imp}}} \left(c_{i\sigma}^{\dagger} c_{j\sigma} + \text{h.c.} \right) + U \sum_{i=1}^{N_{\text{imp}}} n_{i\uparrow} n_{i\downarrow} - \mu \sum_{\sigma} \sum_{i=1}^{N_{\text{imp}}} n_{i\sigma} \tag{8.1}$$

As for the case of single-site DMFT (see section O.3), the resulting cluster-impurity is connected to a dynamical bath (described by a frequency-dependent Weiss field) and the resulting embedding Hamiltonian is solved in open boundary conditions.[1]

The extension of the DMFT embedding to a cluster of impurities, promotes the dynamical Weiss field, the impurity self-energy and the local Green's function to a $N_{\text{imp}} \times N_{\text{imp}}$ matrix structure, as they explicitly depend on the real-space degrees of freedom of the cluster. In particular, given an impurity self-energy $\mathbf{\Sigma}_{\text{imp}}(z)$, the local Green's function is obtained as

$$\mathbf{G}_{\text{loc}}(z) = \frac{1}{N_{\boldsymbol{k}}} \sum_{\boldsymbol{k}} \big(z + \mu - \mathbf{H}(\boldsymbol{k}) - \mathbf{\Sigma}_{\text{imp}}(z) \big)^{-1} \tag{8.2}$$

where the crystalline momentum $\boldsymbol{k}$ and the reciprocal one-body Hamiltonian $\mathbf{H}(\boldsymbol{k})$ must be defined in the so-called *reduced* Brillouin zone, generated by the tiling of the original lattice with $n \to \infty$ copies of the cluster [189]. To illustrate the procedure, we consider the simplest case of a linear chain tiled by two-site clusters. The original noninteracting lattice Hamiltonian, considering a tight-binding approximation involving only the nearest-neighbor hopping, is given by $H(k) = -2t \cos(ka)$, where a is the lattice spacing and k spans the entire Brillouin zone $k \in [-\pi/a, \pi/a]$. To describe a tiling of the chain into two-site clusters, we can rewrite the Hamiltonian considering a two-site unit cell

$$\mathbf{H}(k) = \begin{pmatrix} 0 & -t(1 + \mathrm{e}^{-i2k}) \\ -t(1 + \mathrm{e}^{+i2k}) & 0 \end{pmatrix},$$

where the restriction of $k \in [-\pi/(2a), \pi/(2a)]$, defines the reduced Brillouin zone [7, 8].

[1] An alternative scheme, involving the solution of the embedded cluster in periodic boundary conditions has been extensively explored, under the name of dynamical cluster approximation (DCA). A review of these two alternative cluster extensions of DMFT and a comparison with other quantum cluster theories can be found in Ref. [189].

In general, for a d-dimensional hyper-cubic lattice we can always define a tiling in clusters of shape $N_1 \times \cdots \times N_d$, reducing the Brillouin zone in all directions k_i, by a factor of N_i. The $d = 2$ case, defining the square lattice, is illustrated in the left panel of Fig. 8.1, for a cluster of shape 2×2.

Once this *cluster-superlattice* mixed representation is defined, in terms of real-space matrices for the cluster degrees of freedom and reduced crystalline momentum vectors for the inter-cluster band structure, the CDMFT self-consistency condition results as a direct generalization of the single-site theory: $\mathbf{G}_{\text{loc}}(i\omega_n) \equiv \mathbf{G}_{\text{imp}}(i\omega_n)$.

8.2 Bath optimization to enforce the self-consistency

In principle, on implementations relying on a discretized bath, the iterative procedure to obtain a Hamiltonian for the bath that satisfies the self-consistency condition is directly extended from the single-site case, exploiting the cluster-superlattice mixed representation described above. Yet, the optimization of the bath becomes significantly more delicate, essentially for two independent reasons:

1. the Green's functions and self-energies of the embedded interacting cluster must not artificially break the symmetries of the original lattice (or those remaining after some symmetry is spontaneously broken), which implies that the bath parameters must respect these symmetries, resulting in a highly constrained search for the optimal bath configuration.

2. the off-diagonal components of the hybridization function, and consequently of the Weiss field are not normalized and can in practice be of a completely different order of magnitude with respect to the diagonal part. This means that our optimization has to treat very different objects at the same time.

There are several strategies to alleviate the first point. One can explicitly take into account the desired symmetries of the cluster and generate the bath parametrization by leveraging the irreducible representations of the corresponding point group [310] or, equivalently, one can group the bath sites into noninteracting *replicas* of the cluster-impurity, suppressing all the hybridization amplitudes that do not connect the sites with the same index $i = 1, \ldots, N_{\text{imp}}$ (see the schematic representation in the right panel of Fig. 8.1). The bath Hamiltonian is then given as a sum over the replica index $r = 1, \ldots, N_{\text{repl}}$ of the one-body Hamiltonian of the cluster, where the relevant physical terms (*e.g.* the hopping and the chemical potential, for the simple case of the single-orbital Hubbard model) are

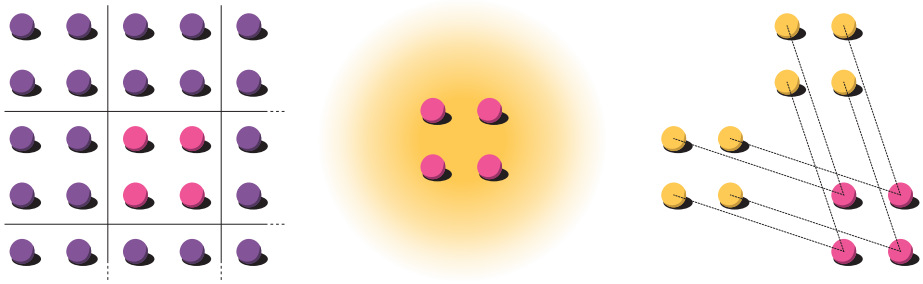


Fig. 8.1.: Schematic representation of the cellular extension of dynamical mean-field theory. On the left we highlight a 2×2 *plaquette* in a square lattice, defining the enlarged unit-cell for the periodic tiling. The middle panel represents the embedding of the interacting plaquette in a dynamical bath, defining the CDMFT mapping to an effective cluster impurity problem. On the right we give a scheme of the *replica* parametrization of the dynamical bath, where the impurity plaquette is connected to its noninteracting replicas by the impurity-bath hybridization amplitudes, represented by dashed lines. The one-body Hamiltonian of the replicas and the hybridization amplitudes are jointly optimized to satisfy the self-consistency condition $\mathbf{G}_{\mathrm{loc}}(i\omega_n) = \mathbf{G}_{\mathrm{imp}}(i\omega_n)$.

made replica-dependent and, together with the $V(i,r)$ hybridization amplitudes[2], constitute the parameters to optimize:

$$\mathbf{H}_{\mathrm{bath}} = \sum_{r=1}^{N_{\mathrm{repl}}} \left(-\lambda_t(r) \sum_{\sigma} \sum_{\langle ij \rangle = 1}^{N_{\mathrm{imp}}} \left(b^{\dagger}_{i\sigma} b_{j\sigma} + \mathrm{h.c.} \right) - \lambda_{\mu}(r) \sum_{\sigma} \sum_{i=1}^{N_{\mathrm{imp}}} b^{\dagger}_{i\sigma} b_{i\sigma} \right) . \tag{8.3}$$

We observe that Eq. 8.3 features a *paramagnetic constraint*, as the two spin polarizations are controlled by the same bath parameters and there is no freedom to develop spin-dependent features in the effective impurity problem. In our calculation, this choice has the crucial role of preventing magnetic ordering, so to allow the study the pure paramagnetic Mott-Hubbard transition at zero temperature. If one is instead interested in studying a magnetically active system, as *e.g.* a Mott-Heisenberg insulator, the constraint can be easily removed by doubling the the number of optimization parameters and letting them depend on the spin polarization: $\{\lambda_t(r), \lambda_{\mu}(r)\} \mapsto \{\lambda_t(r,\sigma), \lambda_{\mu}(r,\sigma)\}$. Analogously, one can describe other broken-symmetry solutions using a suitable form of the bath.

Alternatively, one can simply consider the original formulation of the DMFT embedding in terms of the Anderson impurity model, where the bath is constituted by N_{bath} independent noninteracting sites, each one parametrized by a spin-independent (spin-dependent, for a magnetic calculation) energy and a hybridization amplitude connecting it to *every* impurity

[2] We clarify that the original replica-scheme features an impurity-independent hybridization $V(r)$, to enforce exactly the symmetries [167, 311]. Hence a $V(i,r)$ hybridization is in fact not completely equivalent to the group-theory approach of Ref. [310]. Nevertheless, we find that the convergent self-consistent hybridization is indeed independent on the impurity index, up to a very small numerical error, and that the additional freedom we provide results often in an easier convergence.

site. In this "all-to-all" scheme all the complexity of the hopping structure in the replicas is transferred to the nondiagonal structure of the impurity-bath hybridization and no explicit enforcement of the lattice symmetries is present. Yet, provided that one has enough degrees of freedom (a large number of bath sites), it has been shown that modern conic optimization schemes can find the correct bath configuration, without any prior knowledge of the lattice symmetries [312]. As we will discuss in detail in section 8.5, our calculations leverage both the replica-scheme and the all-to-all conic optimization, depending on the size of the addressed cluster impurity model.

Concerning the second difficulty in the bath optimization, arising from the matrix structure of the hybridization function and the Weiss field, the essential strategy lies in a generalization of the cost function. Instead of the usual *chi-squared* distance [54]

$$\chi^2 = \frac{1}{M}\sum_{n=1}^{M}\sum_{ij=1}^{N_{\text{imp}}} \left|\mathcal{F}_{ij}(i\omega_n) - \mathcal{F}_{ij}^{\text{bath}}(i\omega_n)\right|^2, \tag{8.4}$$

where $\mathcal{F}$ represents either the dynamical Weiss matrix or the hybridization function matrix and M is the number of considered Matsubara frequencies, we define:

$$\chi^q = \frac{1}{M}\sum_{n=1}^{M}\frac{1}{W_n}\sum_{ij=1}^{N_{\text{imp}}}\frac{1}{W_{ij}}\left|\mathcal{F}_{ij}(i\omega_n) - \mathcal{F}_{ij}^{\text{bath}}(i\omega_n)\right|^q. \tag{8.5}$$

We underline in particular the presence of the W_{ij} weight, with the role of tailoring the treatment of the off-diagonal matrix elements $\mathcal{F}_{ij}$. Defining it as

$$W_{ij} = \frac{1}{M}\sum_{n=1}^{M}\left|\mathcal{F}_{ij}(i\omega_n)\right| \tag{8.6}$$

in general avoids the overlooking of small off-diagonal features of the given dynamical matrix. However, we stress that no universal solution is given, as one can easily fall in the situation of a vanishing (or particularly small) off-diagonal component, invalidating the whole procedure. In those cases one could exclude selected matrix elements from the optimization or change the definition of W_{ij} as necessary. In general the preferred strategy has to be carefully evaluated on a case-by-case basis. Analogously, there is no universal recipe to choose the imaginary axis weight W_n and/or the exponent q. We report that in our calculations for the Mott-Hubbard transition on the square lattice we usually take $q = 2, 3$ and $W_n = 1, n, \omega_n$. We notice that, under rather general circumstances, the converged results do not depend significantly on these choices, except for the most delicate parameter regimes close to phase transitions, and these dependencies are reduced when we increase the number of bath sites.

8.3 Reconstructing the momentum dependence

All the quantities computed in the CDMFT approximation are inherently defined in the cluster-sublattice mixed representation, as described in section 8.1. Consequently, the local Green's function matrix defined in Eq. 8.2 provides a complete description of the physical properties that are defined within the cluster, which we shall refer to as the *quasilocal* observables. We should not forget that the whole CDMFT construction is designed for an infinite lattice, whose properties are obviously those that can be compared with experiments and non-cluster methods. In single-site DMFT these are directly computable from the (scalar) local Green's function, as its $\boldsymbol{k}$-dependency is defined over the whole Brillouin zone. Unfortunately, this is not the case for CDMFT, as the inherent mixed representation of its predictions introduces some arbitrariness in the reconstruction of the full lattice periodicity. Generally, one relies on *ad-hoc* recipes that assemble a *periodized* version of the real-space degrees of freedom in the cluster, on a quantity of choice. Two prominent examples are given by the so-called G-scheme [313] and Σ-scheme [167, 231], referring to the periodization of the Green's function matrix or the self-energy matrix, respectively:

$$G(\boldsymbol{k}, z) = \frac{1}{N_{\text{imp}}} \sum_{ij=1}^{N_{\text{imp}}} \mathrm{e}^{-i\boldsymbol{k}(r_i - r_j)} \left[\mathbf{G}_{\text{loc}}\right]_{ij}(\boldsymbol{k}, z) \tag{8.7}$$

$$\Sigma(\boldsymbol{k}, z) = \frac{1}{N_{\text{imp}}} \sum_{ij=1}^{N_{\text{imp}}} \mathrm{e}^{-i\boldsymbol{k}(r_i - r_j)} \left[\mathbf{\Sigma}_{\text{loc}}\right]_{ij}(z) \tag{8.8}$$

Different choices, in general, result in different features of the periodized observables, underling the non-uniqueness of the procedure that stems from the finite size of the cluster. In many cases, both the G-scheme and the Σ-scheme can introduce artifacts leading, in the worst-case scanerios, even to wrong predictions. The reason behind these pathologies lies in the possible nonanalyticity of the considered quantities, which cannot in any way be regularized by an average over a small number of sites, as Eqs. 8.7 and 8.8 indeed are. The text-book example comes from addressing Mott-Hubbard insulators within the Σ-scheme: as the opening of the Mott gap is associated with the development of pole-like divergences in the cluster self-energy, the periodized $\Sigma(\boldsymbol{k}, z)$ acquires nonphysical features, ultimately leading to the manifestly wrong prediction of a finite spectral weight at the Fermi level. We underline that such an nonphysical result is not only in contrast with intuition, but also in stark conflict with the information obtained from the cluster quantities obtained within the same calculation.

Despite all the subtleties, many CDMFT studies have successfully described physical phenomena associated with an interaction-induced strong $\boldsymbol{k}$-dependence, where the most important examples are given by the *d*-wave superconductor and the pseudogap metal found

in the doped Hubbard model on the square lattice [109, 198, 230, 308, 309, 314]. The resulting predictions are essentially confirmed by the dynamical cluster approximation [199, 315, 316] (which solves the embedded cluster in periodic boundary conditions, so to define coarse *patches* that cover the entire Brillouin zone of the lattice [189]), sophisticated alternative periodization schemes in CDMFT that exploit the natural inhomogeneous of large clusters to isolate the "center-focused" physics [317], and finally by numerical methods not based on the concept of clusters [200, 318].

8.4 Short-range correlations and Mott physics

As extensively discussed in section O.3, the main achievement in the early days of dynamical mean-field theory has been the successful merge of two partial descriptions of the interaction-driven Mott-Hubbard transition. One one hand, the Fermi liquid theory of metals, that describes the interaction effects as a progressive renormalization of the electron effective mass, that eventually diverges at the metal-insulator transition signaling the breakdown of the model. On the other hand, the original arguments proposed by Hubbard to model the insulating phase starting from the atomic limit, that captures the high energy features of the insulating phase, at the cost of a little success in describing the weakly-interacting metal [27–30]. Both descriptions are essentially unsatisfactory, as they approach the problem from one side or the other, but they can hardly be relied on when approaching or even crossing the Mott transition. The inclusion of the full dynamical fluctuation effects at the cost of freezing all the spatial correlations, consecrates the dynamical mean-field theory of the Mott-Hubbard transition as the first consistent account of the two competing regimes. In the upper panel of Fig. 8.2 we report the paramagnetic DMFT phase diagram for the Hubbard model on the square lattice, at varying interaction strength and finite temperature, as computed in Ref. [232]. At weak interaction and low temperature, we have a Fermi liquid metal that is adiabatically connected to the noninteracting limit. On the contrary, at strong coupling, we find a paramagnetic insulator, adiabatically connected to the atomic limit. In between, there is a region of strict coexistence between the two solutions (in green), delimited by two spinoidal lines that are traditionally denotes as $U_{c1}(T) \leqslant U_{c2}(T)$. Hence, at a given temperature:

- The metallic solution extends up to U_{c2}, where the quasiparticle weight, given in the DMFT approximation as $Z = (1 - \partial_\omega \Sigma(0))^{-1}$, in terms of the local self-energy $\Sigma(z)$, vanishes as a signal of the divergence of the effective electron mass.

- The insulating solution is found down to U_{c1}, where the Mott gap vanishes as the high-energy incoherent bands collapse into each other, recovering the original Hubbard picture of the transition.

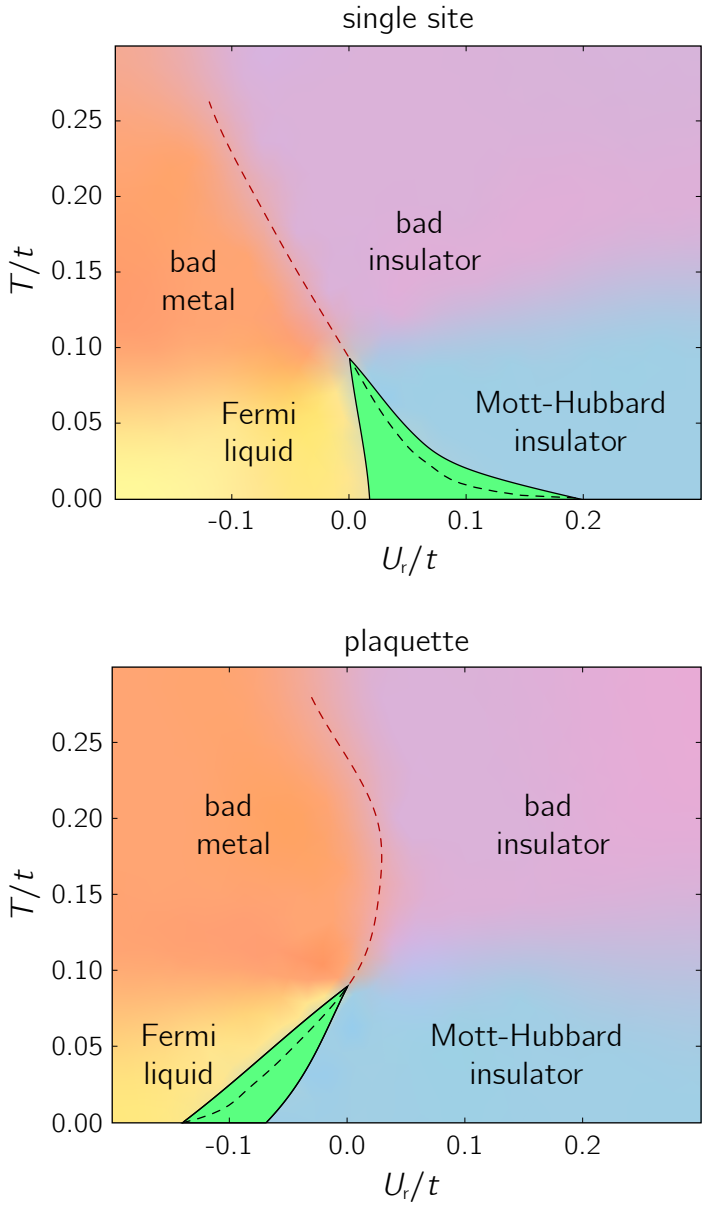


Fig. 8.2.: Paramagnetic phase-diagram of the Hubbard model on the half-filled square lattice, at finite temperature, within single site and 2×2 cluster (*plaquette*) DMFT. The horizontal axis is measured as U_r/t, where $U_r = (U - U_c)/U_c$ and U_c identifies the thermal critical point. The dashed red line above the thermal critical point marks a crossover between a small-DOS metal and a small-gap insulator. The green region below the thermal critical point identifies a coexistence region for the Fermi liquid and the Mott insulating solutions, delimited by spinoidal lines $U_{c1}(T)$ and $U_{c2}(T)$. The dashed line in-between marks equal free energies for the two solutions. Notably, in the limit of small temperature $T \ll t$, it coalesces with U_{c2} or U_{c1}, respectively for the DMFT and CDMFT simulations. Figures adapted from Ref. [232].

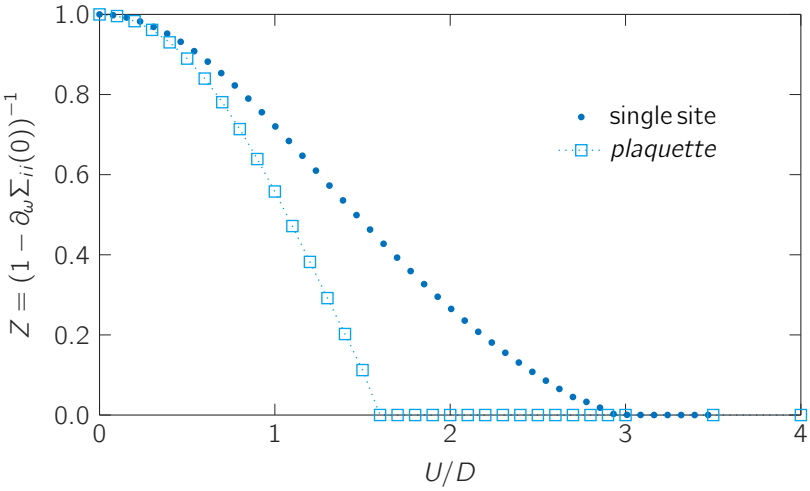


Fig. 8.3.: Quasiparticle weight of the Hubbard model on the half-filled square lattice, at zero temperature, within single site and 2×2 *plaquette* CDMFT. At $U = 0$ both calculations find $Z = 1$, as quasiparticles saturate all spectral weight. The point at which Z vanishes defines the quantum critical point for the MIT. The inclusion of short-range off-diagonal self-energy terms significantly moves the quantum critical point, towards weaker interactions. The horizontal axis is measured as U/D, where $D = 4t$ is the half-bandwidth of the square lattice.

- The dashed line between the two spinodals marks a first-order phase transition, that in the limit of zero temperature has been proven to coincide with U_{c2} [38], de facto removing the discontinuous character of the transition.

- At high temperature the transition line ends in a classical critical point, above which the interaction drives a supercritical crossover, marked by a Widom line.

One of the possible objections to the above picture when dealing with finite-dimensional models lies, of course, in the complete neglect of possible nonlocal correlation effects. Indeed, the extension of the impurity model to a cluster of just 4 sites (a 2×2 plaquette), qualitatively changes some key aspects of the phase diagram, as reported in the lower panel of Fig. 8.2. In particular, the slope of all the separation lines is inverted, at low enough temperature, and the zero-temperature extrapolation of the first-order quantum critical point completely disconnects from U_{c2} and instead appears to join U_{c1}. On the other hand, as we show in Fig. 8.3 for our own calculation of Z, within both DMFT and plaquette CDMFT, the absolute value of the critical interaction for the zero temperature MIT is substantially reduced, highlighting the rich influence of nonlocal correlations on the physics of the Mott-Hubbard transition, as they both reduce the overall scale of the interaction strength needed for localizing the electrons and invert the slope of the U_{c2} spinoidal, making the insulating phase less and less favorable at higher temperatures.

The early explanation of this peculiar effect, due to Park, Haule and Kotliar [232], amounts to a simple thermodynamic argument, that we proceed to describe in light of our introductory discussion on the nature of local correlations (section O.5) and of the forthcoming analysis of nonlocal correlations under the lens of quantum information theory (chapter 9).

The single-site DMFT description of the transition completely removes the role of spatial antiferromagnetic correlations, therefore describing the local projection of the insulating many-body state as a perfectly balanced mixture of single-occupied orbitals either in the $|\uparrow\rangle$ or $|\downarrow\rangle$ spin configuration. As the Hubbard model conserves the total magnetization and local projections of the global many-body state must inherit this property, such mixture has to be classical (*i.e.* incoherent) as indeed we have shown to be in the single-site reduced density matrix (see section O.5). A classical mixture leads to a large thermodynamic entropy, even at zero temperature, and the DMFT prediction for this quantity in a Mott insulator indeed approaches the extensive value of $\log(2)$ per site [232], corresponding to an additive contribution the from asymptotic value of the single-site von Neumann entropy.

A cluster theory of the Mott-Hubbard transition, on the other hand, allows for antiferromagnetic correlation within the cluster. For example, at the two-site level, it describes the paramagnetic Mott phase as a *quantum* superposition of the two degenerate antiferromagnetic solutions of an isolated Hubbard dimer periodically repeated on the whole lattice. With larger cluster the correlations extend to more distant sites, as we will carefully discuss in chapter 9. As we will see, the single-orbital von Neumann entropy, evaluated on a cluster, does still approach $\log(2)$ in the Mott-Hubbard insulator. Yet, the von Neumann entropy of larger subsystems is strictly subadditive, leading to large nonlocal correlations and quantum entanglement between orbitals at different lattice sites. Hence, we foresee the possibility of a clear-cut relationship between the development of nonlocal (short-range) correlations and the subadditivity of the quantum entropy. The matter will be rigorously settled in sections 9.1 and 9.3.

Finally, returning to the original argument in Ref. [232], the significant reduction of the thermodynamic entropy found in the CDMFT calculations of Fig. 8.2 clearly reduces the free energy of the insulating solution as the temperature grows, explaining the negative slope of the spinodal lines.

8.5 Implementation details

In this section we give a brief overview of our implementation of a cluster dynamical mean-field theory for the Hubbard model on the square lattice.

To solve the auxiliary quantum cluster problem at zero temperature, we rely on a combined numerical analysis, based on two different Hamiltonian-based solvers: a Lanczos/Arnoldi exact diagonalization (ED) [54, 165, 166] and the adaptive sampling configuration interac-

tion (ASCI) [243, 244, 319, 320]. Both methods parameterize the noninteracting bath in terms of a finite number of non-interacting levels (which we shall henceforth call bath sites), but employ different algorithms to obtain the frequency-dependent self-energy and the local Green's function that are necessary to enforce the CDMFT self-consistency.

Our ED solver leverages on the massively parallel implementation of the `EDIpack` software [166], naturally generalized to treat clusters.[3] To reduce the number of variables to be optimized, we employ the above discussed representation of the bath in terms of non-interacting *replicas* of the correlated cluster, diagonally coupled to the corresponding impurity sites (see section 8.2). Their internal parameters, corresponding to on-site energies and nearest-neighbor hoppings, are optimized, together with the impurity-bath hybridization amplitudes, in an iterative procedure that enforces the self-consistency condition on the cluster Green's function. At each loop, the cost function in Eq. 8.5 is minimized by a conjugate-gradient algorithm, with numerically evaluated derivatives. With the resulting CDMFT/ED scheme, we address clusters of shape 1×2 and 2×2, changing the number of replicas as to keep the total number of sites in the impurity model fixed to $N_s = N_{imp} + N_{bath} = N_{imp}(1 + N_{repl}) = 12$.

In addition to the exact diagonalization, as mentioned above, we exploit the recently introduced CDMFT/ASCI implementation [243] to benchmark our results and study larger cluster sizes with respect to those accessible with the ED algorithm. This method is capable of alleviating the ED limitations related to the exponential growth of the Hilbert space: the ASCI Ansatz corresponds to an adaptively optimized truncation of the impurity model Hilbert space, in terms of a subset of selected Slater determinants, which together reconstruct the most-significant part of the ground state wavefunction [244, 319, 320].
It further relies on optimizing the orbital active space by constructing a suitable natural basis, from an approximated one-body reduced density matrix of the bath [243, 321, 322]. This results in a highly compact and accurate representation of the ground state [323] and the one-body Green's functions [243], while reducing substantially the overall computational cost. In the CDMFT/ASCI method the bath sites are split into groups of N_{imp} degenerate levels, with an all-to-all amplitude to the cluster impurity sites (see section 8.2).
The bath parameters are self-consistently determined, loop by loop, by means of a modern conic optimizer [312]. In chapter 9 we report ASCI calculations for cluster with $N \times 2$ shape, where N ranges from 1 to 4. We fix the number of bath sites to 6 times the number of cluster impurities, in order to always have 6 nondegenerate bath energies, according to the degeneracy structure determined in Ref. [312].

[3] An unpublished version of the implemented cluster extension can be found at `https://doi.org/10.5281/zenodo.10628156`

8.5.1 Calculation of reduced density matrices

In this thesis a central role is played by the evaluation of different measures of entanglement and correlation which in turn rely on the calculation of reduced density matrices of the system. Since this evaluation in CDMFT is by far less standard then all the other quantities that we compute, we discuss it in some details. The two impurity solvers, ED and ASCI, grant us direct access to an explicit representation of the ground state of the cluster impurity model. Using this information, we can build the zero temperature RDM for any cluster subsystem (*e.g.* two sites) performing an *on-the-fly* trace over the bath and complementary impurity degrees of freedom. The local RDM, thoroughly studied in Refs. [61–64], is obtained by further tracing over all but one site, matching the analytic expression in terms of spin-density averages and the local occupancy, given in Eq. 7.2.

To elucidate the need of computing the trace *on-the-fly*, we give the explicit expression for the density matrix of the full cluster-impurity model, at zero temperature. It reads:

$$\rho_{\text{gs}} = \frac{1}{\Omega}\sum_{\nu}^{\Omega} \left|\Psi^{\nu}_{\text{gs}}\right\rangle\!\left\langle\Psi^{\nu}_{\text{gs}}\right| = \frac{1}{\Omega}\sum_{\nu}^{\Omega}\sum_{n=1}^{4^{N_s}}\sum_{m=1}^{4^{N_s}} C^{\nu}_{nm}\,|\,n\,\rangle\!\langle\,m\,|\,, \tag{8.9}$$

where Ω is the ground state degeneracy, $N_s = N_{\text{imp}} + N_{\text{bath}}$ the total number of sites in the effective impurity model, and $|n\rangle$ and $|m\rangle$ are Fock basis states stored in the digital memory as integers whose binary decomposition gives the occupation number vector, with a 0 or 1 bit for each spin-orbital. The coefficients defining the matrix elements of ρ_{gs} are given by the Ω ground state eigenvectors retrieved by either the Lanczos procedure or the ASCI algorithm. Hence, the relevant dimension of the matrix is given by $\Omega 16^{N_s}$, a gargantuan number, due to the dramatic exponential scaling of the fermionic Fock space. Let us take $\Omega = 1$, and consider real matrix elements in double precision: the needed memory to store the full ρ_{gs} for a typical ED calculation with $N_s = 12$, amounts to approximately 2 petabytes! Even implementing all the symmetries of the model, to decompose the Fock space into independent sectors (as we indeed do [166]), the relevant dimension of the matrix is still of the order of 10^6, amounting to 100^6 reals numbers for approximately 8 terabytes of memory. Hence, to trace away the bath[4] from ρ_{gs} without storing the full matrix, we need to efficiently track what are the allowed bath states for each impurity state, within a given symmetry sector. Indeed, writing explicitly the decomposition of ρ_{gs} into the impurity and bath subspaces we have, for a sector of dimension $\mathcal{D} = \mathcal{D}_{\text{imp}} \times \mathcal{D}_{\text{bath}}$,

$$\rho^{\mathcal{D}}_{\text{gs}} = \frac{1}{\Omega}\sum_{\nu}^{\Omega}\sum_{i=1}^{\mathcal{D}_{\text{imp}}}\sum_{j=1}^{\mathcal{D}_{\text{imp}}}\sum_{p=1}^{\mathcal{D}_{\text{bath}}}\sum_{q=1}^{\mathcal{D}_{\text{bath}}} C^{\nu}_{ijpq}\,|\,p\,\rangle \otimes |\,i\,\rangle\!\langle\,j\,|\otimes \langle\,q\,|\,, \tag{8.10}$$

[4] Or the bath plus some impurity site, of course, with minimal modifications in the argument. The only important detail to keep in mind is to consider the fermionic signs, if a swap in the Fock state is needed.

so that the partial trace over the bath can be written as

$$
\begin{aligned}
\mathrm{tr}_{\mathrm{b}}\, \rho_{\mathrm{gs}}^{\mathscr{D}} &= \frac{1}{\Omega} \sum_{\nu}^{\Omega} \sum_{b=1}^{N_{\mathrm{bath}}} \langle\, b \,|\, \rho_{\mathrm{gs}} \,|\, b \,\rangle \\
&= \frac{1}{\Omega} \sum_{\nu}^{\Omega} \sum_{b=1}^{\mathscr{D}_{\mathrm{bath}}} \sum_{i=1}^{\mathscr{D}_{\mathrm{imp}}} \sum_{j=1}^{\mathscr{D}_{\mathrm{imp}}} \sum_{p=1}^{\mathscr{D}_{\mathrm{bath}}} \sum_{q=1}^{\mathscr{D}_{\mathrm{bath}}} \mathcal{C}_{ijpq}^{\nu} \langle\, b \,|\, p \,\rangle \otimes |\, i \,\rangle\langle\, j \,| \otimes \langle\, q \,|\, b \,\rangle \\
&= \frac{1}{\Omega} \sum_{\nu}^{\Omega} \sum_{b=1}^{\mathscr{D}_{\mathrm{bath}}} \sum_{i=1}^{\mathscr{D}_{\mathrm{imp}}} \sum_{j=1}^{\mathscr{D}_{\mathrm{imp}}} \sum_{p=1}^{\mathscr{D}_{\mathrm{bath}}} \sum_{q=1}^{\mathscr{D}_{\mathrm{bath}}} \mathcal{C}_{ijpq}^{\nu} \delta_{bp} \,|\, i \,\rangle\langle\, j \,| \,\delta_{qb} \\
&= \frac{1}{\Omega} \sum_{\nu}^{\Omega} \sum_{b=1}^{\mathscr{D}_{\mathrm{bath}}} \sum_{i=1}^{\mathscr{D}_{\mathrm{imp}}} \sum_{j=1}^{\mathscr{D}_{\mathrm{imp}}} \mathcal{C}_{ijbb}^{\nu} \,|\, i \,\rangle\langle\, j \,| \\
&= \sum_{i=1}^{\mathscr{D}_{\mathrm{imp}}} \sum_{j=1}^{\mathscr{D}_{\mathrm{imp}}} |\, i \,\rangle\langle\, j \,| \left(\frac{1}{\Omega} \sum_{\nu}^{\Omega} \sum_{b=1}^{\mathscr{D}_{\mathrm{bath}}} \mathcal{C}_{ijbb}^{\nu} \right) = \rho_{\mathrm{imp}}^{\mathscr{D}}
\end{aligned}
\tag{8.11}
$$

where we have grouped in parentheses the explicit expression for the matrix elements of the impurity reduced density matrix ρ_{imp}, in the given sector $\mathscr{D}$.

Hence it becomes clear that in order to compute the (ij)-th matrix element of ρ_{imp} one has to sum over all the sectors, the degenerate ground states and the bath states compatible with both the impurity states $|\, i \,\rangle$ and $|\, j \,\rangle$, according to the symmetries of each sector. To achieve this in an efficient algorithm it is then necessary to pre-compute all the compatible bath states, for each impurity state on each sector, and store the information in a suitable data structure (*e.g.* a *hash-table*, where the impurity state serves as the *key*, and the list of compatible bath states is the stored *value*). Finally, a suitable implementation of the set-intersection between bath state lists would allow to directly implement the formula in Eq. 8.11. If, as usual, the number of impurity sites (or in general the dimension of the subsystem of interest) is much smaller than the number of bath sites (or in general the number of traced sites), then the double summation runs on a small set of indices, providing an efficient implementation of the partial trace.

Finally, we observe that a recent work by Roósz *et al.* [65] provides a recipe to obtain single-orbital and two-orbital reduced density matrices from the knowledge of single-particle and two-particle Green's functions alone, giving access to the quasilocal entanglement and correlation measures introduced in chapter 7 to a broad variety of many-body methods. Moreover, a feasible tomography protocol has been recently proposed for dot-cavity devices, giving experimental access to the single-site and two-site RDM [324]. Hence we foresee the opportunity of applying our methodologies in the emerging field of entanglement detection in realistic open quantum impurity systems [269].

9 Quasilocal entanglement of a Mott-Hubbard insulator

In this chapter we present numerical CDMFT results for the evolution of quasilocal entanglement and correlations, across the interaction-driven Mott-Hubbard transition of the half-filled square lattice. We will start, in section 9.1, with a discussion of the scaling of the von Neumann entropy as a function of the cluster-size used in CDMFT and on the subsystem-size, based on our ED and ASCI calculations for $N \times 2$ ladders. We find a weak dependence which supports the reliability of our results. A comparison with data recently appeared for the 2-Renyi entropy [234, 235], a close relative of the von Neumann entropy [76, 325, 326], will further confirm that the qualitative behavior of the entanglement entropy does not fundamentally change by increasing the size of the selected subsystem. We first reproduce the results for the single-site entropy across the interaction-driven Mott transition within CDMFT [62], then we briefly check in section 9.2 the behavior of the intra-orbital mutual information (Eq. O.34), to confirm that the local correlation picture of the Mott-Hubbard transition, analyzed in chapter O, does not depend on the specific details of the lattice geometry and survives the inclusion of off-diagonal self-energy terms in the DMFT self-consistency.

After these benchmarks, we will proceed in section 9.3 with the analysis of upper and lower bounds to the entanglement and correlation between neighboring sites, in terms of the two-site mutual information, two-site negativity and two-site superselected relative entropy of entanglement (REE). The robustness of von Neumann entropy, mutual information and negavitity to the SSR-filtering will be assessed in section 9.4. In section 9.5 we will explore the spatial decay of entanglement and correlations, discussing the behavior of the two-site mutual information and negativity beyond nearest neighbors. Finally, in section 9.6 we will give some perspectives and draw our conclusions about the performance of our measures of entanglement for the Mott-Hubbard transition.

9.1 Size scaling of the von Neumann entropy

We begin by investigating the local and the nearest-neighbor entanglement entropies across the Mott transition. All energies will be measured in units of the half-bandwidth of the noninteracting model, $D = 4t$. As expected for a CDMFT analysis [232, 317, 327, 328] the critical interaction for the metal-insulator transition is expected to depend on the size of the embedded cluster. We tracked the quantum critical point for all the investigated cluster shapes, namely different clusters with two sites along one direction and ranging from 1 to 4 sites in the other direction, and estimated it to be placed in the interval $U/D = [1.5, 1.6]$. However, a precise determination of the transition point is beyond the scope of this thesis work, as we are mainly interested in a qualitative spatial characterization of short-ranged entanglement and correlations in the Mott-Hubbard insulating phase.

In Fig. 9.1 we report the behavior of s_i and $s_{\langle ij \rangle}$ as a function of the interaction strength. We compare the results for the different cluster sizes and effective bath sizes, obtained either with the ED or the ASCI impurity solvers, at zero temperature, as indicated in the legend. We remark that all these calculations refer to a lattice system in the thermodynamic limit, and the size of the cluster should not be seen as a real finite-size effect, but rather as the range of the dynamical correlations included in the calculation.

The behavior of the local entanglement entropy, reported in Fig. 9.1(a), is essentially insensitive to the cluster size and the size of the bath, even in the proximity of the Mott transition point. As we discussed, s_i is a decreasing function of U which displays a discontinuous jump at the Mott transition. This confirms that s_i is properly captured in CDMFT indeed represents an effective marker for the quantum Mott-Hubbard transition, in agreement with extensive explorations of the finite temperature phase diagram in the recent literature [62–64]. It also shows that our calculations with a finite bath correctly reproduce the behavior of their finite-temperature counterparts with a continuous bath solved using a CTQMC solver.

The nearest-neighbor entanglement entropy $s_{\langle ij \rangle}$, see Fig. 9.1(b), displays a more noticeable dependence on the size of the CDMFT cluster, even if the overall qualitative behavior is robust. Interestingly, significant quantitative discrepancies arise between clusters of different sizes deep in the metallic and insulating regimes, while smaller effects are found in the intermediate region close to the Mott transition. We relate this behavior to the fact that some choices of the cluster shape (*e.g.* 3×2 and 4×2) can break the symmetries of the full lattice, a well-known drawback of the cellular extension of DMFT, that can be fully resolved only in the limit of infinite cluster size (amounting to a solution of the full Hubbard model). However, as far as the qualitative behavior across the Mott transition is concerned, we can interpret $s_{\langle ij \rangle}$ to be well converged.

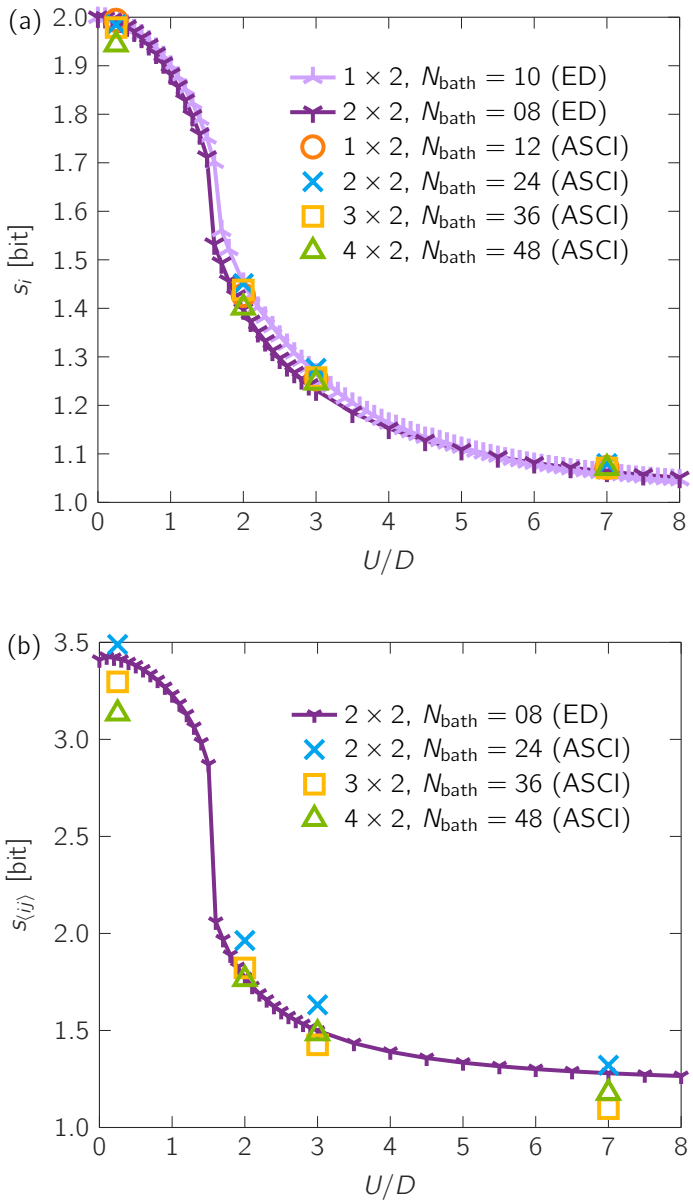


Fig. 9.1.: Local (a) and nearest-neighbor (b) entanglement entropies, respectively s_i and $s_{\langle ij \rangle}$, across the interaction-driven metal-insulator transition. Data from ED (lines and symbols) and ASCI (open symbols), for different combinations of cluster sizes and bath levels. Clusters have ladder shape $N \times 2$.

Having clarified the scaling behavior of the local and nearest-neighbor entanglement entropy with respect to cluster and bath size, in the following we focus on the 2×2 *plaquette*, for an in-depth analysis of the CDMFT/ED results. We will return to larger clusters, addressed with the ASCI solver in section 9.5, for the analysis of the spatial decaying of entanglement and correlations between pairs of sites at a generic distance.

To start, we characterize the behavior of the single- and two-site von Neumann entropy for the plaquette cluster in the two extreme regimes of the model. In the noninteracting system ($U = 0$), the local entropy approaches the value $s_i = 2\log(2)$, corresponding to a maximally entangled single-site state. This is easily interpreted as the model, at half-filling, is particle-hole symmetric, so that the noninteracting metal is a Fermi gas with equal populations of empty, doubly and singly occupied electronic states. On the contrary, we do not find a maximally entangled state for the two-site nearest-neighbor sites, as the corresponding two-site entanglement entropy assumes a value smaller than $4\log(2)$. This is a direct consequence of the spatial correlation between the neighboring sites: if $s_{\langle ij \rangle} = 4\log(2)$, then we would have zero mutual information $I_{\langle ij \rangle} = s_i + s_j - s_{\langle ij \rangle} = 2s_i - s_{\langle ij \rangle} = 0$ between i and j, given that any of the four single-site RDM is equivalent in the 2×2 plaquette. According to Eq. 7.5 this in turn would imply that no finite correlation function exists, for any pair of operators acting on the two neighboring sites. The fact that finite two-site correlations exist, even in the noninteracting limit, clarifies that the *inter*-orbital mutual information assumes a very different role from that of the intra-orbital mutual information introduced in section O.5, highlighting the importance of considering explicit measures for the nonlocal correlations in CDMFT. Indeed, in section 9.2 we will verify that the intra-orbital mutual information preserves its properties, when extending the analysis from single-site DMFT to CDMFT.

In the left panels of Fig. 9.2 we report the spectral analysis of the single-site and nearest-neighbor RDM, *i.e.* we quantify the contribution of the different basis states in the single-site and two-site Fock spaces. To accommodate and illustrate as clearly as possible the nested structure of the spectrum, with (i) the probability distribution given by the RDM eigenvalues, describing the statistical weight of each pure state and (ii) a quantum probability distribution, given for each pure state by the square moduli of the coefficients of their expansion on the given Fock basis (according to Born's rule), we represent such spectra as *treemaps* [329, 330].

We start from the non-interacting regime $U/D = 0$ (left panels in Fig. 9.2). As discussed in section O.5, the single-site RDM is diagonal on the spin-orbital occupation basis, leading to a very simple treemap representation, as a set of four squares of equal area, representing the equal diagonal matrix elements of ρ_i. On the other hand, the two-site RDM is far more complex, leading to a hierarchy of rectangle sizes, with area proportional to the eigenvalues of $\rho_{\langle ij \rangle}$ for the outer ones (outlined in black), and proportional to the Born

weights for the inner (colored) ones. Equal colors correspond to equal basis Fock states (regardless of the pure state they come from) and for the dominant configurations (larger rectangles) we report explicitly the coefficient of the expansion in the Fock space, as a pre-factor to the basis state. Panel (c) shows that in the noninteracting limit, all the 16 two-site pure states contribute, although differently, to the spectrum of $\rho_{\langle ij \rangle}$, reflecting the itinerant character of the solution, which on a two site system is represented by fluctuation in the local charge $\langle n_i \rangle$ and $\langle n_j \rangle$.

In the strong coupling regime, $U \gg D$, both the local and nearest-neighbor von Neumann entropies slowly approach log(2), highlighting a strong subadditivity of the quantum entropy in the Mott phase, which again suggests the development of strong spatial correlations between the sites (see section 9.3). A deeper analysis of the underlying pure states, represented in the right panels of Fig. 9.2, reveals the presence of remarkable differences in the two corresponding description of the local and quasilocal electronic configurations. The local entropy is largely dominated by the equally weighted pure states $|\uparrow\rangle$ and $|\downarrow\rangle$, demonstrating the expected local description of a paramagnetic Mott insulator: for a single-site, the long tail in the von Neumann entropy simply arises from the progressively suppressed populations of *holons* and *doublons*, which vanish exactly only at the atomic limit ($D = 0$). On the other hand, $s_{\langle ij \rangle}$ is dominated by four pure states, *i.e.* the spin-singlet $(|\uparrow\downarrow\rangle - |\downarrow\uparrow\rangle)/\sqrt{2}$, accounting for about 75% of the statistical mixture, and the spin-triplet states $|\uparrow\uparrow\rangle$, $|\downarrow\downarrow\rangle$ and $(|\uparrow\downarrow\rangle + |\downarrow\uparrow\rangle)/\sqrt{2}$, adding up for almost all the rest, in equal parts. Such relative composition of singlet and triplet states in the nearest-neighbor dimer has been checked to be consistent across all the addressed cluster and bath sizes: the numerical differences in the von Neumann entropies for the larger clusters are due to a different cumulative weight of all the remnant 12 pure states. This once again confirms that the two-site reduced density matrices are qualitatively consistent across all the cluster realizations.

Before proceeding with the analysis of intra-orbital correlations, we briefly compare our result to those obtained in recent works [234, 235], that compute within three different methods, the *collision* entropy of subsystems of more than two sites. This quantity is often referred to as 2-Rényi, where the α-Rényi entropy is a generalization of the von Neumann entropy, defined for a generic density matrix ρ as

$$S_\alpha = \frac{1}{1-\alpha} \log(\mathrm{tr}\, \rho^\alpha)\,, \tag{9.1}$$

with $0 < \alpha < \infty$ and $\alpha \neq 1$. Remarkably, the singularity in $\alpha = 0$ can be removed, so to recover von Neumann entropy in the $\alpha \to 1$ limit. The $\alpha = 2$ case has been increasily used to estimate the entanglement in complex systems, as it can be sampled in several quantum Monte Carlo schemes [333, 334], and other methods that have no access to the von Neumann entropy [234, 335]. Despite some undesirable properties, like the lack

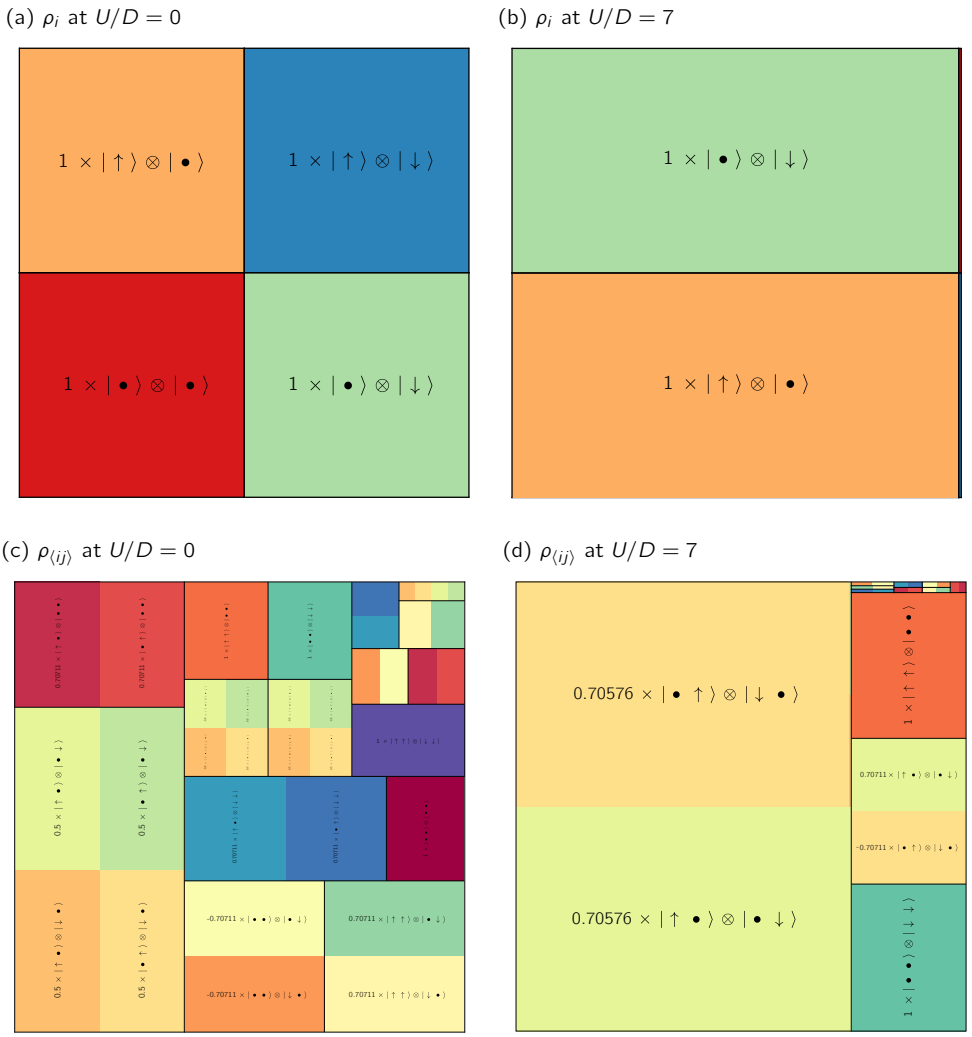


Fig. 9.2.: Treemap visualization [329, 330] of single-site and nearest-neighbor RDM at the noninteracting and strong coupling limits. Outlined rectangles represent pure (eigen) states of the given RDM, with an area proportional to the corresponding eigenvalue. All pure states are further partitioned into colored rectangles, representing their expansion into the Fock space basis for the given subsystem. The area of each colored rectangle is proportional to the square modulus of the corresponding expansion coefficient, according to Born's rule [331] for quantum measurements on pure states. Explicit expressions for the basis-states and their coefficients in the given pure state are reported for the rectangles that dominate the treemap. Same basis states are represented in equal color, with no influence by the expansion coefficient. Overall the sum of the areas of rectangles with the same color, is proportional to the probability associated to generalized quantum measurements on mixed states (the so called POVM) [66, 332]. Data from the 2×2 CDMFT/ED simulation with $N_{\text{bath}} = 8$.

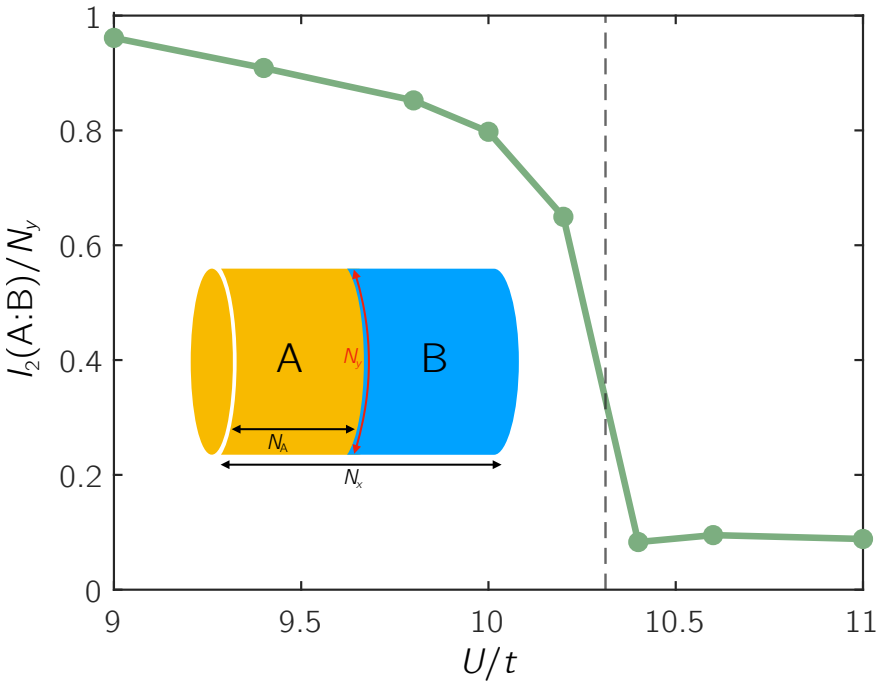


Fig. 9.3.: 2-Rényi mutual information for $T = 0.16t$ in a $N_A = N_B = 8$, $N_y = 16$ cylinder geometry, computed within a suitably modified single-site DMFT approximation, tailored to sample 2-Renyi entropies via an effective quench [234]. Adapted from the original reference.

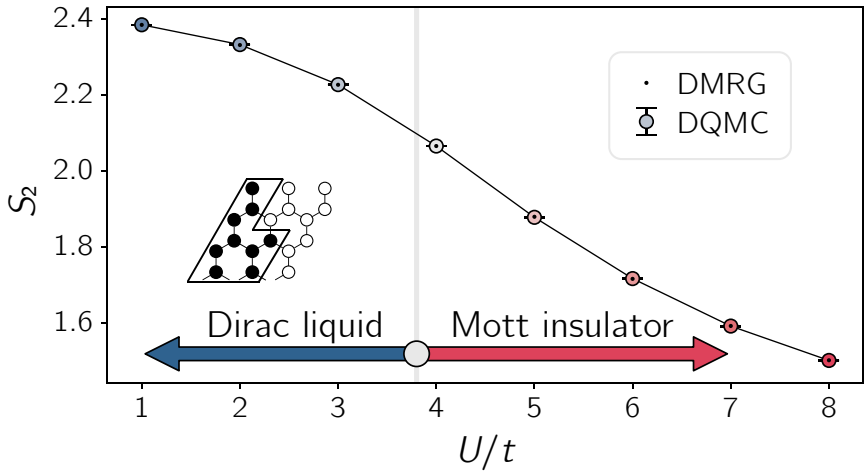


Fig. 9.4.: 2-Rényi entropy for the Mott-Heisenberg transition of Dirac fermions on the honeycomb lattice, as computed within the density matrix renormalization group (DMRG) and determinant quantum Monte Carlo (DQMC), for a small cylinder geometry [235]. Adapted from the original reference.

of subadditivity and the possible lack of positivity for the correspoding 2-Rényi mutual information I_2 [325, 326], the collision entropy S_2 has been successfully applied to many systems of strongly correlated electrons [334, 336–338].

In particular, in Fig. 9.3 we report the 2-Rényi mutual information for a global bipartition of the Hubbard model, defined on a finite square lattice of 16×16 sites. It is evaluated from a newly introduced extension of single-site DMFT, that modifies the effective action (Eq. O.11) so to allow the sampling of the 2-Rényi entropy from a nonequilibrium evolution [234]. On the other hand, in Fig. 9.4 we report the 2-Rényi entropy for the Hubbard model on the honeycomb lattice, evaluated again on a global bipartition of a cylinder of 18 sites, within both *determinant* quantum Monte Carlo and the density matrix renormalization group. The latter calculation is technically less relevant to the MIT of the Hubbard model on the square lattice, as it describes a semimetal-insulator transition (SMIT), and more importantly, the resulting correlated insulator is of the Mott-Heisenberg type. Nevertheless, we have discussed at length in sections O.4 and O.5 how the Mott-Hubbard and Mott-Heisenberg insulators are very similar with respect to their local correlations and showed in Fig.O.4 that the single-site von Neumann entropy does not behave in a drastically different way across the transition, as it decreases monotonically in both cases, with just a different asymptotic value at the atomic limit.

The complete picture formed by the results of all these calculations, coming from very different methods, predicts an entanglement entropy for $N = 1, 2, 8, 128$ sites that monotonically decreases as we increase the Hubbard interaction U/D, even when entering the strongly correlated insulator (with or without magnetic ordering).

This means that nonlocal estimates of the entanglement do not properly reproduce the expectation about the entengled nature of the Mott insulator. Hence, we deem this description of the entanglement properties of strongly correlated materials insufficient and propose a spatially resolved study of the nonlocal quantum correlations (measured by the entanglement between two lattice sites with no contribution from their environment) as a necessary tool for a proper characterization of the Mott state.

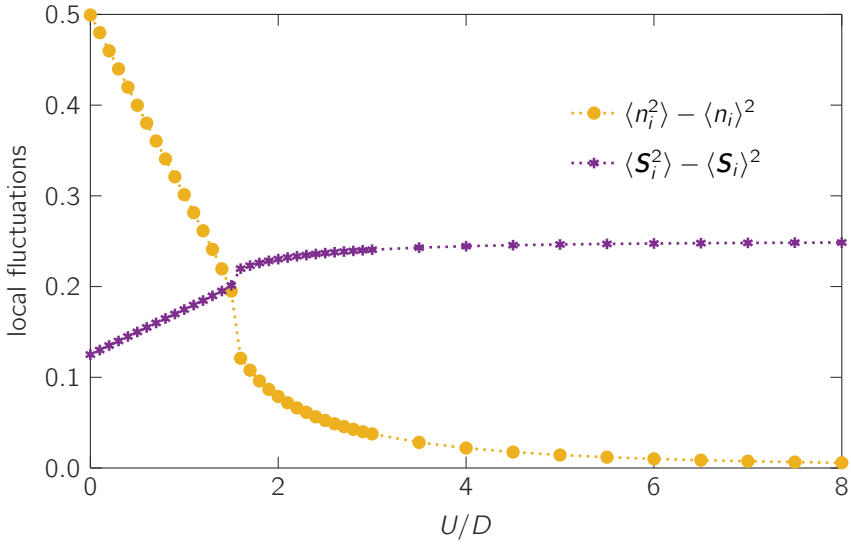


Fig. 9.5.: Local charge and spin fluctuations, for the Hubbard model on the square lattice. Data from the 2×2 CDMFT/ED simulation with $N_{\text{bath}} = 8$.

9.2 Local fluctuations and correlations

In this section we take a short interlude from our main program, with the aim of showcasing, in a precise way, in which sense the single-site entropy deserves its nickname of *local* entropy. First of all, as we have already discussed in section 7.1, s_i has nothing to do with a concept of entanglement confined in the local single site. On the contrary, it includes contributions associated with the entanglement at all possible distances in the system, with no general criterion or algorithm to filter or pinpoint the effect of any one term [70]. But, recalling the discussion in section 7.2, we know that s_i describes also the *self-information* contained in the single-site reduced density matrix, so that, by virtue of Eq. O.28, it bounds from above the fluctuations of all local observables.

In Fig. 9.5 we report the evolution as a function of the interaction strength of the local charge and spin fluctuations, across the MIT. These quantities notoriously give valuable insight on the physics of Mott insulators, as they clearly unveil the freezing of charge degrees of freedom and the formation of interaction-induced local magnetic moments. We notice that the upper envelope of the two curves in Fig. 9.5 has a behavior that follows qualitatively that of s_i. This is clearly compatible with the fact that s_i bounds from above all the local fluctuations, and suggests that the monotonically decreasing behavior of s_i is dictated by the evolution of these two relevant observables. Of course this a purely evocative argument which is not automatically implied by the upper-bound property. In fact, it is evident that the local charge fluctuation dominate in the Fermi liquid and are quickly

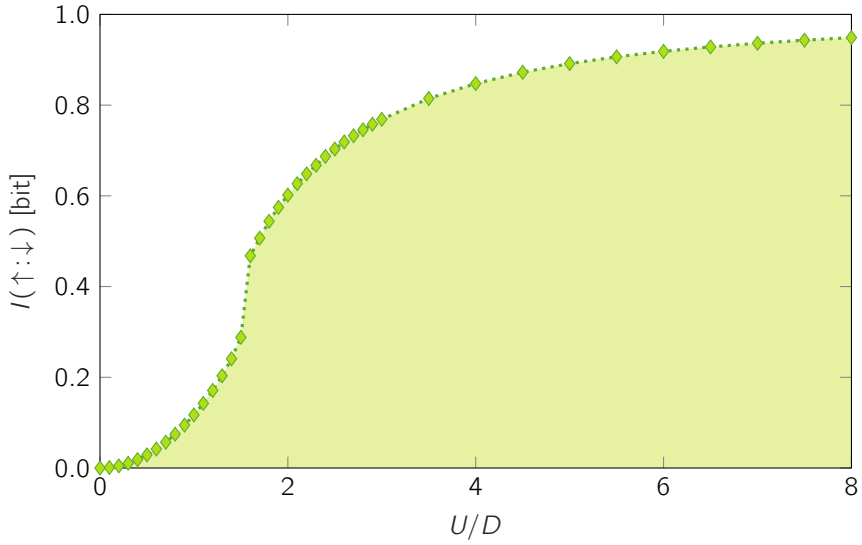


Fig. 9.6.: Intra-orbital mutual information for the Hubbard model on the square lattice. The shaded area represents the range in which lie all correlation function involving the two local spin states. Data from the 2×2 CDMFT/ED simulation with $N_{\text{bath}} = 8$.

damped by Mott localization, while, on the other hand, the spin fluctuations increase monotonically with U/D, eventually surpassing the charge fluctuations as the Mott state is stabilized. Moreover, we know that for a Mott-Heisenberg insulator the strong-coupling limit of s_i is smaller than log(2) (see Fig. O.4) and that the local magnetic moments eventually are suppressed to their minimum value, typical of a Fermi gas, deep in the antiferromagnetic phase (see Fig. O.3). Hence, the concept of local self-information is shown to provide valuable insight also on the physics of Mott antiferromagnets.

To complete the strictly local (*i.e.* information contained in a single site, with no reference to its environment) quantum information description of the Mott-Hubbard transition, we recall the definition of intra-orbital correlations, as the mutual information shared by the two local spin states: $I(\uparrow:\downarrow) = s_{i\uparrow} + s_{i\downarrow} - s_i$ (Eq. O.34). Given its role as a measure of all the correlations encoded in the local spin-orbital pair $\{|\, i\uparrow\rangle, |\, i\downarrow\rangle\}$ (see section O.5), it bounds from above also the correlation contribution to the local mean square moments, that is precisely given by the local spin fluctuations, subtracted of the contribution of Fermi statistics $\mu_z^2|_{\text{FG}} = 1/8$ (from Eq. O.21, evaluated at half-filling). The resemblance of the two quantities in Figs. 9.5 and 9.6 is unquestionable.

Finally, we recall that in the single-band Hubbard model, the local charge and magnetization are conserved in ρ_i, forcing all the off-diagonal elements to vanish [61–65]. As discussed in section O.5, the diagonal form of ρ_i (in the spin-orbital occupation basis), makes it a classically correlated state, with respect to the bipartition in the two local spin states, in

the sense of section A.3 in the appendix. Hence all the correlation measured by $I(\uparrow:\downarrow)$ should be considered classical, with respect to the local Fock space (our description of the single-site as an open quantum system). Nevertheless, all correlations in the global lattice at zero temperature, at least in the absence of degeneracy, must be fully determined by quantum entanglement, as it is in a pure ground state [224]. Hence we are readily lead to suspect that classical correlations in an embedded subsystem can indeed be generated by quantum correlations in its environment. In fact, this statement can be precisely formalized, in terms of the so called *Naimark theorem* [173, 275]. This last consideration leads us again to the main objective of the chapter, as the accumulation of a large classical intra-orbital correlation in the paramagnetic Mott transition (Fig. 9.6), clearly suggest the presence of large nonlocal quantum correlations.

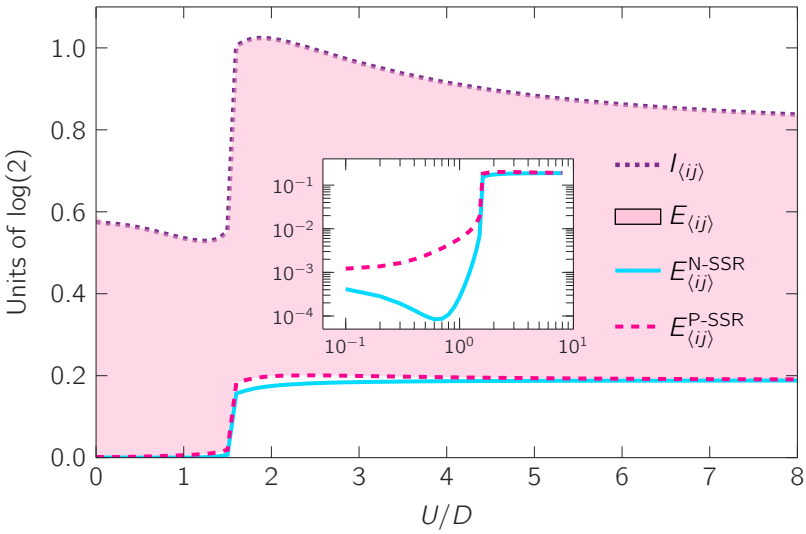


Fig. 9.7.: Nearest-neighbor mutual information $I_{\langle ij\rangle}$, and charge and parity superselected nearest-neighbor entanglement $E^{\text{N(P)-SSR}}_{\langle ij\rangle}$, as a function of the interaction strength. The shaded area represents the unconstrained nearest-neighbor entanglement, given the bound $E^{\text{P-SSR}}_{\langle ij\rangle} \leqslant E_{\langle ij\rangle} \leqslant I_{\langle ij\rangle}$. The latter curves are also reported in log-log scale in the inset, highlighting the different behavior in the Fermi liquid. Data from the 2×2 CDMFT/ED simulation with $N_{\text{bath}} = 8$.

9.3 Entanglement between nearest neighbors

In this section we finally move to the main goal of the chapter, that is to investigate in detail the quantum correlations between adjacent lattice sites, as described in the 2×2 CDMFT/ED solution of the model. Indeed, in section 9.1 we have shown that a 2×2 plaquette is able to capture all the essential features of the local and nearest-neighbor density matrices. In Fig. 9.7 we show the nearest-neighbor mutual information $I_{\langle ij\rangle}$ (Eq. 7.5) and the charge (parity) superselected measures of the nearest-neighbor entanglement $E^{\text{N(P)-SSR}}_{\langle ij\rangle}$, in the simplified implementation of Eqs. 7.15 and 7.16, as the system is particle-hole symmetric and we checked numerically the condition on ρ_{ij} that is ensured by a global singlet state. Recalling the bounds $E^{\text{N-SSR}}_{\langle ij\rangle} \leqslant E^{\text{P-SSR}}_{\langle ij\rangle} \leqslant E_{\langle ij\rangle} \leqslant I_{\langle ij\rangle}$, we can identify a region (the shaded area in Fig. 9.7) in which the unconstrained nearest-neighbor entanglement $E_{\langle ij\rangle}$ must lie.

Remarkably, both the upper and lower bounds to $E_{\langle ij\rangle}$ show a sudden rise at the Mott transition, in sharp contrast with the monotonic reduction of the single-site von Neumann entropy, and in agreement with the physical insight about the nature of a Mott insulator. This observation is the first signature of a key result of this chapter that we can interpret as a signature of the intimate relationship between strong correlations at the two-site level and Mott localization.

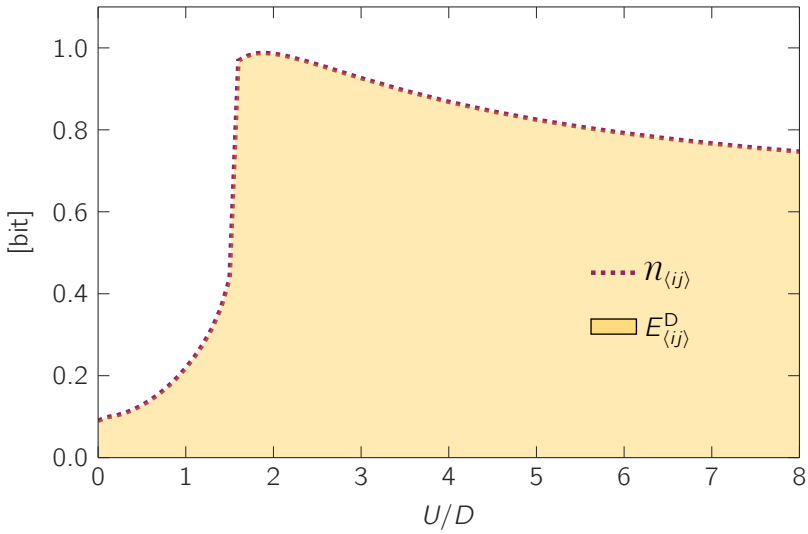


Fig. 9.8.: Nearest-neighbor negativity $n_{\langle ij\rangle}$ as a function of the interaction strength. The shaded area defines the range in which lies the distillable entanglement, given the bound $E^{\mathrm{D}}_{\langle ij\rangle} \leqslant n_{\langle ij\rangle}$. Data from the 2×2 CDMFT/ED simulation with $N_{\mathrm{bath}} = 8$.

Moreover, we observe that both $E^{\text{P-SSR}}_{\langle ij\rangle}$ and $E^{\text{N-SSR}}_{\langle ij\rangle}$ almost vanish throughout the whole metallic phase, and quickly saturate to their maximum value once the Mott insulator is stabilized. The presence of two sharply distinct entanglement scales clearly identifies the two phases, suggesting that these superselected measures are able to capture the adiabatic connection to either the noninteracting and the strong coupling limit, at all intermediate strongly correlated regimes. It is worth remarking that a deeper inspection (inset in Fig. 9.7) reveals a qualitatively different behavior of $E^{\text{P-SSR}}_{\langle ij\rangle}$ and $E^{\text{N-SSR}}_{\langle ij\rangle}$ in the the Fermi liquid. After the Mott transition the superselection rules instead become quickly indistinguishable on the nearest-neighbor entanglement. This can be readily understood by looking at their expressions, see Eqs. 7.15 and 7.16: the two quantities differ by a term depending on the populations of doublons and holons, which asymptotically vanish in the Mott state.

Finally, to further corroborate our results, we compute the nearest-neighbor (logarithmic) negativity $n_{\langle ij\rangle}$, as defined in Eq. 7.19. Its behavior in the Mott phase closely resembles that of the nearest-neighbor mutual information. Recalling that $I_{\langle ij\rangle} \geqslant E_{\langle ij\rangle}$ and that $n_{\langle ij\rangle} \geqslant E^{\mathrm{D}}_{\langle ij\rangle}$, where $E^{\mathrm{D}}_{\langle ij\rangle} \leqslant E_{\langle ij\rangle}$ is the nearest-neighbor distillable entanglement, we cannot give any strong upper bound on the nearest-neighbor entanglement beyond what is already provided by $I_{\langle ij\rangle}$. Yet, one can hypothesize that in the Mott state a good portion of the entanglement is distillable in pure Bell states, in good agreement with the spectral decomposition of $\rho_{\langle ij\rangle}$ at strong coupling (panel (d) in Fig. 9.2), that is largely dominated by a two-site singlet. On the other hand, we find a noninteracting negativity that is much

closer to the superselected lower bounds, than to $I_{\langle ij\rangle}$. This may suggest that a great portion of the nearest-neighbor correlations contained in the Fermi liquid could be classical.

Overall, we can safely affirm that all evidenced we have gathered through our upper and lower bounds to the two-site REE, and the two-site negativity, supports the idea that the quantum and classical correlations contained in pairs of adjacent sites (essentially the lattice bonds, in the Hubbard model), are largely increased by the Mott-Hubbard transition, suggesting that these quantities are able to properly characterize the two phases.

9.4 Role of the SSR on computable quantities

In this section we sharpen our analysis by applying the N-SSR and P-SSR to the other nonlocal correlation markers we have discussed so far, *i.e.* the (single-site) von Neumann entropy, the nearest-neighbor mutual information and the nearest-neighbor negativity. This enables us to understand in a specific and relevant case the effect of the superselection rules, with possible practical relevance for the definition of experimentally accessible entanglement and correlations in realistic protocols based on operations performed onto individual local electronic degrees of freedom [215–220, 236–242]. Moreover, an assessment on the portion of correlations that the SSR remove from these computable quantities, will give valuable insight into what to expect for the non-superselected relative entropy of entanglement, for which an accessible expression is not available.

In order to measure this effect, we introduce the *superselection factors* as

$$\xi_{E_i}^{\text{N(P)-SSR}} \stackrel{\text{def}}{=} \frac{E_i}{E_i^{\text{N(P)-SSR}}} \geqslant 1, \tag{9.2}$$

$$\xi_{I_{ij}}^{\text{N(P)-SSR}} \stackrel{\text{def}}{=} \frac{I_{ij}}{I_{ij}^{\text{N(P)-SSR}}} \geqslant 1, \tag{9.3}$$

$$\xi_{n_{ij}}^{\text{N(P)-SSR}} \stackrel{\text{def}}{=} \frac{n_{ij}}{n_{ij}^{\text{N(P)-SSR}}} \geqslant 1. \tag{9.4}$$

As per their definition, the closer these factors are to the unity, the less relevant the superselection rules become in defining the corresponding restricted measure. The explicit expressions or the algorithms that define the superselected quantities appearing in the denominator are given in sections 7.3.1, 7.3.3 and 7.4.

In Fig. 9.9 we report the local entanglement entropy s_i, the nearest-neighbor mutual-information $I_{\langle ij\rangle}$ and the nearest-neighbor negativity $n_{\langle ij\rangle}$, together with the respective superselected lower bounds and the corresponding superselection factors.

Let us start by discussing the behavior of the local entanglement under both superselection rules: in the noninteracting limit the structure of ρ_i is well understood as a statistical mixture

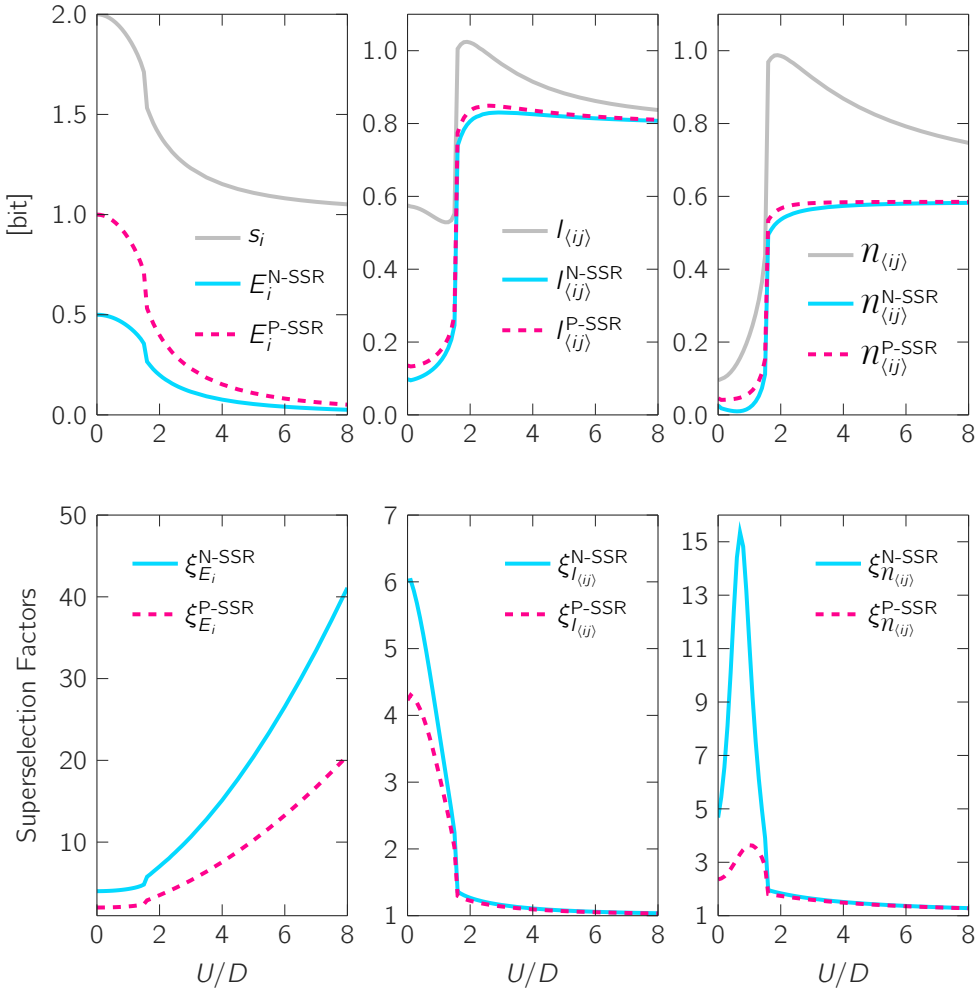


Fig. 9.9.: Effect of charge and particle superselection rules on the local entanglement entropy (left), nearest-neighbor mutual information (middle) and nearest-neighbor negativity (right). The respective *superselection factors* $\xi_{\circ}^{\square\text{-SSR}} = \circ/\circ^{\square\text{-SSR}}$, elucidate the filtering power of the superselection rule on each quantity, for the different regimes. Data from the 2×2 CDMFT/ED simulation with $N_{\text{bath}} = 8$.

of doublons, holons ans single-electron states (in either of the two spin polarizations), whose weights are all equal. As discusses in section 9.1, this is a clear explanation for the value of $s_i = 2\log(2)$, as the local reduced density matrix is maximally entangled. The parity superselection rule halves the corresponding local entanglement to $E_i^{\text{P-SSR}} = \log(2)$, as can be explicitly seen in Eq. 7.10. The further restriction to the charge superselection rule results in a further halving $E_i^{\text{N-SSR}} = \log(2)/2$, as again directly encoded in the relevant expression Eq. 7.9. As can be readily seen by looking at the corresponding superselection factors (respectively 4 and 2, for $U = 0$), the depletion grows larger and larger with the increasing interaction, eventually suppressing the single-site entanglement, in the strong coupling limit. Hence, in general, the highly nonlocal nature of the information that is shared by a single site and the rest of the whole system, makes more and more difficult to extract the corresponding entanglement, as the interaction increases, within protocols that involve only operations that commute with either the local electron number, or its parity. Deep in the Mott state the effect is drastic, as the superselected single-site entanglement asymptotically vanishes.

The nearest-neighbor mutual information, behaves much similarly to the single-site entanglement in the noninteracting metal, with even larger superselection factors. However, once the interaction is switched on, entering the interacting metal described by Fermi liquid theory, both factors start to quickly decrease, up to the point where the qualitative behavior becomes completely the opposite: the unrestricted mutual information decreases with U/D, whereas its superselected lower bounds increase. Eventually, once the MIT is reached, the superselection factors are significantly close to unity, and start approaching it asymptotically. Furthermore, we have also a full coalescence of the two superselection rules in the Mott phase, which can be explained as above, with the near-vanishing of double occupancy (and holon population, by particle-hole symmetry), which renders the effect of the two restrictions imposed by SSR effectively equivalent.

Finally, the behavior of the nearest-neighbor negativity under the charge and parity superselection rules, is remarkably similar to what observed on the mutual information, in the Mott insulator. The fact that the remaining "tails" in the superselection factors are larger for the negativity, with respect to the mutual information, gives probably no significant insight: as the two quantities define upper bounds for different measures of entanglement, their values are not strictly related. We just observe that the qualitative behavior in the Mott state is essentially equivalent. On the contrary, the negativity superselected factors appear to have a strongly varying behavior in the Fermi liquid, which is not monotonic and so does not resemble either of the two other quantities. However, a direct observation of the superselected negativities, reveals that the variations in the superselection factors are just exasperated by the already small value of $\mathcal{N}_{\langle ij\rangle}$, in the weakly interacting metal. Overall, the correct deduction is that nearest-neighbor negativity is the only computable quantity that is not significantly depleted in the Fermi liquid, by enforcing the SSR. As the

negativity does not measure, in principle, any classical correlation (in stark contrast to the mutual information), we could again hypothesize that the two-site correlations in the Fermi liquid are mostly classical and can be ascribed to the itinerant nature of the electronic state. Then, the comparison of the negativity and mutual information superselection factors at low U/D would suggest that the two-site classical correlations are significantly more affected by the superselection rule, if compared with the entanglement.

Overall, the fact that $I_{\langle ij \rangle}$ and $\mathcal{N}_{\langle ij \rangle}$ are much less affected by the SSR, with respect to the single-site entanglement, suggests that the nearest-neighbor (or more in general two-site) quantities are better suited for the characterization of correlated insulators. Furthermore, the superselected measures of mutual information and negativity display a step-like character that is significantly similar to what observed for $E^{\text{P-SSR}}_{\langle ij \rangle}$ and $E^{\text{N-SSR}}_{\langle ij \rangle}$, suggesting that such behavior might be an intrinsic typical feature of the superselection rules. Indeed, the signature of Mott physics is the freezing of local charge fluctuations, thus the N-SSR would constitute a natural physical stage to reveal the underpinning role of strong correlations.

9.5 Entanglement beyond nearest neighbors

In the previous sections we have established that the two-site entanglement between nearest-neighbor sites has several desired features that allow us to overcome the limitations of the local Von Neumann entropy. In this section we explore the entanglement between pair of sites at larger distances. To this end we consider a 4×2 embedded cluster, which we solve in CDMFT/ASCI.

In Fig. 9.10 we show the mutual information I_{ij} between two lattice sites i and j, at distances $d = a, \sqrt{2}a, 2a, \sqrt{5}a, 3a$, where a is the lattice constant. Recalling that I_{ij} represents an upper bound for the two-site quantum correlations, including entanglement (see appendix A, in particular Eq. A.17), we can readily infer that all the quantum correlations between pairs of sites are decay fast with the distance between the two chosen sites, even if they essentially share the same qualitative behavior of the nearest-neighbor quantity. This result suggests that the nearest-neighbor mutual information is indeed the key quantity that provides an effective characterization of the paramagnetic Mott transition of the Hubbard model in terms of entanglement.

We can push further the resulting physical picture thanks to a comparison between the local entanglement entropy and the nearest-neighbor mutual information. Elaborating on the strong subadditivity property of the von Neumann entropy [339] we can write the following inequality (see appendix B):

$$\langle I_{ij} \rangle_{\text{cluster}} \stackrel{\text{def}}{=} \frac{1}{\ell - 1} \sum_{j \neq i} I_{ij} \leqslant 2 s_i, \tag{9.5}$$

where ℓ is the number of sites in the cluster and we recall that I_{ij} represents the mutual information between two arbitrary sites i and j. Hence the local entanglement entropy bounds from above the *cluster-averaged* two-site mutual information $\langle I_{ij} \rangle_{\text{cluster}}$.

The expression for $\langle I_{ij} \rangle_{\text{cluster}}$ contains ζ identical terms, all equal to $I_{\langle ij \rangle}$, where ζ is the number of nearest neighbors of site i in the cluster.

In light of our results (Fig. 9.10), we can assume that the remaining terms in the expression for $\langle I_{ij} \rangle_{\text{cluster}}$ decay with the inter-site distance. Their contribution is then at most a negative additive shift to the value of the local entanglement entropy. This explains the similar tail behavior[1] of s_i and $I_{\langle ij \rangle}$ in the Mott regime.

The latter observation further underlines the quasilocal nature of the two-site entanglement across the whole phase diagram of the model, as the asymptotic behavior of the entanglement between a single-site and all the rest of the lattice is determined by the

[1] *en passant*, the dependency of the tail on the number of nearest neighbors ζ, explains why the 2×2 plaquette and the 4×2 ladder have a significantly different tail in Figs. 9.10: the plaquette is severely underconnected!

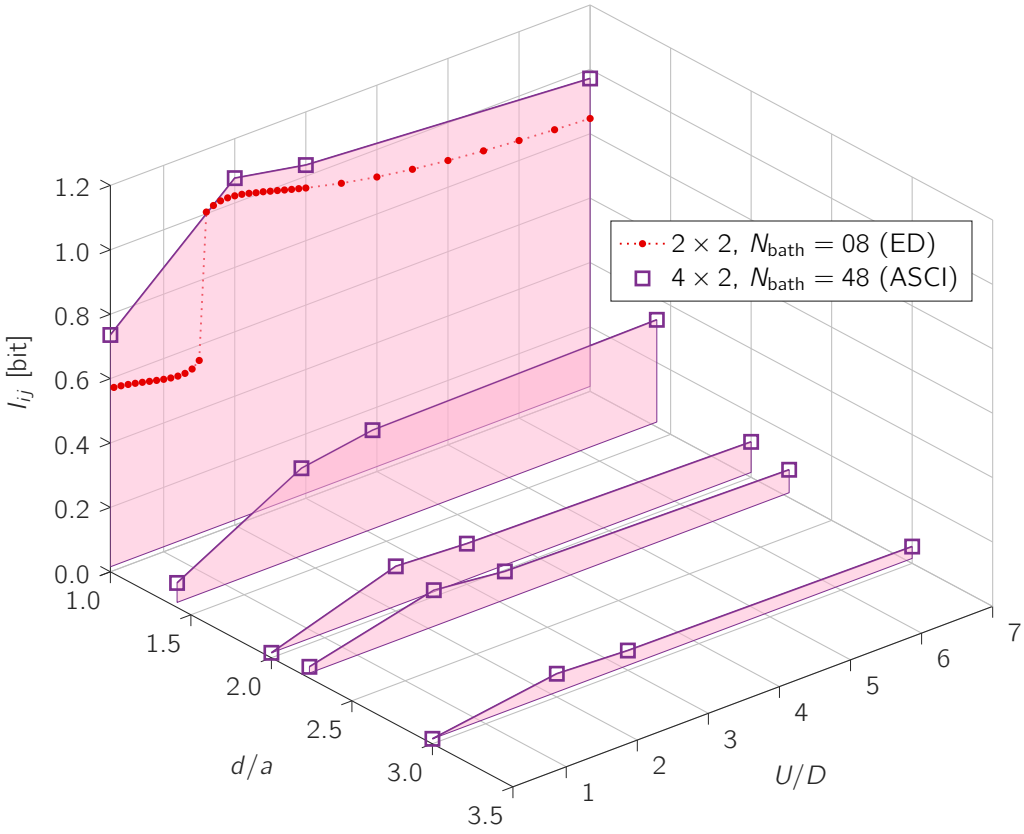


Fig. 9.10.: Two-site mutual information I_{ij} as a function of inter-site distance d/a (with a the lattice spacing) and interaction strength U/D. For $d/a = 1$ it reduces to the nearest-neighbor mutual information $I_{\langle ij \rangle}$ (see main text). The shaded area represents the inequality $E_{ij} \leqslant I_{ij}$, as well as the bound on all correlation functions (Eq. 7.5). Data from ASCI calculations on the 4×2 cluster (squares) and ED calculations for $d/a = 1$ on the 2×2 cluster (filled symbols and dotted line).

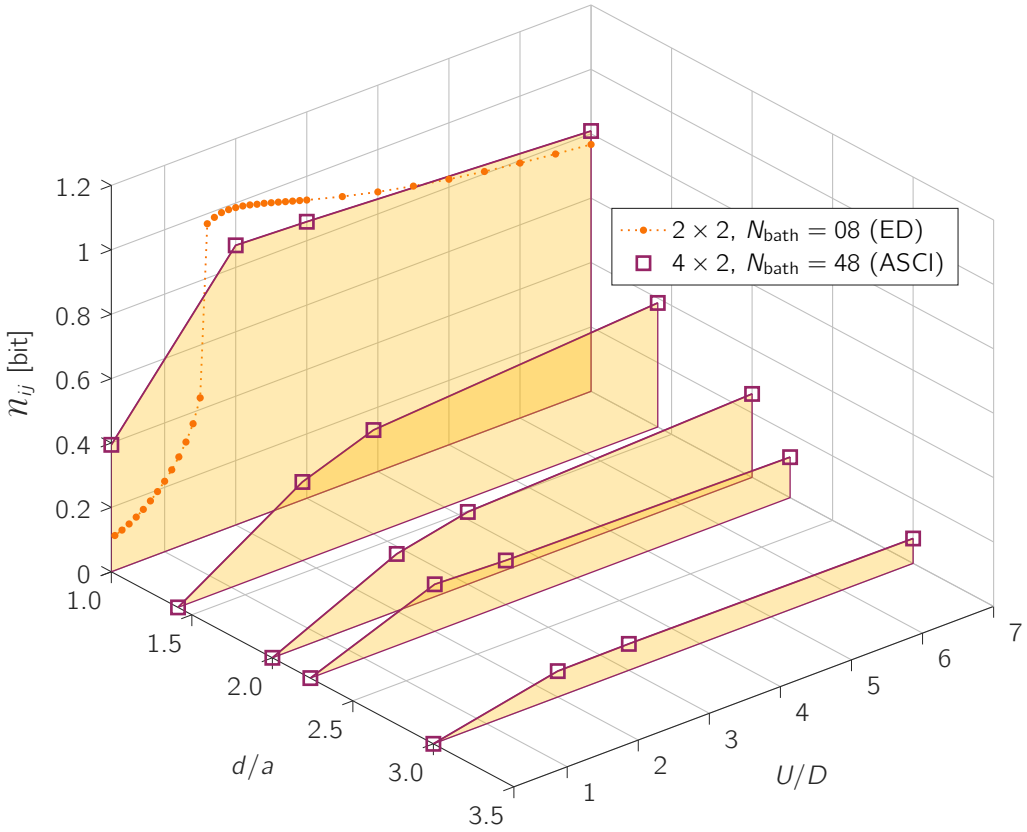


Fig. 9.11.: Two-site negativity n_{ij} as a function of inter-site distance d/a (with a the lattice spacing) and interaction strength U/D. For $d/a = 1$ it reduces to the nearest-neighbor negativity $n_{\langle ij \rangle}$ (see main text). The shaded area represents the inequality $E_{ij}^{\mathrm{D}} \leqslant n_{ij}$, namely a range in which lies the two-site distillable entanglement. Data from ASCI calculations on the 4×2 cluster (squares) and ED calculations for $d/a = 1$ on the 2×2 cluster (filled symbols and dotted line).

nearest-neighbor mutual information, modulo a rigid shift. In particular, we then expect the Mott insulator to have a shorter range than its parent Fermi liquid state.

In this regard we highlight that a rigorous theorem proven by Wolf *et al.* [74], relates the decay of two-point correlations (hence the two-site mutual information, in a lattice) with entanglement area laws, which have been often allowed to classify traditional and exotic states of matter, in a rigorous unified framework [70, 71, 207–209, 228]. This important relationship has been recently confirmed in cold-atom experiments, by Tajik *et al.* [245], opening an exciting research avenue. In particular, the simulation of larger clusters, or longer-range correlations in alternative frameworks, could allow a determination of the area law classification of strongly correlated electronic systems, with the possibility of experimental verification in quantum simulators.

Finally, we report in Fig. 9.11 the spatial decaying of the two-site negativity $\mathcal{N}_{ij}$, again with a rapid decay as a function of the distance, further corroborating the physical picture obtained by the mutual information. Most remarkably, it has recently been shown that the logarithmic negativity of two disjoint subsystems is exponentially suppressed with their distance, in a large class of resonating-valence-bond states [246], thus providing a possible path to test the seminal idea of Anderson, that a Mott-Hubbard insulator might be described in terms of resonating valence bonds [24], with significant consequences in the understanding of cuprates [25].

9.6 Summary and outlook

The local entanglement entropy has been extensively studied through the last decade as a first natural tool to attempt to revisit the physics of the Mott-Hubbard transition under the lens of quantum information theory [61–64]. Although this quantity allows for a full characterization of the quantum phase transition and both its sub- and super-critical thermal signatures, its physical interpretation has been hindered by the lack of a clear distinction between genuinely local and nonlocal contributions [70].

Based on a cluster dynamical mean-field theory analysis of the two dimensional Hubbard model we clarified the role of local and *quasilocal* entanglement and correlations across the Mott transition. In particular, we leveraged the notion of entanglement between local single-particle states (orbitals), to analyze the bipartite entanglement between adjacent and distant sites with no reference to the rest of the system. The two-site entanglement has been shown to give a genuine account of the quasilocal quantum correlation in the Fermi liquid and Mott phases of the paramagnetic Hubbard model.

Despite being well defined as the relative entropy of entanglement (REE), namely the minimal quantum relative entropy (QRE) with respect to the set of two-site separable states, such two-site entanglement has no accessible general expression and its determination

represents an open problem in quantum information theory [271–273]. To circumvent this limitation, we carefully analyze upper and lower bounds to the REE. The former is obtained by a rigorous interpretation of the mutual information as the minimal QRE with respect to the set of uncorrelated states. In this framework several inequalities can be proven (see appendix A), establishing the two-site mutual information as an upper bound for all possibile two-site correlation, as well for the two-site REE and the two-site measure of quantum and classical correlations. The latter are based on recently derived expression for the two-site REE, under charge and parity superselection rules (SSR) [219], amounting to constrain the accessible coherent superposition of quantum states to those conserving the local electron number or its parity, respectively.

For the Mott-Hubbard insulator found in the two-dimensional Hubbard model on the square lattice we proved that the nearest-neighbor total correlation is almost unaffected by the charge and parity SSR. Moreover, the charge and parity superselected two-site entanglement formulas have been proven indistinguishable in the Mott phase, as a direct consequence of charge freezing and localization. Hence we propose the two-site measures of entanglement and correlation as reliable markers for the study of localized phases of matter.

Following the evolution of the entanglement bounds as a function of the interaction strength, we predict a sharp increase of the nearest-neighbor entanglement at the transition point between a metal and a paramagnetic Mott insulator, in contrast with the well-known picture provided by the single-site entanglement entropy, which decreases mononotonically as a function of the interaction, mirroring the behavior of the double occupancy.

Consequently, while the Mott insulator might globally result less spatially entangled than the weak coupling Fermi liquid state according to the single-site entanglement entropy, we argue that the genuine quasilocal quantum correlation is actually increased by Mott localization, thus reconciling with the paradigmatic view of a Mott insulator as a strongly correlated localized system. Further evidence about the quasilocal nature of the two-site entanglement, in both the Fermi liquid and Mott regimes, has been secured by extending our analysis beyond nearest neighbors. Here we use the expression quasilocal precisely to mean that the nonlocal quantum correlation is indeed rapidly decaying with the distance and the main contribution comes from the closest possible sites, the nearest neighbors, even if the qualitative behavior as a function of U is the same for all the distances we could access in our numerical analysis.

All the results have been finally benchmarked with a more conventional, yet less rigorous, measure of the two-site entanglement: the logarithmic negativity, defined as a suitable quantification of violations in the Peres-Horodecki PPT separability criterion, that does not increase under local operations and classical communication, and provides an upper

bound to the distillable entanglement. The physical pictures enlighted by the REE and the negativity are essentially the same, corroborating our findings and their interpretation.

Overall, our results shed new light on the mechanism underlying the transformation of a Fermi liquid metal into a strongly correlated insulator, in the absence of symmetry breaking, bridging the fertile field of quantum information theory with the notoriously tough problem of describing strongly correlated electrons. The analysis is based on CDMFT calculations with clusters sizes ranging up to 8 sites, hence providing a reasonably complete description of the essential physics of the Mott transition, as extensively benchmarked against complementary methods [317, 340]. The addressed cluster sizes allow us for a systematic and computationally affordable study in a well-documented setting. Hence, we emphasize that our results provide a clear characterization of the entanglement properties of the metallic and insulating solutions in the paramagnetic two-dimensional Hubbard model, whose essential details are expected to be valid regardless of the approximation we used to identify it. Yet, there are several directions to verify the robustness of our results, including the analysis of larger clusters within CDMFT or the dynamical cluster approximation (DCA) [189], or even the adoption of different algorithms ranging from quantum Monte Carlo to tensor networks [305–307] and finally the recently demonstrated possibility of measuring the two-site mutual information in cold-atom quantum simulators.

Different fruitful research directions can be envisaged in this respect. Our information theory perspective can indeed provide precious information on the intriguing analogy between nonlocal correlations of the single-band Hubbard model and correlations between different atomic orbitals in multi-orbital systems [109, 112, 341] and, in more general terms, identify a conceptual framework to address the role of nonlocal correlations arising from local interactions in multi-component quantum systems, including unconventional superconductors [115, 116], correlated topological insulators [93] and SU(N) cold-atom systems [125–127].

10 Quasilocal entanglement of a pseudogap metal

In this final chapter of the second part of the thesis, we want to briefly extend our analysis of local classical correlations and quasilocal quantum entanglement in the two-dimensional Hubbard model, beyond half-filling.

As we have discussed in the introductory section O.7, while the Mott transition at half-filling represents the most direct signature of electron-electron correlations, the effect of doping a Mott insulator has proven to be a natural path to exotic strongly correlated phases of matter and it is widely believed to be at least the main ingredient behind high-temperature superconductivity[26]. In this perspective, the pseudogap metal found in copper oxides at intermediate hole-doping and relatively high-temperature (just above the superconducting dome, see Fig. O.8), has attracted a lot of attention, due to both its very peculiar experimental features [55, 104] and contrasting theoretical insights from field-theoretical treatments and numerical simulation on the Hubbard model and close relatives. In particular there has been, on a hand, a growing consensus on the leading role of short-range antiferromagnetic correlations [198–200] and possibly entanglement [202, 338, 342]. On the other hand significant insights have come from detailed analyses of correlation effects on the Fermi surface, [109, 308, 314–316], even relating the onset of the pseudogap with a Lifshitz transition (a sudden change of the Fermi surface topology), for the Hubbard model on the square lattice, in the limit of zero temperature [318].

In the following we attack this subject within the quasilocal picture that we derived at half filling, extending our analysis of the interaction-driven metal-insulator transition. We will leave an analysis of the momentum structure of the entanglement in the doped Hubbard model for future study. Some perspectives on this regard will be given at the end of the thesis (chapter "Conclusion: future directions").

10.1 CDMFT modeling of the pseudogap metal

In the last two decades, cluster dynamical mean-field theory has proven to capture the essential physics of the pseudogap metal in the square lattice in many respects [109, 198, 199, 308, 309, 314, 317, 343, 344], in stark contrast to single-site DMFT, which features a direct transition from the half-filled Mott-Hubbard insulator to the hole-doped Fermi liquid, as long as one considers only single-orbital interactions [345]. In particular, even in the basic 2×2 plaquette theory, the transition between the hole-doped Fermi liquid and the strongly-correlated pseudogap metal, can be tracked by a discontinuous jump in the local density [343]. In Fig. 10.1 we report our own CDMFT/ED calculation of the single-site electron density $\langle n_i \rangle$, at fixed interaction strength $U/D = 2.3$ and varying chemical potential μ/D, for the usual 2×2 plaquette that has lead the stage in chapter 9. To allow a clean analysis of the entanglement properties of the encountered electronic phases we solve the model at zero temperature, constraining the solution to not develop any magnetic or superconducting ordering. Consistently with the low-temperature results of Sordi *et al.* [343], starting from deep in the hole-dominated Fermi liquid metal, we obtain a linearly increasing density $\langle n_i \rangle < 1$ up to a critical value of the chemical potential, at which the computed density experiences the aforementioned discontinuous jump. This marks a first-order transition into the pseudogap phase of the plaquette CDMFT. The resulting pseudogap metal has approximately the same compressibility of the Fermi liquid, resulting in the same linear increase of the density (except for the obvious upwards shift). Finally, the half-filled Mott-Hubbard insulator is approached smoothly, hinting at a second order transformation from one strongly correlated solution to the other. Our estimates of the critical chemical potential values for the two transitions are, respectively, $\mu_{\text{pg}}/D = [-0.72, -0.71]$ and $\mu_{\text{mit}}/D = -0.48$. For easier reference they will be indicated, as vertical dotted lines, in all figures reporting our data. Before proceeding, we point out that our choice for the interaction strength ($U/D = 2.3$) placed the half-filled point in a "weak" (nearly-localized) Mott insulator (compare with the data presented in chapter 9). This will have significant consequences in the following discussion of the observed entanglement properties.

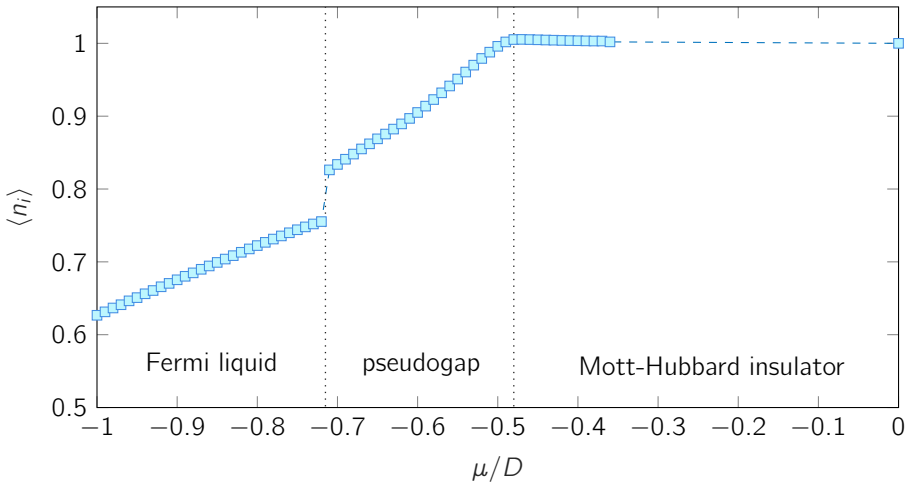


Fig. 10.1.: Hole-doping of the Mott-Hubbard insulator, for $U/D = 2.3$ at zero temperature, in *plaquette* CDMFT/ED with 2×2 impurities and 8 bath sites. The starting point of the calculation is at large doping, deep in hole-dominated the Fermi liquid metal. At intermediate doping a discontinuous jump in the computed density signals a first-order transition into the strongly-correlated pseudogap metal. Approaching half-filling ($\langle n_i \rangle = 1$), the insulating solution is recovered with a smooth, second-order transition.

10.2 Hole-doping phase diagram

A schematic representation of the phase-diagram of the model, on the whole (μ, U) plane is given in the left panel of Fig. 10.2, where the black arrow gives a visual indication of how we traverse the parameter space in our calculations. As a function of the chemical potential, the Mott-Hubbard phase extends more and more as the interaction strength is increased. This is a consequence of the ever-growing gap between the Hubbard bands, approximately linear in U, that has to be overcome by the chemical potential, to introduce a finite doping.

In the right panel of Fig. 10.2 we show, instead, the (δ, U) version of the same phase-diagram, where $\delta = 1 - n$ is the fraction of injected holes in the doped system. Two notable differences immediately strike our eyes: the Mott-Hubbard phases shrinks in the $\delta = 0$ line, as the insulator can exist only at exact half-filling; the boundary between the Fermi liquid metal and the pseudogap phase is "fractured" by the discontinuity in the density: at a given U/D, for certain density values, no solution can be found.

While in principle the two parametrizations in terms of μ and δ are completely equivalent, we choose to always present our data in function of the chemical potential μ as we are interested in probing the robustness of the results for the Mott-Hubbard insulators discussed in chapter 9, for which a study of the μ-dependence of our quasilocal entanglement measures is highly desired.

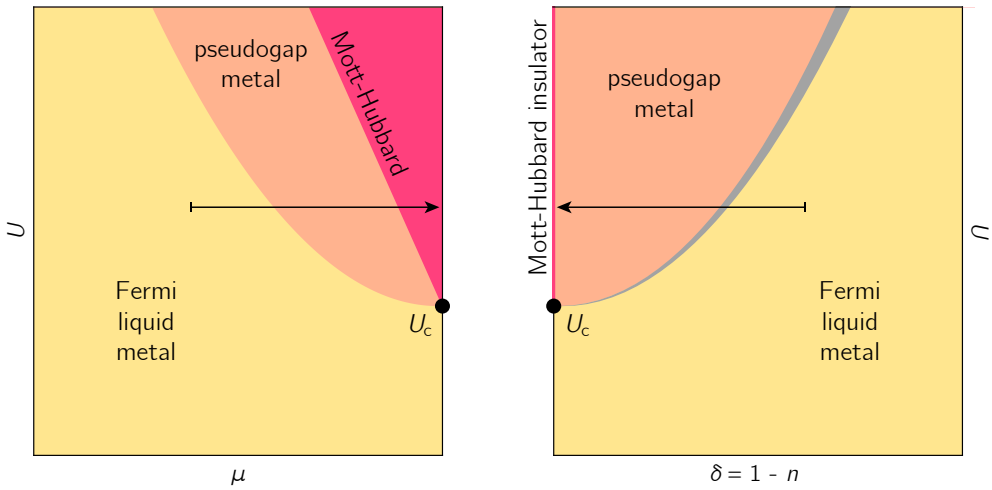


Fig. 10.2.: Qualitative phase-diagram of the hole-doped Hubbard model on the square lattice, at low (zero) temperature and with the exclusion of magnetic ordering. On the left we measure the horizontal axis in values of chemical potential. On the right, instead, we parameterize the phase diagram with the fraction of injected holes $\delta = 1 - n$. U_c is the critical interaction for the metal-insulator transition at half filling ($\delta = 0$). The arrows indicate the direction of our fixed-interaction traversal. Finally the grey area in the right panel indicates the first-order phase transition separating the hole-dominated Fermi liquid and the pseudogap metal. Adapted from Walsh *et al.* [63].

10.3 Single-site von Neumann entropy and local classical correlations

Before delving in the zero temperature analysis of entanglement and correlations, let us briefly give an intuition for the doping dependence of the single-site von Neumann entropy. For that we take intermediate temperature data from Walsh *et al.* [63], where the evolution is smooth and easy to follow in all the regimes. We recall that, in all generality for a single-orbital Hubbard model, the single-site density matrix is diagonal, with elements corresponding to (for the i-th site) $p_1 = 1 - \langle n_i \rangle - \langle n_{i\uparrow} n_{i\downarrow} \rangle = \delta_i - \mathcal{D}_i$, $p_2 = \langle n_{i\uparrow} \rangle - \mathcal{D}_i$, $p_3 = \langle n_{i\downarrow} \rangle - \mathcal{D}_i$ and $p_4 = \mathcal{D}_i$, where $\mathcal{D}_i$ is the double occupancy and δ_i is the fraction of injected holes (see section O.5). Hence all the properties of the single-site von Neumann entropy will directly descend from the behavior of the density and double occupancy.

In the noninteracting limit, marked in Fig. 10.3 with a solid yellow line, the single-site von Neumann entropy decreases monotonically from its value at half-filling, to zero. This can be directly understood from the fact that the the double occupancy is simply given by $\mathcal{D}_i = n_i^2/4$, so that one can easily prove that p_1 gradually approaches the unity, for an increasing hole-doping δ_i, and p_2, p_3 and p_4 all decrease monotonically towards zero. In

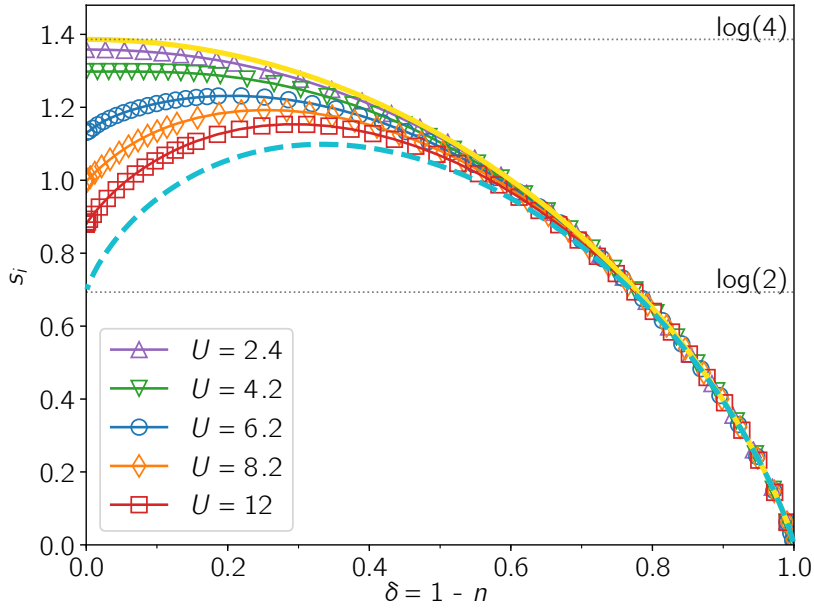


Fig. 10.3.: Doping dependency of the single-site von Neumann entropy at $T = 0.1$, for several values of the Hubbard interaction. Please not that here U is expressed in units of $t = 0.25D$, and that the entropies are expressed in natural units, rather than bits. The solid yellow line marks the noninteracting limit $U = 0$ and the dashed aquamarine line represents the atomic limit $t = 0$. Adapted from Walsh *et al.* [63].

the language of information theory, the more holes are injected into the system, the less uncertain the local electronic configuration becomes, resulting in a ever-decreasing entropy.

On the contrary, in the atomic limit $t = 0$ (dashed aquamarine line in Fig. 10.3) one has a perfect atomic Mott insulator at half-filling $\delta_i = 0$, that is progressively delocalized by doping, with a consequent increase of the entropy up to a given maximum value of log(3) [63]. After that it starts to decrease and eventually vanishes, also in this case because of the complete removal of the uncertainty in the local configuration (given that for $\delta_i = 1$ there are only empty sites in the lattice).

For generic finite interaction values (all the other curves in Fig. 10.3) the results follow qualitatively one or the other behavior, depending on whether the half-filled solution is metallic or insulating. The reduction of s_i at $\delta_i = 0$ reflects the well-known behavior of the single-site entropy accross the interaction driven metal-insulator transition, discussed at length in chapter 9. However, we observe that all the curves in Fig. 10.3 are almost indistinguishable for $\delta_i \gtrsim 0.7$, signaling the presence of a strong competition between the interaction-driven Mott localization and a density-driven delocalization, supported by Fermi statistics.

Hence, as usual, the single-site local entropy is very sensitive to the local physics of the system and interprets well the behavior of the *fluctuations* in the single-site electronic configuration. Furthermore, as for the case if the interaction-driven Mott transition, Walsh *et al.* demonstrate how it can be used to track the position of the supercritical Widom line, the critical end-point and, at low temperatures the first-order transition between the pseudogap metal and the weakly correlated Fermi liquid metal.

In Fig. 10.4 we report our CDMFT/ED data at zero temperature, for the single-site entropy s_i, the single-spin entropy $s_{i\sigma}$ (Eq. O.33) and the intra-orbital classical correlation $I(\uparrow:\downarrow)$ (Eq. O.34). The first quantity correctly captures the discontinuous transition, as an obvious consequence of the behavior of the local density (see Fig. 10.1). Hence we readily confirm the low-temperature predictions of Ref. [63].

The two single-spin entropies coincide exactly at all chemical potential values as the calculation is enforced to be paramagnetic (to avoid antiferromagnetism). They are not, however, fixed at log(2), as the average spin-orbital occupation is decreased by doping.

Finally, the intra-orbital correlation between the two spin-orbitals provides once more a physically sound account of the development of strong correlations across the density-driven MIT. We start with a moderately correlated configuration, corresponding to the Fermi liquid at low density, then we transition with a significant jump to a regime in which $I(\uparrow:\downarrow)$ grows more than linearly and finally we reach a highly correlated state, corresponding to the half-filled Mott-Hubbard insulator. We remark that the zero-doping limit in Fig. 10.4 does not correspond to the maximally correlated spin-orbital pair that we predicted in section O.5 for a deep Mott insulating phase. This is just a consequence of the relatively small value of the interaction we use in the calculation.

Once again, the development of strong classical correlations in an embedded part of a quantum many-body system often implies the presence of large quantum entanglement in the environment (see sections O.5 and 9.2). We proceed to analyze its presence via upper and lower bounds to the nearest-neighbor entanglement in the following section.

10.4 Two-site entanglement and a hint on the quasilocal nature of the pseudogap

In Fig. 10.5 we report, on the left panel, the upper and lower bounds for the nearest-neighbor relative entropy of entanglement (REE) and on the right panel the nearest-neighbor logarithmic negativity, bounding from above the corresponding distillable entanglement.

In the Mott-Hubbard phase (at half-filling), the mutual information $I_{\langle ij\rangle}$ and the negativity $\mathcal{N}_{\langle ij\rangle}$ confirm the similarity of their behavior. Similarly, in the hole-dominated Fermi liquid, both these quantities are significantly smaller with respect to the other phases. In fact,

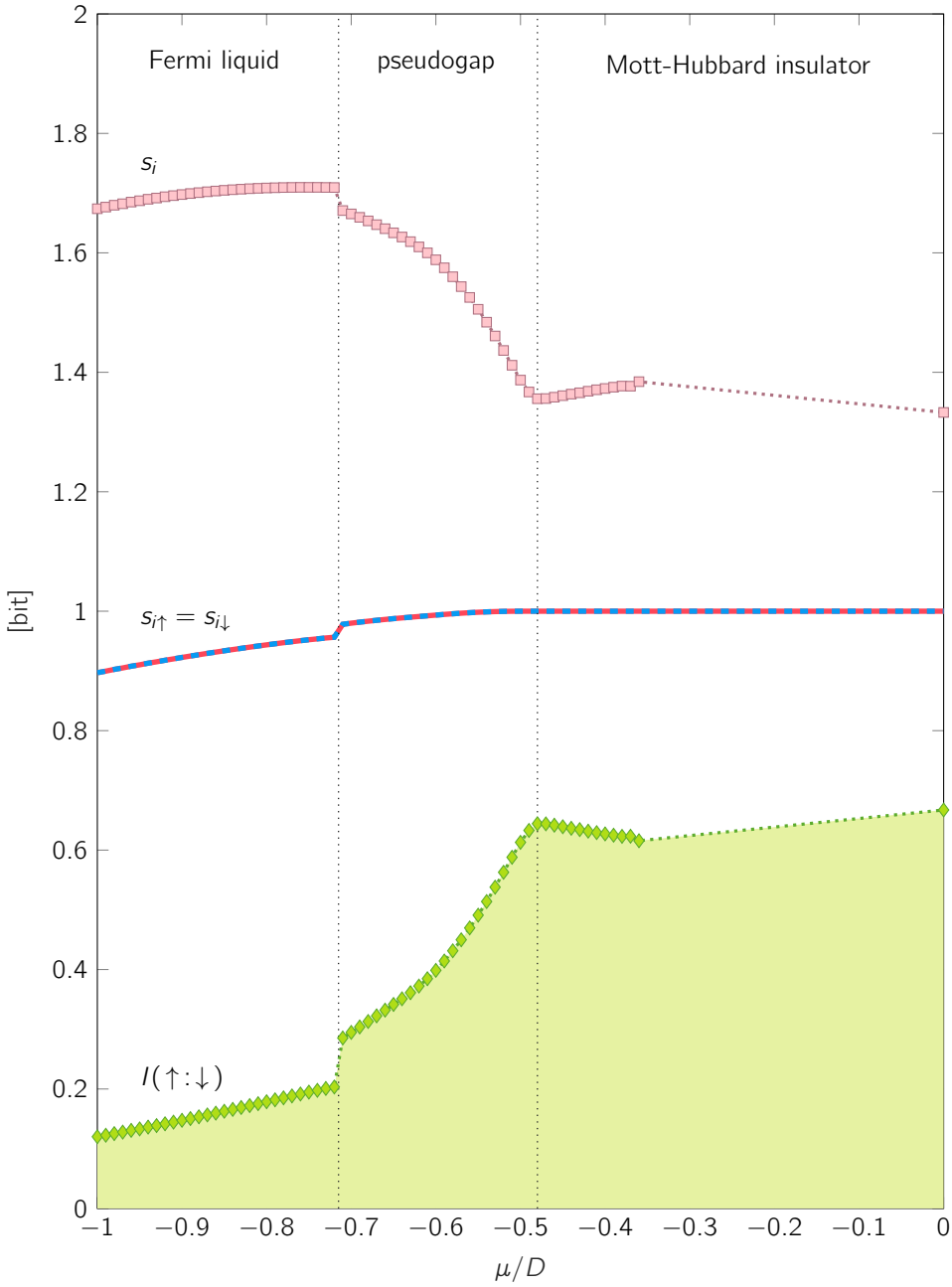


Fig. 10.4.: Evolution of the single-site s_i and single-spin $s_{i\sigma}$ von Neumann entropy and of the intra-orbital correlation $I(\uparrow:\downarrow)$, for $U/D = 2.3$ at zero temperature, in *plaquette* CDMFT/ED with 2×2 impurities and 8 bath sites. The green-shaded area represent all classical correlations in ρ_i, according to Eq. O.28.

especially the negativity assumes a value that is almost identical to the one of the half-filled, weakly interacting metal (compare with Fig. 9.8).

On the other hand, both the charge and parity superselected REE resemble very closely the scenario we have discussed for the interaction-driven MIT: they are essentially vanishing in the Fermi liquid metal, while they are almost pinned to a single value in the Mott-Hubbard insulator. With respect to Fig. 9.7 we see a significant difference in the N-SSR and P-SSR values for the Mott insulator, consistently to the choice of an intermediate interaction value, defining a nearly-localized Mott insulator in which the double occupancy has still an appreciable finite value.

Finally, we come to the intermediate pseudogap regime. Therein, we observe that the nearest-neighbor entanglement varies very rapidly with the chemical potential, essentially interpolating within the large window defined by the values in the strongly correlated insulator and the in the weakly correlated metal. Yet, it appears to be connected continuously (though not necessarily smoothly, in the derivatives) to the Mott insulator, whereas it is separated by a (comparatively small) discontinuity from the Fermi liquid. Thus, we have evidence of a strongly correlated metallic phase that, despite being delocalized and thus subject in principle to large classical correlations, stemming just from the itinerant character of the underlying many-body state, has entanglement properties that possibly suggest an intriguing closer similarity to the Mott-Hubbard state.

10.5 Final remarks

In this chapter, we first gave an overview of some literature results on the single-site entropy in marking distinct feature of the hole-doped phase diagram of the two-dimensional Hubbard model, with an highlight on the physical interpretation in terms of quantification of the local fluctuations in the electronic occupation. Then we reconnected to the *leitmotiv* of this thesis, namely measuring the correlation between two orbitals (or spin-orbitals), first within a single site, so to analyze the classical intra-orbital correlation across the density-driven Mott-Hubbard transition, and finally the inter-orbital entanglement (and correlations) between adjacent sites. Remarkably, a comparison of Figs. 10.4 and 10.5 reveals that, even more that in the case of an interaction-driven MIT, the density-driven Mott transition has a very similar description in terms of classical and local inter-spin correlations or quantum and nonlocal inter-site entanglement. This finding further emphasizes the intimate connection between large nonlocal entanglement and strong local correlations of classical nature, suggesting pathways to make quantum information concepts and tools popular in the realm of local or quasilocal many body methods.

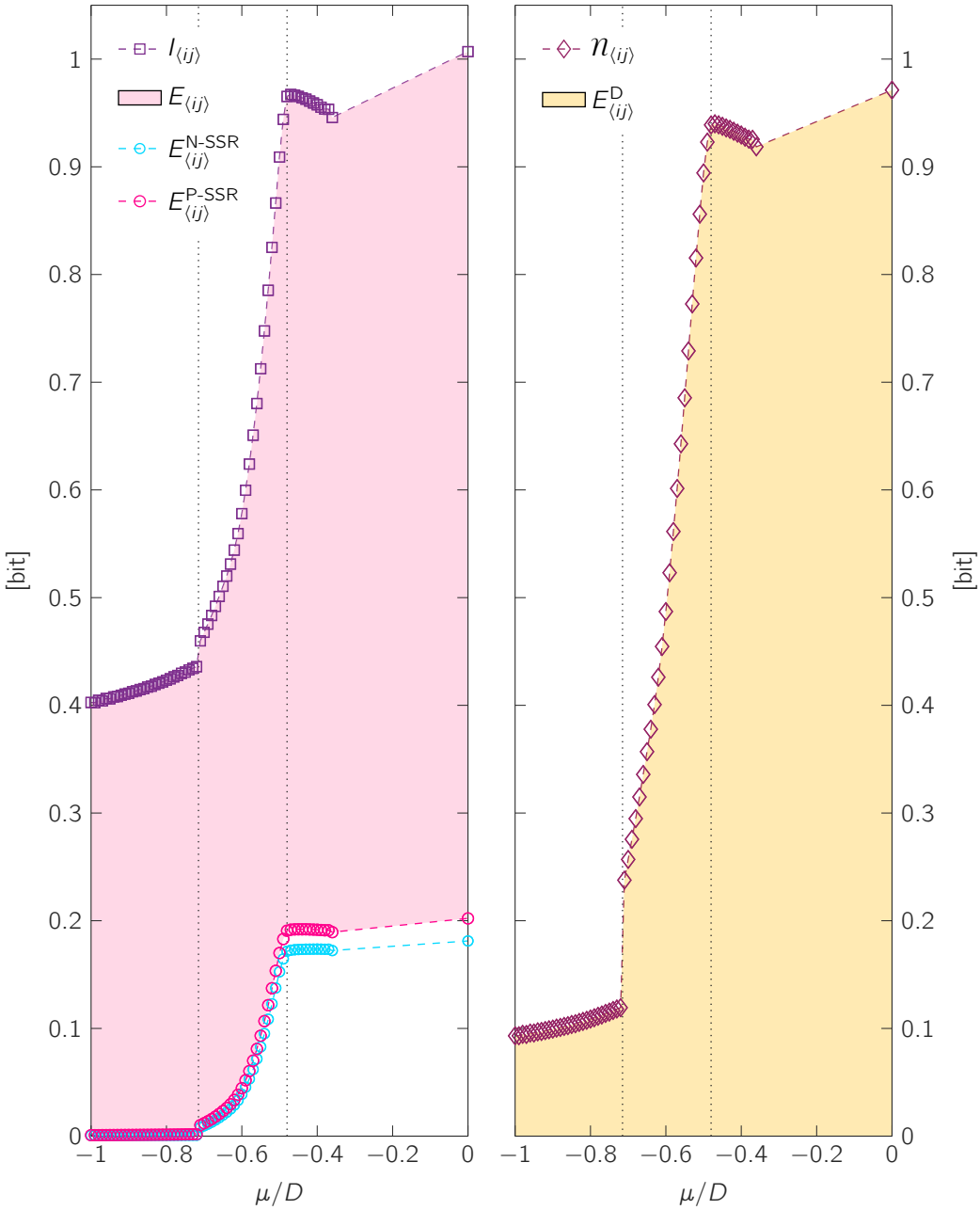


Fig. 10.5.: On the left, nearest-neighbor entanglement, as bounded by the mutual information $I_{\langle ij\rangle}$ and the charge and parity superselected relative entropy of entanglement $E^{\text{N(P)-SSR}}_{\langle ij\rangle}$. The shaded area represents the region in which $E_{\langle ij\rangle}$ must lie. On the right, nearest-neighbor distillable entanglement, as bounded from above by the logarithmic negativity $n_{\langle ij\rangle}$. The shaded area represents the region in which $E^{\text{D}}_{\langle ij\rangle}$ must lie. Data for $U/D = 2.3$ and zero temperature, computed in *plaquette* CDMFT/ED with 2×2 impurities and 8 bath sites. The vertical lines mark the two quantum phase transitions.

Conclusion: future directions

In this thesis we have discussed different aspects of strongly correlated electronic systems, analyzed under the lens of quantum information theory. While we have provided conclusive thoughts for each main line, namely in chapters 5, 9 and 10, with a focus generally confined to the specific topic or area of interest, here we want to give a bird-eye view of what has been discussed and examine broader aspects that deserve further investigation.

In the first part, we focused on the description of the local physics of interacting topological insulators, as provided by dynamical mean-field theory (DMFT) on the Kane-Mele-Hubbard model [87, 88, 130]. We complemented a standard analysis of antiferromagnetic transitions, in terms of the magnetic order parameter and the single-particle gap, with a quantum-information inspired notion of pseudo-distance from the set of uncorrelated states, as provided by mutual information in the framework of the quantum relative entropy. This quantity, defined for two localized spin-orbitals, has been proven to exactly vanish in any Hartree-Fock calculation, giving a valuable interpretative key for the difference between the two methods and their characterization of the model and its phase diagram.

Furthermore, the same analysis has been applied to the paramagnetic Mott transition of topological Dirac fermions, demonstrating the development of maximal correlations between the two local spin orbitals. This in turn has suggested the possible presence of nonlocal quantum entanglement in Mott-Hubbard insulators, according to the principle that classical correlations in an open quantum system, at zero temperature, are usually generated by quantum correlations in its environment [173].

Guided by this intriguing result, in the second part of the thesis, we turned to the popular two-dimensional Hubbard model, for which we have constructed and computed suitable measures of quasilocal (short-range) quantum correlation, in terms of the bipartite entanglement between two electronic orbitals located at different lattice sites. Our results, obtained within a well-studied and successful cluster extension of DMFT (CDMFT), confirm the physical intuition and expectations for Mott-Hubbard insulators, as strongly correlated localized systems, and, most importantly, shed new light on the quasilocal properties of the doped pseudogap metal, suggesting a deep connection with the Mott state. However, the pseudogap has yet a Fermi surface, whose strongly anisotropic features hint at a significant interplay between the quasilocal picture and the long-distance properties. We prospect a

careful extension of our analysis, targeting the bipartite entanglement between $\boldsymbol{k}$ points (or patches) and eventually complementing the existing description of the pseudogap metal as a momentum-selective Mott phase [308, 314–316]. This program could be tackled both within the dynamical cluster approximation (DCA), an alternative extensions of DMFT that naturally lives in $\boldsymbol{k}$-space, or by *periodizing* the reduced density matrix of the full cluster in CDMFT and subsequently tracing from it the reduced density matrices for given, discrete, reciprocal lattice points (see section 8.3).

At this point, it is important for us to provide a brief discussion about the possible limitations of our approach, in particular concerning the evaluation of reduced density matrices, a wavefunction-based object, within a Green's function method. The dynamical mean-field theory, as well as its cellular extension, is formulated around a self-consistency at the single-particle level [38], whereas the reduced density matrices for a two-orbital subsystem, or even a single-orbital subsystem, are respectively four-particle and two-particle operators. We observe, however, that the long wielded expectation value for the population of double occupied orbitals, the double occupancy, is a two-particle property that has been frequently and extensively analyzed in DMFT calculations, with the appearance of careful studies on the best strategy to evaluate it, starting from a self-consistent single-particle Green's function [346]. The resulting predictions are indeed always qualitatively correct and often essentially accurate. Hence we can assume that our analysis of entanglement properties is likely to inherit at least the qualitative truthfulness of established CDMFT literature.

The straightforward quantitative extension of our analysis is naturally rooted in *diagrammatic* extensions of dynamical mean-field theory [293–295], which bring the theory beyond the single-particle level, with the nontrivial bonus of inserting long-range correlations into the picture. In light of this perspective, a particularly interesting work by Roosz *et al.* [65] has captured our attention, as it gives a closed expression for two-orbital reduced density matrices in terms of two-particle Green's functions. The result is remarkable in a twofold way: (i) as mentioned above, the two-orbital reduced density matrix is in principle a four-particle quantity, so we find particularly fortunate that it can be expressed in terms of the two-particle propagator and (ii) two-particle vertices and Green's functions are a common language of a great multitude of many body methods, whereas our *ad hoc* evaluation of the reduced density matrices is inherently bound to applying exact diagonalization and closely related methods to the solution of the auxiliary impurity problem. Hence, we prospect a flourishing interconnection between our proposed physical interpretation of two-orbital measures of entanglement, as a guiding light for the understanding of exemplary phases of strongly correlated electrons, and this new universal methodology, which gives access to the relevant quantities to the broader field of diagrammatic many-body methods.

On the other hand, the recent advent of alternative, wavefunction-based, quantum embedding schemes [347–352] gives the potential to extend our analysis also beyond the

DMFT world, in a class of methods that are increasingly proving to be well-suited to treat strongly correlated electrons in realistic models for solid-state materials [353] and molecular systems [354], at a fraction of the computational cost.

Finally, in the area of fundamental quantum mechanics of many-body systems, we find particularly interesting the investigation of possible strong connections between the long-standing framework of Fermionic entanglement constrained by superselection rules [215–218, 220, 236–242] and the concept of symmetry-resolved entanglement, as recently introduced in statistical physics and gauge theory [267, 285–289].



Pictorial representation of some future directions to extend the research reported in this thesis. The Feynman diagram represents diagrammatic extensions of DMFT, such as the dynamical vertex approximation (DΓA), "periodization" is referred to direct extensions to momentum space within CDMFT or the dynamical cluster approximation (DCA) and "RISB++" stands for quantum embedding schemes based on the rotationally invariant slave-boson (RISB) formalism [347], such as the cluster-RISB method [348, 349] and the ghost-Gutzwiller variational approximation [350–353]. The "hardness" of the paths represents a rough estimation of the *numerical* complexity of the different methods, with no reference to conceptual challenges.

Appendix

A Geometrical approach to entanglement and correlations

In this appendix we briefly review a relative entropy based, geometrical method to measure and classify different kind of bipartite correlations, valid for generic mixed quantum states. We mainly follow Refs. [72, 73, 260, 280], but the reader can find a broader account to the emerging field of quantum information geometrical in Refs. [262, 263], where the discussion is extended also to multipartite entanglement. For a general introduction to the theory of entanglement measures, please refer to Refs. [247, 248].

A.1 An information distance for quantum states

Let us start by considering a complex Hilbert space $\mathbb{H}$ of dimension d. The corresponding set $\mathbb{D}$ of density matrices is given by all Hermitian operators ρ acting on the corresponding Fock space $\mathbb{F}$ [356–358], that are positive semi-definite and have normalized trace:

$$\mathbb{D} = \left\{ \rho : \mathbb{F} \xmapsto{\text{linear}} \mathbb{F} \;\middle|\; \rho^\dagger = \rho,\ \langle\psi|\rho|\psi\rangle \geqslant 0\ \ \forall\, |\psi\rangle \in \mathbb{F},\ \ \mathrm{tr}(\rho) = 1 \right\} . \tag{A.1}$$

As sketched in Fig. A.1, $\mathbb{D}$ is a convex set [359], given that $\lambda\rho + (1-\lambda)\rho' \in \mathbb{D}$ for any two density matrices ρ, $\rho' \in \mathbb{D}$ and real $\lambda \in [0,1]$. Moreover, $\mathbb{D}$ is bounded and closed (*i.e.* compact) and we can relate its boundary with an important limit in quantum information theory. Indeed, it can be proved that a density matrix ρ lies on the boundary of $\mathbb{D}$ if at least one of its eigenvalues vanishes and that if all eigenvalues but one vanish then ρ which cannot be written as a convex combination [359] of other elements of $\mathbb{D}$. Hence, the set of extreme points of $\mathbb{D}$ is given by all pure states in $\mathbb{F}$:

$$\mathrm{extreme}(\mathbb{D}) = \left\{ \rho : \mathbb{F} \xmapsto{\text{linear}} \mathbb{F} \;\middle|\; \rho = |\psi\rangle\langle\psi|\ \ \forall\, |\psi\rangle \in \mathbb{F} \right\} . \tag{A.2}$$

It follows that, for Hilbert spaces of dimension $d = 2$ (describing qubits), the boundary of $\mathbb{D}$ degenerates into the two pure states.

A general and natural way to quantify the similarity of quantum states entails the introduction of a notion of distance in the $\mathbb{D}$ space. The main advantage of a distance-based comparison lies in the universality of its predictions: whenever two density matrices are close to each other in $\mathbb{D}$, their expectation values for *any* observable are close in $\mathbb{R}$, coalescing in the limit of zero distance. The generality of this approach ultimately allows a unified

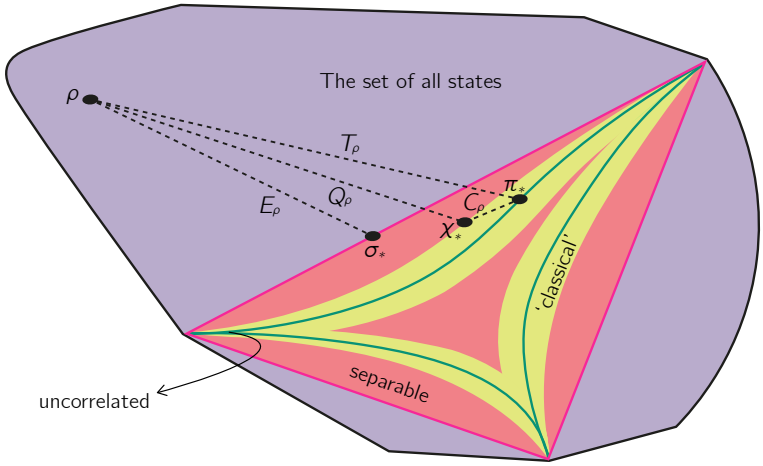


Fig. A.1.: Schematic illustration of the state space $\mathbb{D}$. The subsets of uncorrelated ($\mathbb{D}_\otimes$), classically correlated ($\mathbb{D}_{\text{cl}}$) and separable states ($\mathbb{D}_{\text{sep}}$) are shown in green, yellow and red, respectively. The geometric measures of total correlation T_ρ, quantum correlation Q_ρ and entanglement E_ρ are given by the quantum relative entropy of ρ, minimized with respect to those sets, with corresponding "closest states" π_*, χ_* and σ_*. The measure of classical correlations C_ρ arises as the distance between the closest uncorrelated π_* and the closest classically correlated χ_* states. Picture adapted from Refs. [73, 247, 248]. A realistic representation of the geometry of $\mathbb{D}$ for a simple system of two qubits can be found in [355].

and rigorous quantification of quantum and classical correlations, on the basis of quantum geometry.

In principle, the choice of a distance for the space of quantum states is completely arbitrary, as long as it satisfies a minimal set of required properties. A prominent choice is given by the *quantum relative entropy* [72, 73, 257–260, 270, 280, 360, 361]:

$$S(\rho||\rho') \stackrel{\text{def}}{=} \text{tr}\left(\rho\log\rho - \rho\log\rho'\right) . \tag{A.3}$$

In a strict mathematical sense the quantum relative entropy does not define a metric, as it is not symmetric (*i.e.* $S(\rho||\rho') \neq S(\rho'||\rho)$) and does not obey the triangle inequality. Nevertheless, it is always non-negative, vanishing only for $\rho \equiv \rho'$ [66, 270], and it can be seen as a measure of the *information distance* of the two density matrices ρ and ρ' [258, 259, 270], similarly to how two classical probability distributions can be compared by computing their Shannon relative entropy [76, 362]. Other choices, as *e.g.* the *Bures-Wootters-Fisher* metric or the trace distance, have been explored [261, 363–366] with great success for the extension to multipartite systems [247, 255, 263].

A.2 Quantifying correlations

The quantum information concepts of correlation and entanglement in a quantum state ρ cannot be defined without a notion of partition into subsystems [66, 69]. While the usual subsystems studied in quantum information theory are individual particles, effectively *distinguishable* by virtue of a significant spatial separation, in condensed matter systems the so-called *particle picture* remains much less understood [215, 218, 268] and most progress has been achieved in the alternative *orbital picture*: in this framework, the system is partitioned in orbital space and the fundamental subsystems are not particles but localized single-particle states [216, 218], which are naturally distinguishable by application of local operations. Therefore, in order to discuss bipartite entanglement and correlations within condensed matter systems, we will consider a Fock space in the form

$$\mathbb{F} = \mathbb{F}_\mathrm{A} \otimes \mathbb{F}_\mathrm{B}, \tag{A.4}$$

where A and B are two complementary orbital subsets of the whole system. The tensor product structure of the Fock space arises naturally in second quantization, from a *direct sum* decomposition of the single particle Hilbert space $\mathbb{H} = \mathbb{H}_\mathrm{A} \oplus \mathbb{H}_\mathrm{B}$ [211, 356–358].

Local measurements in A and B are represented by Hermitian observables $\mathcal{O}_\mathrm{A}$ and $\mathcal{O}_\mathrm{B}$ acting respectively on $\mathbb{F}_\mathrm{A}$ and $\mathbb{F}_\mathrm{B}$. The correlation between these two measurements is described by the correlation function

$$\begin{aligned} \mathrm{corr}(\mathcal{O}_\mathrm{A}, \mathcal{O}_\mathrm{B}) &= \langle \mathcal{O}_\mathrm{A} \otimes \mathcal{O}_\mathrm{B} \rangle_\rho - \langle \mathcal{O}_\mathrm{A} \otimes \mathbb{1}_\mathrm{B} \rangle_\rho \langle \mathbb{1}_\mathrm{A} \otimes \mathcal{O}_\mathrm{B} \rangle_\rho \\ &= \langle \mathcal{O}_\mathrm{A} \otimes \mathcal{O}_\mathrm{B} \rangle_\rho - \langle \mathcal{O}_\mathrm{A} \rangle_{\rho_\mathrm{A}} \langle \mathcal{O}_\mathrm{B} \rangle_{\rho_\mathrm{B}} , \end{aligned} \tag{A.5}$$

where $\rho_{\{\mathrm{A,B}\}} = \mathrm{tr}_{\{\mathrm{B,A}\}}(\rho)$ is the reduced density matrix for subsystem A or B and $\mathbb{1}_{\{\mathrm{A,B}\}}$ the identity operator acting on the local Fock space $\mathbb{F}_{\{\mathrm{A,B}\}}$.
A density matrix ρ is uncorrelated with respect to the bipartition into subsystems A and B if and only if Eq. A.5 vanishes for *all* pairs of local Hermitian observables $\mathcal{O}_\mathrm{A}, \mathcal{O}_\mathrm{B}$. This is equivalent to the factorization of ρ into its reduced density matrices:

$$\mathrm{corr}(\mathcal{O}_\mathrm{A}, \mathcal{O}_\mathrm{B}) = 0 \ \ \forall \mathcal{O}_\mathrm{A}, \mathcal{O}_\mathrm{B} \quad \Leftrightarrow \quad \rho = \rho_\mathrm{A} \otimes \rho_\mathrm{B}. \tag{A.6}$$

The corresponding set of uncorrelated (*i.e.* product) states,

$$\mathbb{D}_\otimes \stackrel{\mathrm{def}}{=} \{ \pi \in \mathbb{D} \ \mid \ \pi = \pi_\mathrm{A} \otimes \pi_\mathrm{B} \} , \tag{A.7}$$

is schematically illustrated in Figure A.1 as a solid green line. We observe that a product state $\pi \in \mathbb{D}_\otimes$ is pure if both its reduced density matrices π_A and π_B are pure. Hence all pure product states must lie on the extreme of $\mathbb{D}$ (Eq. A.2).

Having identified the set of all uncorrelated states, with respect to the $\mathbb{F} = \mathbb{F}_A \otimes \mathbb{F}_B$ bipartition, a natural geometrical measure of the *total* correlation contained in a quantum state ρ is given as its minimal relative quantum entropy with respect to the $\mathbb{D}_\otimes$ set

$$T_\rho(A:B) \stackrel{\text{def}}{=} \min_{\pi \in \mathbb{D}_\otimes} S(\rho||\pi)\,, \tag{A.8}$$

Remarkably, the set minimization in A.8 can be performed analytically [72], finding the closest uncorrelated state as $\pi_* = \rho_A \otimes \rho_B$ and identifying the total correlation with the mutual information between A and B

$$T_\rho(A:B) \equiv I(A:B) \stackrel{\text{def}}{=} s(\rho_A) + s(\rho_B) - s(\rho)\,, \tag{A.9}$$

where $s(\circ) = -\operatorname{tr}(\circ \log \circ)$ denotes the von Neumann entropy. As already mentioned in the main text (see section O.5), all bipartite correlation functions (Eq. A.5) are bound from above as

$$\frac{|\operatorname{corr}(\mathcal{O}_A, \mathcal{O}_B)|}{\sqrt{2}\|\mathcal{O}_A\|\,\|\mathcal{O}_B\|} \leqslant \sqrt{T_\rho(A:B)} \tag{A.10}$$

(corresponding to Eq. O.28 in the main text)

where $\|\mathcal{O}_\circ\|$ denotes the Euclidean operator norm of $\mathcal{O}_\circ$, namely its largest singular value. Eq. A.10 reveals the quantitative power of the geometrical approach based on the quantum relative entropy, given that whenever a quantum state results arbitrarily close to $\mathbb{D}_\otimes$, correlation functions must vanish for *any* choice of local observables $\mathcal{O}_A, \mathcal{O}_B$.

A.3 Classifying correlations

Due to the statistical meaning of the quantum relative entropy [76, 259, 270, 362], the total correlation (Eqs. A.8 and A.9) quantifies the additional information content that the state ρ carries with respect to the product state $\rho_A \otimes \rho_B$. The adjective "total" has been traditionally used [72, 260] to emphasize that $T_\rho(A:B)$ includes both classical and quantum correlations. Given that physical systems and their states cannot really be decomposed in separate classical and quantum parts, all attempts in classifying phenomena as either classical or genuinely quantum keep generating heated debates, especially in relation to the possibility of devising quantum protocols that outperform any classical counterpart, in data processing and computational tasks [66, 366–373]. In the following we will define suitable supersets of $\mathbb{D}_\otimes$, allowing a clear definition of disentangled (separable) and classically correlated (pseudo-classical) states. The pseudo-metric induced by the quantum relative entropy will then allow a rigorous quantification of entanglement, quantum correlations beyond entanglement and classical correlations, all within the same unified geometrical picture [72, 73, 260].

A.3.1 Separable states and entanglement

Separable states are defined as the density matrices that can be using only local operations and classical communication (LOCC) [66, 69, 247]. With local operations we mean, in this context, all Hermitian operators acting on the subsystem Fock spaces $\mathbb{F}_{\mathrm{A}}$ and $\mathbb{F}_{\mathrm{B}}$. These allow two independent (possibly distant) parties to prepare any uncorrelated state $\rho = \rho_{\mathrm{A}} \otimes \rho_{\mathrm{B}}$, given that all necessary information is contained in the two reduced states alone. Classical communication between the parties further allows the preparation of arbitrary statistical mixtures of uncorrelated states. Hence, the set of separable states can be defined as the *convex hull* [359] of $\mathbb{D}_{\otimes}$:

$$\mathbb{D}_{\mathrm{sep}} \stackrel{\mathrm{def}}{=} \left\{ \sigma \in \mathbb{D} \;\middle|\; \sigma = \sum_i p_i \, \sigma_{\mathrm{A}}^i \otimes \sigma_{\mathrm{B}}^i, \;\; p_i \geqslant 0, \;\; \sum_i p_i = 1 \right\}. \tag{A.11}$$

Any state ρ that is not separable is called entangled and, given the impossibility to be prepared by LOCC, can in principle be used as a *resource* in quantum information and quantum computing protocols [66, 69, 366, 367]. We observe that the extreme points of the separable states (the pure product states), are also extreme points of the set of all states [extreme($\mathbb{D}_{\mathrm{sep}}$) $\subseteq$ extreme($\mathbb{D}$)] as illustrated in Fig. A.1. Furthermore, any separable state can be written as a convex combination of $d + 1$ extreme points, as assured by Carathéodory's theorem [359, 374]. Nevertheless, the complete characterization of the $\mathbb{D}_{\mathrm{sep}}$ set, *i.e.* the determination of its volume and boundary for general quantum systems is a formidable open problem in quantum information theory (known as *separability problem*) [271, 272].

Much as for the total correlation, the bipartite entanglement contained in a given state ρ can be quantified through the quantum relative entropy, as the minimal pseudo-distance between ρ and the $\mathbb{D}_{\mathrm{sep}}$ set [257, 258]:

$$E_\rho(\mathrm{A} : \mathrm{B}) \stackrel{\mathrm{def}}{=} \min_{\sigma \in \mathbb{D}_{\mathrm{sep}}} S(\rho||\sigma) = S(\rho||\sigma_*)\,. \tag{A.12}$$

The result of the minimization, $S(\rho||\sigma_*)$, is traditionally called relative entropy of entanglement (REE) [259, 270] and can be proven to fulfill all the requirements for a faithful measure of bipartite entanglement: it is always non-negative, vanishing only for separable states, it does not increase under LOCC, it does not change under local unitary operations (changes of basis in $\mathbb{F}_{\mathrm{A}}$ and $\mathbb{F}_{\mathrm{B}}$) [247, 257, 270]. Unfortunately, no general closed expression exists for the REE and its numerical evaluation can be proven to be NP-complete, as it is equivalent to the separability problem [273]. However, for pure states $\rho = |\psi\rangle\langle\psi|$, the minimization in Eq. A.12 can be carried out analytically, recovering the von Neumann entropy [257, 270]

$$E_{|\psi\rangle\langle\psi|}(\mathrm{A} : \mathrm{B}) \equiv s(\rho_{\mathrm{A}}) \equiv s(\rho_{\mathrm{B}}). \tag{A.13}$$

A.3.2 Pseudo-classical states and quantum discord

Entanglement has proven to be a key concept in quantum information theory and many body physics [73, 203–214], with a broad relevance as a resource for quantum information and quantum computing tasks [66, 366, 367]. Yet, quantum correlations are not limited to entanglement, as they can be detected and exploited as a quantum resource on (mixed) separable states too, giving rise to the notion of *quantum discord* [173, 375–380]. The necessary and sufficient conditions to observe quantum discord are well-known [355] and lead to the definition of *pseudo-classical* (classically correlated) states, as the family of separable states with zero quantum correlation [72, 73, 378, 381]:

$$\mathbb{D}_{\text{cl}} \stackrel{\text{def}}{=} \left\{ \chi \in \mathbb{D}_{\text{sep}} \;\middle|\; \chi = \sum_{a,b} p_{ab} \, |a\rangle\langle a| \otimes |b\rangle\langle b| \right\}. \tag{A.14}$$

where $\{|a\rangle\}$ and $\{|b\rangle\}$ could be *any* bases for the two local Fock spaces $\mathbb{F}_{\text{A}}$ and $\mathbb{F}_{\text{B}}$, respectively and $p_{ab} \geqslant 0$, $\sum_{ab} p_{ab} = 1$. To understand why the states in $\mathbb{D}_{\text{cl}}$ should be regarded as effectively classical, we observe that there exists joint (simultaneous) local measurements $\{\mathscr{P}_a \otimes \mathscr{P}_b\}$ which leave the state χ unchanged, as $\{\mathscr{P}_a\}$ and $\{\mathscr{P}_b\}$ are projectors onto the local eigenstates $\{|a\rangle\}$ and $\{|b\rangle\}$, respectively. Therefore all correlations encoded in the resulting joint probability distribution $\{p_{ab}\}$ are to be considered of a classical nature [72, 260, 381]. Any state not in $\mathbb{D}_{\text{cl}}$ then contains quantum correlations, either beyond entanglement or comprising it, depending on whether the state is separable or not.

By invoking again the geometrical picture of quantum states (Fig. A.1), we quantify quantum correlations as the minimum relative entropy of the given state, with respect to the set of pseudo-classical states [72, 73, 260, 361]:

$$Q_\rho(\text{A} : \text{B}) \stackrel{\text{def}}{=} \min_{\chi \in \mathbb{D}_{\text{cl}}} S(\rho||\chi) = S(\rho||\chi_*). \tag{A.15}$$

We observe that $\mathbb{D}_\otimes \subseteq \mathbb{D}_{\text{cl}}$, since every uncorrelated state can be written in the form of Eq. A.14:

$$\rho_{\text{A}} \otimes \rho_{\text{B}} = \left(\sum_a p_a \, |a\rangle\langle a| \right) \otimes \left(\sum_b p_b \, |b\rangle\langle b| \right). \tag{A.16}$$

Indeed taking a factorized joint probability $p_{ab} = p_a \times p_b$ is equivalent to assume the outcomes of measurements on the two subsystems as independent variables, in classical probability theory. On the other hand, the set $\mathbb{D}_{\text{sep}}$ is a superset of $\mathbb{D}_{\text{cl}}$, as the reduced states $\{\sigma^i_{\text{A}}\}$ and $\{\sigma^i_{\text{B}}\}$ in Eq. A.11 are typically not simultaneously diagonalizable for all i. Thanks to the geometrical properties of the quantum relative entropy, these inclusion relations result in the following inequality chain:

$$\mathbb{D}_\otimes \subseteq \mathbb{D}_{\text{cl}} \subseteq \mathbb{D}_{\text{sep}} \iff T_\rho(\text{A} : \text{B}) \geqslant Q_\rho(\text{A} : \text{B}) \geqslant E_\rho(\text{A} : \text{B}). \tag{A.17}$$

For pure states $\rho = |\psi\rangle\langle\psi|$, the only possible source of quantum correlations is entanglement, so that quantum discord and the REE coalesce into the von Neumann entropy [376]

$$Q_{|\psi\rangle\langle\psi|}(\mathrm{A}:\mathrm{B}) = E_{|\psi\rangle\langle\psi|}(\mathrm{A}:\mathrm{B}) \equiv s(\rho_\mathrm{A}) \equiv s(\rho_\mathrm{B}). \tag{A.18}$$

As for the REE, the computation of quantum discord for generic mixed states is NP-complete [382] and closed formulas are known only for some classes of two-qubit systems [381, 383, 384]. Numerical computation is still viable for a small enough dimension of the Hilbert space (d), resorting to statistical sampling of the $\mathbb{D}_{\mathrm{cl}}$ set [73].

A.3.3 Classical correlations and correlation sum rule

Granted that quantum correlations can exist beyond entanglement and are measured by the relative entropy with respect to the closest pseudo-classical state Eq. A.15, a natural way to define classical correlations would be to compute the quantum relative entropy between the closest classically correlated state and the closest uncorrelated state/

To further motivate this choice, we first rewrite Eq. A.15 as [381]

$$Q_\rho(\mathrm{A}:\mathrm{B}) = \min_{\{\mathscr{P}^i_\mathrm{A},\mathscr{P}^j_\mathrm{B}\}} S\left(\rho \,\middle\|\, \sum_{ij} \mathscr{P}^i_\mathrm{A} \otimes \mathscr{P}^j_\mathrm{B}\ \rho\ \mathscr{P}^i_\mathrm{A} \otimes \mathscr{P}^j_\mathrm{B}\right) \tag{A.19}$$

where $\mathscr{P}^i_\mathrm{A}$ and $\mathscr{P}^j_\mathrm{B}$ are two projective measurements, satisfying $\left(\mathscr{P}^i_{\{\mathrm{A,B}\}}\right)^2 = \mathscr{P}^i_{\{\mathrm{A,B}\}}$ and $\sum_i \mathscr{P}^i_{\{\mathrm{A,B}\}} = \mathbb{1}_{\{\mathrm{A,B}\}}$. The closest classical state χ_* is then the state resulting from ρ after the optimal projective measurements has been performed. Accordingly, the total correlation in χ_* is then nothing else than the classical correlation in ρ [72]

$$C_\rho(\mathrm{A}:\mathrm{B}) \equiv T(\chi_*). \tag{A.20}$$

Since quantum states cannot be dissected into classical and quantum parts in a strict mathematical sense, it is not surprising that our measures do typically not obey the relation $T_\rho(\mathrm{A}:\mathrm{B}) = Q_\rho(\mathrm{A}:\mathrm{B}) + C_\rho(\mathrm{A}:\mathrm{B})$. However, this exact additive relation is valid whenever the closest pseudo-classical state χ_* and the closest uncorrelated state π_* have the same eigenstates. When instead χ_* and π_* are not simultaneously diagonalizable, a general inequality applies, relating the total, quantum, and classical correlation as [73]

$$T_\rho(\mathrm{A}:\mathrm{B}) \geqslant Q_\rho(\mathrm{A}:\mathrm{B}) + C_\rho(\mathrm{A}:\mathrm{B}). \tag{A.21}$$

A.4 Effect of restrictions on local operations

Before ending this appendix, let us briefly demonstrate the effect of any restriction on the set of allowed local operations $\{\mathcal{O}_A\}$ and $\{\mathcal{O}_B\}$. In Eq. A.6 we have defined the notion of uncorrelated state as equivalent to a state that does not produce a finite correlation function $\mathrm{corr}(\mathcal{O}_A, \mathcal{O}_B)$, for any possible pair of Hermitian operators $\mathcal{O}_A$ and $\mathcal{O}_B$. However, if we restrict to a subset of the Hermitian operators, for either fundamental or operational reasons, there would be some correlated states that we cannot classify as such, for that we have no access to the corresponding finite correlation functions. Correspondingly, the set of *observable* correlated states is reduced and the measure of total correlation is decreased. As we have discussed above, the set of separable states is obtained by applying classical communication to the set of uncorrelated states, so that the enlargement of the latter implies also a decrease of the relative entropy of entanglement, *i.e.* the geometrical measure of bipartite entanglement. In general, all the correlation measures based on the quantum relative entropy and the geometry of quantum states are always decreased by the introduction of restrictions on the set of allowed local operations, providing a natural path for the construction of lower bounds to the relative entropy of entanglement and the quantum discord. In chapter 7 of the main text, we report two recently introduced examples of such strategy, providing lower bounds to the *two-orbital* relative entropy of entanglement (*i.e.* the system is made of two electronic orbitals and the bipartition is in orbital A and orbital B). In particular Ding *et al.* [219, 220] have leveraged the physically and operationally motivated charge and parity superselection rules to restrict the set of allowed operators to those commuting with the local (in this case single-orbital) electron number or only its parity, respectively.

Sum-rule for the two-site mutual information

B

For any state of a generic quantum tripartite system, either $\mathbb{H}_{ABC} = \mathbb{H}_A \otimes \mathbb{H}_B \otimes \mathbb{H}_C$ or $\mathbb{F}_{ABC} = \mathbb{F}_A \otimes \mathbb{F}_B \otimes \mathbb{F}_C$, a *strong subadditivity* property has been proven to relate the von Neumann entropies of all its subsystems and the whole density matrix ρ_{ABC}. In standard notation it reads [339]

$$s(\rho_{ABC}) + s(\rho_B) \leqslant s(\rho_{AB}) + s(\rho_{BC}). \tag{B.1}$$

Adding the von Neumann entropy of subsystem A on both sides, we can recast the inequality in terms of suitable mutual informations, as

$$s(\rho_{ABC}) + s(\rho_A) + s(\rho_B) \leqslant s(\rho_{AB}) + s(\rho_A) + s(\rho_{BC})$$

$$s(\rho_A) + s(\rho_B) - s(\rho_{AB}) \leqslant s(\rho_A) + s(\rho_{BC}) - s(\rho_{ABC})$$

$$I(\rho_A : \rho_B) \leqslant I(\rho_A : \rho_{BC}) \tag{B.2}$$

Let us consider the CDMFT solution for the Hubbard model and take A and B as single-site orbitals i, j in the cluster and C as the rest of the impurity model. Equation B.2 then becomes $I_{ij} \leqslant I_{i\{k\neq i\}}$. Since the ground state of the impurity model is pure, we have $I_{i\{k\neq i\}} = s_i + s_{\{k\neq i\}} = 2s_i$ and we can further recast the inequality as

$$I_{ij} \leqslant 2s_i, \quad \forall\, i \neq j \tag{B.3}$$

Finally we fix a reference site i and sum over all other possible cluster sites $j \neq i$, to get

$$\sum_{j=1}^{N_{imp}} I_{ij}(1-\delta_{ij}) \leqslant \sum_{j=1}^{N_{imp}} 2s_i(1-\delta_{ij})$$

$$\frac{\sum_{j=1}^{N_{imp}} I_{ij}(1-\delta_{ij})}{2\sum_{j=1}^{N_{imp}}(1-\delta_{ij})} \leqslant s_i \tag{B.4}$$

which is equivalent to Eq. 9.5 in the main text.

Bibliography

1. Bellomia, G. & Resta, R. Drude weight in systems with open boundary conditions. *Phys. Rev. B* **102,** 205123. https://link.aps.org/doi/10.1103/PhysRevB.102.205123 (20 Nov. 2020) (cit. on p. vi).
2. Bellomia, G., Baumann, K., Amaricci, A. & Capone, M. *Mottness, magnetism and topology of interacting Dirac fermions: a dynamical mean-field theory study of intra-orbital correlations* in preparation (cit. on p. vi).
3. Bellomia, G., Mejuto-Zaera, C., Capone, M. & Amaricci, A. Quasilocal entanglement across the Mott-Hubbard transition. *Phys. Rev. B* **109,** 115104. https://link.aps.org/doi/10.1103/PhysRevB.109.115104 (11 Mar. 2024) (cit. on pp. vi, 23, 36, 57, 61, 85, 97).
4. Bellomia, G., Mejuto-Zaera, C., Capone, M. & Amaricci, A. *Quasilocal entanglement in the doped 2d Hubbard model* in preparation (cit. on p. vi).
5. Bloch, F. Über die Quantenmechanik der Elektronen in Kristallgittern. *Zeitschrift für Physik* **52,** 555–600. issn: 0044-3328. https://doi.org/10.1007/BF01339455 (July 1929) (cit. on pp. 1, 2).
6. Wilson, A. H. The theory of electronic semi-conductors. *Proceedings of the Royal Society of London. Series A, Containing Papers of a Mathematical and Physical Character* **133,** 458–491. issn: 2053-9150. http://dx.doi.org/10.1098/rspa.1931.0162 (Oct. 1931) (cit. on pp. 1, 2).
7. Ashcroft, N. W. & Mermin, N. D. *Solid state physics* (Cengage Learning, New Delhi, 1976) (cit. on pp. 1, 2, 7, 16, 104).
8. Grosso, G. & Parravicini, G. P. *Solid State Physics* isbn: 9780123850300. http://dx.doi.org/10.1016/C2010-0-66724-1 (Elsevier, 2014) (cit. on pp. 1, 2, 7, 104).
9. Phillips, P. *Advanced Solid State Physics* isbn: 9781139031066. http://dx.doi.org/10.1017/CBO9781139031066 (Cambridge University Press, Mar. 2012) (cit. on pp. 1, 7).
10. Landau, L. D. The Theory of a Fermi Liquid. *Zh. Eksp. Teor. Fiz.* **30,** 1058. https://doi.org/10.1016/B978-0-08-010586-4.50095-X (1956) (cit. on p. 1).
11. Abrikosov, A. A. & Khalatnikov, I. M. The theory of a fermi liquid (the properties of liquid 3He at low temperatures). *Reports on Progress in Physics* **22,** 329. https://dx.doi.org/10.1088/0034-4885/22/1/310 (Jan. 1959) (cit. on p. 1).
12. Pines, D. & Nozières, P. *The Theory of Quantum Liquids: Normal Fermi Liquids* isbn: 9780429492662. http://dx.doi.org/10.4324/9780429492662 (CRC Press, Mar. 2018) (cit. on pp. 1, 13).

13. Giuliani, G. & Vignale, G. *Quantum Theory of the Electron Liquid* isbn: 9780511619915. http://dx.doi.org/10.1017/CBO9780511619915 (Cambridge University Press, Mar. 2005) (cit. on pp. 1, 7).

14. Coleman, P. *Introduction to Many-Body Physics* isbn: 9781139020916. http://dx.doi.org/10.1017/CBO9781139020916 (Cambridge University Press, Nov. 2015) (cit. on pp. 1, 7).

15. Burke, K. & Kozlowski, J. *Lies My Teacher Told Me About Density Functional Theory: Seeing Through Them with the Hubbard Dimer* 2022. arXiv: 2108.11534 [cond-mat.str-el] (cit. on p. 2).

16. Kohn, W. & Sham, L. J. Self-Consistent Equations Including Exchange and Correlation Effects. *Phys. Rev.* **140,** A1133–A1138. https://link.aps.org/doi/10.1103/PhysRev.140.A1133 (4A Nov. 1965) (cit. on p. 2).

17. Mott, N. F. The Basis of the Electron Theory of Metals, with Special Reference to the Transition Metals. *Proceedings of the Physical Society. Section A* **62,** 416–422. issn: 0370-1298. http://dx.doi.org/10.1088/0370-1298/62/7/303 (July 1949) (cit. on pp. 2, 3, 83).

18. Mott, N. *Metal-Insulator Transitions* https://doi.org/10.1201/b12795 (CRC Press, Jan. 1974) (cit. on pp. 2, 83).

19. Mott, N. F. Metal-Insulator Transition. *Rev. Mod. Phys.* **40,** 677–683. https://link.aps.org/doi/10.1103/RevModPhys.40.677 (4 Oct. 1968) (cit. on pp. 2, 83).

20. Gebhard, F. *The Mott Metal-Insulator Transition: Models and Methods* isbn: 9783540148586. http://dx.doi.org/10.1007/3-540-14858-2 (Springer Berlin Heidelberg, 1997) (cit. on pp. 2, 16).

21. De Boer, J. H. & Verwey, E. J. W. Semi-conductors with partially and with completely filled 3d-lattice bands. *Proceedings of the Physical Society* **49,** 59. https://dx.doi.org/10.1088/0959-5309/49/4S/307 (Aug. 1937) (cit. on p. 2).

22. Slater, J. C. Magnetic Effects and the Hartree-Fock Equation. *Phys. Rev.* **82,** 538–541. https://link.aps.org/doi/10.1103/PhysRev.82.538 (4 May 1951) (cit. on pp. 2, 6, 7).

23. Bednorz, J. G. & Müller, K. A. Possible high T_c superconductivity in the Ba-La-Cu-O system. *Zeitschrift fur Physik B Condensed Matter* **64,** 189–193 (June 1986) (cit. on p. 3).

24. Anderson, P. Resonating valence bonds: A new kind of insulator? *Materials Research Bulletin* **8,** 153–160. issn: 0025-5408. http://dx.doi.org/10.1016/0025-5408(73)90167-0 (Feb. 1973) (cit. on pp. 3, 30, 83, 86, 137).

25. Anderson, P. W. The Resonating Valence Bond State in La_2CuO_4 and Superconductivity. *Science* **235,** 1196–1198. eprint: https://www.science.org/doi/pdf/10.1126/science.235.4793.1196. https://www.science.org/doi/abs/10.1126/science.235.4793.1196 (1987) (cit. on pp. 3, 30, 83, 86, 137).

26. Lee, P. A., Nagaosa, N. & Wen, X.-G. Doping a Mott insulator: Physics of high-temperature superconductivity. *Rev. Mod. Phys.* **78,** 17–85. https://link.aps.org/doi/10.1103/RevModPhys.78.17 (1 Jan. 2006) (cit. on pp. 3, 30, 31, 83, 141).

27. Hubbard, J. Electron correlations in narrow energy bands. *Proceedings of the Royal Society of London. Series A. Mathematical and Physical Sciences* **276,** 238–257. issn: 2053-9169. http://dx.doi.org/10.1098/rspa.1963.0204 (Nov. 1963) (cit. on pp. 3, 4, 18, 109).

28. Hubbard, J. Electron correlations in narrow energy bands. II. The degenerate band case. *Proceedings of the Royal Society of London. Series A. Mathematical and Physical Sciences* **277,** 237–259. issn: 2053-9169. http://dx.doi.org/10.1098/rspa.1964.0019 (Jan. 1964) (cit. on pp. 3, 4, 18, 109).

29. Hubbard, J. Electron correlations in narrow energy bands III. An improved solution. *Proceedings of the Royal Society of London. Series A. Mathematical and Physical Sciences* **281,** 401–419. issn: 2053-9169. http://dx.doi.org/10.1098/rspa.1964.0190 (Sept. 1964) (cit. on pp. 3, 4, 18, 109).

30. Hubbard, J. Electron correlations in narrow energy bands - IV. The atomic representation. *Proceedings of the Royal Society of London. Series A. Mathematical and Physical Sciences* **285,** 542–560. issn: 2053-9169. http://dx.doi.org/10.1098/rspa.1965.0124 (May 1965) (cit. on pp. 3, 4, 18, 109).

31. Kanamori, J. Electron Correlation and Ferromagnetism of Transition Metals. *Progress of Theoretical Physics* **30,** 275–289. issn: 0033-068x. https://doi.org/10.1143/PTP.30.275 (Sept. 1963) (cit. on pp. 3, 4).

32. Gutzwiller, M. C. Effect of Correlation on the Ferromagnetism of Transition Metals. *Phys. Rev. Lett.* **10,** 159–162. https://link.aps.org/doi/10.1103/PhysRevLett.10.159 (5 Mar. 1963) (cit. on pp. 3, 4).

33. Arovas, D. P., Berg, E., Kivelson, S. A. & Raghu, S. The Hubbard Model. *Annual Review of Condensed Matter Physics* **13,** 239–274. issn: 1947-5462. http://dx.doi.org/10.1146/annurev-conmatphys-031620-102024 (Mar. 2022) (cit. on pp. 3, 9).

34. Qin, M., Schäfer, T., Andergassen, S., Corboz, P. & Gull, E. The Hubbard Model: A Computational Perspective. *Annual Review of Condensed Matter Physics* **13,** 275–302. issn: 1947-5462. http://dx.doi.org/10.1146/annurev-conmatphys-090921-033948 (Mar. 2022) (cit. on pp. 3, 9).

35. Wannier, G. H. The Structure of Electronic Excitation Levels in Insulating Crystals. *Phys. Rev.* **52,** 191–197. https://link.aps.org/doi/10.1103/PhysRev.52.191 (3 Aug. 1937) (cit. on p. 4).

36. Lieb, E. H. & Wu, F. Y. Absence of Mott Transition in an Exact Solution of the Short-Range, One-Band Model in One Dimension. *Phys. Rev. Lett.* **20,** 1445–1448. https://link.aps.org/doi/10.1103/PhysRevLett.20.1445 (25 June 1968) (cit. on p. 4).

37. Metzner, W. & Vollhardt, D. Correlated Lattice Fermions in $d = \infty$ Dimensions. *Phys. Rev. Lett.* **62,** 324–327. https://link.aps.org/doi/10.1103/PhysRevLett.62.324 (3 Jan. 1989) (cit. on pp. 4, 9, 44).

38. Georges, A., Kotliar, G., Krauth, W. & Rozenberg, M. J. Dynamical mean-field theory of strongly correlated fermion systems and the limit of infinite dimensions. *Rev. Mod. Phys.* **68,** 13–125. https://link.aps.org/doi/10.1103/RevModPhys.68.13 (1 Jan. 1996) (cit. on pp. 4, 6, 12, 44, 58, 64, 65, 71, 111, 152).

39. Byczuk, K. & Vollhardt, D. Correlated bosons on a lattice: Dynamical mean-field theory for Bose-Einstein condensed and normal phases. *Phys. Rev. B* **77,** 235106. https://link.aps.org/doi/10.1103/PhysRevB.77.235106 (23 June 2008) (cit. on p. 6).

40. Hu, W.-J. & Tong, N.-H. Dynamical mean-field theory for the Bose-Hubbard model. *Phys. Rev. B* **80,** 245110. https://link.aps.org/doi/10.1103/PhysRevB.80.245110 (24 Dec. 2009) (cit. on p. 6).

41. Anders, P., Gull, E., Pollet, L., Troyer, M. & Werner, P. Dynamical mean-field theory for bosons. *New Journal of Physics* **13,** 075013. issn: 1367-2630. http://dx.doi.org/10.1088/1367-2630/13/7/075013 (July 2011) (cit. on p. 6).

42. Scarlatella, O., Clerk, A. A., Fazio, R. & Schiró, M. Dynamical Mean-Field Theory for Markovian Open Quantum Many-Body Systems. *Phys. Rev. X* **11,** 031018. https://link.aps.org/doi/10.1103/PhysRevX.11.031018 (3 July 2021) (cit. on p. 6).

43. Seclí, M., Capone, M. & Schiró, M. Steady-state quantum Zeno effect of driven-dissipative bosons with dynamical mean-field theory. *Phys. Rev. A* **106,** 013707. https://link.aps.org/doi/10.1103/PhysRevA.106.013707 (1 July 2022) (cit. on p. 6).

44. MacDonald, A. H., Girvin, S. M. & Yoshioka, D. $\frac{t}{U}$ expansion for the Hubbard model. *Phys. Rev. B* **37,** 9753–9756. https://link.aps.org/doi/10.1103/PhysRevB.37.9753 (16 June 1988) (cit. on p. 8).

45. Anderson, P. W. An Approximate Quantum Theory of the Antiferromagnetic Ground State. *Phys. Rev.* **86,** 694–701. https://link.aps.org/doi/10.1103/PhysRev.86.694 (5 June 1952) (cit. on p. 8).

46. Eskes, H. & Jefferson, J. H. Superexchange in the cuprates. *Phys. Rev. B* **48,** 9788–9798. https://link.aps.org/doi/10.1103/PhysRevB.48.9788 (13 Oct. 1993) (cit. on p. 8).

47. Pesin, D. & Balents, L. Mott physics and band topology in materials with strong spin–orbit interaction. *Nature Physics* **6,** 376–381. issn: 1745-2481. http://dx.doi.org/10.1038/nphys1606 (Mar. 2010) (cit. on pp. 9, 29, 36, 42, 59, 80).

48. Savary, L. & Balents, L. Quantum spin liquids: a review. *Reports on Progress in Physics* **80,** 016502. issn: 1361-6633. http://dx.doi.org/10.1088/0034-4885/80/1/016502 (Nov. 2016) (cit. on pp. 9, 30, 83, 84, 86).

49. Pustogow, A., Kawasugi, Y., Sakurakoji, H. & Tajima, N. Chasing the spin gap through the phase diagram of a frustrated Mott insulator. *Nature Communications* **14.** https://doi.org/10.1038/s41467-023-37491-z (Apr. 2023) (cit. on p. 9).

50. Jung, T. S., Xu, X., Kim, J., *et al.* Unconventional room-temperature carriers in the triangular-lattice Mott insulator TbInO3. *Nature Physics.* https://doi.org/10.1038/s41567-023-02174-5 (Aug. 2023) (cit. on p. 9).

51. Anderson, P. W. Localized Magnetic States in Metals. *Phys. Rev.* **124,** 41–53. https://link.aps.org/doi/10.1103/PhysRev.124.41 (1 Oct. 1961) (cit. on pp. 11, 45).

52. Schrieffer, J. R. & Wolff, P. A. Relation between the Anderson and Kondo Hamiltonians. *Phys. Rev.* **149,** 491–492. https://link.aps.org/doi/10.1103/PhysRev.149.491 (2 Sept. 1966) (cit. on p. 12).

53. Ferrero, M., De Leo, L., Lecheminant, P. & Fabrizio, M. Strong correlations in a nutshell. *Journal of Physics: Condensed Matter* **19,** 433201. issn: 1361-648X. http://dx.doi.org/10.1088/0953-8984/19/43/433201 (Oct. 2007) (cit. on p. 12).

54. Caffarel, M. & Krauth, W. Exact diagonalization approach to correlated fermions in infinite dimensions: Mott transition and superconductivity. *Phys. Rev. Lett.* **72,** 1545–1548. https://link.aps.org/doi/10.1103/PhysRevLett.72.1545 (10 Mar. 1994) (cit. on pp. 12, 44, 85, 107, 112).

55. Damascelli, A., Hussain, Z. & Shen, Z.-X. Angle-resolved photoemission studies of the cuprate superconductors. *Rev. Mod. Phys.* **75,** 473–541. https://link.aps.org/doi/10.1103/RevModPhys.75.473 (2 Apr. 2003) (cit. on pp. 13, 30, 83, 141).

56. Berovic, M. *Exploring Hund's correlated metals: charge instabilities and effect of selective interactions* PhD thesis (SISSA, 2018). https://hdl.handle.net/20.500.11767/84088 (cit. on p. 14).

57. Sorella, S. & Tosatti, E. Semi-Metal-Insulator Transition of the Hubbard Model in the Honeycomb Lattice. *Europhysics Letters (EPL)* **19,** 699–704. issn: 1286-4854. http://dx.doi.org/10.1209/0295-5075/19/8/007 (Aug. 1992) (cit. on pp. 16, 35, 42, 50).

58. Castro Neto, A. H., Guinea, F., Peres, N. M. R., Novoselov, K. S. & Geim, A. K. The electronic properties of graphene. *Rev. Mod. Phys.* **81,** 109–162. https://link.aps.org/doi/10.1103/RevModPhys.81.109 (1 Jan. 2009) (cit. on pp. 16, 35, 42).

59. Sakurai, J. J. & Napolitano, J. *Modern Quantum Mechanics* isbn: 9781108473224. http://dx.doi.org/10.1017/9781108587280 (Cambridge University Press, Sept. 2020) (cit. on p. 18).

60. Ballentine, L. E. *Quantum Mechanics: A Modern Development* isbn: 9789814578592. http://dx.doi.org/10.1142/9038 (World Scientific, Nov. 2014) (cit. on p. 18).

61. Su, D. D., Dai, X. & Tong, N. H. Local Entanglement Entropy At The Mott Metal-insulator Transition In Infinite Dimensions. *Modern Physics Letters B* **27,** 1350034. https://doi.org/10.1142/S0217984913500346 (2013) (cit. on pp. 18, 19, 23, 47, 57, 83, 84, 89, 114, 126, 137).

62. Walsh, C., Sémon, P., Poulin, D., Sordi, G. & Tremblay, A.-M. S. Local Entanglement Entropy and Mutual Information across the Mott Transition in the Two-Dimensional Hubbard Model. *Phys. Rev. Lett.* **122,** 067203. https://link.aps.org/doi/10.1103/PhysRevLett.122.067203 (6 Feb. 2019) (cit. on pp. 18, 19, 23, 47, 57, 84, 89, 114, 117, 118, 126, 137).

63. Walsh, C., Sémon, P., Poulin, D., Sordi, G. & Tremblay, A.-M. S. Entanglement and Classical Correlations at the Doping-Driven Mott Transition in the Two-Dimensional Hubbard Model. *PRX Quantum* **1,** 020310. https://link.aps.org/doi/10.1103/PRXQuantum.1.020310 (2 Nov. 2020) (cit. on pp. 18, 19, 47, 57, 84, 89, 114, 118, 126, 137, 144–146).

64. Walsh, C., Charlebois, M., Sémon, P., Sordi, G. & Tremblay, A.-M. S. Information-theoretic measures of superconductivity in a two-dimensional doped Mott insulator. *Proceedings of the National Academy of Sciences* **118,** e2104114118. https://doi.org/10.1073/pnas.2104114118 (June 2021) (cit. on pp. 18, 19, 47, 84, 89, 114, 118, 126, 137).

65. Roósz, G., Kauch, A., Bippus, F., Wieser, D. & Held, K. *Two-site reduced density matrix from one- and two-particle Green's functions* 2023. arXiv: 2312.14275 [cond-mat.str-el] (cit. on pp. 18, 19, 47, 98, 115, 126, 152).

66. Nielsen, M. A. & Chuang, I. L. *Quantum Computation and Quantum Information: 10th Anniversary Edition* isbn: 9780511976667. http://dx.doi.org/10.1017/CBO9780511976667 (Cambridge University Press, June 2012) (cit. on pp. 19, 122, 158–162).

67. Peres, A. Separability Criterion for Density Matrices. *Phys. Rev. Lett.* **77,** 1413–1415. https://link.aps.org/doi/10.1103/PhysRevLett.77.1413 (8 Aug. 1996) (cit. on pp. 19, 88, 95).

68. Horodecki, P. Separability criterion and inseparable mixed states with positive partial transposition. *Physics Letters A* **232,** 333–339. issn: 0375-9601. https://www.sciencedirect.com/science/article/pii/S0375960197004167 (1997) (cit. on pp. 19, 88, 95, 99).

69. Horodecki, R., Horodecki, P., Horodecki, M. & Horodecki, K. Quantum entanglement. *Rev. Mod. Phys.* **81,** 865–942. https://link.aps.org/doi/10.1103/RevModPhys.81.865 (2 June 2009) (cit. on pp. 19, 87, 88, 159, 161).

70. Amico, L., Fazio, R., Osterloh, A. & Vedral, V. Entanglement in many-body systems. *Rev. Mod. Phys.* **80,** 517–576. https://link.aps.org/doi/10.1103/RevModPhys.80.517 (2 May 2008) (cit. on pp. 19, 84, 87, 89, 125, 137).

71. Laflorencie, N. Quantum entanglement in condensed matter systems. *Physics Reports* **646,** 1–59. issn: 0370-1573. http://dx.doi.org/10.1016/j.physrep.2016.06.008 (Aug. 2016) (cit. on pp. 19, 84, 87, 90, 137).

72. Modi, K., Paterek, T., Son, W., Vedral, V. & Williamson, M. Unified View of Quantum and Classical Correlations. *Phys. Rev. Lett.* **104,** 080501. https://link.aps.org/doi/10.1103/PhysRevLett.104.080501 (8 Feb. 2010) (cit. on pp. 19, 157, 158, 160, 162, 163).

73. Ding, L., Knecht, S., Zimborás, Z. & Schilling, C. Quantum correlations in molecules: from quantum resourcing to chemical bonding. *Quantum Science and Technology* **8,** 015015. https://dx.doi.org/10.1088/2058-9565/aca4ee (Dec. 2022) (cit. on pp. 19, 83, 85, 87, 92, 157, 158, 160, 162, 163).

74. Wolf, M. M., Verstraete, F., Hastings, M. B. & Cirac, J. I. Area Laws in Quantum Systems: Mutual Information and Correlations. *Phys. Rev. Lett.* **100,** 070502. https://link.aps.org/doi/10.1103/PhysRevLett.100.070502 (7 Feb. 2008) (cit. on pp. 19, 85, 90, 137).

75. Cover, T. M. & Thomas, J. A. *Elements of Information Theory* isbn: 9780471748823. http://dx.doi.org/10.1002/047174882X (Wiley, Apr. 2005) (cit. on pp. 22, 23, 58, 90).

76. Rioul, O. *This is IT: A Primer on Shannon's Entropy and Information* in *Information Theory: Poincaré Seminar 2018* (eds Duplantier, B. & Rivasseau, V.) 49–86 (Springer International Publishing, Cham, 2021). isbn: 978-3-030-81480-9. https://doi.org/10.1007/978-3-030-81480-9_2 (cit. on pp. 22, 58, 117, 158, 160).

77. *On the theory of superconductivity* in *Collected Papers of L.D. Landau* (ed Ter Haar, D.) 217–225 (Pergamon, 1965). isbn: 978-0-08-010586-4. https://www.sciencedirect.com/science/article/pii/B9780080105864500353 (cit. on p. 26).

78. Kotliar, G., Lange, E. & Rozenberg, M. J. Landau Theory of the Finite Temperature Mott Transition. *Phys. Rev. Lett.* **84,** 5180–5183. https://link.aps.org/doi/10.1103/PhysRevLett.84.5180 (22 May 2000) (cit. on pp. 26, 30).

79. König, M., Wiedmann, S., Brüne, C., *et al.* Quantum Spin Hall Insulator State in HgTe Quantum Wells. *Science* **318,** 766–770. eprint: https://www.science.org/doi/pdf/10.1126/science.1148047. https://www.science.org/doi/abs/10.1126/science.1148047 (2007) (cit. on pp. 26, 27).

80. Moore, J. E. The birth of topological insulators. *Nature* **464,** 194–198. issn: 1476-4687. http://dx.doi.org/10.1038/nature08916 (Mar. 2010) (cit. on pp. 26, 35).

81. Hasan, M. Z. & Kane, C. L. Colloquium: Topological insulators. *Rev. Mod. Phys.* **82,** 3045–3067. https://link.aps.org/doi/10.1103/RevModPhys.82.3045 (4 Nov. 2010) (cit. on pp. 26, 28, 35, 41).

82. Qi, X.-L. & Zhang, S.-C. Topological insulators and superconductors. *Rev. Mod. Phys.* **83,** 1057–1110. https://link.aps.org/doi/10.1103/RevModPhys.83.1057 (4 Oct. 2011) (cit. on pp. 26, 35, 41).

83. Fiete, G. A., Chua, V., Kargarian, M., *et al.* Topological insulators and quantum spin liquids. *Physica E: Low-dimensional Systems and Nanostructures* **44,** 845–859. issn: 1386-9477. http://dx.doi.org/10.1016/j.physe.2011.11.011 (Feb. 2012) (cit. on pp. 26, 27, 35, 41).

84. Haldane, F. D. M. Model for a Quantum Hall Effect without Landau Levels: Condensed-Matter Realization of the "Parity Anomaly". *Phys. Rev. Lett.* **61,** 2015–2018. https://link.aps.org/doi/10.1103/PhysRevLett.61.2015 (18 Oct. 1988) (cit. on pp. 26, 35, 41).

85. Kane, C. L. & Mele, E. J. Quantum Spin Hall Effect in Graphene. *Phys. Rev. Lett.* **95,** 226801. https://link.aps.org/doi/10.1103/PhysRevLett.95.226801 (22 Nov. 2005) (cit. on pp. 27, 29, 35, 39, 41).

86. Kane, C. L. & Mele, E. J. $\mathbb{Z}_2$ Topological Order and the Quantum Spin Hall Effect. *Phys. Rev. Lett.* **95,** 146802. https://link.aps.org/doi/10.1103/PhysRevLett.95.146802 (14 Sept. 2005) (cit. on pp. 27, 29, 35, 39).

87. Hohenadler, M. & Assaad, F. F. Correlation effects in two-dimensional topological insulators. *Journal of Physics: Condensed Matter* **25,** 143201. https://dx.doi.org/10.1088/0953-8984/25/14/143201 (Mar. 2013) (cit. on pp. 29, 35, 36, 41, 49, 60, 63, 79, 151).

88. Rachel, S. Interacting topological insulators: a review. *Reports on Progress in Physics* **81,** 116501. https://dx.doi.org/10.1088/1361-6633/aad6a6 (Oct. 2018) (cit. on pp. 29, 35, 36, 41, 49, 60, 63, 79, 151).

89. Budich, J. C., Trauzettel, B. & Sangiovanni, G. Fluctuation-driven topological Hund insulators. *Phys. Rev. B* **87,** 235104. https://link.aps.org/doi/10.1103/PhysRevB.87.235104 (23 June 2013) (cit. on pp. 29, 36, 44).

90. Roy, B., Goswami, P. & Sau, J. D. Continuous and discontinuous topological quantum phase transitions. *Phys. Rev. B* **94,** 041101. https://link.aps.org/doi/10.1103/PhysRevB.94.041101 (4 July 2016) (cit. on pp. 29, 79).

91. Amaricci, A., Budich, J. C., Capone, M., Trauzettel, B. & Sangiovanni, G. First-Order Character and Observable Signatures of Topological Quantum Phase Transitions. *Phys. Rev. Lett.* **114,** 185701. https://link.aps.org/doi/10.1103/PhysRevLett.114.185701 (18 May 2015) (cit. on pp. 29, 36, 44, 79).

92. Amaricci, A., Budich, J. C., Capone, M., Trauzettel, B. & Sangiovanni, G. Strong correlation effects on topological quantum phase transitions in three dimensions. *Phys. Rev. B* **93,** 235112. https://link.aps.org/doi/10.1103/PhysRevB.93.235112 (23 June 2016) (cit. on pp. 29, 44, 79).

93. Crippa, L., Amaricci, A., Adler, S., Sangiovanni, G. & Capone, M. Local versus nonlocal correlation effects in interacting quantum spin Hall insulators. *Phys. Rev. B* **104,** 235117. https://link.aps.org/doi/10.1103/PhysRevB.104.235117 (23 Dec. 2021) (cit. on pp. 29, 139).

94. Mong, R. S. K., Essin, A. M. & Moore, J. E. Antiferromagnetic topological insulators. *Phys. Rev. B* **81,** 245209. https://link.aps.org/doi/10.1103/PhysRevB.81.245209 (24 June 2010) (cit. on pp. 29, 36, 50).

95. Li, J., Li, Y., Du, S., *et al.* Intrinsic magnetic topological insulators in van der Waals layered $MnBi_2Te_4$-family materials. *Science Advances* **5,** eaaw5685. https://www.science.org/doi/abs/10.1126/sciadv.aaw5685 (2019) (cit. on pp. 29, 36, 50).

96. Misawa, T. & Yamaji, Y. Zeros of Green functions in topological insulators. *Phys. Rev. Res.* **4,** 023177. https://link.aps.org/doi/10.1103/PhysRevResearch.4.023177 (2 June 2022) (cit. on pp. 29, 36, 59).

97. Blason, A. & Fabrizio, M. Unified role of Green's function poles and zeros in correlated topological insulators. *Phys. Rev. B* **108,** 125115. https://link.aps.org/doi/10.1103/PhysRevB.108.125115 (12 Sept. 2023) (cit. on pp. 29, 36, 59).

98. Zhao, J., Mai, P., Bradlyn, B. & Phillips, P. Failure of Topological Invariants in Strongly Correlated Matter. *Phys. Rev. Lett.* **131,** 106601. https://link.aps.org/doi/10.1103/PhysRevLett.131.106601 (10 Sept. 2023) (cit. on pp. 29, 36, 59).

99. Wagner, N., Guerci, D., Millis, A. J. & Sangiovanni, G. *Edge zeros and boundary spinons in topological Mott insulators* 2023. arXiv: 2312.13226 [cond-mat.str-el] (cit. on pp. 29, 36, 42, 59, 80).

100. Wagner, N., Crippa, L., Amaricci, A., *et al.* Mott insulators with boundary zeros. *Nature Communications* **14.** issn: 2041-1723. http://dx.doi.org/10.1038/s41467-023-42773-7 (Nov. 2023) (cit. on pp. 29, 36, 42, 44, 59, 80).

101. Logan, D. E. & Galpin, M. R. Mott insulators and the doping-induced Mott transition within DMFT: exact results for the one-band Hubbard model. *Journal of Physics: Condensed Matter* **28,** 025601. issn: 1361-648X. http://dx.doi.org/10.1088/0953-8984/28/2/025601 (Dec. 2015) (cit. on p. 30).

102. Sen, S., Wong, P. J. & Mitchell, A. K. The Mott transition as a topological phase transition. *Phys. Rev. B* **102,** 081110. https://link.aps.org/doi/10.1103/PhysRevB.102.081110 (8 Aug. 2020) (cit. on pp. 30, 197).

103. Fabrizio, M. Spin-Liquid Insulators Can Be Landau's Fermi Liquids. *Phys. Rev. Lett.* **130,** 156702. https://link.aps.org/doi/10.1103/PhysRevLett.130.156702 (15 Apr. 2023) (cit. on pp. 30, 83, 86).

104. Hashimoto, M., Vishik, I. M., He, R.-H., Devereaux, T. P. & Shen, Z.-X. Energy gaps in high-transition-temperature cuprate superconductors. *Nature Physics* **10,** 483–495. issn: 1745-2481. http://dx.doi.org/10.1038/nphys3009 (June 2014) (cit. on pp. 30, 83, 141).

105. Varma, C. M. Colloquium: Linear in temperature resistivity and associated mysteries including high temperature superconductivity. *Rev. Mod. Phys.* **92,** 031001. https://link.aps.org/doi/10.1103/RevModPhys.92.031001 (3 July 2020) (cit. on p. 31).

106. Chowdhury, D., Georges, A., Parcollet, O. & Sachdev, S. Sachdev-Ye-Kitaev models and beyond: Window into non-Fermi liquids. *Rev. Mod. Phys.* **94,** 035004. https://link.aps.org/doi/10.1103/RevModPhys.94.035004 (3 Sept. 2022) (cit. on p. 31).

107. Sachdev, S. *Statistical mechanics of strange metals and black holes* 2022. arXiv: 2205.02285 [hep-th] (cit. on p. 31).

108. Huang, E. W., Sheppard, R., Moritz, B. & Devereaux, T. P. Strange metallicity in the doped Hubbard model. *Science* **366,** 987–990. issn: 1095-9203. http://dx.doi.org/10.1126/science.aau7063 (Nov. 2019) (cit. on p. 31).

109. Capone, M., Fabrizio, M., Castellani, C. & Tosatti, E. Strongly Correlated Superconductivity and Pseudogap Phase near a Multiband Mott Insulator. *Phys. Rev. Lett.* **93,** 047001. https://link.aps.org/doi/10.1103/PhysRevLett.93.047001 (4 July 2004) (cit. on pp. 31, 109, 139, 141, 142).

110. Capone, M., Fabrizio, M., Castellani, C. & Tosatti, E. Colloquium: Modeling the unconventional superconducting properties of expanded A_3C_{60} fullerides. *Rev. Mod. Phys.* **81,** 943–958. https://link.aps.org/doi/10.1103/RevModPhys.81.943 (2 June 2009) (cit. on p. 31).

111. Mazin, I. I. Superconductivity gets an iron boost. *Nature* **464,** 183–186. issn: 1476-4687. http://dx.doi.org/10.1038/nature08914 (Mar. 2010) (cit. on p. 31).

112. De'Medici, L., Giovannetti, G. & Capone, M. Selective Mott Physics as a Key to Iron Superconductors. *Phys. Rev. Lett.* **112,** 177001. https://link.aps.org/doi/10.1103/PhysRevLett.112.177001 (17 Apr. 2014) (cit. on pp. 31, 139).

113. Zhang, P., Wang, Z., Wu, X., *et al.* Multiple topological states in iron-based superconductors. *Nature Physics* **15,** 41–47. issn: 1745-2481. https://doi.org/10.1038/s41567-018-0280-z (2019) (cit. on p. 31).

114. Zhang, P., Yaji, K., Hashimoto, T., *et al.* Observation of topological superconductivity on the surface of an iron-based superconductor. *Science* **360,** 182–186. issn: 0036-8075. https://science.sciencemag.org/content/360/6385/182 (2018) (cit. on p. 31).

115. Tomczak, J. M., Van Schilfgaarde, M. & Kotliar, G. Many-body effects in iron pnictides and chalcogenides: Nonlocal versus dynamic origin of effective masses. *Phys. Rev. Lett.* **109,** 237010. issn: 00319007 (2012) (cit. on pp. 31, 139).

116. Villar Arribi, P. & de'Medici, L. Hund's metal crossover and superconductivity in the 111 family of iron-based superconductors. *Phys. Rev. B* **104,** 125130. https://link.aps.org/doi/10.1103/PhysRevB.104.125130 (12 Sept. 2021) (cit. on pp. 31, 139).

117. Li, D., Lee, K., Wang, B. Y., *et al.* Superconductivity in an infinite-layer nickelate. *Nature* **572,** 624–627. issn: 1476-4687. http://dx.doi.org/10.1038/s41586-019-1496-5 (Aug. 2019) (cit. on p. 31).

118. Fowlie, J., Hadjimichael, M., Martins, M. M., *et al.* Intrinsic magnetism in superconducting infinite-layer nickelates. *Nature Physics* **18,** 1043–1047. issn: 1745-2481. http://dx.doi.org/10.1038/s41567-022-01684-y (Aug. 2022) (cit. on p. 31).

119. Egami, T., Ishihara, S. & Tachiki, M. Lattice Effect of Strong Electron Correlation: Implication for Ferroelectricity and Superconductivity. *Science* **261,** 1307–1310. issn: 1095-9203. http://dx.doi.org/10.1126/science.261.5126.1307 (Sept. 1993) (cit. on p. 31).

120. Fabrizio, M., Gogolin, A. O. & Nersesyan, A. A. From Band Insulator to Mott Insulator in One Dimension. *Phys. Rev. Lett.* **83,** 2014–2017. https://link.aps.org/doi/10.1103/PhysRevLett.83.2014 (10 Sept. 1999) (cit. on p. 31).

121. Zhou, Y., Guan, X., Zhou, H., *et al.* Strongly correlated perovskite fuel cells. *Nature* **534,** 231–234. issn: 1476-4687. http://dx.doi.org/10.1038/nature17653 (May 2016) (cit. on p. 31).

122. Blason, A. & Fabrizio, M. Local Kekulé distortion turns twisted bilayer graphene into topological Mott insulators and superconductors. *Phys. Rev. B* **106,** 235112. https://link.aps.org/doi/10.1103/PhysRevB.106.235112 (23 Dec. 2022) (cit. on p. 31).

123. Song, Z.-D. & Bernevig, B. A. Magic-Angle Twisted Bilayer Graphene as a Topological Heavy Fermion Problem. *Phys. Rev. Lett.* **129,** 047601. https://link.aps.org/doi/10.1103/PhysRevLett.129.047601 (4 July 2022) (cit. on p. 31).

124. Crippa, L., Bae, H., Wunderlich, P., *et al.* Heavy fermions vs doped Mott physics in heterogeneous Ta-dichalcogenide bilayers. *Nature Communications* **15.** issn: 2041-1723. http://dx.doi.org/10.1038/s41467-024-45392-y (Feb. 2024) (cit. on p. 31).

125. Richaud, A., Ferraretto, M. & Capone, M. Interaction-resistant metals in multicomponent Fermi systems. *Phys. Rev. B* **103,** 205132. https://link.aps.org/doi/10.1103/PhysRevB.103.205132 (20 May 2021) (cit. on pp. 31, 139).

126. Tusi, D., Franchi, L., Livi, L. F., *et al.* Flavour-selective localization in interacting lattice fermions. *Nature Physics* **18,** 1201–1205. issn: 1745-2481. https://doi.org/10.1038/s41567-022-01726-5 (Oct. 2022) (cit. on pp. 31, 139).

127. Le, D.-A., Tran, T.-M. T. & Tran, M.-T. Swap Mott transition in multicomponent fermion systems. *Phys. Rev. B* **109,** 115105. https://link.aps.org/doi/10.1103/PhysRevB.109.115105 (11 Mar. 2024) (cit. on pp. 31, 139).

128. Weber, C., O'Regan, D. D., Hine, N. D. M., *et al.* Importance of Many-Body Effects in the Kernel of Hemoglobin for Ligand Binding. *Phys. Rev. Lett.* **110,** 106402. https://link.aps.org/doi/10.1103/PhysRevLett.110.106402 (10 Mar. 2013) (cit. on p. 31).

129. Weber, C., Cole, D. J., O'Regan, D. D. & Payne, M. C. Renormalization of myoglobin–ligand binding energetics by quantum many-body effects. *Proceedings of the National Academy of Sciences* **111,** 5790–5795. issn: 1091-6490. http://dx.doi.org/10.1073/pnas.1322966111 (Apr. 2014) (cit. on p. 31).

130. Rachel, S. & Le Hur, K. Topological insulators and Mott physics from the Hubbard interaction. *Phys. Rev. B* **82,** 075106. https://link.aps.org/doi/10.1103/PhysRevB.82.075106 (7 Aug. 2010) (cit. on pp. 35, 41, 49, 63, 151).

131. Wang, F. Schwinger boson mean field theories of spin liquid states on a honeycomb lattice: Projective symmetry group analysis and critical field theory. *Phys. Rev. B* **82,** 024419. https://link.aps.org/doi/10.1103/PhysRevB.82.024419 (2 July 2010) (cit. on pp. 35, 41, 63).

132. Lu, Y.-M. & Ran, Y. $\mathbb{Z}_2$ spin liquid and chiral antiferromagnetic phase in the Hubbard model on a honeycomb lattice. *Phys. Rev. B* **84,** 024420. https://link.aps.org/doi/10.1103/PhysRevB.84.024420 (2 July 2011) (cit. on pp. 35, 41, 63).

133. Lee, D.-H. Effects of Interaction on Quantum Spin Hall Insulators. *Phys. Rev. Lett.* **107,** 166806. https://link.aps.org/doi/10.1103/PhysRevLett.107.166806 (16 Oct. 2011) (cit. on pp. 35, 41, 63).

134. Griset, C. & Xu, C. Phase diagram of the Kane-Mele-Hubbard model. *Phys. Rev. B* **85,** 045123. https://link.aps.org/doi/10.1103/PhysRevB.85.045123 (4 Jan. 2012) (cit. on pp. 35, 41–43, 47, 63).

135. Quan, Y.-M., Bao, W.-C., Wang, W.-H. & Liu, D.-Y. Phase diagrams of the Kane-Mele-Hubbard model in the presence of an external magnetic field. *Journal of Physics: Conference Series* **827,** 012009. issn: 1742-6596. http://dx.doi.org/10.1088/1742-6596/827/1/012009 (May 2017) (cit. on pp. 35, 41, 63, 69).

136. Meng, Z. Y., Lang, T. C., Wessel, S., Assaad, F. F. & Muramatsu, A. Quantum spin liquid emerging in two-dimensional correlated Dirac fermions. *Nature* **464,** 847–851. issn: 1476-4687. http://dx.doi.org/10.1038/nature08942 (Apr. 2010) (cit. on pp. 35, 41, 79).

137. Hohenadler, M., Lang, T. C. & Assaad, F. F. Correlation Effects in Quantum Spin-Hall Insulators: A Quantum Monte Carlo Study. *Phys. Rev. Lett.* **106,** 100403. https://link.aps.org/doi/10.1103/PhysRevLett.106.100403 (10 Mar. 2011) (cit. on pp. 35, 41, 63, 79).

138. Sorella, S., Otsuka, Y. & Yunoki, S. Absence of a Spin Liquid Phase in the Hubbard Model on the Honeycomb Lattice. *Scientific Reports* **2.** issn: 2045-2322. http://dx.doi.org/10.1038/srep00992 (Dec. 2012) (cit. on pp. 35, 41, 50, 79).

139. Hassan, S. R. & Sénéchal, D. Absence of Spin Liquid in Nonfrustrated Correlated Systems. *Phys. Rev. Lett.* **110,** 096402. https://link.aps.org/doi/10.1103/PhysRevLett.110.096402 (9 Feb. 2013) (cit. on pp. 35, 41, 50, 79).

140. Zeng, T.-S., Zhu, W., Zhu, J.-X. & Sheng, D. N. Nature of continuous phase transitions in interacting topological insulators. *Phys. Rev. B* **96,** 195118. https://link.aps.org/doi/10.1103/PhysRevB.96.195118 (19 Nov. 2017) (cit. on pp. 35, 41, 63).

141. Yu, S.-L., Xie, X. C. & Li, J.-X. Mott Physics and Topological Phase Transition in Correlated Dirac Fermions. *Phys. Rev. Lett.* **107,** 010401. https://link.aps.org/doi/10.1103/PhysRevLett.107.010401 (1 June 2011) (cit. on pp. 35, 41, 49, 63).

142. Budich, J. C., Thomale, R., Li, G., Laubach, M. & Zhang, S.-C. Fluctuation-induced topological quantum phase transitions in quantum spin-Hall and anomalous-Hall insulators. *Phys. Rev. B* **86,** 201407. https://link.aps.org/doi/10.1103/PhysRevB.86.201407 (20 Nov. 2012) (cit. on pp. 35, 41, 63).

143. Jafari, S. A. Dynamical mean field study of the Dirac liquid. *The European Physical Journal B* **68,** 537–542. issn: 1434-6036. http://dx.doi.org/10.1140/epjb/e2009-00128-1 (Apr. 2009) (cit. on pp. 35, 41).

144. Tran, M.-T. & Kuroki, K. Finite-temperature semimetal-insulator transition on the honeycomb lattice. *Phys. Rev. B* **79,** 125125. https://link.aps.org/doi/10.1103/PhysRevB.79.125125 (12 Mar. 2009) (cit. on pp. 35, 41, 50).

145. Wu, W., Chen, Y.-H., Tao, H.-S., Tong, N.-H. & Liu, W.-M. Interacting Dirac fermions on honeycomb lattice. *Phys. Rev. B* **82,** 245102. https://link.aps.org/doi/10.1103/PhysRevB.82.245102 (24 Dec. 2010) (cit. on pp. 35, 41, 50, 103).

146. Wu, W., Rachel, S., Liu, W.-M. & Le Hur, K. Quantum spin Hall insulators with interactions and lattice anisotropy. *Phys. Rev. B* **85,** 205102. https://link.aps.org/doi/10.1103/PhysRevB.85.205102 (20 May 2012) (cit. on pp. 35, 41, 63, 103).

147. Wu, W. & Tremblay, A.-M. S. Phase diagram and Fermi liquid properties of the extended Hubbard model on the honeycomb lattice. *Phys. Rev. B* **89,** 205128. https://link.aps.org/doi/10.1103/PhysRevB.89.205128 (20 May 2014) (cit. on pp. 35, 41, 50).

148. Raczkowski, M., Peters, R., Phùng, T. T., *et al.* Hubbard model on the honeycomb lattice: From static and dynamical mean-field theories to lattice quantum Monte Carlo simulations. *Phys. Rev. B* **101,** 125103. https://link.aps.org/doi/10.1103/PhysRevB.101.125103 (12 Mar. 2020) (cit. on pp. 35, 41, 49, 50, 65).

149. Sangiovanni, G., Toschi, A., Koch, E., *et al.* Static versus dynamical mean-field theory of Mott antiferromagnets. *Phys. Rev. B* **73,** 205121. https://link.aps.org/doi/10.1103/PhysRevB.73.205121 (20 May 2006) (cit. on pp. 36, 49, 50).

150. Taranto, C., Sangiovanni, G., Held, K., *et al.* Signature of antiferromagnetic long-range order in the optical spectrum of strongly correlated electron systems. *Phys. Rev. B* **85,** 085124. https://link.aps.org/doi/10.1103/PhysRevB.85.085124 (8 Feb. 2012) (cit. on p. 36).

151. Yoshida, T., Peters, R., Fujimoto, S. & Kawakami, N. Topological antiferromagnetic phase in a correlated Bernevig-Hughes-Zhang model. *Phys. Rev. B* **87,** 085134. https://link.aps.org/doi/10.1103/PhysRevB.87.085134 (8 Feb. 2013) (cit. on pp. 36, 50, 79).

152. Amaricci, A., Valli, A., Sangiovanni, G., Trauzettel, B. & Capone, M. Coexistence of metallic edge states and antiferromagnetic ordering in correlated topological insulators. *Phys. Rev. B* **98,** 045133. https://link.aps.org/doi/10.1103/PhysRevB.98.045133 (4 July 2018) (cit. on pp. 36, 44, 50, 71, 79).

153. Miyakoshi, S. & Ohta, Y. Antiferromagnetic topological insulator state in the correlated Bernevig-Hughes-Zhang model. *Phys. Rev. B* **87,** 195133. https://link.aps.org/doi/10.1103/PhysRevB.87.195133 (19 May 2013) (cit. on pp. 36, 50, 79).

154. Soni, R., Radhakrishnan, H., Rosenow, B., Alvarez, G. & Maestro, A. D. *Topological and magnetic properties of the interacting Bernevig-Hughes-Zhang model* 2023. arXiv: 2310.17614 [cond-mat.str-el] (cit. on pp. 36, 50, 79).

155. Soluyanov, A. A. & Vanderbilt, D. Computing topological invariants without inversion symmetry. *Phys. Rev. B* **83,** 235401. https://link.aps.org/doi/10.1103/PhysRevB.83.235401 (23 June 2011) (cit. on p. 41).

156. Gresch, D., Autès, G., Yazyev, O. V., *et al.* Z2Pack: Numerical implementation of hybrid Wannier centers for identifying topological materials. *Phys. Rev. B* **95,** 075146. https://link.aps.org/doi/10.1103/PhysRevB.95.075146 (7 Feb. 2017) (cit. on p. 41).

157. Hohenadler, M., Parisen Toldin, F., Herbut, I. F. & Assaad, F. F. Phase diagram of the Kane-Mele-Coulomb model. *Phys. Rev. B* **90,** 085146. https://link.aps.org/doi/10.1103/PhysRevB.90.085146 (8 Aug. 2014) (cit. on p. 42).

158. Hirsch, J. E. Two-dimensional Hubbard model: Numerical simulation study. *Phys. Rev. B* **31,** 4403–4419. https://link.aps.org/doi/10.1103/PhysRevB.31.4403 (7 Apr. 1985) (cit. on p. 42).

159. White, S. R., Scalapino, D. J., Sugar, R. L., *et al.* Numerical study of the two-dimensional Hubbard model. *Phys. Rev. B* **40,** 506–516. https://link.aps.org/doi/10.1103/PhysRevB.40.506 (1 July 1989) (cit. on p. 42).

160. Kotliar, G., Savrasov, S. Y., Haule, K., *et al.* Electronic structure calculations with dynamical mean-field theory. *Rev. Mod. Phys.* **78,** 865–951. https://link.aps.org/doi/10.1103/RevModPhys.78.865 (3 Aug. 2006) (cit. on pp. 44, 71).

161. Amaricci, A., Privitera, L., Petocchi, F., *et al.* Edge state reconstruction from strong correlations in quantum spin Hall insulators. *Phys. Rev. B* **95,** 205120. https://link.aps.org/doi/10.1103/PhysRevB.95.205120 (20 May 2017) (cit. on pp. 44, 71).

162. Crippa, L., Amaricci, A., Wagner, N., *et al.* Nonlocal annihilation of Weyl fermions in correlated systems. *Phys. Rev. Res.* **2,** 012023. https://link.aps.org/doi/10.1103/PhysRevResearch.2.012023 (1 Jan. 2020) (cit. on pp. 44, 79).

163. Crippa, L., Amaricci, A., Adler, S., Sangiovanni, G. & Capone, M. Local versus nonlocal correlation effects in interacting quantum spin Hall insulators. *Phys. Rev. B* **104,** 235117. https://link.aps.org/doi/10.1103/PhysRevB.104.235117 (23 Dec. 2021) (cit. on p. 44).

164. Amaricci, A., Mazza, G., Capone, M. & Fabrizio, M. Exciton condensation in strongly correlated quantum spin Hall insulators. *Phys. Rev. B* **107,** 115117. https://link.aps.org/doi/10.1103/PhysRevB.107.115117 (11 Mar. 2023) (cit. on p. 44).

165. Capone, M., de'Medici, L. & Georges, A. Solving the dynamical mean-field theory at very low temperatures using the Lanczos exact diagonalization. *Phys. Rev. B* **76,** 245116. https://link.aps.org/doi/10.1103/PhysRevB.76.245116 (24 Dec. 2007) (cit. on pp. 44, 65, 85, 112).

166. Amaricci, A., Crippa, L., Scazzola, A., *et al.* EDIpack: A parallel exact diagonalization package for quantum impurity problems. *Computer Physics Communications* **273,** 108261. issn: 0010-4655. https://www.sciencedirect.com/science/article/pii/S0010465521003738 (2022) (cit. on pp. 44, 65, 85, 112–114).

167. Capone, M., Civelli, M., Kancharla, S. S., Castellani, C. & Kotliar, G. Cluster-dynamical mean-field theory of the density-driven Mott transition in the one-dimensional Hubbard model. *Phys. Rev. B* **69,** 195105. https://link.aps.org/doi/10.1103/PhysRevB.69.195105 (19 May 2004) (cit. on pp. 45, 103, 106, 108).

168. Ishikawa, K. & Matsuyama, T. Magnetic field induced multi-component QED_3 and quantum Hall effect. *Z. Phys. C - Particles and Fields* **33,** 41–45. issn: 1434-6052. http://dx.doi.org/10.1007/BF01410451 (Mar. 1986) (cit. on p. 46).

169. Ishikawa, K. & Matsuyama, T. A microscopic theory of the quantum Hall effect. *Nuclear Physics B* **280,** 523–548. issn: 0550-3213. http://dx.doi.org/10.1016/0550-3213(87)90160-X (1987) (cit. on p. 46).

170. Wang, Z., Qi, X.-L. & Zhang, S.-C. Topological Order Parameters for Interacting Topological Insulators. *Phys. Rev. Lett.* **105,** 256803. https://link.aps.org/doi/10.1103/PhysRevLett.105.256803 (25 Dec. 2010) (cit. on p. 46).

171. Wang, Z. & Zhang, S.-C. Simplified Topological Invariants for Interacting Insulators. *Phys. Rev. X* **2,** 031008. https://link.aps.org/doi/10.1103/PhysRevX.2.031008 (3 Aug. 2012) (cit. on p. 46).

172. Wang, Z. & Yan, B. Topological Hamiltonian as an exact tool for topological invariants. *Journal of Physics: Condensed Matter* **25,** 155601. issn: 1361-648x. http://dx.doi.org/10.1088/0953-8984/25/15/155601 (Mar. 2013) (cit. on p. 46).

173. Zurek, W. H. Decoherence, einselection, and the quantum origins of the classical. *Rev. Mod. Phys.* **75,** 715–775. https://link.aps.org/doi/10.1103/RevModPhys.75.715 (3 May 2003) (cit. on pp. 47, 61, 127, 151, 162).

174. Rozenberg, M. J., Zhang, X. Y. & Kotliar, G. Mott-Hubbard transition in infinite dimensions. *Phys. Rev. Lett.* **69,** 1236–1239. https://link.aps.org/doi/10.1103/PhysRevLett.69.1236 (8 Aug. 1992) (cit. on p. 58).

175. Zhang, X. Y., Rozenberg, M. J. & Kotliar, G. Mott transition in the $d = \infty$ Hubbard model at zero temperature. *Phys. Rev. Lett.* **70,** 1666–1669. https://link.aps.org/doi/10.1103/PhysRevLett.70.1666 (11 Mar. 1993) (cit. on p. 58).

176. Rozenberg, M. J., Kotliar, G. & Zhang, X. Y. Mott-Hubbard transition in infinite dimensions. II. *Phys. Rev. B* **49,** 10181–10193. https://link.aps.org/doi/10.1103/PhysRevB.49.10181 (15 Apr. 1994) (cit. on p. 58).

177. Gull, E. *Continuous-Time Quantum Monte Carlo Algorithms for Fermions* PhD thesis (ETH Zurich, 2008). http://hdl.handle.net/20.500.11850/104013 (cit. on p. 64).

178. Valli, A. *Electronic correlations at the nanoscale* PhD thesis (TU Wien, 2013). http://hdl.handle.net/20.500.12708/9973 (cit. on p. 64).

179. Deisz, J. J., Hess, D. W. & Serene, J. W. Vertex symmetry and the asymptotic frequency dependence of the self-energy. *Phys. Rev. B* **55,** 2089–2094. https://link.aps.org/doi/10.1103/PhysRevB.55.2089 (4 Jan. 1997) (cit. on p. 64).

180. Potthoff, M., Wegner, T. & Nolting, W. Interpolating self-energy of the infinite-dimensional Hubbard model: Modifying the iterative perturbation theory. *Phys. Rev. B* **55,** 16132–16142. https://link.aps.org/doi/10.1103/PhysRevB.55.16132 (24 June 1997) (cit. on p. 64).

181. Freericks, J. K. & Turkowski, V. Inhomogeneous spectral moment sum rules for the retarded Green function and self-energy of strongly correlated electrons or ultracold fermionic atoms in optical lattices. *Phys. Rev. B* **80,** 115119. https://link.aps.org/doi/10.1103/PhysRevB.80.115119 (11 Sept. 2009) (cit. on p. 64).

182. Wang, X., Dang, H. T. & Millis, A. J. High-frequency asymptotic behavior of self-energies in quantum impurity models. *Phys. Rev. B* **84,** 073104. https://link.aps.org/doi/10.1103/PhysRevB.84.073104 (7 Aug. 2011) (cit. on p. 64).

183. Leonov, I., Korotin, D., Binggeli, N., Anisimov, V. I. & Vollhardt, D. Computation of correlation-induced atomic displacements and structural transformations in paramagnetic $KCuF_3$ and $LaMnO_3$. *Phys. Rev. B* **81,** 075109. https://link.aps.org/doi/10.1103/PhysRevB.81.075109 (7 Feb. 2010) (cit. on p. 64).

184. Bulla, R., Costi, T. A. & Pruschke, T. Numerical renormalization group method for quantum impurity systems. *Rev. Mod. Phys.* **80,** 395–450. https://link.aps.org/doi/10.1103/RevModPhys.80.395 (2 Apr. 2008) (cit. on p. 65).

185. Valli, A., Amaricci, A., Toschi, A., *et al.* Effective magnetic correlations in hole-doped graphene nanoflakes. *Phys. Rev. B* **94,** 245146. https://link.aps.org/doi/10.1103/PhysRevB.94.245146 (24 Dec. 2016) (cit. on pp. 71, 72, 75).

186. Valli, A., Amaricci, A., Brosco, V. & Capone, M. Quantum Interference Assisted Spin Filtering in Graphene Nanoflakes. *Nano Letters* **18,** 2158–2164. issn: 1530-6992. http://dx.doi.org/10.1021/acs.nanolett.8b00453 (Feb. 2018) (cit. on p. 71).

187. Schüler, M., Barthel, S., Wehling, T., *et al.* Realistic theory of electronic correlations in nanoscopic systems. *The European Physical Journal Special Topics* **226,** 2615–2640. issn: 1951-6401. http://dx.doi.org/10.1140/epjst/e2017-70049-3 (July 2017) (cit. on p. 71).

188. Valli, A., Sangiovanni, G., Gunnarsson, O., Toschi, A. & Held, K. Dynamical Vertex Approximation for Nanoscopic Systems. *Phys. Rev. Lett.* **104,** 246402. https://link.aps.org/doi/10.1103/PhysRevLett.104.246402 (24 June 2010) (cit. on p. 71).

189. Maier, T., Jarrell, M., Pruschke, T. & Hettler, M. H. Quantum cluster theories. *Rev. Mod. Phys.* **77,** 1027–1080. https://link.aps.org/doi/10.1103/RevModPhys.77.1027 (3 Oct. 2005) (cit. on pp. 71, 84, 103, 104, 109, 139).

190. Baumann, K., Valli, A., Amaricci, A. & Capone, M. Inducing and controlling magnetism in the honeycomb lattice through a harmonic trapping potential. *Phys. Rev. A* **101,** 033611. https://link.aps.org/doi/10.1103/PhysRevA.101.033611 (3 Mar. 2020) (cit. on pp. 72, 73, 75).

191. Bellomia, G. *HoneyTools v0.2.3, Zenodo* version v0.2.3. 2024. https://zenodo.org/doi/10.5281/zenodo.10622563 (cit. on p. 72).

192. Baù, N. & Marrazzo, A. *Theory of local $\mathbb{Z}_2$ topological markers for finite and periodic two-dimensional systems* 2024. arXiv: 2404.04598 [cond-mat.mes-hall] (cit. on p. 72).

193. Marrazzo, A., Beck, S., Margine, E. R., *et al. The Wannier-Functions Software Ecosystem for Materials Simulations* 2023. arXiv: 2312.10769 [cond-mat.mtrl-sci] (cit. on p. 72).

194. Snoek, M., Titvinidze, I., Tőke, C., Byczuk, K. & Hofstetter, W. Antiferromagnetic order of strongly interacting fermions in a trap: real-space dynamical mean-field analysis. *New Journal of Physics* **10,** 093008. issn: 1367-2630. http://dx.doi.org/10.1088/1367-2630/10/9/093008 (Sept. 2008) (cit. on p. 73).

195. Gorelik, E. V., Titvinidze, I., Hofstetter, W., Snoek, M. & Blümer, N. Néel Transition of Lattice Fermions in a Harmonic Trap: A Real-Space Dynamic Mean-Field Study. *Phys. Rev. Lett.* **105,** 065301. https://link.aps.org/doi/10.1103/PhysRevLett.105.065301 (6 Aug. 2010) (cit. on p. 73).

196. Amaricci, A., Privitera, A. & Capone, M. Inhomogeneous BCS-BEC crossover for trapped cold atoms in optical lattices. *Phys. Rev. A* **89,** 053604. https://link.aps.org/doi/10.1103/PhysRevA.89.053604 (5 May 2014) (cit. on p. 73).

197. Imada, M., Fujimori, A. & Tokura, Y. Metal-insulator transitions. *Rev. Mod. Phys.* **70,** 1039–1263. https://link.aps.org/doi/10.1103/RevModPhys.70.1039 (4 Oct. 1998) (cit. on p. 83).

198. Kyung, B., Kancharla, S. S., Sénéchal, D., *et al.* Pseudogap induced by short-range spin correlations in a doped Mott insulator. *Phys. Rev. B* **73,** 165114. https://link.aps.org/doi/10.1103/PhysRevB.73.165114 (16 Apr. 2006) (cit. on pp. 83, 103, 109, 141, 142).

199. Macridin, A., Jarrell, M., Maier, T., Kent, P. R. C. & D'Azevedo, E. Pseudogap and Antiferromagnetic Correlations in the Hubbard Model. *Phys. Rev. Lett.* **97,** 036401. https://link.aps.org/doi/10.1103/PhysRevLett.97.036401 (3 July 2006) (cit. on pp. 83, 109, 141, 142).

200. Gunnarsson, O., Schäfer, T., LeBlanc, J. P. F., *et al.* Fluctuation Diagnostics of the Electron Self-Energy: Origin of the Pseudogap Physics. *Phys. Rev. Lett.* **114,** 236402. https://link.aps.org/doi/10.1103/PhysRevLett.114.236402 (23 June 2015) (cit. on pp. 83, 109, 141).

201. Vedral, V. High-temperature macroscopic entanglement. *New Journal of Physics* **6,** 102–102. issn: 1367-2630. http://dx.doi.org/10.1088/1367-2630/6/1/102 (Aug. 2004) (cit. on pp. 83, 86, 87).

202. Scheurer, M. S., Chatterjee, S., Wu, W., *et al.* Topological order in the pseudogap metal. *Proceedings of the National Academy of Sciences* **115.** issn: 1091-6490. http://dx.doi.org/10.1073/pnas.1720580115 (Apr. 2018) (cit. on pp. 83, 86, 141).

203. Osterloh, A., Amico, L., Falci, G. & Fazio, R. Scaling of entanglement close to a quantum phase transition. *Nature* **416,** 608–610. issn: 1476-4687. https://doi.org/10.1038/416608a (Apr. 2002) (cit. on pp. 83, 87, 162).

204. Osborne, T. J. & Nielsen, M. A. Entanglement in a simple quantum phase transition. *Phys. Rev. A* **66,** 032110. https://link.aps.org/doi/10.1103/PhysRevA.66.032110 (3 Sept. 2002) (cit. on pp. 83, 87, 162).

205. Vidal, G., Latorre, J. I., Rico, E. & Kitaev, A. Entanglement in Quantum Critical Phenomena. *Phys. Rev. Lett.* **90,** 227902. https://link.aps.org/doi/10.1103/PhysRevLett.90.227902 (22 June 2003) (cit. on pp. 83, 162).

206. Squillante, L., Ricco, L. S., Ukpong, A. M., *et al.* Grüneisen parameter as an entanglement compass and the breakdown of the Hellmann-Feynman theorem. *Phys. Rev. B* **108,** L140403. https://link.aps.org/doi/10.1103/PhysRevB.108.L140403 (14 Oct. 2023) (cit. on pp. 83, 162).

207. Kitaev, A. & Preskill, J. Topological Entanglement Entropy. *Phys. Rev. Lett.* **96,** 110404. https://link.aps.org/doi/10.1103/PhysRevLett.96.110404 (11 Mar. 2006) (cit. on pp. 83, 87, 137, 162).

208. Levin, M. & Wen, X.-G. Detecting Topological Order in a Ground State Wave Function. *Phys. Rev. Lett.* **96,** 110405. https://link.aps.org/doi/10.1103/PhysRevLett.96.110405 (11 Mar. 2006) (cit. on pp. 83, 137, 162).

209. Chen, X., Gu, Z.-C. & Wen, X.-G. Local unitary transformation, long-range quantum entanglement, wave function renormalization, and topological order. *Phys. Rev. B* **82,** 155138. https://link.aps.org/doi/10.1103/PhysRevB.82.155138 (15 Oct. 2010) (cit. on pp. 83, 137, 162).

210. Boguslawski, K., Tecmer, P., Barcza, G., Legeza, Ö. & Reiher, M. Orbital Entanglement in Bond-Formation Processes. *Journal of Chemical Theory and Computation* **9.** Pmid: 26583979, 2959–2973. https://doi.org/10.1021/ct400247p (2013) (cit. on pp. 83, 162).

211. Szalay, S., Barcza, G., Szilvasi, T., Veis, L. & Legeza, Ö. The correlation theory of the chemical bond. *Scientific Reports* **7,** 2237. issn: 2045-2322. https://doi.org/10.1038/s41598-017-02447-z (May 2017) (cit. on pp. 83, 85, 159, 162).

212. White, S. R. Density matrix formulation for quantum renormalization groups. *Phys. Rev. Lett.* **69,** 2863–2866. https://link.aps.org/doi/10.1103/PhysRevLett.69.2863 (19 Nov. 1992) (cit. on pp. 83, 162).

213. Legeza, Ö. & Sólyom, J. Optimizing the density-matrix renormalization group method using quantum information entropy. *Phys. Rev. B* **68,** 195116. https://link.aps.org/doi/10.1103/PhysRevB.68.195116 (19 Nov. 2003) (cit. on pp. 83, 162).

214. Stein, C. J. & Reiher, M. Automated Selection of Active Orbital Spaces. *Journal of Chemical Theory and Computation* **12,** 1760–1771. https://doi.org/10.1021/acs.jctc.6b00156 (2016) (cit. on pp. 83, 162).

215. Bañuls, M.-C., Cirac, J. I. & Wolf, M. M. Entanglement in fermionic systems. *Phys. Rev. A* **76,** 022311. https://link.aps.org/doi/10.1103/PhysRevA.76.022311 (2 Aug. 2007) (cit. on pp. 83, 85, 91, 130, 153, 159).

216. Friis, N., Lee, A. R. & Bruschi, D. E. Fermionic-mode entanglement in quantum information. *Phys. Rev. A* **87,** 022338. https://link.aps.org/doi/10.1103/PhysRevA.87.022338 (2 Feb. 2013) (cit. on pp. 83, 85, 91, 130, 153, 159).

217. Friis, N. Reasonable fermionic quantum information theories require relativity. *New Journal of Physics* **18,** 033014. https://doi.org/10.1088/1367-2630/18/3/033014 (Mar. 2016) (cit. on pp. 83, 85, 91, 130, 153).

218. Benatti, F., Floreanini, R., Franchini, F. & Marzolino, U. Entanglement in indistinguishable particle systems. *Physics Reports* **878,** 1–27. issn: 0370-1573. https://www.sciencedirect.com/science/article/pii/S0370157320302520 (2020) (cit. on pp. 83, 85, 91, 130, 153, 159).

219. Ding, L., Zimboras, Z. & Schilling, C. *Quantifying Electron Entanglement Faithfully* 2022. arXiv: 2207.03377 [quant-ph]. https://arxiv.org/abs/2207.03377 (cit. on pp. 83, 85, 87, 88, 91, 93, 97, 130, 138, 164).

220. Ding, L., Dünnweber, G. & Schilling, C. Physical entanglement between localized orbitals. *Quantum Science and Technology* **9,** 015005. https://dx.doi.org/10.1088/2058-9565/ad00d9 (Oct. 2023) (cit. on pp. 83, 85, 87, 88, 91, 93, 130, 153, 164).

221. Loh, E. Y., Gubernatis, J. E., Scalettar, R. T., *et al.* Sign problem in the numerical simulation of many-electron systems. *Phys. Rev. B* **41,** 9301–9307. https://link.aps.org/doi/10.1103/PhysRevB.41.9301 (13 May 1990) (cit. on p. 83).

222. Troyer, M. & Wiese, U.-J. Computational Complexity and Fundamental Limitations to Fermionic Quantum Monte Carlo Simulations. *Phys. Rev. Lett.* **94,** 170201. https://link.aps.org/doi/10.1103/PhysRevLett.94.170201 (17 May 2005) (cit. on p. 83).

223. Pan, G. & Meng, Z. Y. *The sign problem in quantum Monte Carlo simulations* in *Encyclopedia of Condensed Matter Physics* 879–893 (Elsevier, 2024). isbn: 9780323914086. http://dx.doi.org/10.1016/B978-0-323-90800-9.00095-0 (cit. on p. 83).

224. Cirac, J. I., Pérez-García, D., Schuch, N. & Verstraete, F. Matrix product states and projected entangled pair states: Concepts, symmetries, theorems. *Rev. Mod. Phys.* **93,** 045003. https://link.aps.org/doi/10.1103/RevModPhys.93.045003 (4 Dec. 2021) (cit. on pp. 83, 87, 89, 127).

225. Silvi, P., Tschirsich, F., Gerster, M., *et al.* The Tensor Networks Anthology: Simulation techniques for many-body quantum lattice systems. *SciPost Phys. Lect. Notes,* 8. https://scipost.org/10.21468/SciPostPhysLectNotes.8 (2019) (cit. on p. 83).

226. Felser, T., Notarnicola, S. & Montangero, S. Efficient Tensor Network Ansatz for High-Dimensional Quantum Many-Body Problems. *Phys. Rev. Lett.* **126,** 170603. https://link.aps.org/doi/10.1103/PhysRevLett.126.170603 (17 Apr. 2021) (cit. on p. 83).

227. Lami, G., Carleo, G. & Collura, M. Matrix product states with backflow correlations. *Phys. Rev. B* **106,** L081111. https://link.aps.org/doi/10.1103/PhysRevB.106.L081111 (8 Aug. 2022) (cit. on p. 83).

228. Eisert, J., Cramer, M. & Plenio, M. B. Colloquium: Area laws for the entanglement entropy. *Rev. Mod. Phys.* **82,** 277–306. https://link.aps.org/doi/10.1103/RevModPhys.82.277 (1 Feb. 2010) (cit. on pp. 84, 90, 137).

229. Hettler, M. H., Tahvildar-Zadeh, A. N., Jarrell, M., Pruschke, T. & Krishnamurthy, H. R. Nonlocal dynamical correlations of strongly interacting electron systems. *Phys. Rev. B* **58,** R7475–r7479. https://link.aps.org/doi/10.1103/PhysRevB.58.R7475 (12 Sept. 1998) (cit. on pp. 84, 103).

230. Lichtenstein, A. I. & Katsnelson, M. I. Antiferromagnetism and d-wave superconductivity in cuprates: A cluster dynamical mean-field theory. *Phys. Rev. B* **62,** R9283–r9286. https://link.aps.org/doi/10.1103/PhysRevB.62.R9283 (14 Oct. 2000) (cit. on pp. 84, 103, 109).

231. Kotliar, G., Savrasov, S. Y., Pálsson, G. & Biroli, G. Cellular Dynamical Mean Field Approach to Strongly Correlated Systems. *Phys. Rev. Lett.* **87,** 186401. https://link.aps.org/doi/10.1103/PhysRevLett.87.186401 (18 Oct. 2001) (cit. on pp. 84, 103, 108).

232. Park, H., Haule, K. & Kotliar, G. Cluster Dynamical Mean Field Theory of the Mott Transition. *Phys. Rev. Lett.* **101,** 186403. https://link.aps.org/doi/10.1103/PhysRevLett.101.186403 (18 Oct. 2008) (cit. on pp. 84, 103, 109, 110, 112, 118).

233. Cocchi, E., Miller, L. A., Drewes, J. H., *et al.* Measuring Entropy and Short-Range Correlations in the Two-Dimensional Hubbard Model. *Phys. Rev. X* **7,** 031025. https://link.aps.org/doi/10.1103/PhysRevX.7.031025 (3 Aug. 2017) (cit. on p. 84).

234. Bera, S., Haldar, A. & Banerjee, S. Dynamical mean-field theory for Rényi entanglement entropy and mutual information in the Hubbard model. *Phys. Rev. B* **109,** 035156. https://link.aps.org/doi/10.1103/PhysRevB.109.035156 (3 Jan. 2024) (cit. on pp. 84, 117, 121, 123, 124).

235. D'Emidio, J., Orús, R., Laflorencie, N. & de Juan, F. Universal Features of Entanglement Entropy in the Honeycomb Hubbard Model. *Phys. Rev. Lett.* **132,** 076502. https://link.aps.org/doi/10.1103/PhysRevLett.132.076502 (7 Feb. 2024) (cit. on pp. 84, 117, 121, 123).

236. Wick, G. C., Wightman, A. S. & Wigner, E. P. The Intrinsic Parity of Elementary Particles. *Phys. Rev.* **88,** 101–105. https://link.aps.org/doi/10.1103/PhysRev.88.101 (1 Oct. 1952) (cit. on pp. 85, 91, 130, 153).

237. Wick, G. C., Wightman, A. S. & Wigner, E. P. Superselection Rule for Charge. *Phys. Rev. D* **1,** 3267–3269. https://link.aps.org/doi/10.1103/PhysRevD.1.3267 (12 June 1970) (cit. on pp. 85, 91, 130, 153).

238. Bartlett, S. D. & Wiseman, H. M. Entanglement Constrained by Superselection Rules. *Phys. Rev. Lett.* **91,** 097903. https://link.aps.org/doi/10.1103/PhysRevLett.91.097903 (9 Aug. 2003) (cit. on pp. 85, 91, 130, 153).

239. Vidal, N. T., Bera, M. L., Riera, A., Lewenstein, M. & Bera, M. N. Quantum operations in an information theory for fermions. *Phys. Rev. A* **104,** 032411. https://link.aps.org/doi/10.1103/PhysRevA.104.032411 (3 Sept. 2021) (cit. on pp. 85, 91, 130, 153).

240. Galler, A. & Thunström, P. Orbital and electronic entanglement in quantum teleportation schemes. *Phys. Rev. Res.* **3,** 033120. https://link.aps.org/doi/10.1103/PhysRevResearch.3.033120 (3 Aug. 2021) (cit. on pp. 85, 91, 130, 153).

241. Costa de Almeida, R. & Hauke, P. From entanglement certification with quench dynamics to multipartite entanglement of interacting fermions. *Phys. Rev. Res.* **3,** L032051. https://link.aps.org/doi/10.1103/PhysRevResearch.3.L032051 (3 Aug. 2021) (cit. on pp. 85, 87, 91, 130, 153).

242. Shen, T., Barghathi, H., Maestro, A. D. & Rubenstein, B. *Disentangling the Physics of the Attractive Hubbard Model via the Accessible and Symmetry-Resolved Entanglement Entropies* 2023. arXiv: 2312.11746 [cond-mat.str-el] (cit. on pp. 85, 91, 130, 153).

243. Mejuto-Zaera, C., Tubman, N. M. & Whaley, K. B. Dynamical mean field theory simulations with the adaptive sampling configuration interaction method. *Phys. Rev. B* **100,** 125165. https://link.aps.org/doi/10.1103/PhysRevB.100.125165 (12 Sept. 2019) (cit. on pp. 85, 113).

244. Williams-Young, D. B., Tubman, N. M., Mejuto-Zaera, C. & de Jong, W. A. A parallel, distributed memory implementation of the adaptive sampling configuration interaction method. *The Journal of Chemical Physics* **158,** 214109. issn: 0021-9606. https://doi.org/10.1063/5.0148650 (June 2023) (cit. on pp. 85, 113).

245. Tajik, M., Kukuljan, I., Sotiriadis, S., *et al.* Verification of the area law of mutual information in a quantum field simulator. *Nature Physics* **19,** 1022–1026. https://doi.org/10.1038/s41567-023-02027-1 (Apr. 2023) (cit. on pp. 85, 90, 137).

246. Parez, G., Berthiere, C. & Witczak-Krempa, W. Separability and entanglement of resonating valence-bond states. *SciPost Phys.* **15,** 066. https://scipost.org/10.21468/SciPostPhys.15.2.066 (2023) (cit. on pp. 85, 137).

247. Plenio, M. B. & Virmani, S. An introduction to entanglement measures. *Quantum Info. Comput.* **7,** 1–51. issn: 1533-7146 (Jan. 2007) (cit. on pp. 87, 88, 91, 99, 157, 158, 161).

248. Gühne, O. & Tóth, G. Entanglement detection. *Physics Reports* **474,** 1–75. issn: 0370-1573. http://dx.doi.org/10.1016/j.physrep.2009.02.004 (Apr. 2009) (cit. on pp. 87, 88, 99, 157, 158).

249. Calabrese, P. & Cardy, J. Entanglement entropy and conformal field theory. *J. Phys. A Math. Theor.* **42,** 504005 (Dec. 2009) (cit. on p. 87).

250. Calabrese, P., Cardy, J. & Doyon, B. Entanglement entropy in extended quantum systems. *Journal of Physics A: Mathematical and Theoretical* **42,** 500301. issn: 1751-8121. http://dx.doi.org/10.1088/1751-8121/42/50/500301 (Dec. 2009) (cit. on p. 87).

251. Hauke, P., Heyl, M., Tagliacozzo, L. & Zoller, P. Measuring multipartite entanglement through dynamic susceptibilities. *Nature Physics* **12,** 778–782. issn: 1745-2481. http://dx.doi.org/10.1038/nphys3700 (Mar. 2016) (cit. on p. 87).

252. Bengtsson, I. & Zyczkowski, K. *A brief introduction to multipartite entanglement* 2016. arXiv: 1612.07747 [quant-ph] (cit. on p. 87).

253. Ma, M., Li, Y. & Shang, J. *Multipartite entanglement measures: a review* 2023. arXiv: 2309.09459 [quant-ph] (cit. on p. 87).

254. Gabbrielli, M., Smerzi, A. & Pezzè, L. Multipartite Entanglement at Finite Temperature. *Scientific Reports* **8.** issn: 2045-2322. http://dx.doi.org/10.1038/s41598-018-31761-3 (Oct. 2018) (cit. on p. 87).

255. Braunstein, S. L. & Caves, C. M. Statistical distance and the geometry of quantum states. *Phys. Rev. Lett.* **72,** 3439–3443. https://link.aps.org/doi/10.1103/PhysRevLett.72.3439 (22 May 1994) (cit. on pp. 87, 158).

256. De Chiara, G. & Sanpera, A. Genuine quantum correlations in quantum many-body systems: a review of recent progress. *Reports on Progress in Physics* **81,** 074002. issn: 1361-6633. http://dx.doi.org/10.1088/1361-6633/aabf61 (June 2018) (cit. on p. 87).

257. Vedral, V., Plenio, M. B., Rippin, M. A. & Knight, P. L. Quantifying Entanglement. *Phys. Rev. Lett.* **78,** 2275–2279. https://link.aps.org/doi/10.1103/PhysRevLett.78.2275 (12 Mar. 1997) (cit. on pp. 87, 88, 158, 161).

258. Vedral, V. & Plenio, M. B. Entanglement measures and purification procedures. *Phys. Rev. A* **57,** 1619–1633. https://link.aps.org/doi/10.1103/PhysRevA.57.1619 (3 Mar. 1998) (cit. on pp. 87, 158, 161).

259. Henderson, L. & Vedral, V. Information, Relative Entropy of Entanglement, and Irreversibility. *Phys. Rev. Lett.* **84,** 2263–2266. https://link.aps.org/doi/10.1103/PhysRevLett.84.2263 (10 Mar. 2000) (cit. on pp. 87, 88, 158, 160, 161).

260. Henderson, L. & Vedral, V. Classical, quantum and total correlations. *Journal of Physics A: Mathematical and General* **34,** 6899. https://dx.doi.org/10.1088/0305-4470/34/35/315 (Aug. 2001) (cit. on pp. 87, 157, 158, 160, 162).

261. Wei, T.-C. & Goldbart, P. M. Geometric measure of entanglement and applications to bipartite and multipartite quantum states. *Phys. Rev. A* **68,** 042307. https://link.aps.org/doi/10.1103/PhysRevA.68.042307 (4 Oct. 2003) (cit. on pp. 87, 158).

262. Lambert, J. & Sørensen, E. S. From classical to quantum information geometry: a guide for physicists. *New Journal of Physics* **25,** 081201. issn: 1367-2630. http://dx.doi.org/10.1088/1367-2630/aceb14 (Aug. 2023) (cit. on pp. 87, 88, 157).

263. Bengtsson, I. & Zyczkowski, K. *Geometry of Quantum States: An Introduction to Quantum Entanglement* (Cambridge University Press, 2006) (cit. on pp. 87, 88, 157, 158).

264. Shapourian, H., Shiozaki, K. & Ryu, S. Partial time-reversal transformation and entanglement negativity in fermionic systems. *Phys. Rev. B* **95,** 165101. https://link.aps.org/doi/10.1103/PhysRevB.95.165101 (16 Apr. 2017) (cit. on pp. 87, 99).

265. Shapourian, H. & Ryu, S. Finite-temperature entanglement negativity of free fermions. *Journal of Statistical Mechanics: Theory and Experiment* **2019,** 043106. issn: 1742-5468. http://dx.doi.org/10.1088/1742-5468/ab11e0 (Apr. 2019) (cit. on pp. 87, 99).

266. Shapourian, H., Ruggiero, P., Ryu, S. & Calabrese, P. Twisted and untwisted negativity spectrum of free fermions. *SciPost Phys.* **7,** 037. https://scipost.org/10.21468/SciPostPhys.7.3.037 (2019) (cit. on pp. 87, 99).

267. Murciano, S., Vitale, V., Dalmonte, M. & Calabrese, P. Negativity Hamiltonian: An Operator Characterization of Mixed-State Entanglement. *Phys. Rev. Lett.* **128,** 140502. https://link.aps.org/doi/10.1103/PhysRevLett.128.140502 (14 Apr. 2022) (cit. on pp. 87, 99, 100, 153).

268. Ding, L. & Schilling, C. Correlation Paradox of the Dissociation Limit: A Quantum Information Perspective. *Journal of Chemical Theory and Computation* **16.** Pmid: 32433873, 4159–4175. eprint: https://doi.org/10.1021/acs.jctc.0c00054. https://doi.org/10.1021/acs.jctc.0c00054 (2020) (cit. on pp. 87, 159).

269. Carisch, C. & Zilberberg, O. Efficient separation of quantum from classical correlations for mixed states with a fixed charge. *Quantum* **7,** 954. issn: 2521-327x. https://doi.org/10.22331/q-2023-03-20-954 (Mar. 2023) (cit. on pp. 87, 91, 115).

270. Vedral, V. The role of relative entropy in quantum information theory. *Rev. Mod. Phys.* **74,** 197–234. https://link.aps.org/doi/10.1103/RevModPhys.74.197 (1 Mar. 2002) (cit. on pp. 87–89, 99, 158, 160, 161).

271. Życzkowski, K., Horodecki, P., Sanpera, A. & Lewenstein, M. Volume of the set of separable states. *Phys. Rev. A* **58,** 883–892. https://link.aps.org/doi/10.1103/PhysRevA.58.883 (2 Aug. 1998) (cit. on pp. 87, 93, 138, 161).

272. Krueger, O. & Werner, R. F. *Some Open Problems in Quantum Information Theory* 2005. arXiv: quant-ph/0504166 [quant-ph] (cit. on pp. 87, 93, 138, 161).

273. Ioannou, L. M. Computational complexity of the quantum separability problem. *Quantum Info. Comput.* **7,** 335–370. issn: 1533-7146 (May 2007) (cit. on pp. 88, 91, 93, 138, 161).

274. Ptaszyński, K. & Esposito, M. Fermionic One-Body Entanglement as a Thermodynamic Resource. *Phys. Rev. Lett.* **130,** 150201. https://link.aps.org/doi/10.1103/PhysRevLett.130.150201 (15 Apr. 2023) (cit. on pp. 88, 91).

275. Ding, L. *Fermionic Entanglement and Correlation* 2022. arXiv: 2207.03848 [quant-ph] (cit. on pp. 88, 92, 127).

276. Srednicki, M. Entropy and area. *Phys. Rev. Lett.* **71,** 666–669. https://link.aps.org/doi/10.1103/PhysRevLett.71.666 (5 Aug. 1993) (cit. on p. 90).

277. Holzhey, C., Larsen, F. & Wilczek, F. Geometric and renormalized entropy in conformal field theory. *Nuclear Physics B* **424,** 443–467. issn: 0550-3213. http://dx.doi.org/10.1016/0550-3213(94)90402-2 (Aug. 1994) (cit. on p. 90).

278. Hawking, S., Maldacena, J. & Strominger, A. DeSitter entropy, quantum entanglement and ADS/CFT. *Journal of High Energy Physics* **2001,** 001–001. issn: 1029-8479. http://dx.doi.org/10.1088/1126-6708/2001/05/001 (May 2001) (cit. on p. 90).

279. Giulini, D. *Superselection Rules* 2009. arXiv: 0710.1516 [quant-ph] (cit. on p. 91).

280. Ding, L., Mardazad, S., Das, S., *et al.* Concept of Orbital Entanglement and Correlation in Quantum Chemistry. *Journal of Chemical Theory and Computation* **17.** Pmid: 33430597, 79–95. https://doi.org/10.1021/acs.jctc.0c00559 (2021) (cit. on pp. 91–93, 98, 157, 158).

281. Boguslawski, K. & Tecmer, P. Orbital entanglement in quantum chemistry. *International Journal of Quantum Chemistry* **115,** 1289–1295. issn: 1097-461x. http://dx.doi.org/10.1002/qua.24832 (Dec. 2014) (cit. on pp. 94, 98).

282. Vidal, G. & Werner, R. F. Computable measure of entanglement. *Phys. Rev. A* **65,** 032314. https://link.aps.org/doi/10.1103/PhysRevA.65.032314 (3 Feb. 2002) (cit. on p. 99).

283. Plenio, M. B. Logarithmic Negativity: A Full Entanglement Monotone That is not Convex. *Phys. Rev. Lett.* **95,** 090503. https://link.aps.org/doi/10.1103/PhysRevLett.95.090503 (9 Aug. 2005) (cit. on p. 99).

284. Horodecki, M., Horodecki, P. & Horodecki, R. Mixed-State Entanglement and Distillation: Is there a "Bound" Entanglement in Nature? *Phys. Rev. Lett.* **80,** 5239–5242. https://link.aps.org/doi/10.1103/PhysRevLett.80.5239 (24 June 1998) (cit. on p. 99).

285. Goldstein, M. & Sela, E. Symmetry-Resolved Entanglement in Many-Body Systems. *Phys. Rev. Lett.* **120,** 200602. https://link.aps.org/doi/10.1103/PhysRevLett.120.200602 (20 May 2018) (cit. on pp. 100, 153).

286. Murciano, S. *Entanglement and symmetries in many-body quantum systems* PhD thesis (SISSA, 2022). https://hdl.handle.net/20.500.11767/129390 (cit. on pp. 100, 153).

287. Vitale, V. *Probing and detecting entanglement in synthetic quantum matter* PhD thesis (SISSA, 2022). https://hdl.handle.net/20.500.11767/129911 (cit. on pp. 100, 153).

288. Neven, A., Carrasco, J., Vitale, V., *et al.* Symmetry-resolved entanglement detection using partial transpose moments. *npj Quantum Information* **7.** issn: 2056-6387. http://dx.doi.org/10.1038/s41534-021-00487-y (Oct. 2021) (cit. on pp. 100, 153).

289. Vitale, V., Elben, A., Kueng, R., *et al.* Symmetry-resolved dynamical purification in synthetic quantum matter. *SciPost Phys.* **12,** 106. https://scipost.org/10.21468/SciPostPhys.12.3.106 (2022) (cit. on pp. 100, 153).

290. Biroli, G. & Kotliar, G. Cluster methods for strongly correlated electron systems. *Phys. Rev. B* **65,** 155112. https://link.aps.org/doi/10.1103/PhysRevB.65.155112 (15 Apr. 2002) (cit. on p. 103).

291. Rubtsov, A. N., Stepanov, E. A. & Lichtenstein, A. I. Collective magnetic fluctuations in Hubbard plaquettes captured by fluctuating local field method. *Phys. Rev. B* **102,** 224423. https://link.aps.org/doi/10.1103/PhysRevB.102.224423 (22 Dec. 2020) (cit. on p. 103).

292. Linnér, E., Lichtenstein, A. I., Biermann, S. & Stepanov, E. A. Multichannel fluctuating field approach to competing instabilities in interacting electronic systems. *Phys. Rev. B* **108,** 035143. https://link.aps.org/doi/10.1103/PhysRevB.108.035143 (3 July 2023) (cit. on p. 103).

293. Lyakhova, Y. S., Astretsov, G. V. & Rubtsov, A. N. The mean-field concept and post-DMFT methods in the contemporary theory of correlated systems. *Phys-usp+.* [Phys. Usp. (2023)]. http://dx.doi.org/10.3367/UFNe.2022.09.039231 (2023) (cit. on pp. 103, 152).

294. Rohringer, G., Hafermann, H., Toschi, A., *et al.* Diagrammatic routes to nonlocal correlations beyond dynamical mean field theory. *Rev. Mod. Phys.* **90,** 025003. https://link.aps.org/doi/10.1103/RevModPhys.90.025003 (2 May 2018) (cit. on pp. 103, 152).

295. Fotso, H. F., Tam, K.-M. & Moreno, J. Beyond quantum cluster theories: multiscale approaches for strongly correlated systems. *Quantum Science and Technology* **7,** 033001. issn: 2058-9565. http://dx.doi.org/10.1088/2058-9565/ac676b (May 2022) (cit. on pp. 103, 152).

296. Biermann, S., Aryasetiawan, F. & Georges, A. First-Principles Approach to the Electronic Structure of Strongly Correlated Systems: Combining the *GW* Approximation and Dynamical Mean-Field Theory. *Phys. Rev. Lett.* **90,** 086402. https://link.aps.org/doi/10.1103/PhysRevLett.90.086402 (8 Feb. 2003) (cit. on p. 103).

297. Rubtsov, A. N., Katsnelson, M. I. & Lichtenstein, A. I. Dual fermion approach to nonlocal correlations in the Hubbard model. *Phys. Rev. B* **77,** 033101. https://link.aps.org/doi/10.1103/PhysRevB.77.033101 (3 Jan. 2008) (cit. on p. 103).

298. Rubtsov, A., Katsnelson, M. & Lichtenstein, A. Dual boson approach to collective excitations in correlated fermionic systems. *Annals of Physics* **327,** 1320–1335. issn: 0003-4916. http://dx.doi.org/10.1016/j.aop.2012.01.002 (May 2012) (cit. on p. 103).

299. Toschi, A., Katanin, A. A. & Held, K. Dynamical vertex approximation: A step beyond dynamical mean-field theory. *Phys. Rev. B* **75,** 045118. https://link.aps.org/doi/10.1103/PhysRevB.75.045118 (4 Jan. 2007) (cit. on p. 103).

300. Ayral, T. & Parcollet, O. Mott physics and spin fluctuations: A unified framework. *Phys. Rev. B* **92,** 115109. https://link.aps.org/doi/10.1103/PhysRevB.92.115109 (11 Sept. 2015) (cit. on p. 103).

301. Ayral, T. & Parcollet, O. Mott physics and spin fluctuations: A functional viewpoint. *Phys. Rev. B* **93,** 235124. https://link.aps.org/doi/10.1103/PhysRevB.93.235124 (23 June 2016) (cit. on p. 103).

302. Vandelli, M., Kaufmann, J., El-Nabulsi, M., *et al.* Multi-band D-TRILEX approach to materials with strong electronic correlations. *SciPost Phys.* **13,** 036. https://scipost.org/10.21468/SciPostPhys.13.2.036 (2022) (cit. on p. 103).

303. Chatzieleftheriou, M., Biermann, S. & Stepanov, E. A. *Local and nonlocal electronic correlations at the metal-insulator transition in the Hubbard model in two dimensions* 2023. arXiv: 2312.03123 [cond-mat.str-el] (cit. on p. 103).

304. Krien, F., Valli, A. & Capone, M. Single-boson exchange decomposition of the vertex function. *Phys. Rev. B* **100,** 155149. https://link.aps.org/doi/10.1103/PhysRevB.100.155149 (15 Oct. 2019) (cit. on p. 103).

305. Zheng, B.-X., Chung, C.-M., Corboz, P., *et al.* Stripe order in the underdoped region of the two-dimensional Hubbard model. *Science* **358,** 1155–1160. issn: 1095-9203. http://dx.doi.org/10.1126/science.aam7127 (Dec. 2017) (cit. on pp. 103, 139).

306. Wietek, A., Rossi, R., Šimkovic, F., *et al.* Mott Insulating States with Competing Orders in the Triangular Lattice Hubbard Model. *Phys. Rev. X* **11,** 041013. https://link.aps.org/doi/10.1103/PhysRevX.11.041013 (4 Oct. 2021) (cit. on pp. 103, 139).

307. Xu, H., Chung, C.-M., Qin, M., *et al. Coexistence of superconductivity with partially filled stripes in the Hubbard model* 2023. arXiv: 2303.08376 [cond-mat.supr-con] (cit. on pp. 103, 139).

308. Stanescu, T. D. & Kotliar, G. Fermi arcs and hidden zeros of the Green function in the pseudogap state. *Phys. Rev. B* **74,** 125110. https://link.aps.org/doi/10.1103/PhysRevB.74.125110 (12 Sept. 2006) (cit. on pp. 103, 109, 141, 142, 152).

309. Zhang, Y. Z. & Imada, M. Pseudogap and Mott transition studied by cellular dynamical mean-field theory. *Phys. Rev. B* **76,** 045108. https://link.aps.org/doi/10.1103/PhysRevB.76.045108 (4 July 2007) (cit. on pp. 103, 109, 142).

310. Koch, E., Sangiovanni, G. & Gunnarsson, O. Sum rules and bath parametrization for quantum cluster theories. *Phys. Rev. B* **78,** 115102. https://link.aps.org/doi/10.1103/PhysRevB.78.115102 (11 Sept. 2008) (cit. on pp. 105, 106).

311. Crippa, L. *Local and non-local correlations in Topological Insulators and Weyl Semimetals* PhD thesis (SISSA, 2020). https://hdl.handle.net/20.500.11767/114413 (cit. on p. 106).

312. Mejuto-Zaera, C., Zepeda-Núñez, L., Lindsey, M., *et al.* Efficient hybridization fitting for dynamical mean-field theory via semi-definite relaxation. *Phys. Rev. B* **101,** 035143. https://link.aps.org/doi/10.1103/PhysRevB.101.035143 (3 Jan. 2020) (cit. on pp. 107, 113).

313. Sénéchal, D., Perez, D. & Pioro-Ladrière, M. Spectral Weight of the Hubbard Model through Cluster Perturbation Theory. *Phys. Rev. Lett.* **84,** 522–525. https://link.aps.org/doi/10.1103/PhysRevLett.84.522 (3 Jan. 2000) (cit. on p. 108).

314. Civelli, M., Capone, M., Kancharla, S. S., Parcollet, O. & Kotliar, G. Dynamical Breakup of the Fermi Surface in a Doped Mott Insulator. *Phys. Rev. Lett.* **95,** 106402. https://link.aps.org/doi/10.1103/PhysRevLett.95.106402 (10 Sept. 2005) (cit. on pp. 109, 141, 142, 152).

315. Gull, E., Parcollet, O., Werner, P. & Millis, A. J. Momentum-sector-selective metal-insulator transition in the eight-site dynamical mean-field approximation to the Hubbard model in two dimensions. *Phys. Rev. B* **80,** 245102. https://link.aps.org/doi/10.1103/PhysRevB.80.245102 (24 Dec. 2009) (cit. on pp. 109, 141, 152).

316. Gull, E., Ferrero, M., Parcollet, O., Georges, A. & Millis, A. J. Momentum-space anisotropy and pseudogaps: A comparative cluster dynamical mean-field analysis of the doping-driven metal-insulator transition in the two-dimensional Hubbard model. *Phys. Rev. B* **82,** 155101. https://link.aps.org/doi/10.1103/PhysRevB.82.155101 (15 Oct. 2010) (cit. on pp. 109, 141, 152).

317. Meixner, M., Menke, H., Klett, M., *et al. Mott transition and pseudogap of the square-lattice Hubbard model: results from center-focused cellular dynamical mean-field theory* 2024. arXiv: 2310.17302 [cond-mat.str-el] (cit. on pp. 109, 118, 139, 142).

318. Wu, W., Scheurer, M. S., Chatterjee, S., *et al.* Pseudogap and Fermi-Surface Topology in the Two-Dimensional Hubbard Model. *Phys. Rev. X* **8,** 021048. https://link.aps.org/doi/10.1103/PhysRevX.8.021048 (2 May 2018) (cit. on pp. 109, 141).

319. Tubman, N. M., Lee, J., Takeshita, T. Y., Head-Gordon, M. & Whaley, K. B. A deterministic alternative to the full configuration interaction quantum Monte Carlo method. *The Journal of Chemical Physics* **145.** https://doi.org/10.1063/1.4955109 (July 2016) (cit. on p. 113).

320. Levine, D. S., Hait, D., Tubman, N. M., *et al.* CASSCF with Extremely Large Active Spaces Using the Adaptive Sampling Configuration Interaction Method. *Journal of Chemical Theory and Computation* **16,** 2340–2354. https://doi.org/10.1021/acs.jctc.9b01255 (Feb. 2020) (cit. on p. 113).

321. Mejuto-Zaera, C., Weng, G., Romanova, M., *et al.* Are multi-quasiparticle interactions important in molecular ionization? *The Journal of Chemical Physics* **154,** 121101. https://doi.org/10.1063/5.0044060 (Mar. 2021) (cit. on p. 113).

322. Mejuto-Zaera, C., Tzeli, D., Williams-Young, D., *et al.* The Effect of Geometry, Spin, and Orbital Optimization in Achieving Accurate, Correlated Results for Iron–Sulfur Cubanes. *Journal of Chemical Theory and Computation* **18,** 687–702. https://doi.org/10.1021/acs.jctc.1c00830 (2022) (cit. on p. 113).

323. Bravyi, S. & Gosset, D. Complexity of Quantum Impurity Problems. *Communications in Mathematical Physics* **356,** 451–500. https://doi.org/10.1007/s00220-017-2976-9 (Aug. 2017) (cit. on p. 113).

324. Stocker, L., Sack, S. H., Ferguson, M. S. & Zilberberg, O. Entanglement-based observables for quantum impurities. *Phys. Rev. Res.* **4,** 043177. https://link.aps.org/doi/10.1103/PhysRevResearch.4.043177 (4 Dec. 2022) (cit. on p. 115).

325. Adesso, G., Girolami, D. & Serafini, A. Measuring Gaussian Quantum Information and Correlations Using the Rényi Entropy of Order 2. *Phys. Rev. Lett.* **109,** 190502. https://link.aps.org/doi/10.1103/PhysRevLett.109.190502 (19 Nov. 2012) (cit. on pp. 117, 124).

326. Kudler-Flam, J. Rényi Mutual Information in Quantum Field Theory. *Phys. Rev. Lett.* **130,** 021603. https://link.aps.org/doi/10.1103/PhysRevLett.130.021603 (2 Jan. 2023) (cit. on pp. 117, 124).

327. Balzer, M., Kyung, B., Sénéchal, D., Tremblay, A.-M. S. & Potthoff, M. First-order Mott transition at zero temperature in two dimensions: Variational plaquette study. *EPL (Europhysics Letters)* **85,** 17002. issn: 1286-4854. http://dx.doi.org/10.1209/0295-5075/85/17002 (Jan. 2009) (cit. on p. 118).

328. LeBlanc, J. P. F., Antipov, A. E., Becca, F., *et al.* Solutions of the Two-Dimensional Hubbard Model: Benchmarks and Results from a Wide Range of Numerical Algorithms. *Phys. Rev. X* **5,** 041041. https://link.aps.org/doi/10.1103/PhysRevX.5.041041 (4 Dec. 2015) (cit. on p. 118).

329. Shneiderman, B. Tree visualization with tree-maps: 2-d space-filling approach. *ACM Transactions on Graphics* **11,** 92–99. issn: 1557-7368. http://dx.doi.org/10.1145/102377.115768 (Jan. 1992) (cit. on pp. 120, 122).

330. Kong, N., Heer, J. & Agrawala, M. Perceptual Guidelines for Creating Rectangular Treemaps. *IEEE Transactions on Visualization and Computer Graphics* **16,** 990–998. issn: 1941-0506 (Nov. 2010) (cit. on pp. 120, 122).

331. Born, M. Zur Quantenmechanik der Stoßvorgänge. *Zeitschrift für Physik* **37,** 863–867. issn: 1434-601x. http://dx.doi.org/10.1007/BF01397477 (Dec. 1926) (cit. on p. 122).

332. Peres, A. & Terno, D. R. Quantum information and relativity theory. *Rev. Mod. Phys.* **76,** 93–123. https://link.aps.org/doi/10.1103/RevModPhys.76.93 (1 Jan. 2004) (cit. on p. 122).

333. Grover, T. Entanglement of Interacting Fermions in Quantum Monte Carlo Calculations. *Phys. Rev. Lett.* **111,** 130402. https://link.aps.org/doi/10.1103/PhysRevLett.111.130402 (13 Sept. 2013) (cit. on p. 121).

334. Zhao, J., Chen, B.-B., Wang, Y.-C., *et al.* Measuring Rényi entanglement entropy with high efficiency and precision in quantum Monte Carlo simulations. *npj Quantum Materials* **7.** issn: 2397-4648. http://dx.doi.org/10.1038/s41535-022-00476-0 (June 2022) (cit. on pp. 121, 124).

335. D'Emidio, J. Entanglement Entropy from Nonequilibrium Work. *Phys. Rev. Lett.* **124,** 110602. https://link.aps.org/doi/10.1103/PhysRevLett.124.110602 (11 Mar. 2020) (cit. on p. 121).

336. Assaad, F. F., Lang, T. C. & Parisen Toldin, F. Entanglement spectra of interacting fermions in quantum Monte Carlo simulations. *Phys. Rev. B* **89,** 125121. https://link.aps.org/doi/10.1103/PhysRevB.89.125121 (12 Mar. 2014) (cit. on p. 124).

337. Parisen Toldin, F., Sato, T. & Assaad, F. F. Mutual information in heavy-fermion systems. *Phys. Rev. B* **99,** 155158. https://link.aps.org/doi/10.1103/PhysRevB.99.155158 (15 Apr. 2019) (cit. on p. 124).

338. Jiang, W., Liu, Y., Klein, A., *et al.* Monte Carlo study of the pseudogap and superconductivity emerging from quantum magnetic fluctuations. *Nature Communications* **13.** issn: 2041-1723. http://dx.doi.org/10.1038/s41467-022-30302-x (May 2022) (cit. on pp. 124, 141).

339. Lieb, E. H. & Ruskai, M. B. A Fundamental Property of Quantum-Mechanical Entropy. *Phys. Rev. Lett.* **30,** 434–436. https://link.aps.org/doi/10.1103/PhysRevLett.30.434 (10 Mar. 1973) (cit. on pp. 134, 165).

340. Schäfer, T., Wentzell, N., Šimkovic, F., *et al.* Tracking the Footprints of Spin Fluctuations: A MultiMethod, MultiMessenger Study of the Two-Dimensional Hubbard Model. *Phys. Rev. X* **11,** 011058. https://link.aps.org/doi/10.1103/PhysRevX.11.011058 (1 Mar. 2021) (cit. on p. 139).

341. Werner, P., Hoshino, S. & Shinaoka, H. Spin-freezing perspective on cuprates. *Phys. Rev. B* **94,** 245134. https://link.aps.org/doi/10.1103/PhysRevB.94.245134 (24 Dec. 2016) (cit. on p. 139).

342. Lee, P. A. From high temperature superconductivity to quantum spin liquid: progress in strong correlation physics. *Reports on Progress in Physics* **71,** 012501. issn: 1361-6633. http://dx.doi.org/10.1088/0034-4885/71/1/012501 (Dec. 2007) (cit. on p. 141).

343. Sordi, G., Haule, K. & Tremblay, A.-M. S. Mott physics and first-order transition between two metals in the normal-state phase diagram of the two-dimensional Hubbard model. *Phys. Rev. B* **84,** 075161. https://link.aps.org/doi/10.1103/PhysRevB.84.075161 (7 Aug. 2011) (cit. on p. 142).

344. Alloul, H. What is the simplest model that captures the basic experimental facts of the physics of underdoped cuprates? en. *Comptes Rendus. Physique* **15,** 519–524 (2014) (cit. on p. 142).

345. Chatzieleftheriou, M., Kowalski, A., Berović, M., *et al.* Mott Quantum Critical Points at Finite Doping. *Phys. Rev. Lett.* **130,** 066401. https://link.aps.org/doi/10.1103/PhysRevLett.130.066401 (6 Feb. 2023) (cit. on p. 142).

346. Van Loon, E. G. C. P., Krien, F., Hafermann, H., *et al.* Double occupancy in dynamical mean-field theory and the dual boson approach. *Phys. Rev. B* **93,** 155162. https://link.aps.org/doi/10.1103/PhysRevB.93.155162 (15 Apr. 2016) (cit. on p. 152).

347. Lechermann, F., Georges, A., Kotliar, G. & Parcollet, O. Rotationally invariant slave-boson formalism and momentum dependence of the quasiparticle weight. *Phys. Rev. B* **76,** 155102. https://link.aps.org/doi/10.1103/PhysRevB.76.155102 (15 Oct. 2007) (cit. on pp. 152, 153).

348. Ayral, T., Lee, T.-H. & Kotliar, G. Dynamical mean-field theory, density-matrix embedding theory, and rotationally invariant slave bosons: A unified perspective. *Phys. Rev. B* **96,** 235139. https://link.aps.org/doi/10.1103/PhysRevB.96.235139 (23 Dec. 2017) (cit. on pp. 152, 153).

349. Lechermann, F., Georges, A., Kotliar, G. & Parcollet, O. Rotationally invariant slave-boson formalism and momentum dependence of the quasiparticle weight. *Phys. Rev. B* **76,** 155102. https://link.aps.org/doi/10.1103/PhysRevB.76.155102 (15 Oct. 2007) (cit. on pp. 152, 153).

350. Lanatà, N., Lee, T.-H., Yao, Y.-X. & Dobrosavljević, V. Emergent Bloch excitations in Mott matter. *Phys. Rev. B* **96,** 195126. https://link.aps.org/doi/10.1103/PhysRevB.96.195126 (19 Nov. 2017) (cit. on pp. 152, 153).

351. Frank, M. S., Lee, T.-H., Bhattacharyya, G., *et al.* Quantum embedding description of the Anderson lattice model with the ghost Gutzwiller approximation. *Phys. Rev. B* **104,** L081103. https://link.aps.org/doi/10.1103/PhysRevB.104.L081103 (8 Aug. 2021) (cit. on pp. 152, 153).

352. Lee, T.-H., Lanatà, N. & Kotliar, G. Accuracy of ghost rotationally invariant slave-boson and dynamical mean field theory as a function of the impurity-model bath size. *Phys. Rev. B* **107,** L121104. https://link.aps.org/doi/10.1103/PhysRevB.107.L121104 (12 Mar. 2023) (cit. on pp. 152, 153).

353. Mejuto-Zaera, C. & Fabrizio, M. Efficient computational screening of strongly correlated materials: Multiorbital phenomenology within the ghost Gutzwiller approximation. *Phys. Rev. B* **107,** 235150. https://link.aps.org/doi/10.1103/PhysRevB.107.235150 (23 June 2023) (cit. on p. 153).

354. Mejuto-Zaera, C. *Quantum embedding for molecules using auxiliary particles – The ghost Gutzwiller Ansatz* 2024. arXiv: 2403.05157 [physics.chem-ph] (cit. on p. 153).

355. Daki ć, B., Vedral, V. & Brukner, C. Č. Necessary and Sufficient Condition for Nonzero Quantum Discord. *Phys. Rev. Lett.* **105,** 190502. https://link.aps.org/doi/10.1103/PhysRevLett.105.190502 (19 Nov. 2010) (cit. on pp. 158, 162).

356. Fetter, A. L. & Walecka, J. D. *Quantum theory of many-particle systems* isbn: 9780486428277 (Dover Publications, Mineola, NY, June 2003) (cit. on pp. 157, 159).

357. Negele, J. W. & Orland, H. *Quantum Many-Particle Systems* isbn: 9780429497926. http://dx.doi.org/10.1201/9780429497926 (CRC Press, Mar. 2018) (cit. on pp. 157, 159).

358. Beggi, A., Siloi, I., Benedetti, C., *et al.* Back and forth from Fock space to Hilbert space: a guide for commuters. *European Journal of Physics* **39,** 065401. https://dx.doi.org/10.1088/1361-6404/aad760 (Aug. 2018) (cit. on pp. 157, 159).

359. Rockafellar, R. T. *Convex analysis* en (Princeton University Press, Princeton, NJ, Dec. 1996) (cit. on pp. 157, 161).

360. Lindblad, G. Expectations and entropy inequalities for finite quantum systems. *Communications in Mathematical Physics* **39,** 111–119. issn: 1432-0916. http://dx.doi.org/10.1007/BF01608390 (June 1974) (cit. on p. 158).

361. Horodecki, M., Horodecki, P., Horodecki, R., *et al.* Local versus nonlocal information in quantum-information theory: Formalism and phenomena. *Phys. Rev. A* **71,** 062307. https://link.aps.org/doi/10.1103/PhysRevA.71.062307 (6 June 2005) (cit. on pp. 158, 162).

362. Hiai, F. & Petz, D. The proper formula for relative entropy and its asymptotics in quantum probability. *Communications in Mathematical Physics* **143,** 99–114. issn: 1432-0916. http://dx.doi.org/10.1007/BF02100287 (Dec. 1991) (cit. on pp. 158, 160).

363. Hübner, M. Explicit computation of the Bures distance for density matrices. *Physics Letters A* **163,** 239–242. issn: 0375-9601. http://dx.doi.org/10.1016/0375-9601(92)91004-B (Mar. 1992) (cit. on p. 158).

364. Petz, D. & Sudár, C. Geometries of quantum states. *Journal of Mathematical Physics* **37,** 2662–2673. issn: 1089-7658. http://dx.doi.org/10.1063/1.531535 (June 1996) (cit. on p. 158).

365. Brody, D. C. Information geometry of density matrices and state estimation. *Journal of Physics A: Mathematical and Theoretical* **44,** 252002. issn: 1751-8121. http://dx.doi.org/10.1088/1751-8113/44/25/252002 (May 2011) (cit. on p. 158).

366. Chitambar, E. & Gour, G. Quantum resource theories. *Rev. Mod. Phys.* **91,** 025001. https://link.aps.org/doi/10.1103/RevModPhys.91.025001 (2 Apr. 2019) (cit. on pp. 158, 160–162).

367. Harrow, A. W. & Montanaro, A. Quantum computational supremacy. *Nature* **549,** 203–209. issn: 1476-4687. http://dx.doi.org/10.1038/nature23458 (Sept. 2017) (cit. on pp. 160–162).

368. Howard, M. & Campbell, E. Application of a Resource Theory for Magic States to Fault-Tolerant Quantum Computing. *Phys. Rev. Lett.* **118,** 090501. https://link.aps.org/doi/10.1103/PhysRevLett.118.090501 (9 Mar. 2017) (cit. on p. 160).

369. Liu, Z.-W. & Winter, A. Many-Body Quantum Magic. *PRX Quantum* **3,** 020333. https://link.aps.org/doi/10.1103/PRXQuantum.3.020333 (2 May 2022) (cit. on p. 160).

370. Haug, T. & Kim, M. Scalable Measures of Magic Resource for Quantum Computers. *PRX Quantum* **4,** 010301. https://link.aps.org/doi/10.1103/PRXQuantum.4.010301 (1 Jan. 2023) (cit. on p. 160).

371. Lami, G. & Collura, M. Nonstabilizerness via Perfect Pauli Sampling of Matrix Product States. *Phys. Rev. Lett.* **131,** 180401. https://link.aps.org/doi/10.1103/PhysRevLett.131.180401 (18 Oct. 2023) (cit. on p. 160).

372. Lami, G. & Collura, M. *Learning the stabilizer group of a Matrix Product State* 2024. arXiv: 2401.16481 [quant-ph] (cit. on p. 160).

373. Tarabunga, P. S., Tirrito, E., Bañuls, M. C. & Dalmonte, M. *Nonstabilizerness via matrix product states in the Pauli basis* 2024. arXiv: 2401.16498 [quant-ph] (cit. on p. 160).

374. Carathéodory, C. Über den variabilitätsbereich der fourier'schen konstanten von positiven harmonischen funktionen. *Rendiconti del Circolo Matematico di Palermo* **32,** 193–217. issn: 1973-4409. http://dx.doi.org/10.1007/BF03014795 (Dec. 1911) (cit. on p. 161).

375. Ollivier, H. & Zurek, W. H. Quantum Discord: A Measure of the Quantumness of Correlations. *Phys. Rev. Lett.* **88,** 017901. https://link.aps.org/doi/10.1103/PhysRevLett.88.017901 (1 Dec. 2001) (cit. on p. 162).

376. Giorda, P. & Paris, M. G. A. Gaussian Quantum Discord. *Phys. Rev. Lett.* **105,** 020503. https://link.aps.org/doi/10.1103/PhysRevLett.105.020503 (2 July 2010) (cit. on pp. 162, 163).

377. Gu, M., Chrzanowski, H. M., Assad, S. M., *et al.* Observing the operational significance of discord consumption. *Nature Physics* **8,** 671–675. issn: 1745-2481. http://dx.doi.org/10.1038/nphys2376 (Aug. 2012) (cit. on p. 162).

378. Oppenheim, J., Horodecki, M., Horodecki, P. & Horodecki, R. Thermodynamical Approach to Quantifying Quantum Correlations. *Phys. Rev. Lett.* **89,** 180402. https://link.aps.org/doi/10.1103/PhysRevLett.89.180402 (18 Oct. 2002) (cit. on p. 162).

379. Girolami, D., Souza, A. M., Giovannetti, V., *et al.* Quantum Discord Determines the Interferometric Power of Quantum States. *Phys. Rev. Lett.* **112,** 210401. https://link.aps.org/doi/10.1103/PhysRevLett.112.210401 (21 May 2014) (cit. on p. 162).

380. Pirandola, S. Quantum discord as a resource for quantum cryptography. *Scientific Reports* **4.** issn: 2045-2322. http://dx.doi.org/10.1038/srep06956 (Nov. 2014) (cit. on p. 162).

381. Luo, S. Quantum discord for two-qubit systems. *Phys. Rev. A* **77,** 042303. https://link.aps.org/doi/10.1103/PhysRevA.77.042303 (4 Apr. 2008) (cit. on pp. 162, 163).

382. Huang, Y. Computing quantum discord is NP-complete. *New Journal of Physics* **16,** 033027. issn: 1367-2630. http://dx.doi.org/10.1088/1367-2630/16/3/033027 (Mar. 2014) (cit. on p. 163).

383. Chen, Q., Zhang, C., Yu, S., Yi, X. X. & Oh, C. H. Quantum discord of two-qubit X states. *Phys. Rev. A* **84,** 042313. https://link.aps.org/doi/10.1103/PhysRevA.84.042313 (4 Oct. 2011) (cit. on p. 163).

384. Huang, Y. Quantum discord for two-qubit X states: Analytical formula with very small worst-case error. *Phys. Rev. A* **88,** 014302. https://link.aps.org/doi/10.1103/PhysRevA.88.014302 (1 July 2013) (cit. on p. 163).

Acronyms

AFM antiferromagnet(ic). ix, x, 3, 7, 8, 15, 17, 22, 46, 50, 52, 53, 63, 64, 66–68, 70, 72, 74, 76

$AFM_{\parallel}$ easy-plane antiferromagnet. ix, 44, 45, 49, 51, 53, 54, 57, 60, 62, 63, 65–70, 73, 75, 77

$AFM_{\perp}$ out-of-plane antiferromagnet. ix, 44, 45, 49, 54–57, 60, 62, 63, 65–70, 72, 73, 75, 76

AFMTI antiferromagnetic topological insulator. 29, 36, 50, 79, 80

AFQMC auxiliary-field quantum Monte Carlo. 65

AIM Anderson impurity model. 11, 12, 45

ASCI adaptive sampling configuration interaction. 112–114, 117–120, 134–136

CDMFT cluster dynamical mean-field theory. v, viii, x, xi, 13, 84–86, 103–106, 108–114, 117, 118, 120, 122, 125, 126, 128, 129, 131, 134, 137, 139, 142, 143, 146, 147, 149, 151–153, 165

CTQMC continuous-time quantum Monte Carlo. 118

DCA dynamical cluster approximation. 104, 109, 139, 152, 153

DMFT dynamical mean-field theory. v, vii–ix, 4, 6, 7, 9–17, 21, 24, 25, 30, 35, 36, 41, 44–46, 49–55, 57, 59, 60, 62–72, 79, 83, 84, 103, 104, 106, 108–112, 117, 118, 120, 123, 124, 142, 151–153, 198

DMRG density matrix renormalization group. 50, 79, 103, 123, 124

DΓA dynamical vertex approximation. 103, 153

ED exact diagonalization. ix, 10, 44–46, 63, 65–70, 85, 112–114, 117–120, 122, 125, 126, 128, 129, 131, 135, 136, 142, 143, 146, 147, 149, 152

HF Hartree-Fock. v, viii, 7, 15–17, 21, 29, 36, 42, 43, 45–47, 49–52, 54, 55, 57, 65–70, 79, 151

KMH Kane-Mele-Hubbard (model/Hamiltonian). 29, 35, 41, 42, 57, 63, 69, 71

LOCC local operations and classical communication. 88, 99, 138, 161

MIT metal-insulator transition. vi, vii, 6, 8, 9, 17, 22, 23, 26, 83, 84, 86, 109, 111, 118, 119, 124, 125, 132, 141, 144–146, 148

N-SSR charge superselection rule. 91, 93–98, 100, 101, 128–133, 148, 149

NRG numerical renormalization group. 65

P-SSR parity superselection rule. 91, 93–98, 100, 101, 128–133, 148, 149

POVM positive operator-valued measures. 122

PPT positive partial transpose. 88, 95, 98, 99, 138

QMC quantum Monte Carlo. 35, 79, 83, 84, 103, 121, 123, 124, 139

QRE quantum relative entropy. 87, 91, 96, 99, 137, 138, 151, 158, 160, 161, 163, 164

QSHI quantum spin-Hall insulator. v, viii, ix, 27–29, 35, 36, 39, 41, 49, 51, 53–57, 59, 60

RDM reduced density matrix. 18, 22, 36, 61, 88, 89, 91–94, 98, 100, 112–115, 120, 122, 125, 132, 152, 159

RDMFT real-space dynamical mean-field theory. 71

REE relative entropy of entanglement. 86–88, 90, 91, 93, 99, 117, 130, 137–139, 146, 148, 149, 161, 163, 164

RISB rotationally invariant slave-boson. 153

SMIT semimetal-insulator transition. 16, 21, 24–26, 57, 124

SSR superselection rule. x, 85, 86, 88, 91–93, 95, 98, 100, 101, 117, 128, 130–133, 138, 149, 153, 164

TRILEX triply irreducible local expansion. 103

VCA variational cluster approximation. 50, 79

Acknowledgements

As I recently discovered, with no small dismay, writing a PhD thesis is an extremely hard undertaking, that would be impossible to complete without the help of mentors, fellows and friends. First of all I would like to express my greatest gratitude to Massimo, my *old&wise*[1], but also extremely nerdy and juvenile, advisor. Of course, he has helped and guided me through the whole research journey, almost four full years, never failing to support my excitement for the weirdest idea I would come up with, but also ensuring that my occasional off-track trip would not end up in a ton of wasted time. A bit yes, a ton never, as it should be! However, today, while I write these few lines just before the submission deadline, I would want to especially acknowledge the willingness to join the titanic, excruciating effort that is brought by finalizing a thesis in a mad rush. Yes, this whole manuscript has been written in the silliest, guiltiest and unwisely shortest amount of time. Yet, Massimo has not bailed out of the situation and we had together a bunch of really exhausting days (followed by a long talk, of course). I will never forget, thanks!

To Adriano I surely owe a Shàolín-temple-level training in public debate, over any topic, including *of course* science. Do you still remember my first journal club? About that *topomott*[2] paper... Though times, hahah. But I quickly grew into liking that level of questioning, it is hard, but also hardening. I appreciate it. I guess I also owe you my first nose bump into the *nix shell, but maybe that was too hardening in just three hours :)

Speaking of shells and codes, I'd like to give a big thank to all the guys from the fortran-lang discourse group. Lately I have been so busy with all these projects and the writing (no, that's a lie, again, the writing was a rush! So between the projects and the procrastination) and I truly miss all the debate, the ideas and the learning. I really learnt a lot from all of you. Big, big thank you all!

Well, well, well, I guess it's time to mention aaaaaall the wonderful colleagues I have been in contact with, in this wonderful place that the SISSA school really is. Thanks Fabio for the early debate (I think it was my second or third lunch in the canteen!) about Kohn-Sham theory and why *you are still convinced it cannot work*! And of course about all the other chats we had later! Thanks Martino for extremely long hours in the sun of the sixth floor, talking about topology, about movies, books, sleeping, even serial killers, damn! I miss

[1] sorry
[2] [102]

those, a lot. Thanks Seclì for the unprecedented and probably ever unmatched amount of *nerdichloria* in your veins. It is really contagious. I learned a lot, I'm still inspired a lot. I miss you a lot. Thanks Davide for always downright saying the most politically incorrect sentence imaginable, in every situation. But most importantly, thanks for being always so damn cheerful, even when it is clearly nonsense. Truly unique. Well, and for all the reels. There is another master of reels to acknowledge: thanks Ricardo, you really gave one of the few lights in the dark time of frantically writing, super appreciated! Well, also thanks to Erik, I don't know exactly why, but I guess I should thank you too (everything said with the straightest, unbearable poker face ever seen on earth... but maybe on that other exoplanet, how was called, you never remind us the name, mmm Svedden, right?). Thanks Alberto for finally making me understand what the DMFT loop is, under the hood. I should have known, of course, but sometimes you just really need the right words, from someone that sees it in the completely opposite way as you do. Oh, and well, thanks also to Carlos, for giving me yet another completely different way of thinking about it. Mmm, maybe I still don't know what it really is, exciting! Of course to *Don Carlos* I have to say much much more. Thanks for being a truly wonderful coauthor. I have very little experience, but I really suspect your human and professional approach is truly precious. Thanks for always annoying me with nonsense[3] verses. And thanks for somehow always getting it right when it comes to decide whether you should be serious o el mas grande payaso de Melide. Thanks to Pablo, you're always kind and never nervous, I admire it! Thanks to Laura Fanfarillo for being so damn funny, I never suspected it and it was a pleasure to uncover this truth! Also thanks to Argo, for... all the energy and life that he really sprinkles everywhere.

Thanks to my old and new office mates. Sam for always beating me (violence hot-line do you copy?? pleease) and, jokes apart, for reminding me that no, whatever it happens around you, whatever damn inevitable doom you think you are facing, you can always say "ma sticaaazzi" and work for what you want, demand it, strive for it. I had forgot. Thanks to Matto the runner for being so kind, always attentive, never, ever inappropriate. True rarity. Oh, and thanks Claudia, for a very very short "cohabitation" in room 301, but equally pleasant! Thanks to Francesca for all the time spent together during the pandemics, it has been a lot of fun. Thanks Andrea for our chatting on why the SSH model is not a topological insulator and a lot of arguing about the right way to understand the Mott transition in cluster methods, but always with really thoughtful observations. And yeah, I know that you all are thinking that I have forgot, but come on, how would I? Thaaanks to the mighty *bad batch*: the scourge of Fabrizio, the CFU undercollectors, the enders of the solid state problems course hahaha. Thanks to Nishan for a looot of fast chat, for a long long night at ICTP, for always bringing the most surprising gadgets to office. Thanks to Guglielmo, for all the music and physics we shared. Thanks to Pietro,

[3] lo siento, *it is what it is*

big-time confidant, brave opponent of guilty silence and unmatched expert on colors (ops! haha). Thanks to Ali! I still remember our crazy days tinkering with nanotubes, good memories! Thanks to Matej for always having a kind word of encouragement for me and thanks Matteo for the longest, looongest night hours talking about physics. You're crazier than me, damn! Thanks to Neven for revealing to me that github is so great and thanks Mina, for finding the time to hear me play, even down there in Muggia!

Outside of the CM gang, thanks Chiaretta for all the peeping at my brain, at some point I bailed you and I still feel deeply sorry about that. But they are fun and warm memories to me. Thanks Guido for being my Cicero at the very start, thanks also for having shown me that even the most brilliant minds, sometimes, have doubts about the future and where they are heading. Thanks to Laura for trying to help in what definitely was one of the darkest moments in my life. It didn't work out between us, but I appreciate the effort!

Finito con la SISSA, direi che passiamo all'italiano! Grazie a Olga, Sara, Noemi, Franz, Andrea, Matteo, Irina, Luca, Sandro, Elia, Davide, Paola, Laura, Saule, Tijana, Veronica, Fabio, Baya e tutti coloro con cui ho condiviso della Musica in questi anni. Siete importanti, non sapete quanto. Un grazie speciale ai Bohemini a cavallo della pandemia (più grande attesa della storia) e ai Nabucodonosori delle ultime settimane. Che fatica!

Grazie ai miei genitori, sempre presenti e tolleranti della mia assenza, ultimamente troppo spesso reiterata. Papà mi ha donato il bruciante amore per la conoscenza[4] e Mamma il gusto di puntare alto. Ve ne sarò per sempre grato e indubbiamente, assieme agli incoraggiamenti del buon Raffaele, è proprio questa duplice carica che mi ha permesso di essere qui oggi, a scrivere queste righe. Grazie! Infinite grazie di cuore e di pancia a Nataly, per non finire mai di insegnarmi quanto si può essere forti e maledettamente coraggiosi in questo mondo. Più passano gli anni e più ammiro la donna che sei diventata!

Per concludere un abbraccio fortissimo alla mia Trincallegra. Mi hai sostenuto sempre e continui a farlo imperterrita, mi sopporti, mi conforti, mi aiuti a rimettere a fuoco cosa è importante nella vita. Non so cosa farei senza di te e sicuramente non sarei riuscito ad arrivare così... semplicemente *felice* alla fine di questo percorso. Con te ringrazio anche Joulie e Lakshmina del suo cuore (mmm) per come ci riempiono le giornate e le vite. Hai e avete reso tutto speciale.

[4] Sì Lilla, grazie del prestito!